2011

Dynamic Measurements with Scanning Probe Microscopy: Surface Studies Using Nanostructured Test Platforms of Metalloporphyrins, Nanoparticles and Amyloid Fibrils

Wilson K. Serem
Louisiana State University and Agricultural and Mechanical College, wserem1@lsu.edu

DYNAMIC MEASUREMENTS WITH SCANNING PROBE MICROSCOPY: SURFACE STUDIES USING NANOSTRUCTURED TEST PLATFORMS OF METALLOPORPHYRINS, NANOPARTICLES AND AMYLOID FIBRILS

A Dissertation

Submitted to the Graduate Faculty of the
Louisiana State University and
Agricultural and Mechanical College
in partial fulfillment of the
requirements for the degree of
Doctor of Philosophy

In

The Department of Chemistry

by
Wilson K. Serem
B.S., University of Nairobi, 1997
M.S., Moi University, 2002

December, 2011

ACKNOWLEDGEMENTS

I want to start by saying that I could never have reached the heights or accomplished the depths in my academic pursuits without the help, support, guidance and efforts of many people. First, many thanks goes to my advisor Dr. Jayne C. Garno for nurturing her guidance and encouragement in my graduate life. I also would like to thank Dr. Bin Chen, Dr. Philip Adams, Dr. Bing-Hao Luo and Dr. Donghui Zhang for accepting to serve as my committee members.

I would also like to thank past and present members of Dr. Garno group such as Dr. Johnpeter Ngunjiri, Dr. Zorabel Lejeune, Dr. Stephanie Daniels and Dr. Kathie Lusker for their help, valuable suggestions and support over many years. My thanks also go to the current members of Dr. Garno group such as Venetia Lyles, Lauren Englade, ChaMarra Saner, Tian Tian, Shalaka Kulkarni and Lu Lu.

My very special thanks go to two people who I owe everything I am today, my father Peter K. Serem and to my mother Rosaline J. Serem for their unwavering faith and confidence in my abilities. Most of all, my appreciation goes to my daughter Kate Serem and my wife Gladys Serem for their love and support. I would also like to thank my sisters and brothers Dinah, Willy, Walter, Wycliffe, Wilfred, Devenah, Wilberforce and Wellington who showed me the true worth of hard work.

TABLE OF CONTENTS

LIST OF TABLES

LIST OF FIGURES

LIST OF ABBREVIATIONS

Abbreviation	Name
AFM	Atomic Force Microscope or Atomic Force Microscopy
CdSe	Cadmium selenide
DMAP	4-(N,N-dimethylamino)pyridine
DPN	Dip-Pen Nanolithography
EM	Electron Microscopy
$FeNi_3$	Iron(III)-nickel
GUMBOS	Group of Uniform Materials Based on Organic Salts
$HAuCl_4$	Tetrachloroaurate
HOPG	Highly Oriented Pyrolytic Graphite
ILs	Ionic Liquids
MFM	Magnetic Force Microscopy
MPC	Monolayer Protected Clusters
MPTMS	Mercaptopropyltrimethoxysilane
MSM	Magnetic Sample Modulation
NPRW	NanoPen Reader and Writer
OTS	Octadecyltrichlorosilane
SEM	Scanning Electron Microscopy
SERS	Surface Enhanced Raman Spectroscopy
SET	Single Electron Tunneling
SiO_2	Silicon dioxide
SNOM	Scanning Near-field Optical Microscopy
SPL	Scanning Probe Lithography
SPM	Scanning Probe Microscopy
SPR	Surface Plasmon Resonance
STM	Scanning Tunneling Microscopy
TEM	Transmission Electron Microscopy
TM-AFM	Tapping Mode Atomic Force Microscopy
$TPPF_{20}$	5,10,15,20-tetrakis(2,3,4,5,6-pentafluorophenyl) porphyrin
UHV	Ultra High Vacuum
XRD	X-Ray Diffractometry
PDMS	Polydimethylsiloxane
MAC	Magnetic AC
IMM	Indirect Magnetic Modulation
CP-AFM	Conductive Probe AFM

ABSTRACT

A hybrid imaging mode for characterization of magnetic nanomaterials has been developed, using atomic force microscopy (AFM) combined with electromagnetic sample actuation. Instead of using a coated AFM probe as a magnetic sensor; our strategy is to use a nonmagnetic probe with contact mode AFM to characterize the vibration of magnetic and superparamagnetic nanomaterials responding to the flux of an AC electromagnetic field. We refer to the hybrid imaging mode as magnetic sample modulation (MSM-AFM). An oscillating magnetic field is produced by applying an AC current to a wire coil solenoid placed under the sample stage for tuning selected parameters of driving frequency and strength of the magnetic field. When the AC field is on, the AFM probe is scanned in contact with the sample to sense periodic changes in the force and motion of vibrating nanomaterials. With MSM, responses of both the amplitude and phase signal along with spatial maps of the topography channel can be collected simultaneously. A requirement for MSM is that the samples can be free to vibrate, yet remain attached to the surface. Particle lithography was used to prepare well-defined test platforms of ring structures of magnetic or superparamagnetic nanomaterials. Capillary filling of polydimethylsiloxane (PDMS) molds was applied to generate stripes of $FeNi_3$ nanoparticles with microscale dimensions as test platforms. The MSM-AFM imaging mode was used successfully to characterize nanomaterials of $FeNi_3$ nanoparticles, cobalt nanoparticles, octa-substituted porphyrin nanocrystals and ionic liquid nanoGUMBOS with dimensions ranging from 1 to 200 nm. Dynamic MSM-AFM measurements can be obtained by placing the tip on a vibrating nanoparticle and sweeping the frequency or field strength. Changes in frequency spectra and vibrational amplitude can be mapped for nanoparticles of different sizes, shapes and composition. The MSM-AFM imaging mode provides a useful tool for investigating changes in size dependent magnetic properties of materials at the nanoscale. Samples of designed amyloid proteins were characterized *ex situ* using scanning probe microscopy. The progressive growth and fibrillization of amyloid β over extended time intervals was visualized with high resolution using AFM.

CHAPTER 1. INTRODUCTION

The investigations presented in this dissertation apply a strategy of combining nanoscale lithography approaches with ultrasensitive scanning probe measurements to understand fundamental chemical processes of surface reactions. Well-defined, nanostructured test platforms can be successively characterized using high resolution mapping capabilities of atomic force microscopy (AFM) with measurement modes for nanoscale measurements of material properties. A key strategy for developing the new MSM-AFM imaging mode is to use designed nanopatterned arrays of magnetic nanoparticles to evaluate sensitivity and resolution. "Two particle" lithography was used to prepare well-defined test platforms of superparamagnetic cobalt nanoparticles. Particle lithography using an immersion approach was used to generate nanostructures within a film of octadecyltrichlorosilane (OTS) formed on silicon. Nanostructures of octasubstituted cobaltacarborane porphyrins were prepared for MSM-AFM investigations. Several dynamic protocols were developed for characterizing samples of octa-substituted cobaltacarborane porphyrin nanocrystals, $FeNi_3$ nanoGUMBOS, cobalt and $FeNi_3$ nanoparticles using MSM-AFM. Dynamic measurements were acquired for samples when the parameters of the magnetic field strength or the driving frequency were changed *in situ*. An important outcome of developing MSM-AFM will be the contribution of a new magnetic spectroscopy for routinely evaluating and viewing samples with magnetic or superparamagnetic character, enabling exceptional sensitivity and selectivity for detecting the vibrational response of nanomaterials.

As material composition changes, the magnetic moment of nanomaterials are observed to change; however size-dependent magnetic properties often are not well-defined due to the difficulties of making measurements for individual nanoparticles or single molecules. Most

commonly, measurements of magnetic properties are based on bulk samples having hundreds to thousands of nanoparticles in aggregated form, rather than on local measurements of individual, distinct entities. Nanolithography approaches provide a way to position individual nanoparticles or nanocrystals to enable measurements for individual materials without the coupling effects of neighboring entities. The requirement to have increased bit densities and decreased bit sizes[13] makes magnetic nanoparticles excellent candidates for efficient data storage. Studies of magnetic nanoparticles have shown magnetic properties to be strongly dependent on the size of the materials.[14] As the size gets smaller, the number of correlated spins of electrons is reduced, generating magnetism.[15] For example, nanostructured iron, cobalt and nickel have been found to be ferromagnetic.[16] Manganese oxide particles (7 nm) have been reported to exhibit ferromagnetic behavior.[17] Thus far, the MSM-AFM imaging mode has been applied to successfully characterize nanoparticles of iron oxide clusters (6 nm), ferritin[18] and intermetallic $FeNi_3$ nanoparticles with diameters as small as 0.9 nm. The investigations of this dissertation emphasize the development of new dynamic protocols with MSM-AFM, as well as studies of different types of magnetic and superparamagnetic nanomaterials.

1.1 Imaging Modes of AFM Used for This Research

An overview of the background and operating principles of AFM imaging modes used in this dissertation are described in Chapter 2. Contact and intermittent modes of AFM are the most commonly used approaches for surface investigations, and are detailed in Chapter 2. Dynamic modes of AFM are emerging as versatile methods for achieving atomic and nanometer scale characterization of materials. There are two major modes of dynamic AFM operations namely amplitude modulation (AM-AFM) or tapping-mode AFM (TM-AFM), and frequency

modulation (FM-AFM).[19] Vibrating probes are used to characterize the surface morphology in dynamic imaging modes. Tapping-mode AFM has been used to obtain high resolution images of proteins, DNA,[20-23] polymers,[24] cells[25] and nanoparticles.[26] Both ambient and liquid environments have been applied to characterize nanostructures using dynamic modes of AFM.

1.2 Characterization of Nanoparticles and Nanocrystals Using Scanning Probe Microscopy

Chapter 3 provides a detailed review for applying scanning probe microscopy (SPM) to characterize nanoparticles and nanocrystals.[27] An overview of using scanning tunneling microscopy (STM) for characterization and manipulation of nanoparticles, as well lithographic strategies such as NanoPen Reader and Writer (NPRW), nanografting, dip-pen nanolithography (DPN) and particle lithography are also summarized in Chapter 3. Inorganic synthesis and materials chemistry have made it possible to synthesize and tailor the properties of nanoparticles for diverse applications. Nanoparticles have been conjugated with DNA, peptides and antibodies to generate nanoparticle bioconjugates with hybrid functionalities that are useful for a broad range of applications in bioanalytical assays, targeted drug-delivery and nanotechnology. Concurrent with development of synthetic approaches for nanoparticles, new measurements have evolved using scanning probe microscopy (SPM), providing unprecedented resolution and measurement capabilities for characterizations of the morphology and certain properties of nanoparticles and nanocrystals. New measurement technologies with SPM are still being invented, and the tools of SPM have been widely implemented by researchers in both academia and industry. The incentive and primary advantage for SPM measurements are the capabilities of reaching atomic and molecular resolution. Local surface modification can also be accomplished with SPM-based lithographies. In Chapter 3, recent applications of SPM for nanoscale

measurements and nanofabrication with different systems of nanoparticles and nanocrystals are reviewed. Scanning probe measurements provide unprecedented resolution for characterizing nanomaterials to investigate physical, chemical and biochemical properties at the nanoscale. The advantages and limitations of SPM are also discussed, with descriptions of the various imaging and lithography modes that have been applied for characterizing nanoparticles.[27]

1.3 Characterization of $FeNi_3$ Nanoparticles Using Magnetic Sample Modulation-AFM

Micropatterns of $FeNi_3$ generated via capillary filling and characterized using MSM-AFM is presented in Chapter 4. The surface is first scanned in conventional contact mode to acquire topography and lateral force images. The same area of the surface is then scanned again while applying an oscillating electromagnetic field to the sample. The flux of the electromagnetic field causes magnetic nanoparticles to selectively vibrate, and the motion is detected by an AFM probe. The dynamics of actuated nanoparticles can be investigated by changing the modulation frequency and strength of the electromagnetic field. Using capillary filling of PDMS molds, intermetallic $FeNi_3$ nanoparticles were patterned reproducibly at the microscale as test platforms for MSM investigations. Changes in phase and amplitude images induced by MSM-AFM can be used to detect and map the positions of magnetic nanomaterials. The changes in vibrational response of $FeNi_3$ nanoparticles can also be detected as the magnitude of the applied electromagnetic field was increased. With MSM-AFM, responses of both the amplitude and phase signal simultaneously with the topographic channel, as well as spectra of the vibrational response can be acquired at the level of individual nanoparticle. Proof-of-concept images were acquired to demonstrate that $FeNi_3$ composite nanoparticles can be resolved using MSM-AFM, as presented in Chapter 4. (*Manuscript in preparation.*)

1.4 Characterization of Cobalt Nanoparticles Using Magnetic Sample Modulation-AFM

Views of cobalt nanostructures characterized using tapping-mode and MSM-AFM are presented in Chapter 5. Using "Two particle" lithography test structures of metal nanoparticles can be prepared easily and reproducibly. Ring or pores nanostructures were prepared by changing the ratio of the structural template to the nanoparticles. Cobalt nanostructures with well-defined geometries were used as test platforms for MSM-AFM investigations. The information obtained for cobalt nanoparticles demonstrate the capabilities for ultrasensitive magnetic measurements with MSM-AFM. The experiments presented in Chapter 5 demonstrate the applicability of MSM-AFM for characterizing DNA-templated cobalt nanoparticles. (*Manuscript in preparation.*)

1.5 Dynamic Measurements of Porphyrin Using Magnetic Actuation of Samples

Chapter 6 discloses experiments using newly-developed protocols for dynamic MSM-AFM measurements to characterize designed test platforms of octa-substituted cobaltacarborane nanocrystals of porphyrin. Magnetic sample modulation combined with AFM provides a sensitive new way to detect the vibration of magnetic nanomaterials at the level of individual nanoparticles or nanocrystals. Our strategy was to use patterned test platforms prepared using particle lithography with organosilanes, as model surfaces for scanning probe studies. New protocols for dynamic measurements were developed to characterize nanocrystals of cobaltacarborane porphyrins in Chapter 6, with changes of the modulation frequency and the strength of the electromagnetic field. With MSM-AFM, responses of both the amplitude and phase signal along with spatial maps of the topography channel can be collected simultaneously. The MSM-AFM imaging mode has been used successfully to detect the vibration of

nanomaterials with dimensions less than 1.0 nm, and is not limited to ferromagnetic materials. An outcome for MSM-AFM imaging will be a route for magnetic spectroscopy for routinely characterizing magnetic or superparamagnetic properties of nanomaterials. (*Manuscript in preparation.*)

1.6 Mapping Vibrational Responses of nanoGUMBOS

Sensitive mapping and detection of nanoGUMBOS using MSM-AFM is described in Chapter 7. The synthesis of the magnetic micro- and nanoparticles developed from the frozen IL 1-butyl-2,3-dimethylimidazolium hexafluorophosphate ([bm2Im][PF6]) via a melt emulsion quench approach has been accomplished.[28] Dynamic measurements when the parameters of the magnetic field strength or the driving frequency were systematically ramped are demonstrated in Chapter 7 for nanoGUMBOS. Entities with dimensions 1< nm were mapped in phase and amplitude MSM views. (*manuscript in preparation*)

1.7 Progressive Growth of β-Amyloid Fibrils Studied with High-Resolution AFM

Mapping of the progressive growth for amyloid β fibrils over time using *ex-situ* AFM is discussed in Chapter 8.[29] Amyloid peptide (Aβ) is the major protein component of plaques found in Alzheimer's disease, and the aggregation of Aβ into oligomeric and fibrillic assemblies has been shown to be an early event of the disease pathway. Visualization of the progressive evolution of nanoscale changes in the morphology of Aβ oligomeric assemblies and amyloid fibrils has been accomplished *ex situ* using AFM in ambient conditions. In this chapter, the size and the shape of amyloid $\beta_{1\text{-}40}$ fibrils, as well as the secondary organization into aggregate structures were monitored at different intervals over a period of five months. Characterizations with tapping-mode AFM serve to minimize the strong adhesive forces between the probe and the

sample to prevent damage or displacement of fragile fibrils. The early stages of Aβ growth showed a predominance of spherical seed structures, oligomeric assemblies, and protofibrils; however the size and density of fibrils progressively increased with time. Within a few days of incubation, linear assemblies and fibrils became apparent. Over extended time scales of up to 5 months, the fibrils formed dense ensembles spanning lengths of several microns, which exhibit interesting changes due to self-organization of the fibrils into bundles or tangles. Detailed characterization of the Aβ assembly process at the nanoscale will help elucidate the role of Aβ in the pathology of Alzheimer's disease.

1.8 Future Prospectus

Chapter 9 provides a conclusion and future prospectus for this dissertation. Chapter 9 of this dissertation highlights charge transport through stacks of porphyrin molecules using conductive probe AFM (CP-AFM). Proof-of-concept for applying indirect magnetic modulation (IMM-AFM) to map needle structures of porphyrins is also presented in Chapter 9. Indirect magnetic modulation (IMM) mode is an approach for force modulation measurements of the elastic response of samples.

CHAPTER 2. EXPERIMENTAL APPROACH: IMAGING MODES OF SCANNING PROBE MICROSCOPY

2.1 History of Scanning Probe Microscopy

Scanning probe microscopy (SPM) is a family of surface characterization methods which are based on using a probe to scan samples. Scanning tunneling microscopy (STM) was pioneered by Gerd Binnig and Heinrich Rohrer in 1982, who jointly received the 1986 Nobel Prize in Physics.[30] The principle of STM is based on the electrons that tunnel over very short (< 1 nm) distances, and therefore STM imaging is limited to atomically-flat samples that are conductive or semiconducting. The development of atomic force microscopy (AFM) was reported later in 1996 by Binnig, Quate, and Gerber. The invention of AFM has expanded the capabilities of scanning probe instruments to imaging non-conductive or insulating materials.[31] The underlying principle of all AFM imaging modes is the ultrasensitive measurement of forces, (e.g. attractive, repulsive, magnetic, electronic, etc.) using a microfabricated probe. Another advantage of AFM-based measurements is to generate exquisite views of samples both in air and liquid media without requiring a vacuum environment. A unique capability of SPM imaging is that since microfabricated probes are used to interrogate the surface, resolution is not limited by the wavelength of light.

Contact, tapping and non-contact modes are the three operational modes for SPM measurements. The most common imaging modes for AFM are contact mode and tapping mode, where the tip touches the surface to profile topography. Non-contact AFM is usually accomplished in ultrahigh vacuum chambers, and is based on sensing Van der Waals' forces between the probe and sample.[32] There are also other modes which require specific modifications to the instrument configuration or changing the feedback mechanism for controlling tip

positioning. Rich information of structure and properties such as elasticity, adhesion, hardness, conductivity, electronic properties and magnetic forces of materials can be obtained with different SPM instrument configurations.

2.2 Principle of Atomic Force Microscopy

For the most common AFM configuration, light from a diode laser is focused on the backside of a reflective cantilever. The piezo-electric ceramic scanner has 3 segments which enables sub-angstrom resolution in x-, y- and z-directions. The typical resolution routinely achieved is 1 nm or less in the lateral dimension and 0.1 nm in the z- direction.

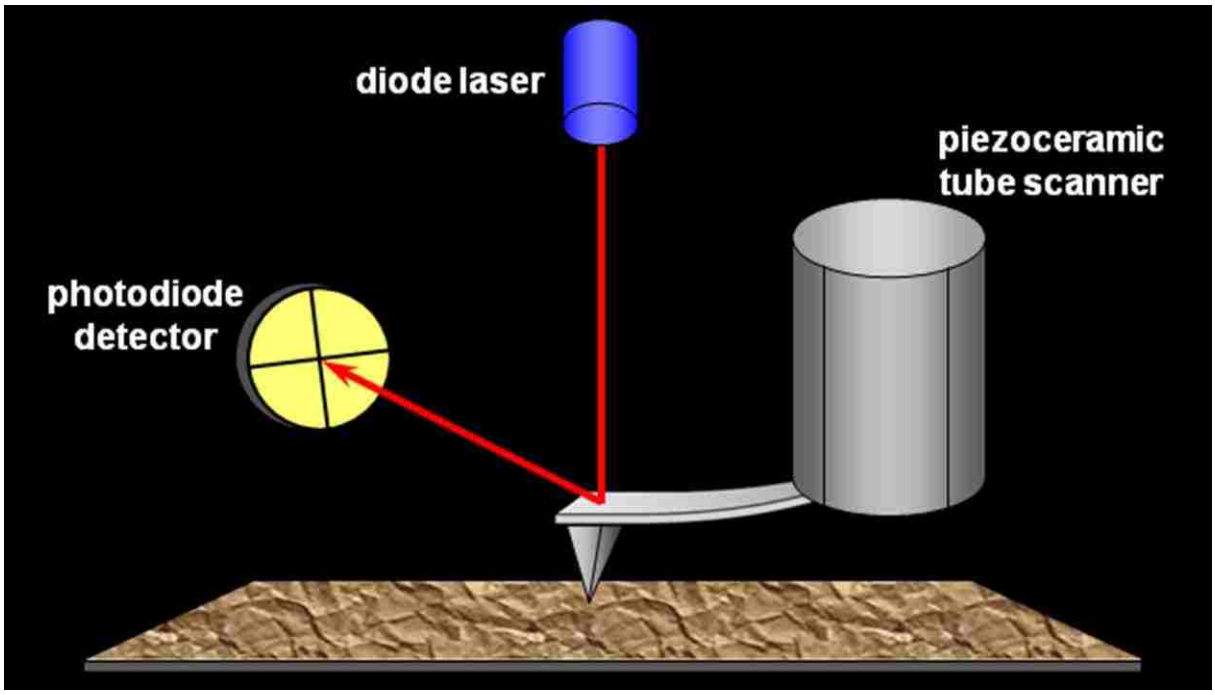

Figure 2.1. Basic principle of AFM.

2.2.1 Contact Mode and Lateral Force AFM

An atomically sharp tip attached to a cantilever is used for contact mode AFM. The cantilever is attached to a piezoelectric scanner. By lowering the tip to touch the sample surface

the force between the sample and tip can be precisely controlled with the piezoscanner. The feedback loop of the computer controller adjusts the voltages applied to the piezoscanner to maintain a constant force setting between the tip and the surface during the imaging process. Contact mode AFM provides unprecedented resolution for viewing the shapes and morphology of surfaces.

Lateral force images are acquired simultaneously with topography frames during steps of AFM characterizations. Lateral force images are constructed by digitally tracking the torsional twisting of the cantilevers attributed to the difference in chemistries on the sample areas. The left and right movements of the probe induce changes in the position of laser spot on the photodetector, which are used to construct lateral force images. Measurements of nanoscale friction can be derived by subtracting the trace and retrace lateral force images. Contact mode and lateral force AFM imaging have been applied for characterization of nanomaterials such as of metals,[33-39] polymers,[40] porphyrins,[41] metal alloys,[42, 43] monolayer protected clusters (MPCs)[44] and nanocrystals of quantum dots.[45-47]

2.2.2 Scanning Force Spectroscopy

Force-distance curves are used to determine elasticity and adhesion at the molecular level. A force-distance curve is generated by plotting cantilever deflection as a function of the sample position along the z-axis. Both approach and retraction probe are obtained. The sensitivity of the force distance curves is at 1 pN.[48, 49] Hooke's law relationship (equation 1) is used to compute the force, F, where k is the spring constant of the cantilever and z is the cantilever deflection.[50]

Hooke's law: $F = -kz$ (eq. 1)

An example force curve acquired in air for a sample of OTS nanostructures on silicon wafer is depicted in Figure 2.2. There is no deflection of the cantilever when the tip is far away from the sample and therefore the interaction forces between the probe and the surface can be considered to be negligible (label A). The interaction between the tip and the sample causes the cantilever to bend upward as the probe approaches the surface, due to the repulsive forces (label B). As the bending continues the tip will ultimately snap into contact with the sample surface. Maximum deflection (label C) of the cantilever is obtained as more force is applied to the tip. On retracting the tip from the surface, the probe will have to overcome the adhesion forces and "jump-off" (label D) of the surface.

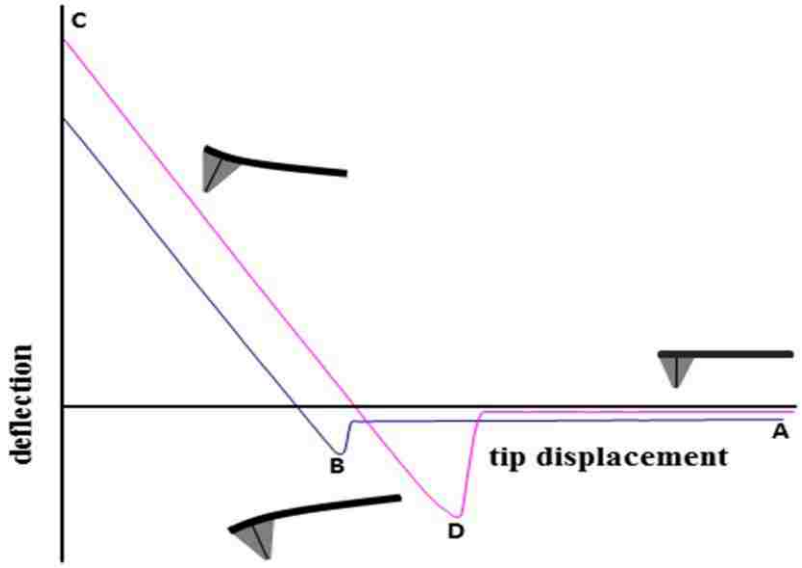

Figure 2.2. Force distance curve acquired in air.

2.2.3 Tapping-mode AFM and Phase Imaging

Tapping-mode AFM is an intermittent mode of AFM imaging. Tapping-mode is also referred to as amplitude modulation or AC mode. A stiff cantilever (higher force constant) is most commonly used for tapping-mode, with certain resonance frequencies (ranging from 160 to 300 kHz). The cantilever is oscillated at or near its free resonance frequency when imaging a sample. Positional feedback for tapping-mode AFM is accomplished by maintaining a constant amplitude of tip oscillation during scans. Tapping-mode AFM provides advantages for characterizing soft and delicate samples or materials that are loosely attached to the substrate. Imaging in continuous contact mode has disadvantages due to shear forces and alteration of the sample by the AFM probe operated under force. Tapping-mode was developed for non-destructive imaging. High resolution images of sticky samples can also be obtained using tapping-mode, which minimizes forces of stick-slip adhesion. Two channels consisting of topography and phase are simultaneously acquired when the tip is driven to "tap" the surface.[23, 51-53] Properties of materials such as viscoelasticity, adhesion and softness are mapped by recording the difference between the phase angle of the signal that drives the tip oscillation relative to changes resulting from tip interactions with the sample. For ambient characterization in air using tapping mode, the typical resonant frequency probes ranges from 160 to 300 kHz, however softer cantilevers with resonances below 100 kHz can be used for imaging in liquid environments.

2.2.4 Principle of Magnetic Sample Modulation AFM

The principle of imaging with magnetic sample modulation AFM (Figure 2.3) is based on selective actuation of magnetic or paramagnetic samples using the typical configuration of

contact mode imaging. An AC-generated electromagnetic field is applied to the samples by a wire coil solenoid located beneath the MAC-mode sample plate. Magnetic nanomaterials are driven to vibrate in response to the magnetic flux and are detected using a soft non-magnetic probe. The surface is first scanned in conventional contact mode to acquire topography and frictional force images. The same area of the surface is then scanned again while applying an oscillating electromagnetic field. The change in polarity drives magnetic nanoparticles to selectively vibrate in response to the flux of the oscillating magnetic field.

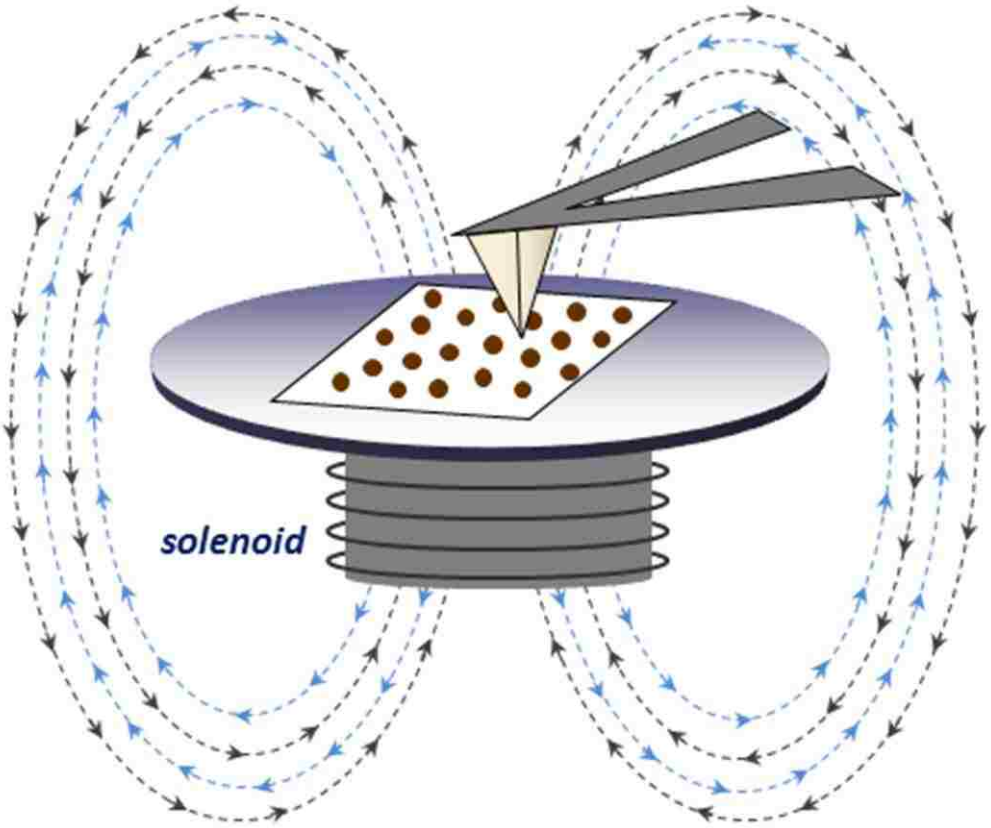

Figure 2.3. Principle of magnetic sample modulation AFM.

There are two general modes for MSM-AFM operation, *static* and *dynamic* approaches. In static MSM-AFM, a chosen driving frequency or selected magnetic field strength is applied to acquire the entire image. Dynamic MSM-AFM is accomplished by changing parameters such as the driving frequency and the electromagnetic field strength while acquiring MSM-AFM frames. To acquire spectra of the resonance responses for the vibration of nanomaterials, the AC drive voltage is swept over a range of different field strengths and frequencies. Dynamic measurements acquired for a specific location when the parameters of the magnetic field strength or the driving frequency are changed can be monitored both with images and spectra. At higher field strength, an increase in vibrational response is observed in MSM amplitude and phase channels. By placing the cantilever precisely on a single nanoparticle or nanocrystal, information of the dynamics of the vibrations can be correlated to size and composition. Characterizations with MSM-AFM provide information of magnetic and superparamagnetic properties at the level of individual nanoparticles.

2.2.5 Principle of Indirect Magnetic Modulation AFM

Indirect magnetic modulation (IMM) mode is an approach for force modulation measurements of the elastic response of samples (Figure 2.4).[54] It is limited to characterizing samples that do not respond to the flux of a magnetic field. A wire coil solenoid placed under the sample stage is used to produce an oscillating magnetic field – which drives vibration of the entire nosecone assembly holding a non-magnetic AFM tip. The typical contact mode AFM configuration is used for imaging and positional feedback, and the vibrating tip is scanned in continuous contact with the sample surface. Standard silicon nitride (non-magnetic) cantilevers are used for IMM-AFM imaging. Indirect magnetic modulation is an approach for force

modulation AFM (FM-AFM) imaging, and is used to probe differences in surface elasticity or

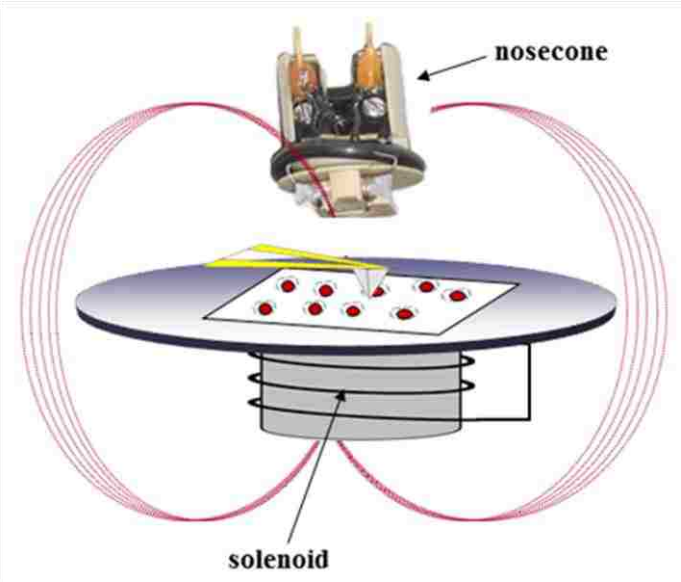

Figure 2.4. Principle of indirect magnetic modulation-AFM

stiffness. Both IMM-AFM and FM-AFM configurations enable sensitive mapping of surface chemistries to differentiate between heterogeneous samples and detecting contaminants on surfaces. The differences in amplitude from the oscillation of the tip holder assembly at the chosen frequency provide a map of relative stiffness of the surface, exhibited by a change in contrast. Preliminary results using IMM-AFM are presented in Chapter 9, in which elasticity measurements of octa-substituted porphyrins were investigated.

2.2.6 Conductive Probe-AFM and I-V Measurements

Conductive probe atomic force microscopy, CP-AFM (Figure 2.5) is accomplished by applying a bias to the sample and measuring the current that is generated through the sample and conductive tip. A sensitive pre-amp is located near the probe in the nosecone assembly. Two types of information are acquired, current-voltage (I-V) spectra and current images. Topography frames are mapped with current images simultaneously. Current images are used to sensitively

map conductive domains of the sample. The substrate must be a conductive or semiconductive to enable the measurement of current when the probe is placed in contact with the surface. Information of the relationship between current *vs.* voltage can be plotted using CP-AFM for samples. A spectrum displaying I-V spectroscopy is acquired over a certain range voltage range (+/- 10 V). The I-V profile is then used to select the optimum region showing high conductivity. Often, small bias (0.1 V) is applied first and then gradually increased until sufficient contrast for imaging is achieved. Reversing the bias will cause the contrast to be switched in current images. Preliminary data using CP-AFM are described in Chapter 9, in which charge transport through octa-substituted porphyrins was investigated.

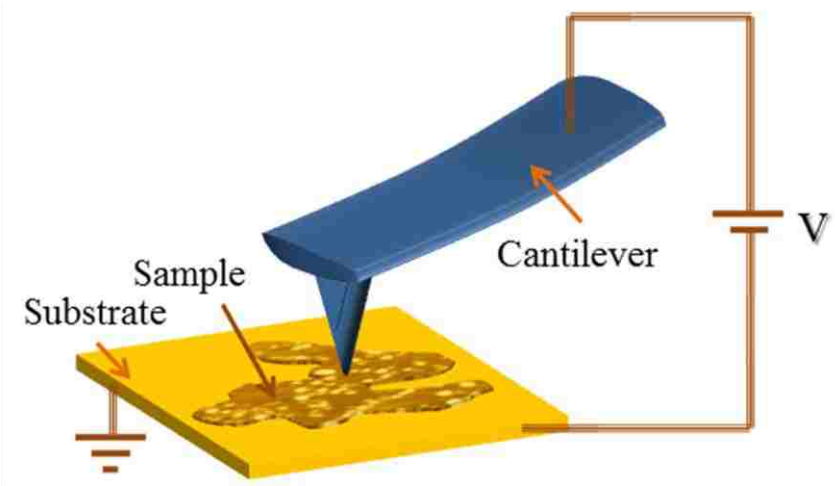

Figure 2.5 Basic set-up for conductive probe AFM

2.2.7 Calibration of the AFM Scanner

Molecular-level calibration of the AFM scanner is accomplished using the real surfaces of atomic and molecular lattices, Au(111), HOPG, and mica(0001). Molecularly-resolved images of self-assembled monolayers or certain flat surfaces are used for scanner calibration. For scales

of microns or hundreds of nanometers, calibration is accomplished by imaging micromachined gratings. As an *in situ* calibration tool for z scales, the height of terrace steps of the underlying gold substrate can be used, which are apparent in AFM images. With known dimensions of approximately 0.25 nm, gold steps provide an excellent standard for height calibration. Another approach for assessing the calibration of an AFM scanner is to image latex or silica spheres. Briefly, the mesosphere particles are deposited on the surface to form highly crystalline layers. The mesosphere layers with approximate known sizes are used to provide simultaneous x, y, and z calibration. Unfortunately, the dimensions of the particles shrink according to humidity conditions, and do not provide definitive reference materials. The well-known thicknesses of *n*-alkanethiol self-assembled monolayers can also be used for AFM calibration at nanometer dimensions, by nanoshaving areas of uncovered substrates for height measurements.

2.2.8 SPM-Based Imaging Modes Used in This Dissertation

An overview of the imaging modes used in this dissertation is presented in Table 2.1. Contact and tapping mode AFM were used to visualize the shapes and morphology of the nanomaterials. The composition of samples at the nanoscale was investigated using frictional force and phase imaging. Magnetic sample modulation was applied to map and obtain the vibrational responses of magnetic nanomaterials. To characterize elasticity of samples, IMM-AFM was used for porphyrin nanocrystals. Conductivity and I-V measurements of porphyrins were investigated using CP-AFM.

Table 2.1. SPM modes used for research experiments

Chapter	SPM Mode	Sample Description
4	contact mode AFM frictional force AFM MSM-AFM	microstructures of $FeNi_3$ nanoparticles prepared on mica(0001) substrates
5	contact mode tapping mode AFM phase imaging MSM-AFM	test platforms of nickel and cobalt nanoparticles patterned using 'two particle' lithography
6	contact mode tapping mode AFM phase imaging MSM-AFM	well-defined structures of porphyrin nanocrystals patterned using particle lithography (immersion approach)
7	tapping mode AFM phase imaging MSM-AFM	nanoGUMBOS particles deposited on mica(0001)
8	tapping mode AFM	samples of amyloid beta fibrils on mica(0001)
9	IMM-AFM CP-AFM I-V Spectroscopy	porphyrin nanocrystals deposited on mica(0001) and Au(111)

CHAPTER 3. USING SCANNING PROBE MICROSCOPY TO CHARACTERIZE NANOPARTICLES AND NANOCRYSTALS

3.1. Introduction

Scanning probe microscopy (SPM) provides a versatile suite of analytical tools for ultrasensitive nanoscale measurements, which are emerging as standard characterizations for nanomaterials. The phrase 'scanning probe microscopy' collectively refers to methods which use a scanning probe to interrogate a sample. Images of the sample are digitally constructed by scanning the probe in a line-by-line raster pattern while recording the probe-surface interaction as a function of position. Measurements are collected in a grid pattern (e.g. 256×256, 512×512 pixels, etc.) to generate a spatial map of changes in force, depending on the instrument configuration. The SPM methods include scanning tunneling microscopy (STM), atomic force microscopy (AFM), scanning near-field optical microscopy (SNOM) and more than 40 different instrument configurations for various surface characterizations and lithography modes. The capabilities and advances in SPM instrumentation continue to set benchmarks for detection limits and measurement sensitivity at the nanoscale. One of the advantages in comparison to other nanoscale measurements is that the versatile approaches of SPM not only provide characterizations that routinely exceed the Rayleigh diffraction limit of conventional optics, but also enable nanofabrication protocols to define the arrangement of thin films and nanoparticles on surfaces, with designed sizes and geometries.

This chapter describes how different modes of SPM have been applied for characterizations and lithography with a wide range of nanoparticles and nanocrystals. In most of the established modes of SPM imaging, the nature of the probe or tip is used as a mechanism for detection of forces. For example, a biased tip is used for scanning polarization force

microscopy, a magnetized tip is used for magnetic force microscopy, a chemically functionalized tip is used for chemical force microscopy, a conductive tip is used for current imaging, and an actuated tip is used for tapping mode AFM (TM-AFM) and phase imaging. Thus, the term 'scanning force microscopy' has often been used interchangeably with 'scanning probe microscopy' to indicate that measurements of forces are obtained. Scanning probe microscopy can also be used to refer to STM, SNOM, etc. Properties such as elasticity, adhesion, conductivity, electronic conductance and magnetic forces of nanomaterials can be obtained, depending on the instrument configurations, and most commercial SPM systems include capabilities for multiple imaging modes. Another way to categorize SPM methods is to define the measurement according to how the tip is operated proximal to the sample. Non-contact, contact and intermittent-contact modes refer to whether the probe is scanned at a discrete distance from the sample, in direct contact with the sample, or oscillates in and out of contact by 'tapping' the sample. Examples for each of these imaging modes will be described in later sections of this chapter. Methods of SPM are based on an operational platform which uses electronic controllers for piezoelectric positioning of a surface probe. The feedback loop for tip-positioning and mechanisms for imaging are distinctly different for each of the various SPM modes and likewise provide a range of detection limits and measurement capabilities.

Depending on elemental composition, size and shape, varied properties are exhibited by nanoparticles and nanocrystals for applications in a broad range of technological and biomedical applications. The synthesis of particles with control over composition, shape, and size distribution has been a major part of colloid chemistry for decades; however, emerging attention focused on the development of new nanomaterials can be largely attributed to more recent

inventions of analytical tools that enable characterization of small structures with atomic resolution. New research protocols have been developed to measure, observe, model and synthesize nanomaterials at the size scales of molecules and atoms. Milestone discoveries related to nanoparticle synthesis have become known, for example, the discovery of Buckminster fullerene,[55] carbon nanotubes,[56] the synthesis and properties of quantum dots,[57] and the shape control of CdSe nanocrystals[58] and gold nanoparticles.[59] The possibilities to tailor the chemical and physical properties of nanoparticles and nanocrystals are evidenced by the libraries of nanoparticle syntheses reported in the recent scientific literature, covering an immense spectrum of compositions, structures, properties and shapes. As tailorable materials, nanoparticles and nanocrystals furnish nanoscale building blocks for device fabrication, and provide opportunities to investigate and exploit the size-dependence of novel electronic, photonic and magnetic properties in fields such as catalysis,[60, 61] nanomedicine[62-64] and electronics.[65-67] Nanoparticles are aggregates of a few or many millions of atoms or molecules and consist of either identical atoms or of different species. Nanocrystals have structures of a well-defined periodic lattice and typically are of semiconductor nanoparticles such as CdS, CdSe, CdTe, and InP that are described as quantum dots,[68, 69] which exhibit characteristic fluorescence wavelengths that are dependent on particle sizes. Nanocrystals of magnetic materials such as cobalt, iron-oxide, and certain metal alloys exhibit novel magnetic or superparamagnetic properties. Later sections of this chapter will describe SPM characterizations, properties and applications of several important classes of nanoparticles and nanocrystals.

Electron microscopies such as scanning electron microscopy (SEM) and transmission electron microscopy (TEM) are still the predominant analytical tools used for characterizing

nanoparticles; however, SPM methods have emerged as valuable characterizations which provide complementary information as well as different measurement capabilities. A benefit of using high-resolution electron microscopes to characterize metal nanoparticles or semiconductor nanocrystals is that the lattice arrangement and periodicity can be revealed. Often, researchers will use SPM as oppose to electron microscopies for investigating the complex nature of samples which are not conducting or that are damaged by electron beams. For example, nanoparticles of ionic liquids cannot sustain their shape when interrogated with TEM, and were found to melt or sinter within a few seconds of irradiation.[3] Samples must be conductive or semiconductive for electron microscopy, so nonconductive samples such as biological films or chemical coatings cannot be imaged without extra steps of sample treatment and modification. Samples of polymeric nanoparticles typically are not conductive and require pretreatment with a sputtered metal or carbon coating, or a heavy metal stain which alters the overall nanoparticle diameter when imaging with electron microscopy. However, samples of nanoparticles can be readily imaged in ambient environments using AFM without sample modification. Core-shell nanoparticles that are coated with an organic thin film or protein are often imaged using both AFM and electron microscopies. The AFM characterizations provide details of the 3D geometries for the entire nanoparticle including the surface coating, whereas SEM or TEM furnish information about the inner diameter of the metal core encapsulated within the shell. Electron microscopies operate on a principle similar to optical microscopy using lenses to focus an electronic beam, and therefore provide 2D planar micrographs, whereas SPM provides 3D information. By tilting the sample or preparing cross sections, 3D information can be obtained with electron microscopes. Another advantage of using SPM measurements for characterizations

is that probes can be operated in nearly any environment (e.g. in liquid media, vacuum environments, or in ambient conditions). High-resolution electron microscopes require that samples be maintained in high vacuum environments because the electron beams interact with air and water. Finally, a key advantage of SPM characterizations for investigations with nanoparticles and nanocrystals is that new information can be obtained about nanoscale properties with unprecedented sensitivity. Specific examples will be described in later sections of this chapter.

This chapter first introduces examples of SPM characterizations of nanoparticles using the three most common imaging modes of SPM: contact mode AFM, tapping mode AFM, and scanning tunneling microscopy (STM). Next, examples of patterning nanoparticles with scanning probe lithography (SPL) and particle lithography will be reviewed. Well-defined arrangements of nanoparticles provide practical test platforms with tailorable sizes and spacing, which can be scaled down to enable studies of size-dependent properties. Next, SPM characterizations of the magnetic properties of nanoparticles will be described. Finally, a prospectus for future directions using SPM and SPL for investigations of the properties and geometries of nanoparticles will be discussed.

3.2 Overview of SPM Imaging Modes

Scanning tunneling microscopy (STM) was discovered by Gerd Binnig and Heinrich Rohrer in 1982, who were jointly awarded the 1986 Nobel Prize in Physics.[30] Measurements with STM rely on the phenomena of electrons tunneling over very short (< 1 nm) distances, and thus STM characterizations are limited to atomically-flat samples that are conductive or semiconducting. The invention of AFM was reported a few years later by Binnig, Quate, and

Gerber in 1986, and expands the capabilities of scanning probe instruments to imaging non-conductive or insulating materials.[31] Since microfabricated probes are used to interrogate the surface, SPM-based imaging techniques are not limited by the wavelength of light; however, the samples must be flat with surface roughness of a few tens to hundreds of nanometers, depending on the SPM scanner specifications.

A general overview of the SPM imaging modes most commonly used for characterizations of nanoparticles and nanocrystals is summarized in Table 3.1 and define the scope of this chapter. There are several key differences when comparing SPM methods beyond the choice of instrument, such as the mechanism of imaging, the type of measurement information that can be acquired, and whether experiments can be accomplished *in situ*. The advantage of using AFM over STM or electron microscopies is that samples do not have to be conductive; both conducting and insulating nanomaterials can be characterized without any modifications. Another advantage of AFM is that it can be used to generate exquisite views of samples both in air and liquid media without a vacuum chamber. The most common imaging modes for AFM are contact mode and tapping mode, although there are other various modes which require specific modifications to the instrument configuration or changing the feedback mechanism. A detailed insight of the structural information and properties such as elasticity, adhesion, conductivity, electronic properties and magnetic forces of materials can be obtained by using different SPM instrument configurations.

Table 3.1. Most Common SPM Imaging Modes Applied for Characterizing Nanoparticles.

SPM Mode	Positional Feedback	Type of Probe	Parameters Measured
Contact mode and frictional force AFM	AFM tip deflection	silicon, silicon nitride	surface profiles, morphology, height changes, frictional forces
Tapping mode AFM and phase imaging	changes in the amplitude of tip oscillation	silicon, silicon nitride	surface profiles, morphology, height changes, elastic response
Scanning Tunneling Microscopy (STM)	changes in the magnitude of the tunneling current	metal wire	surface profiles, morphology, changes in sample currents
Magnetic Force Microscopy (MFM)	surface topography is retraced	AFM probe with a magnetic coating	surface profiles, morphology, relatively long-range magnetic forces
Magnetic Sample Modulation AFM (MSM)	AFM tip deflection	silicon, silicon nitride	surface profiles, morphology, magnetic response induced for individual nanoparticles, changes in vibration amplitude and frequency

3.2.1 Contact Mode AFM Characterizations of Nanoparticles

The most commonly used AFM imaging modes are contact mode and tapping mode, which provide valuable characterizations at an unprecedented level for viewing the shapes and arrangements of individual nanoparticles and nanocrystals. Other modes of lateral force and phase imaging are closely associated with contact and tapping modes, since additional channels of information can be gained simultaneously during a single sweep of the sample surface. For example, phase images are acquired simultaneously with tapping mode AFM, and indicate changes incurred for the tip trajectory or phase lag of oscillation, to be detailed in Section 4. Frictional force AFM is also known as lateral force imaging, and is correlated directly with changes in friction as the probe is dragged across the sample in direct contact with the surface.

Both contact mode and frictional force imaging will be described in this section, since both characterizations are accomplished simultaneously. Contact mode and lateral force AFM imaging have been widely applied for imaging nanoparticles of varied composition, including nanoparticles of metals,[33-39] polymers,[40] porphyrins,[41] metal alloys,[42, 43] monolayer protected clusters (MPCs)[44] and nanocrystals of quantum dots.[45-47]

3.2.2 Contact Mode and Friction Imaging of Nanoparticles

For contact mode AFM imaging, a sharp probe at the end of a cantilever is rastered across a sample using a piezoelectric tube scanner. Light from a diode laser is focused on the backside of the reflective cantilever and deflected to a quadrant photodetector (Figure 3.1). Very small changes in the deflection of the cantilever as it is scanned in contact with the sample consequently produce a change in the position of the laser spot focused on the photodetector. The positions of the probe are mapped with the photodetector measurements to provide digital images of the topography and frictional measurements. When the tip is raster scanned across the surface, it experiences torsional twisting due to the difference in friction between the probe and sample areas with different chemistries. The torsional twisting of the probe induces changes in the position of laser spot in the left and right quadrants and is used to construct lateral force images, whereas changes in surface topography cause changes in the laser position in the top and bottom quadrants of the photodetector as the tip moves up or down over the sample terrain. For positional feedback in the z-direction, a computer program is used to maintain a constant deflection of the tip by adjusting the voltages applied to a piezoceramic tube scanner.[31] Topography frames and lateral force images are acquired simultaneously.

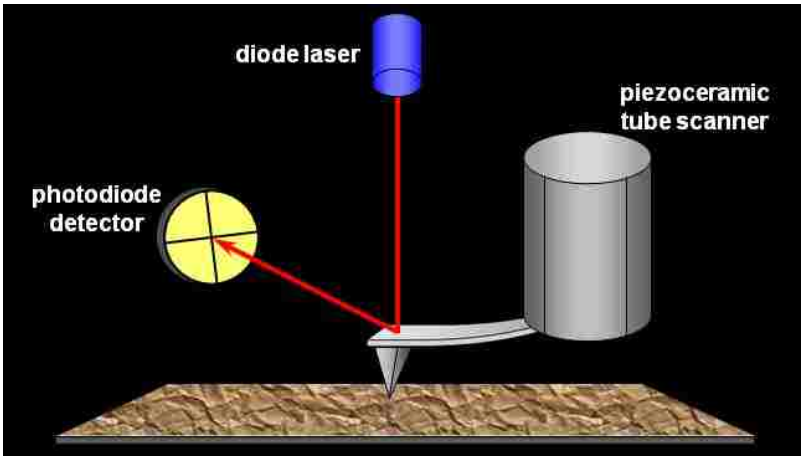

Figure 3.1. Operating principle of contact mode AFM.

Height measurements (*z* dimension) for images obtained with contact mode AFM are very precise, attaining sub-angstrom resolution. However, images obtained using AFM often do not reflect the true lateral dimensions of the sample topography and instead display a convolution of the geometry of the sample and tip.[70] Blunt tips cannot accurately trace the shapes of sample features and therefore will exhibit exaggerated lateral dimensions as depicted in Figure 3.2 A sharp probe can closely follow the surface contours to provide a better approximation of the actual sample morphology, and often the 'art' of SPM imaging requires testing many different probes to find one with a geometry that is well-suited for the sample of interest. In cases where the features of the surface are very small, instead of the tip providing a view of the surface, the small surface features will furnish an image of the shape of the tip. Numerical simulation of the expected shape can be obtained when the geometry of the tip is known, often by *ex situ* characterization of the tip with SEM. Algorithms for deconvolution of the tip and sample shapes have been developed by Villarrubia,[70] Goh,[71] Williams[72] and Wilson.[73] Analogously, the shape of the tip can be similarly reconstructed by using samples with well-defined geometries, such as microfabricated tip-characterization grids that are commercially available.

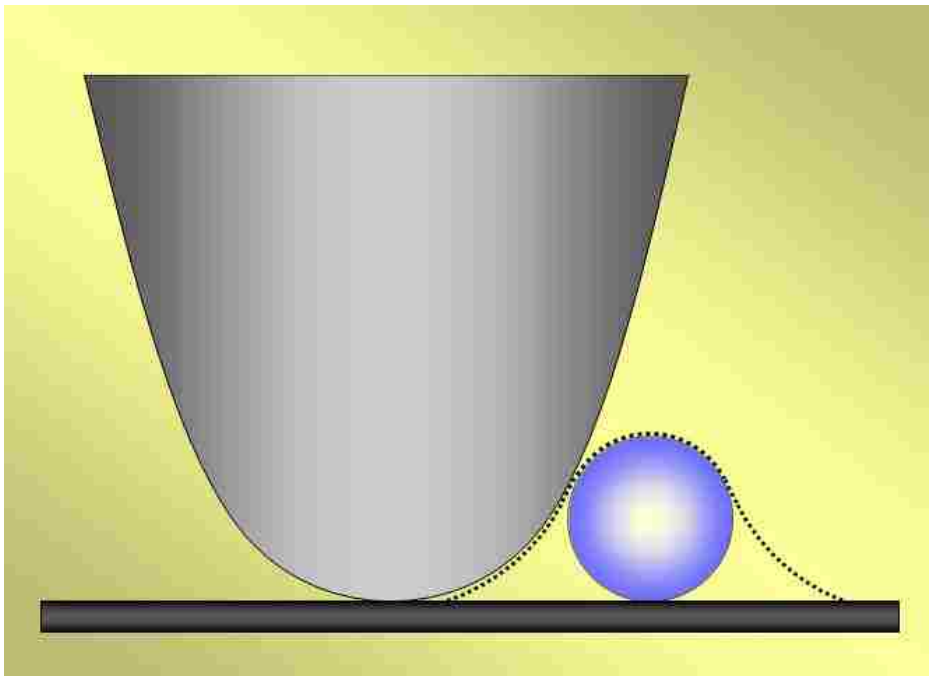

Figure 3.2. Tip-sample convolution occurs when imaging nanoparticles with AFM.

Selection of a suitable probe is a critical parameter for successful investigations with SPM or SPL, and often requires experimentation with several different probe designs. Tremendous progress has been gained during the last decade for the microfabrication capabilities for producing economical probes with highly reproducible geometries and spring constants for SPM imaging. Commercial cantilevers are prepared in clean rooms using 20 or more steps of microlithography (e.g. photolithography and chemical processing). Ultrasharp silicon or silicon nitride probes are attached to either a V-shaped or rectangular (diving board) cantilever. The cantilevers range in length from 10-200 μm with widths of 20-40 μm. The geometries of the apex of the probes are mostly square-based pyramids or cylindrical cones. The back of the cantilevers are coated with a reflective thin film of either gold or aluminum. The resonance frequencies for TM-AFM cantilevers for operation in air range from 20-300 kHz, whereas the resonance frequencies used in liquid more typically range from 5-80 kHz. The spring constants

for commercially manufactured cantilevers vary widely, ranging from 0.005 to tens or hundreds of nN.[74-76]

3.2.3 Metal Nanoparticles of Platinum Imaged with Contact Mode AFM

An emerging application for SPM characterizations are studies of nanoparticles composed of catalytic materials, which often require uniform size distributions and surface arrangements. Methods for synthesis of catalyst nanoparticles are being developed to target certain sizes and geometries, and it is a considerable challenge to obtain monodisperse sizes and uniform surface distributions at the nanoscale. A contact mode topography image of platinum catalyst nanoparticles is presented in Figure 3.3.[12] Platinum nanoparticles were deposited on surfaces of highly oriented pyrolytic graphite (HOPG) by electron beam heating at a pressure of 10^{-8} Torr, using a metal deposition rate of 0.01 nm s^{-1}. After platinum deposition, the samples were removed from vacuum for imaging in ambient conditions with contact mode AFM. Surfaces of HOPG are frequently used for SPM investigations because when cleaved it is atomically flat and pristine, has a well-defined surface structure of an atomic lattice, and is stable when heated. Surfaces of HOPG are the preferred substrate for studies of oxidation and gas-solid surface reactions because of its flatness, relative inertness in air, and chemical stability.[12] Various low-temperature plasma treatments of the surface in vacuum were found to affect the lateral diffusion of the nanoparticles on surfaces of HOPG. Larger sizes were observed for platinum nanoparticles produced on untreated HOPG (6 nm) which were irregularly distributed across the surface (Figure 3.3A). Evaporated platinum nanoparticles prepared on HOPG treated with oxygen plasma exhibited smaller dimensions of 3.5-4 nm and showed a regular surface distribution (Figure 3.3B).

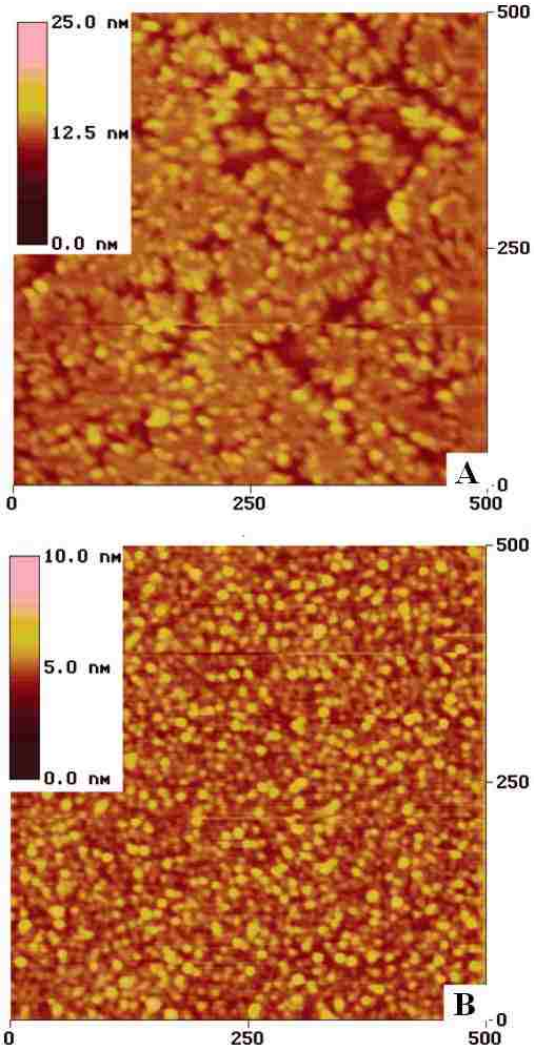

Figure 3.3. Contact mode AFM topography images of nanoparticles prepared by e-beam deposition of 5 nm of platinum on HOPG surfaces. Nanoparticles prepared on (A) unmodified HOPG and (B) an HOPG surface treated with oxygen plasma. Reprinted with permission from reference. [12]

3.2.4 AFM Investigation of Pnictide Nanoparticles

Synthesis of nanoparticles of pnictide transition elements was accomplished by Stamm et al. via reduction of pnictates.[77, 78] Pnictogens (formerly group V elements) consist of nitrogen, phosphorus, arsenic, antimony, bismuth, and ununpentium. Nanocrystals of transition metal pnictides offer interesting magnetic and magneto-optic properties for advancement of

technologies such as magnetoresistive sensing, magnetic refrigeration, and data storage and transmission. Nanoparticles of magnetic iron phosphide were prepared by reducing preformed nanoparticles of iron phosphate deposited on mica and by annealing under hydrogen/argon vapor at 700 °C and 1100 °C.[77] Mica is a naturally formed silicate mineral which produces perfect sheets containing a pristine lattice of hexagonally arranged atoms.

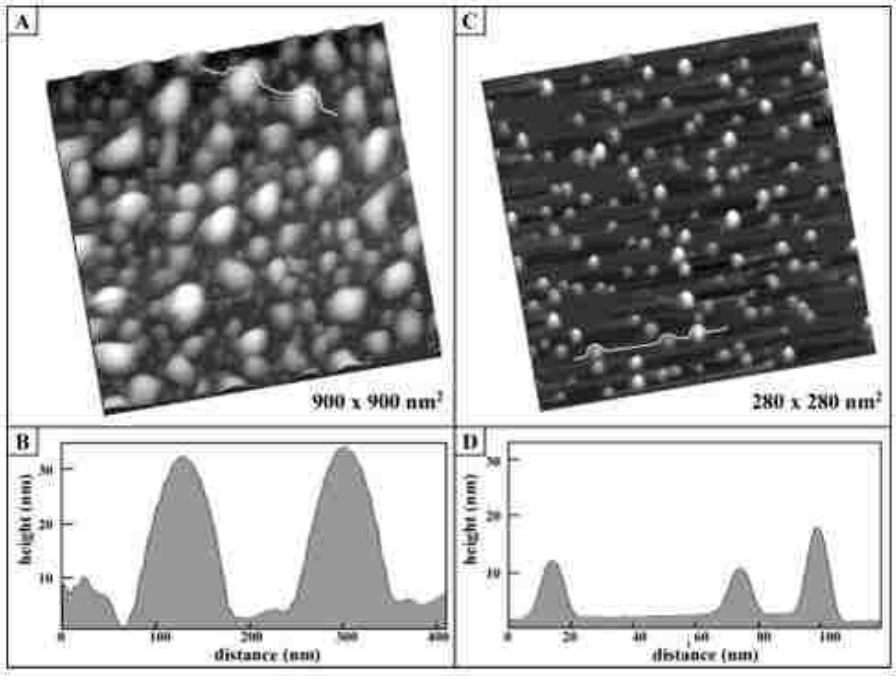

Figure 3.4. Contact mode topographs of iron phosphide nanoparticles. (A) Pnictate precursor concentration prepared at 2.3 mg mL^{-1}. (B) Cursor profile for the line in (A). (C) Nanoparticles formed with a pnictate concentration of 0.19 mg mL^{-1}. (D) Cross-section for the line in (C). Reproduced with permission from.[77]

Muscovite mica is the most common substrate for AFM sample preparation because simple cleavage produces clean, atomically flat substrates. Figure 3.4 displays contact mode topography images for iron phosphide nanoparticles prepared on surfaces of mica, which were synthesized with different pnictogen precursor concentrations. Iron phosphide nanoparticles produced by annealing phosphate nanoparticles prepared at 2.3 mg mL^{-1} (Figure 3.4A) had an

average height of 13.4 ± 8.7 nm (Figure 3.4B), while low precursor concentration (0.19 mg ml^{-1}) yielded iron phosphide nanoparticles with average diameters of 1.41 ± 0.5 nm (Figures 3.4C and 3.4D).

3.2.5 Morphology of Semiconductive Nanocrystals of Silicon Viewed with AFM

Quantum dots are crystalline nanoparticles composed of semiconductors and were discovered by Louis E. Brus at Bell Laboratories.[57] Semiconductor nanocrystals are strongly affected by quantum confinement as a result of dimensions becoming smaller than the exciton diameter of the bulk material. The size and shape of individual nanocrystals determine the properties of quantum dots. A primary research theme in the field of semiconductor nanocrystals is to tailor optical properties by developing synthetic approaches to provide precise control of the size and geometries of nanoparticles. Quantum dots have attractive photophysical properties for applications in biological and medical imaging: size-tunable, narrow emission spectral properties with a broad excitation range, longer lifetimes of fluorescence or luminescence than organic dyes, and negligible photobleaching. Nanocrystalline silicon has recently received attention due to its potential for biocompatibility for *in vivo* imaging.[79] Baldwin et al. have reported a room temperature solution synthesis of crystalline silicon nanoparticles with well-defined crystal facets.[80] A high resolution AFM topograph showing the morphology of a tetrahedral silicon nanoparticle on a mica substrate is displayed in Figure 3.5A. Solution reduction approaches to synthesize silicon nanocrystals had previously been achieved only with elevated temperatures and high pressure. However, silicon nanocrystals with defined facets were prepared at room temperature via solution synthesis. The height of the nanocrystal measured 26 nm, shown in the cursor plot of Figure 3.5B. Views with TEM revealed the crystalline lattice of the nanostructures

(not shown); however, the 2D images did not resolve the 3D tetrahedral shapes of the nanoparticle. In this example, both electron microscopy and AFM imaging were applied to provide complementary information about the silicon nanocrystals. Since single crystal silicon forms the basis of computer microchip industry and polycrystalline silicon is important for photovoltaic device applications, one can likewise predict that silicon nanocrystals will find significant uses in future nanotechnology.

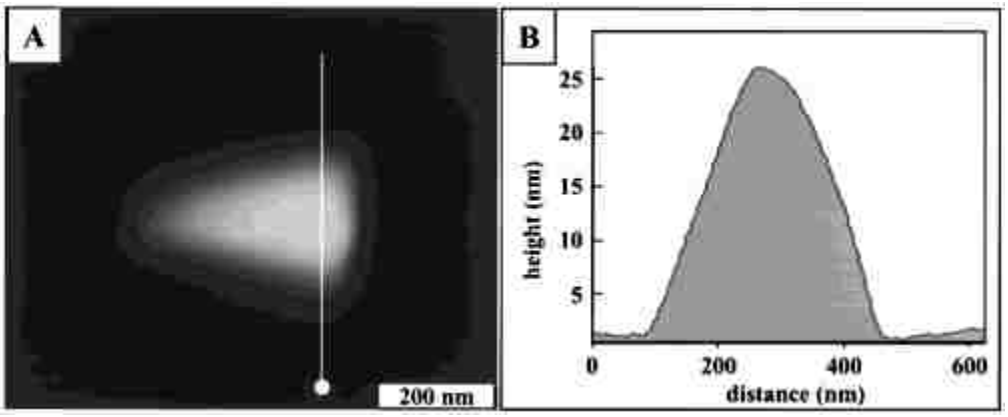

Figure 3.5. A) Silicon nanocrystal imaged using contact mode AFM on the flat surface of mica. (B) Corresponding cursor plot for A. Reproduced with permission from.[80]

3.2.6 Imaging Supramolecular Nanoparticles of Porphyrins with Contact Mode AFM

Porphyrins and metalloporphyrins have unique electronic and chemical properties for photonic, photovoltaic, magnetic and biomedical applications. Because of the rich functional properties of the parent molecules, nanoparticles of porphyrins are a promising new class of nanomaterials with likely potential applications similar to the parent supramolecular systems in photonics, solar energy conversion, catalysis, and molecular electronic devices (e.g. sensors and display technologies). Nanoparticles of porphyrins exhibit unique properties not obtainable with larger-scaled materials containing the macrocycle due to size-dependence. The first synthesis of porphyrin nanoparticles with catalytic properties using mixed solvent approaches was reported

by Gong et al.[81] Synthesis and AFM characterizations of hydrophobic, hydrophilic, amphipathic, and bis-functionalized porphyrins, as well as metalloporphyrins was reported by Drain et al.[82] Contact mode AFM images of nanoparticles prepared from 5,10,15,20-tetrakis(2,3,4,5,6-pentafluorophenyl) porphyrin ($TPPF_{20}$) are shown in Figure 3.6 for samples prepared on different substrates.[82] A small volume of diluted porphyrin solution (10-20 µL) was drop-deposited on either mica (Figure 3.6A) or a clean glass slide (Figure 3.6B) and dried under ambient conditions. The samples of $TPPF_{20}$ nanoparticles deposited on mica display different sizes than those deposited on glass, since colloidal nanoparticles can be induced to disassemble or reorganize on surfaces. For these contact mode AFM images, the particles appear to be quite spherical in shape, which is likely the true sample morphology. Artifacts caused by tip-sample convolution exhibit square or pyramidal shapes indicating the geometry of the tip apex.

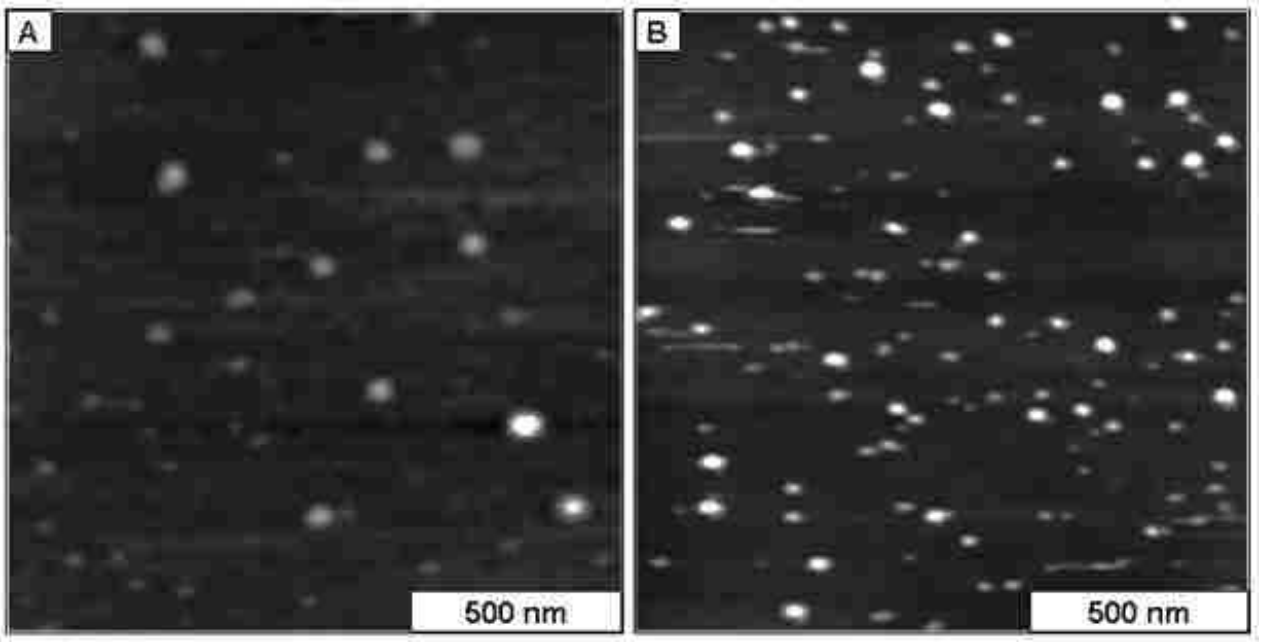

Figure 3.6. AFM topographic views for porphyrin nanoparticles on (A) mica and (B) glass. Reproduced with permission from.[82]

3.3 Application of Tapping Mode AFM for Imaging Nanoparticles

One of the problems encountered with contact mode AFM imaging is that for materials that do not adhere strongly to the substrate, the motion and force of an AFM tip can dislodge the nanoparticles and push them across the surface, particularly for samples prepared on ultraflat surfaces of mica and HOPG. Tapping mode AFM (TM-AFM) is an intermittent imaging mode that was developed to overcome the drawbacks of sample perturbation caused by shear forces of the scanning probe. Instead of operating with the tip placed in continuous contact with the surface, the tip is driven to oscillate in and out of contact, to intermittently 'tap' the sample surface with designated force and tapping rate. Both topography and phase images are acquired simultaneously when operating with TM-AFM. Phase imaging offers the advantage of unique capabilities for detecting and mapping material properties such as tip-sample adhesion and viscoelastic response.[83-86] The capabilities of TM-AFM for characterizations of morphology and surface properties have been applied to characterize a wide variety of nanoparticles and nanocrystals, such as for metal,[1, 87-90] alloy,[91-94] core-shell[10, 95, 96] and polymer[97-99] nanoparticles.

3.3.1 Operating Principle for TM-AFM

Tapping mode offers advantages for characterizing delicate samples or materials that are loosely attached to the surface. The cantilever is driven to oscillate at or near its resonance frequency by either a piezoceramic[100] or magnetic actuator (magnetic AC or MAC-mode).[101] The positional feedback for TM-AFM is accomplished by maintaining a constant oscillating frequency while mapping the changes in tip amplitude (Figure 3.7). High resolution images of soft or sticky samples can also be obtained using TM- AFM since the oscillations are too rapid for transient interfacial bonds to form between the tip and sample, thus minimizing stick-slip

adhesion. Channels of topography and phase are generated simultaneously.[23, 51] Surface properties such as viscoelasticity, adhesion and softness can therefore be mapped by recording the difference between the phase of the signal that drives the tip relative to oscillation of the cantilever.

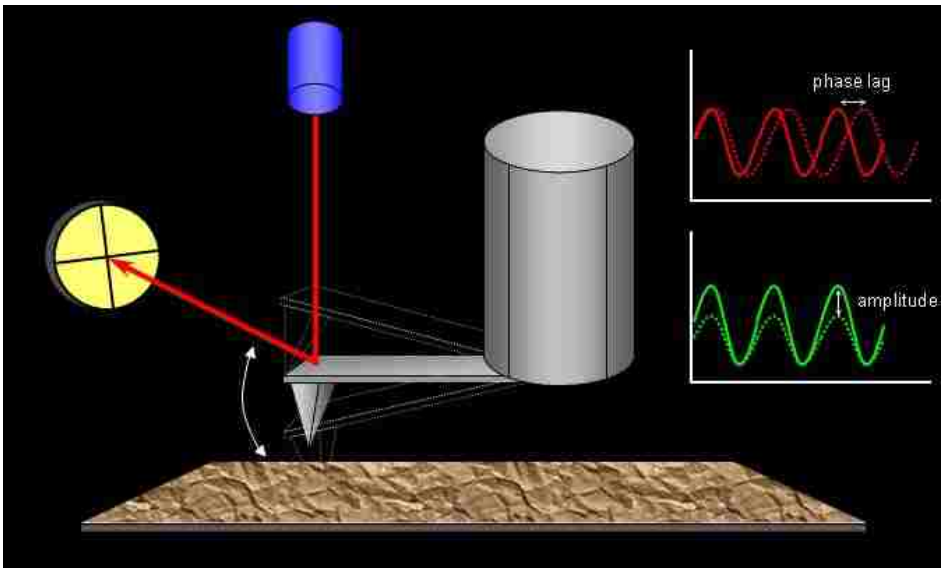

Figure 3.7. Instrument set-up for tapping mode AFM.

Both ambient and liquid environments can be used for investigations with TM-AFM.[51] For ambient characterizations in air, the resonant frequency of the probes typically ranges from 160 to 300 kHz using TM-AFM, whereas softer cantilevers with resonances below 100 kHz can be applied for imaging in liquid environments. Attractive and repulsive regimes influence the oscillation amplitudes, which are determined by the nature of the sample, imaging media and the tip-sample interaction distance.[19, 102, 103] In principle, there is intermittent contact between the tip and the surface when a small amplitude is applied for characterization and the tip is driven to oscillate in the repulsive regime. In contrast, there is a mechanical contact between the tip and the sample for high amplitude oscillation state. When high amplitude is used to drive the tip

motion, the high load force can cause deformation of soft samples. To achieve high resolution imaging with TM-AFM, the analyst must choose optimized conditions for the imaging media, test different types of probes, and determine the suitable driving amplitude and frequency parameters for each sample.

3.3.2 Investigations of Metal Nanoparticles Using TM-AFM

Metal nanoparticles such as gold, silver and copper have been extensively studied because of unique electronic, optical and catalytic properties.[104] Degradation of nanoparticles by partial oxidation or sintering particles is critical to the stability of the nanoparticles.[105] In the recent decade, there have been intensive research efforts for preparing metal nanoparticles both because of fundamental scientific interest and for potential applications. Control of the size and dispersity of the nanoparticles is important because the properties are largely attributable mainly to the nanoscale dimensions. Nanotechnology has made it possible to synthesize and specifically tailor the magnetic properties of nanoparticles.[106] For analytical chemistry applications, metal nanoparticles can be used as substrates for surface enhanced raman spectroscopy (SERS).[38, 107] Dramatic variations in the degree of enhancement, often by many orders of magnitude, have been observed for plasmon resonances of gold and silver nanoparticles. Nanoparticles have also been shown to enhance surface plasmon resonance (SPR) measurements.[108-110] For analytical applications with either SERS and SPR, the nanoparticle substrates must have well-defined morphologies and size dispersity.

There are a range of different strategies that have been developed to synthesize gold nanoparticles which include both physical and chemical reactions.[111] The most common method for synthesis of colloidal gold uses sodium citrate reduction of tetrachloroaurate, $HAuCl_4$, with

tailorable nanoparticle sizes (range of 10-100 nm) that depend on the ratio of citrate and metal salt.[112] The ratio of the $HAuCl_4$ to that of sodium citrate has a critical role in determining the sizes of the nanoparticles generated.[113] An example TM-AFM phase image of the gold nanoparticles is shown in Figure 3.8 for a diluted sample prepared on poly(diallyldimethylammonium) chloride (PDDA) modified glass slides. The preparation and characterization of gold nanoparticles in the presence of unmodified cyclodextrans were investigated by Liu et al. using both AFM and TEM.[1] The size distribution of the gold nanoparticles was confirmed by both AFM and TEM. The AFM results for the average size of different samples of gold nanoparticles prepared with different conditions were found to be in good agreement with the corresponding TEM results.

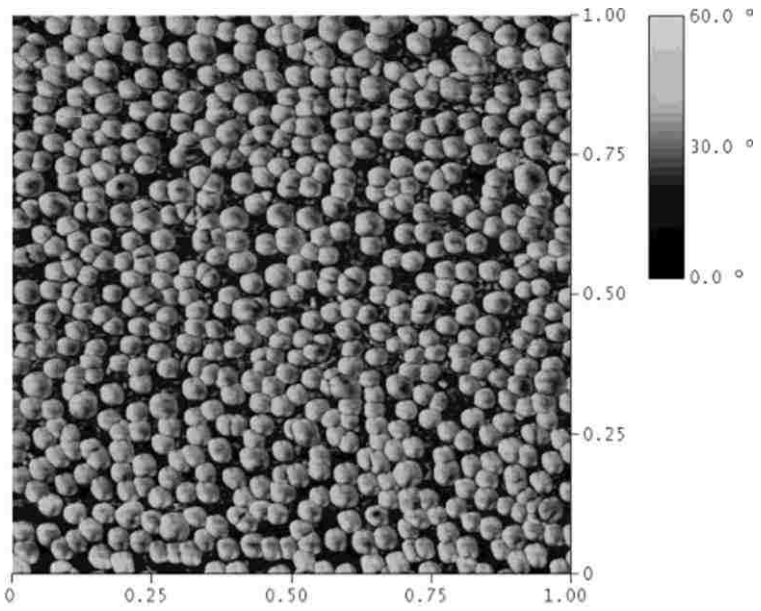

Figure 3.8. TM-AFM phase image of 12 nm gold nanoparticles prepared on a PDDA-modified glass slide. Reproduced with permission from.[1]

3.3.3 TM-AFM Characterizations of Magnetic Alloy Nanoparticles of $FeNi_3$

In materials science, the range of properties of metallic systems can be greatly extended by making mixtures of elements to generate intermetallic compounds and alloys.[114] In many cases, there is an enhancement in specific properties upon alloying due to synergistic effects and a rich diversity of compositions, structures, and properties of metallic alloys has led to widespread applications in electronics, engineering, and catalysis. The desire to fabricate materials with well-defined, controllable properties and structures on the nanometer scale coupled with the flexibility afforded by intermetallic materials has generated interest in bimetallic and trimetallic nanoclusters, referred to as alloy nanoclusters or nanoalloys.[115, 116]

Alloy nanoparticles of iron (III)-nickel ($FeNi_3$) can be synthesized using microwave heating in aqueous solutions.[117] Advantages for using a microwave for synthesis include precise control of heating parameters, greatly reduced reaction times and reagent volumes, and an increase in product yields. The morphology and surface composition of $FeNi_3$ nanoparticles prepared in a microwave under high pressure (above 300 psi) are shown with TM-AFM topography and phase images in Figures 3.9A and 3.9B, respectively. The images reveal that there are roughly 27 nanoparticles within the 2 x 2 μm^2 frames, which appear mostly monodisperse in size. Height measurements from several different areas of topography images (data not shown), indicate that the average size of the nanoparticles measured 3.5±1.5 nm. The phase image in Figure 3.9B reveals that the nanoparticles have homogeneous contrast, which is evidence that the $FeNi_3$ nanoparticles have a uniform composition. The $FeNi_3$ composition was confirmed with X-ray diffractometry, or XRD (data not shown).

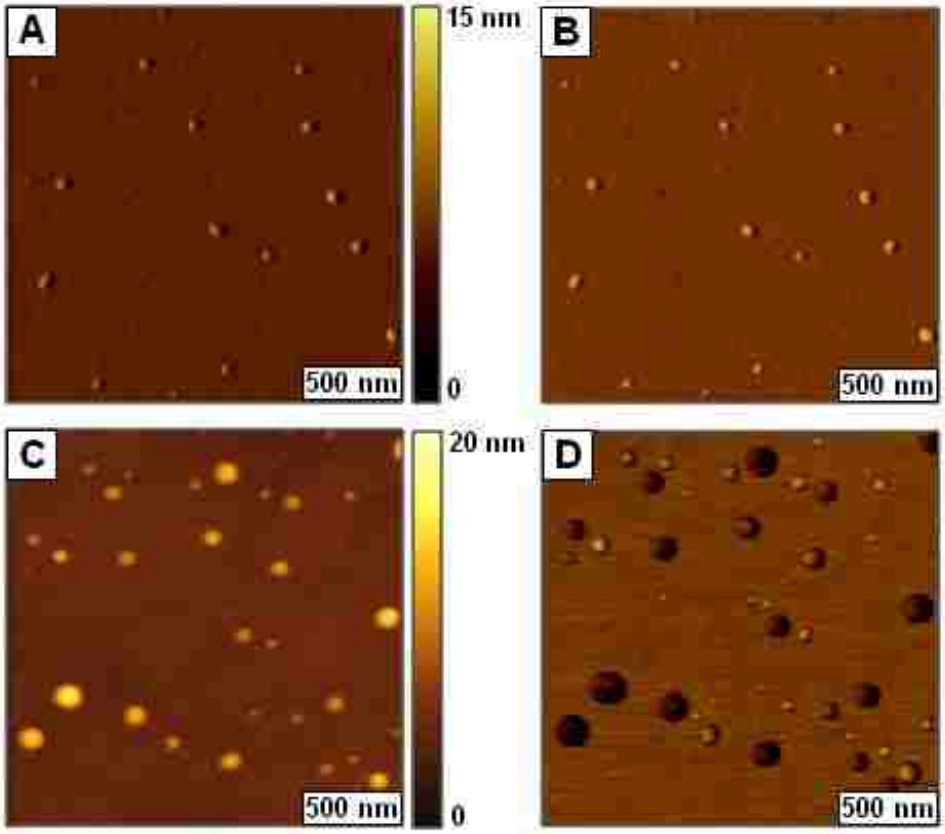

Figure 3.9. Comparison of $FeNi_3$ nanoparticles prepared with microwave heating under different conditions viewed by TM-AFM. A) Topographic view (2 x 2 μm^2) of nanoparticles prepared under optimized pressure; B) corresponding phase image; C) topography image of nanoparticles produced under lower pressure in a microwave (2 x 2 μm^2); D) simultaneously acquired phase image. Reproduced with permission from.[117]

A second batch of $FeNi_3$ nanoparticles was prepared in a microwave using lower pressure (less than 200 psi), shown with representative TM-AFM images in Figures 3.9C and 3.9D. The topography frame (Figure 3.9C) displays a mixture of small and large nanoparticles which have a highly spherical geometry within the 2 x 2 μm^2 scan area. Cursor height profiles indicate that most of the nanoparticles have diameters that fall within range of 2 and 6 nm (~85%) while the larger nanoparticles measured 10 ± 3 nm. The simultaneously acquired phase image displays

dark contrast for the larger nanoparticles, whereas the smaller nanoparticles appear lighter (Figure 3.9D).

The color assignments were assigned arbitrarily for these phase images and do not necessarily reflect which nanoparticles are harder or softer. However, the phase image in Figure 3.9D clearly indicates that the large and small particles have a different material composition. From the comparison of phase images, it is clear that heating conditions under low pressure produced nanoparticles of iron and nickel and that the alloy nanoparticles were not synthesized successfully. Analysis with XRD confirmed that $FeNi_3$ was not produced for the sample prepared with conditions of low pressure (data not shown). The TM-AFM images of $FeNi_3$ nanoparticles in Figure 3.9 reinforce the argument that phase images provide valuable insight about the composition of materials at the level of individual nanoparticles.

3.3.4 Investigations of Ionic Liquid Nanoparticles with TM-AFM

Ionic liquids (ILs) describe a broad class of ionic salts that have a high cohesive energy density and characteristic melting points at or below 100 °C.[118-120] There is a huge variety of possible ion combinations that can be used for tailoring the physical properties of the ionic liquid solvent. Formation of ILs occurs by pairing bulky inorganic anions with highly asymmetric organic cations, which ultimately leads to highly inefficient molecular packing that results in low melting points for ILs.[120] Diverse types of ILs are found in applications for catalysis, optical thermometers, electrolytes, biosensors, lubricants and biocatalytic processes.[121]

Recently, Tesfai et al. developed a novel class of ionic liquid nanoparticles from a group of uniform materials based on organic salts (GUMBOS).[3] Nano-sized GUMBOS were synthesized using an *in situ* ion exchange, water-in-oil microemulsion preparation technique.

Control of nanoparticle size was achieved by altering certain reaction conditions (e.g. surfactant and reagent concentration, choice of nonpolar solvent, temperature).[3] Tapping mode AFM images of nano-GUMBOS composed of $[Bm_2Im][BF_4]$ are displayed in Figures 3.10A-3.10D. The samples were prepared by drying a liquid droplet containing the ionic liquid nanoparticles onto mica substrates. The nanoparticles are spherical in shape and range in size from 20 to 120 nm in diameter, as revealed in the large area topography view (Figure 3.10A).

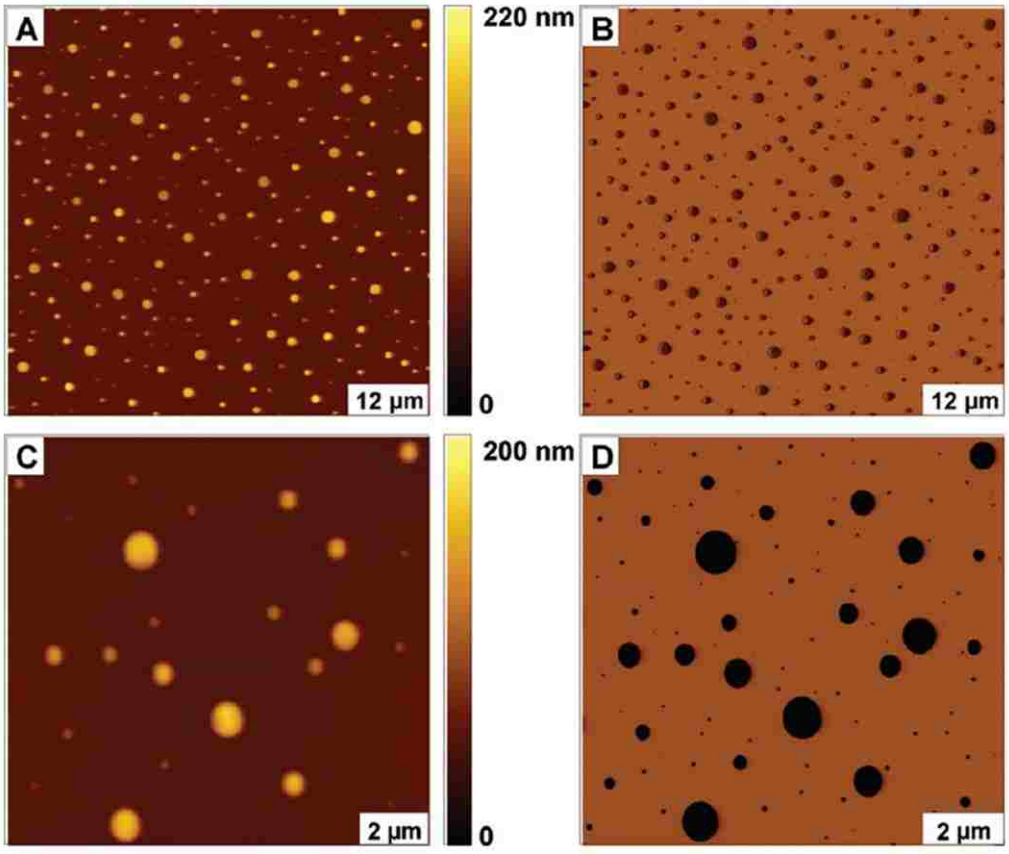

Figure 3.10. Tapping mode AFM images of IL nanoparticles deposited on a mica substrate acquired in ambient conditions. (A) Topography view (60 x 60 μm^2) and (B) corresponding phase image reveals size dispersity and arrangement of isolated nanoparticles. (C) Close-up topography view (12 x 12 μm^2); (D) simultaneously acquired phase image reveals a homogeneous surface composition. Reproduced with permission from.[3]

An interesting imaging artifact can be observed in the simultaneously acquired phase image shown in Figure 3.10B; the bright, crescent-shape features appear on the left side of the spheres, suggesting that this results from a nonsymmetrical tip shape. Nanoscale variations in the size of the nano-GUMBOS become more apparent in the zoom-in view of surface topography (Figure 3.10C). The lateral dimensions of the spherical nano-GUMBOS are broadened and appear slightly larger than their true size. This artifact is a result of tip-sample convolution, in which the size of the AFM tip is considerably large compared to the size of the nano-GUMBOS being imaged.[122, 123] However, the z-resolution of AFM provides a reliable and accurate measurement of the nanoparticle diameters, achieving a sensitivity of 0.01 nm in the z-direction. Regardless of their size, the uniformly dark color in the corresponding phase image in Figure 3.10D indicates that surface composition of the nanoparticles is very homogenous. Notice that many smaller nanoparticles are visible in the phase image of Figure 3.10D that cannot be resolved in the corresponding topography frame of Figure 3.10C. The nanoparticles are present in both frames; however, the effects of size scales with topography images do not produce sufficient contrast for viewing all of the smaller nanoparticles without further zoom-in magnification of the surface.

3.3.5 Monolayer Protected Clusters Imaged with TM-AFM

Alkanethiolate-protected gold nanoparticles, also known as monolayer protected clusters (MPCs) have been synthesized by a two-phase reduction procedure pioneered by Brust et al.[124] Depending on the ratio of gold salt to the alkanethiol ligand, sizes ranging between 1 and 10 nm can be synthesized. Another method for synthesizing MPCs, referred to as ligand place exchange, was developed by Murray and coworkers.[125] Alkanethiolate MPCs can be isolated and redissolved several times in organic solvents without permanent aggregation or degradation. The

dimensions of the core for the MPCs have been determined with close agreement using STM,[9] TM-AFM,[9] and TEM[126, 127] imaging. Electron microscopies do not reveal the dimensions of the organic monolayer coating, whereas AFM and STM topography images furnish views of the core and shell dimensions. Investigations of MPCs have been conducted using STM,[9, 128, 129] contact mode AFM[130] and tapping mode AFM.[131-133] Core-shell nanoparticles such as MPCs that are passivated with alkanethiol shells have been shown to exhibit interesting electrochemical and spectroscopic band gaps attributed to the size of the nanoparticle core.[126] Monolayer protected monolayers have also exhibited quantized charging at room temperature attributed to nanoscale capacitance.[134] Recently, MPCs have been applied for electrocatalysis,[135] metal films,[136] detection of heavy metal ions,[137] and chemical recognition.[138]

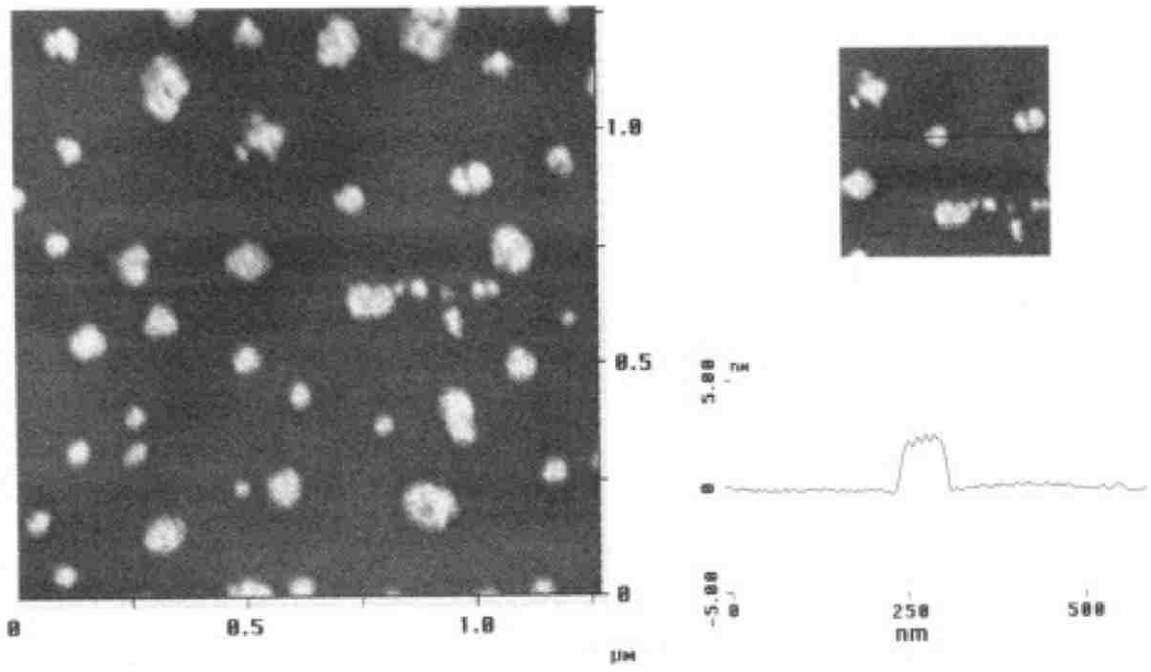

Figure 3.11. Gold nanoparticles protected with a decanethiol monolayer imaged with tapping mode AFM. Reproduced with permission from.[9]

An example TM-AFM image of dodecanethiol protected gold nanoparticles deposited on etched mica is shown in Figure 3.11. The left image with a wider view measures 1.25 x 1.25 μm^2, and the smaller frame on the right side is a zoom in-view with a corresponding cursor profile. The tapping mode image reveals clusters of several MPCs, which have heights of 2.2 ± 0.9 nm based on AFM measurements.

3.4 Measurements of Nanoparticles Acquired with STM

Scanning tunneling microscopy (STM) provides the highest spatial resolution of all the SPM imaging modes for surfaces that are conductive or semiconductive. Typically, STM furnishes information about the electronic states of samples, employing a sharp probe operated in non-contact mode. Routinely, STM images demonstrate true molecular and atomic resolution, revealing the location of atomic or molecular vacancies and adatoms, depending on the nature of the sample. Characterizations with STM have been applied for investigations of metal,[6, 139-142] alloy,[143] semiconductor,[144, 145] and core-shell[146, 147] nanoparticles and nanocrystals, for a broad range of potential applications in catalysis, molecular electronics and chemical sensing.

3.4.1 Operating Principle of STM Imaging

The probe for an STM instrument is a conductive metal wire brought within tunneling range of the surface, without touching the surface. A bias voltage is applied either to the tip or the sample. Electrons tunnel between the surface and the tip producing an electrical signal, as shown schematically in Figure 3.12. The probe is scanned across the surface at a well-controlled distance using a piezoceramic scanner. The wire tip is raised and lowered to keep the signal constant and maintain the tip-sample distance. With STM, imaging and fabrication are

accomplished at a proximal distance from the surface in non-contact mode, within a tunneling range of < 1 nm.

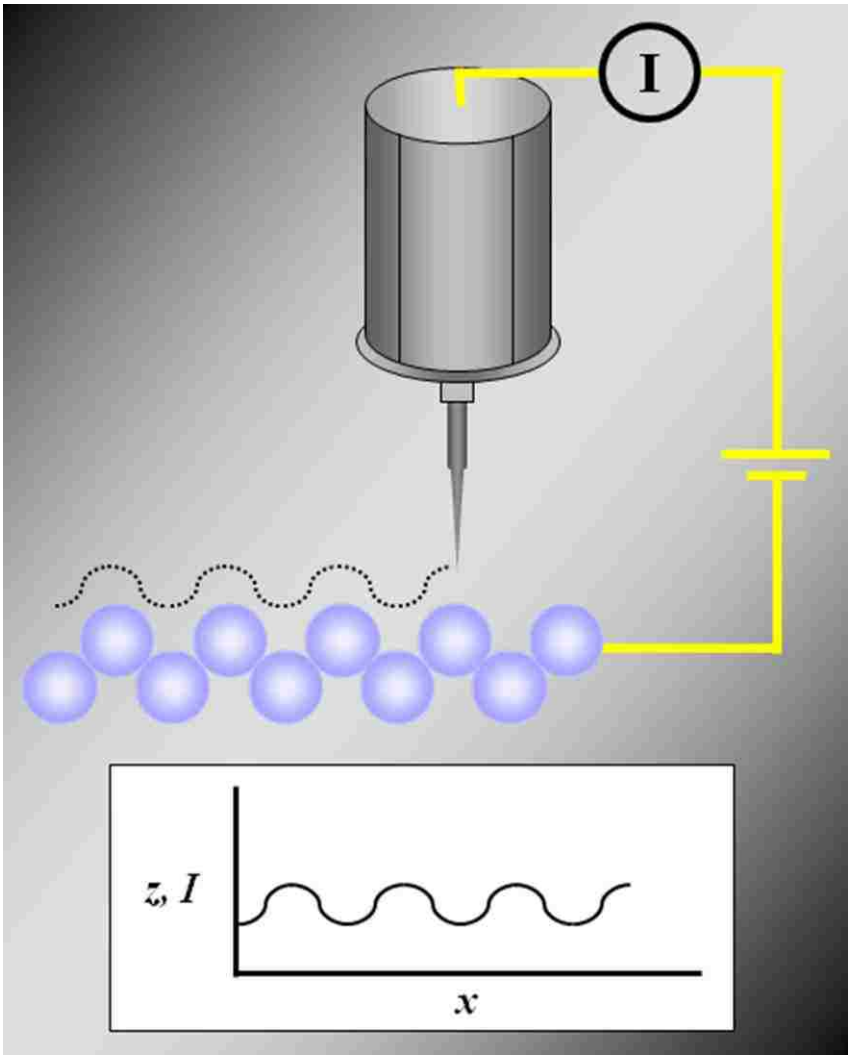

Figure 3.12. Imaging configuration for STM.

The electrical current between the tip and sample can be measured with STM, and images are generated by mapping changes in current. With the tip at close proximity to a sample, the bias voltage causes tunneling of electrons between the tip and sample, producing a current that

can be measured. STM spectroscopies such as current-distance (I-Z) and current-voltage (I-V) measurements can be acquired to evaluate electronic properties of samples at the molecular scale. A limitation of STM is that the sample must be conductive or semiconductive for electron tunneling, and liquid media can influence measurements of current spectroscopies. Typical substrates for STM imaging are HOPG, metal films, silicon and semiconductor crystals. Although the optimal resolution is achieved when STM instruments are operated in ultra-high vacuum (UHV) and at low cryotemperatures, it is also possible to use STM to characterize samples in air or in certain non-conducting solvents.

3.4.2 Single Electron Tunneling Measurements of MPCs

Scanning tunneling spectroscopies such as measurements obtained for single electron tunneling (SET) are important for new developments with single electron devices.[148-150] Measurements of the SET properties of MPCs were accomplished using UHV-STM by several groups.[6, 151, 152] Yang et al. acquired SET spectra for individual core-shell nanoparticles (Figure 3.13) that exhibited a relatively large Coulomb gap of 1.0 eV and fine Coulomb staircases measuring 0.2–0.3 eV at room temperature.[6] The current vs. voltage (*I*-*V*) spectra were acquired at selected pinpoint locations within the STM topography frames, indicated by a white cross in Figures 3.13A-3.13C. For SET spectra acquired with STM, the tip could be precisely positioned over individual MPCs (Figure 3.13A), at locations with aggregates (Figure 3.13B), or the matrix monolayer (Figure 3.13C). Gold nanoparticles were prepared by first passivating the nanoparticle surface with a layer of *n*-octanethiolate, which was then reacted with 1,8-octanedithiol via a place-exchange reaction.[153] The place-exchanged MPCs with a mixed shell of octanethiol and 1,8-octanedithiol were deposited on a gold film. The area surrounding the

nanoparticles was then backfilled with a self-assembled monolayer of decanethiol. The decanethiol monolayer furnished an internal molecular reference for electronic measurements and likewise provided a nanoscale ruler for precise height measurements. Coulomb blockade and staircase spectra were exhibited for individual MPCs and small clusters as shown in Figures 3.13A and 3.13B, respectively. For the surrounding areas of the decanethiol matrix, the *I-V* spectra exhibited some current tunneling through the junctions at the bias applied (Figure 3.13C).

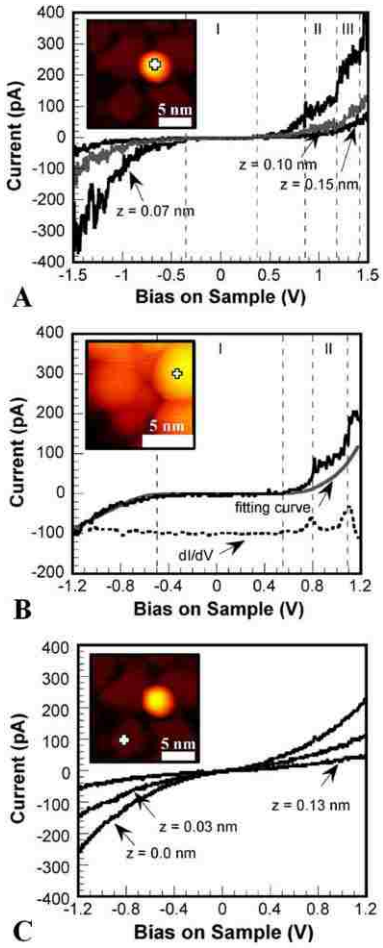

Figure 3.13. Current vs. voltage plots for gold MPCs. (A) *I-V* profile for an individual nanoparticle. (B) *I-V* measurements on a single MPC within an aggregate of nanoparticles and the computed derivative d*I*/d*V*. (C) *I-V* plot acquired on the surrounding decanethiol matrix. Reproduced with permission from.[6]

3.4.3 Manipulation of Metal Nanoparticles Using STM

When imaging with STM, the forces between the tip and the sample can be used to manipulate the position of individual nanoparticles on the surface. By carefully regulating current and voltage, isolated nanoparticles can be detached and manipulated to move across the surface with an STM tip. An example demonstrating STM manipulation of MPCs is presented in Figure 3.14.[6]

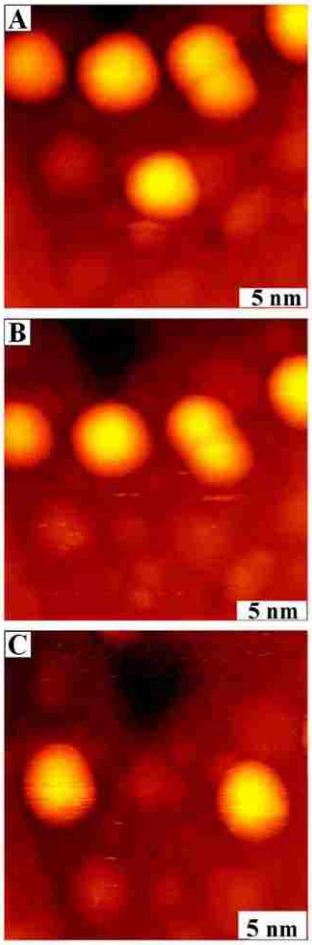

Figure 3.14. STM topography frames demonstrating the manipulation of thiol-passivated gold nanoparticles. (A) Views of five nanoparticles before STM manipulation; (B) after removal of one gold nanoparticle; (C) after extraction of two gold nanoparticles. Reproduced with permission from.[6]

The STM topographic views presented in Figure 3.14 were all obtained at the same local area of the surface. However, the nanoparticles were displaced individually by the action of the STM probe. Figure 3.14A was obtained without perturbing the nanoparticles by imaging locations of the surface. Successive removal of one and two gold nanoparticles is demonstrated in Figures 3.14B and 3.14C, respectively. Nanoparticle displacement from surfaces by STM manipulation can also be accomplished for metal nanoparticles that adhere weakly to the surface. Patterns with silver nanoparticles deposited on a gold substrate were produced using STM manipulation, as shown with STM topographs in Figure 3.15.[7]

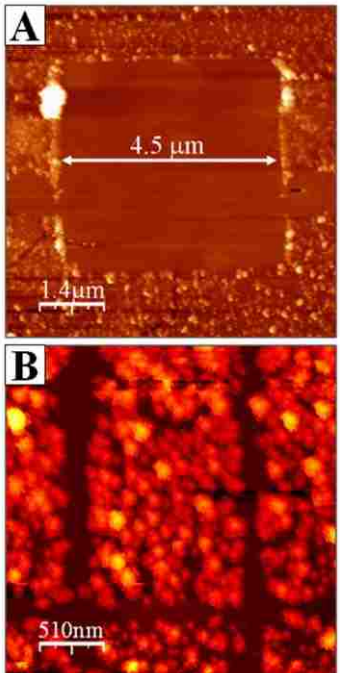

Figure 3.15. Manipulation of silver nanoparticles using STM. (A) Detachment of silver nanoparticles from a 4.5 × 4.5 μm^2 area of the gold surface viewed with an *ex situ* TM-AFM topograph. (B) STM topograph of line patterns formed by desorption of silver nanoparticles. Reproduced with permission from.[7]

In Figure 15A, nearly all of the silver nanoparticles were removed in the square area scanned with STM. The experimental conditions applied to produce three lines to form a cross pattern in

Figure 15B were achieved with a tip bias of 0.5 V and tunneling current of 2 nA. The STM image was acquired with bias of 0.2 V and tunneling current of 1 nA. In this example, STM scanning was found to displace the nanoparticles in areas that were scanned, due to weak adhesion of the silver nanoparticles to the gold substrate.

3.5 Approaches for Nanoscale Patterning of Nanoparticles

Whether using SPM-based approaches or electron microscopies, it is difficult to fully characterize nanoparticles that aggregate on surfaces. With SPM, the size and geometries cannot be clearly resolved if the probe cannot penetrate between individual nanoparticles to trace the outline of the surfaces. Of course, dilution is most often the first step to preparing samples for SPM or electron microscopy characterizations. However, when the solutions of nanoparticles are dried on surfaces the convective forces of liquid evaporation often will pull nanoparticles together into aggregates. Nanoscale lithography approaches for preparing well-defined test arrays of nanoparticles and nanocrystals can provide a practical test platform for sample characterizations. Representative examples of patterning nanoparticles using scanning probe-based lithographies and particle lithography will be described in this section.

An overview of the various lithography methods is presented in Table 3.2, highlighting approaches for patterning nanoparticles. Scanning probe-based techniques applied for lithography with nanoparticles include STM-based manipulation, NanoPen Reader and Writer (NPRW), nanografting, and Dip Pen Nanolithography (DPN). Approaches with polystyrene latex mesospheres have also been used for patterning nanoparticles; these methods are described collectively as particle lithography,[11, 154] colloidal lithography[155] or evaporative lithography.[5] Scanning probe instruments furnish tools for visualization, physical measurements, and precise

and precise manipulation at the nanometer scale. The analytical tools of SPM for nanoscale lithography are accessible to researchers from a broad range of disciplines and do not require expensive instrument modification. In fact, most SPM manufacturers have developed software to give operators complete control of SPL parameters such as the speed, bias, force, direction and residence time of the scanning probe. To progress to the smallest sizes, SPL can be applied to define surface patterns at either nanometer or micrometer scales. With computer automation, the arrangement, alignment and spacing of patterns can be defined precisely. In essence, approaches manipulation at the nanometer scale. The analytical tools of SPM for nanoscale lithography are accessible to researchers from a broad range of disciplines and do not require expensive instrument modification. In fact, most SPM manufacturers have developed software to give operators complete control of SPL parameters such as the speed, bias, force, direction and

with SPL and particle lithography enable new variables for experiments by providing a means to manipulate and define the placement of nanoparticles on surfaces. Another strategy applies nanolithography with self-assembled monolayers, to create nanopatterns of designed surface chemistry which define surface sites for binding nanoparticles and nanocrystals.[5, 8, 11] Each approach for lithography has attributes that largely depend on the nature of the nanoparticles to be investigated, which determine the ease of chemical steps, patterning throughput and types of nanostructures that are produced.

Table 3.2. Methods of Nanolithography Applied for Patterning Nanoparticles and Nanocrystals.

Nanolithography Method	**Mechanism for Nanopatterning**	**Examples of Nanoparticles Patterned**	**Ref.**
STM-based nanomanipulation	Electrical pulses are used to displace nanoparticles from surfaces.	MPCs, metal nanoparticles	[6, 7]
NanoPen Reader & Writer (NPRW)	Elevated force is applied to an AFM tip operated in air, to selectively remove areas of a surface film and replace with nanoparticles from the probe.	MPCs of thiolated gold nanoparticles	[10]
Nanografting	Elevated force is applied to an AFM tip immersed in a solution of nanoparticles to selectively remove areas of a surface layer and replace with nanoparticles from solution.	MPCs of thiolated gold nanoparticles	[10]
Dip-Pen Nanolithography (DPN)	Probe is coated with the nanomaterials to be patterned, which are then transported to the surface via the water meniscus formed at the tip-substrate junction.	Gold, palladium, and iron-oxide nanoparticles capped with different coatings	[156-160]
Two-Particle Lithography	Larger latex mesoparticles are mixed with nanoparticles and deposited on a surface to dry. With water rinsing, the latex floats away to leave regular nanoparticle patterns.	nanocrystals of CdS coated with cysteine	[8]
Evaporative Lithography	Nanoparticles were patterned via particle lithography on organosilane modified glass. Microspheres are removed with adhesive tape.	CdSe nanoparticles	[5]
Particle Lithography with Organosilanes	A surface is patterned with organosilane nanostructures using particle lithography. Nanoparticles chemically attach to defined surface sites.	bare gold nanoparticles, iron-oxide nanoparticles	[5, 11]

3.5.1 Patterning Nanoparticles Using NanoPen Reader and Writer

An SPM-based nanofabrication method known as "NanoPen Reader and Writer" (NPRW) developed by Amro et al. in 1999, was used to write thiolated molecules on organothiol passivated surfaces.[161] Nanopatterns of MPCs can also be produced using NPRW.[10] Basically, the same SPM configuration for contact mode AFM is used to accomplish NPRW, and the only modification is to coat the AFM probe with an ink solution of molecules or thiol-coated nanoparticles. For NPRW, a surface covered with a matrix monolayer of methyl-terminated *n*-alkanethiols serves as the *paper*. The matrix self-assembled monolayer provides a resistive surface which prevents the nonspecific deposition of ink molecules of nanoparticles on the substrate. The ink coating remains on the AFM tip unless high force is applied to the probe. Molecules or nanoparticles adhere to the AFM tip via physisorption (physical adsorption) when scanning across the surface under low force (< 1 nN). When the load on the AFM probe is increased, the ink from the probe is selectively deposited on the underlying gold substrate following the motion of the tip. Under high force, molecules of the matrix monolayer are simultaneously removed and replaced with nanoparticles from the tip. With NPRW, the writing step as well as characterization of nanostructures of MPCs is accomplished *in situ* without changing the tips.

The key steps for patterning nanoparticles using NPRW are outlined in Figure 3.16A and an example rectangular nanopattern of MPCs produced with NPRW is shown in Figure 3.16B. The MPCs used for patterning in Figure 3.16 contain a mixed coating of alkanethiols and alkanedithiols prepared by exchange chemistry. For patterning MPCs with NPRW, the step for coating the AFM tip with nanoparticle solutions is different than for inking the probe with *n*-

alkanethiol molecules, which requires only simple immersion of the entire AFM tip and cantilever in a solution of ink molecules. When a probe is immersed in a solution of nanoparticles, the reflective part of the cantilever can become contaminated with a film of nanoparticles, which is problematic for imaging.

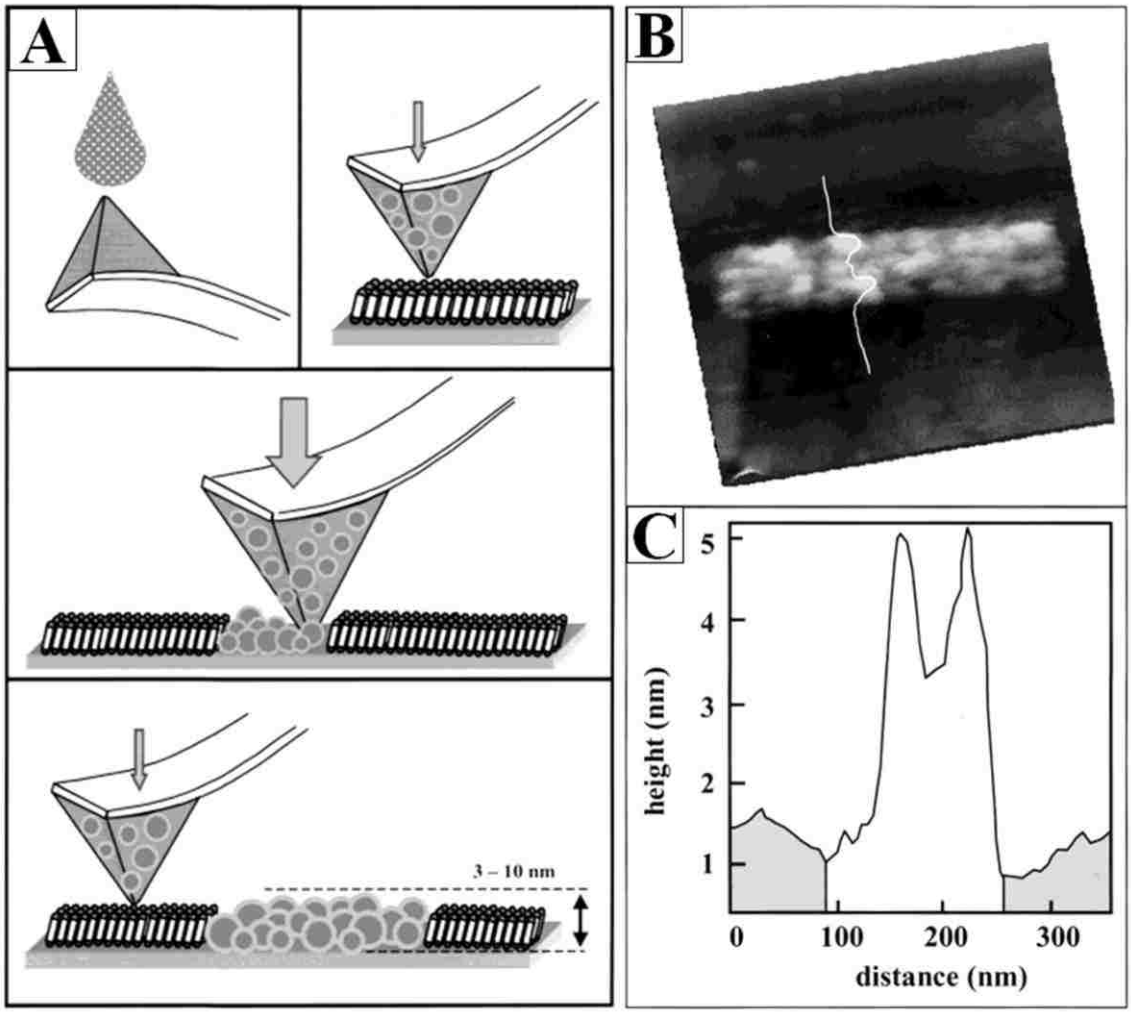

Figure 3.16. Patterning thiol-covered gold nanoparticles using NPRW. (A) Sequence for accomplishing NPRW. The tip is inverted and coated with MPCs, under low force the nanoparticles remain on the tip, while under high force the nanoparticles are transferred by contact with the substrate. Returning to low force the nanopatterns are characterized *in situ*. (B) Contact mode topography of a rectangular nanopattern (150 x 450 nm^2) of gold nanoparticles inscribed within a decanethiol monolayer. (C) Corresponding height profile for the line in **B**. Reproduced with permission from reference.[10]

Since only the tip of the probe needs to be coated with ink, for NPRW the ink was deposited by placing drops of nanoparticle solution directly onto an inverted probe.[162] The coated tip is used for both imaging and high-resolution characterizations of the sample surface. When operated at low force, the MPCs remain attached to the AFM tip because the matrix monolayer (e.g. decanethiol) resists the adsorption of nanoparticles. However, when the force was increased to a certain threshold the tip makes contact with the gold substrate underneath the matrix layer. Nanoparticles of MPCs with place-exchanged thiol endgroups readily adhere to gold through sulfur-gold chemisorption. The nanoparticles preferentially detach from the AFM probe to bind to the gold substrate, forming patterns selectively in areas where the tip was scanned at high force (Figure 3.16B). A cross-section across the fabricated pattern shown in Figure 3.16C reveals that a single layer of nanoparticles was written. The gold core of MPCs measured 1.2 – 8.2 nm and was covered by a monolayer coating containing a mixture of both hexanethiol and 1,6-hexanedithiols. Returning to low force for imaging, individual nanoparticles within the nanostructure can be resolved in the topography image.

3.5.2 Patterning Nanoparticles with Nanografting

Nanografting is an SPL method developed by Xu and Liu in 1997.[163] For nanografting, the '*paper*' is an alkanethiol self-assembled monolayer formed on a gold substrate and the AFM tip is operated under force as a '*pen'* to inscribe nanopatterns. With nanografting, the solution for imaging contains '*ink*' molecules or nanoparticles for writing nanopatterns. Before nanoshaving, a relatively flat area of the matrix monolayer is characterized at low force (~ 1 nN) to identify an area with few defects that is suitable for patterning. To pattern MPCs, nanoshaving is accomplished by applying a high local load (1-10 nN) on the AFM tip to make

contact with the gold substrate as the probe is rastered back and forth. With pressure on the AFM tip, the matrix monolayer is swept off the surface and is either dissolved into the imaging media or deposited at the edges of the nanostructures. Nanoparticles or molecules dispersed in the imaging solvent deposit on the shaved areas along the uncovered track defined by the AFM probe. Returning to a low force, the same AFM tip is used to characterize fabricated nanopatterns *in situ*. Nanografting can be used to fabricate multiple patterns with various components.[164,165]

An example pattern of thiol-coated gold nanoparticles produced with nanografting is displayed in Figure 3.17.[10] Gold nanoparticles were modified by encapsulation with mixed hexanethiol and hexanedithiol molecules to incorporate thiol linker groups for chemisorptive attachment to gold surfaces. First, a rectangular (150 x 300 nm^2) area was nanoshaved within a decanethiol matrix monolayer as shown in Figure 3.17A. Most of matrix adsorbates were removed successfully with a single scan of the AFM tip. After 12 h, MPCs adsorbed selectively on the areas where the matrix had been displaced (Figure 3.17B) to form a single layer of nanoparticles. The areas covered by nanoparticles have a brighter contrast in the topography image indicating that the nanoparticles are taller than decanethiol monolayer. Individual particles with nearly spherical shapes can be discerned from the pattern; approximately 51 nanoparticles were deposited within the fabricated structure. The line profile (Figure 3.17C) indicates that the nanoparticles have a height of 2.3 ± 0.3 nm above the matrix, thus the overall thickness of the nanoparticles measures 3.8 ± 0.3 nm. The rate of adsorption of nanoparticles during nanografting is much slower compared to adsorption of thiol molecules and the adsorption step is dependent upon the concentration of MPCs in the imaging media.

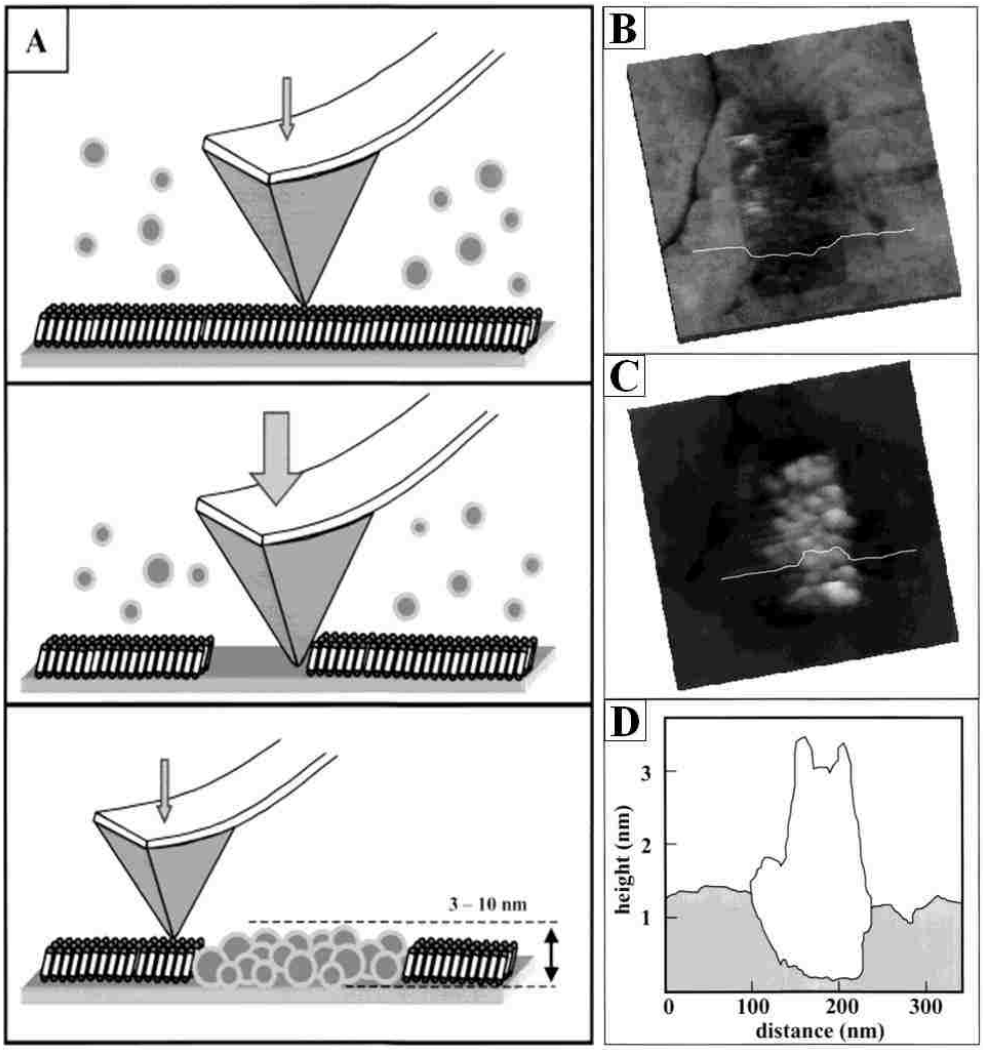

Figure 3.17. Nanostructure of thiol-coated gold nanoparticles produced using SPL. (A) Steps for nanografting nanoparticles. A relatively flat area is shaved within a solution containing nanoparticles. Nanoparticles immediately adsorb on the uncovered area of the matrix. (B) Rectangular pattern shaved within a decanethiol matrix. (C) Nanografted structure of MPCs. (D) Combined cross-sections for B and C corresponding to before (gray) and after (white) nanopatterning, respectively. Reproduced with permission from reference.[10]

3.5.3 Patterning Nanoparticles with Dip-Pen Nanolithography

Dip-Pen nanolithography (DPN) is an SPM-based lithography approach introduced by Piner et al. in 1999.[165] For DPN, a coated tip is used as a pen to directly write with molecules or

nanoparticles on the surface of a clean substrate in ambient environments. The delivery of ink from the probe to form nanopatterns on the substrate is facilitated by the water meniscus formed at the tip-sample junction. Dip-Pen nanolithography was first used to write alkanethiols on gold surfaces, but since then DPN has been applied to generate a broad range of nanostructures.[166, 167] After patterns are written, the writing probe is exchanged for a clean, uncoated probe for *ex situ* characterizations of the nanopatterns. The size of the patterns written with DPN depends on the contact time between the tip and the surface.

Sols of citrate-capped iron-oxide (Fe_2O_3) nanoparticles were patterned on surfaces using DPN and characterized using electron microscopy and MFM.[156] Dip-Pen nanolithography has also been applied to directly deposit gold nanoparticles on surfaces.[157] Using a configuration with two separate AFM probes, one tip was used for depositing modified gold nanoparticles and a second probe was used to characterize the structures formed on a silica surface. An 'ink pot' reservoir was formed by depositing a drop of a solution containing nanoparticles on the surface and the solvent was evaporated in ambient conditions. The probe for printing was immersed in the ink pot for a few seconds and then used to write clusters of gold nanoparticles at designed locations, with heights corresponding to the thickness of a monolayer. The amount of contact force between the tip and the surface influenced the lateral dimensions of the islands, which ranged from 50 to 200 nm in height. Printing of inks of water-based nanoparticles on mica substrates was also accomplished using DPN to produce line patterns as small as 30 nm, by modifying gold and palladium nanoparticles with ionic capping molecules.[158] A method described as 'single particle Dip-Pen nanolithography' was introduced by Wang et al. to manipulate individual gold nanoparticles.[159] Individual gold nanoparticles were picked up and

redeposited at other locations using an AFM tip operated under different forces. Once the particle was deposited on the surface, TM- AFM was used to characterize the nanostructures.

Factors that affect the fabrication of nanopatterns of core-shell gold nanoparticles using DPN were investigated by Wang et al.[160] Gold nanoparticles capped with 4-(*N*,*N*-dimethylamino)pyridine (DMAP) were used to coat an AFM probe for writing patterns on a UV-ozone cleaned silicon oxide surface. Surface structures of DMAP-capped gold nanoparticles produced with DPN are shown in Figure 3.18. To evaluate the thermal stability of the patterns, topography views were also acquired after the patterns were annealed at 165 °C.

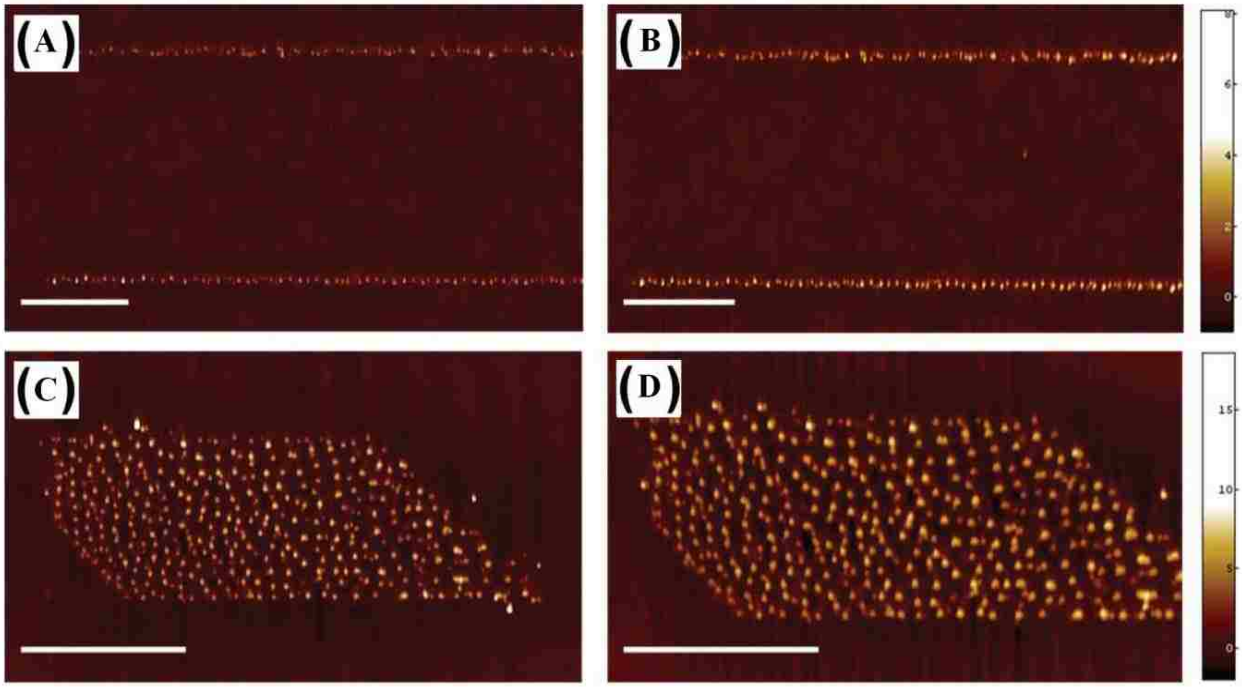

Figure 3.18. Patterns of gold nanoparticles capped with DMAP produced on a silicon-oxide surface using DPN. (A) Line pattern of DMAP-capped gold nanoparticles written with DPN; (B) same pattern after annealing at 165 °C. (C) Micropattern written with DPN; (D) same pattern after annealing (scale bars: 2 μm). Reproduced with permission from reference. [160]

3.5.4 Nanostructures of Quantum Dots Prepared by 'Two-Particle' Lithography

The relatively slow, serial-based approaches of SPM-based methods for writing patterns one-by-one may not be the best approach to scale-up lithography for writing millions of nanostructures. A number of research groups have developed other means for the fabrication of patterns.[168-171] However, approaches based on the natural self-assembly processes of molecules and nanomaterials may be more suitable for high-throughput applications that will require generating millions of patterns or more. Particle lithography, (also known as colloidal lithography) has been used to pattern materials such as metals, proteins, polymers, self-assembled monolayers and quantum dots.[8] A method of 'two-particle' lithography was developed by Lewandowski et al. to produce well-defined arrays of nanostructures of quantum dots.[8] Two-particle lithography was also generically applied to pattern cobalt nanoparticles with an oleic acid and trioctylphosphine oxide coating, as well as metal nanoparticles encapsulated with plasmid DNA (*unpublished*). The basic steps for two-particle lithography are outlined in Figure 3.19A. First, latex or silica mesospheres are washed by centrifugation in ultra pure water to remove contaminants such as dots and the scanning AFM probe. Measurements of the diameter of the ring nanostructures measured approximately 180 nm, as viewed in the high magnification image in Figure 3.19D. The nanopatterns have a geometry that is smaller than the periodicity of the latex structural templates because the location of nanoparticles is defined by the meniscus at the base of the mesospheres formed during the drying step. A cursor profile across two ring nanostructures (Figure 3.19E) reveals that the height of the ring pattern measures 5.6 ± 0.9 nm, corresponding to a single layer of quantum dots.

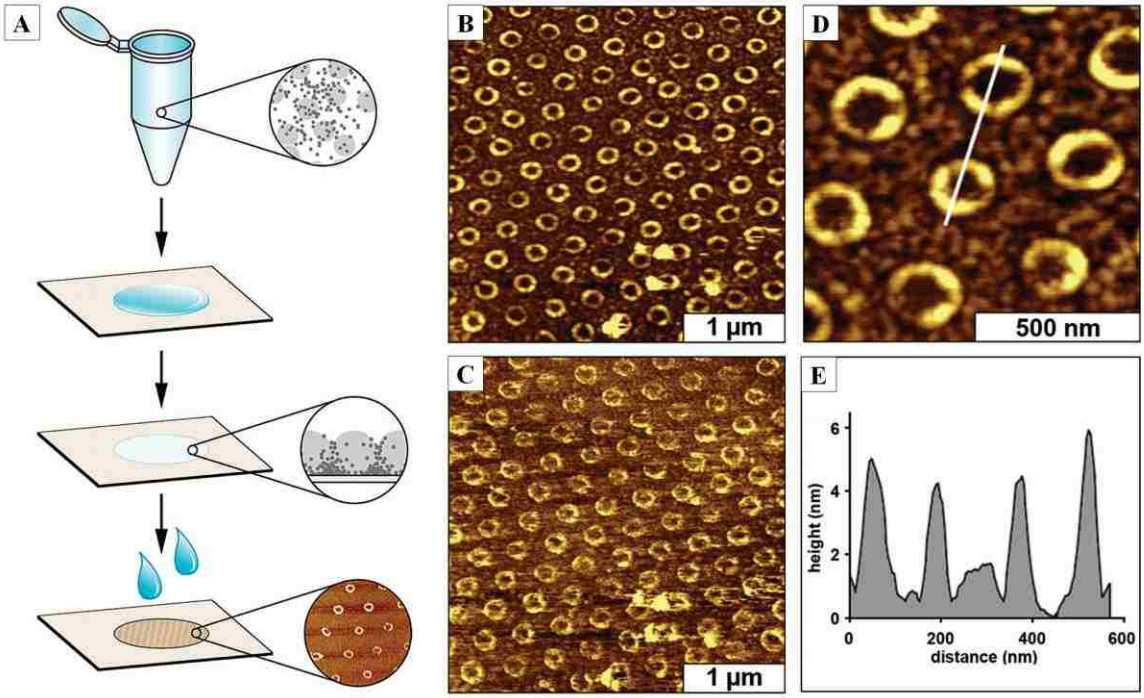

Figure 3.19. Cysteine-coated CdS nanostructures organized on the surface using latex templates. (A) Steps for two-particle lithography; (B) topography image; (C) simultaneously acquired lateral force image; (D) high magnification view of **B**; (E) cursor profile across two rings in **D**. Reproduced with permission from reference. [8]

Ring-shaped nanostructures of quantum dots (CdSe) capped with trioctylphospine oxide were produced using an evaporative templating approach based on particle lithography, developed by Chen et al.[5] Quantum dots were carried with the liquid meniscus of microspheres during evaporation to produce ring assemblies by capillary forces at the interface of the surface and polystyrene spheres. To remove the mesosphere template, adhesive tape was placed in direct contact with the sample to remove the mesospheres rather than removal by liquid rinsing. Hexagonal arrays of nanorings were formed with thicknesses ranging from single dot necklaces to thick multilayer structures over surface areas of many square millimeters, with control of the

ring diameters.[172, 173] Arrays of silver nanoparticles can be used to sense specifically bound analytes with zeptomole sensitivity, using localized surface plasmon resonance (LSPR) spectroscopy. Particle lithography was applied to prepare well-defined surface arrays of silver nanoparticles by line of sight metal deposition through mesosphere masks, by Haynes et al.[172] Ordered arrays of gold nanoparticles were fabricated using particle lithography combined with electron beam evaporation. After preparing metal arrays, reactive ion etching and further chemical steps were used to prepare designed nanostructures.[173] Patterned arrays of semiconductor and metal nanoparticles provide useful test platforms for studying fundamental physical chemistry and molecular interactions and may provide useful building blocks for the development of photonic, electronic, or magnetic devices for sensing applications.

3.5.5 Attaching Metal Nanoparticles to Organosilane Nanopatterns

Well-defined patterns of organosilane self-assembled monolayers can be used to define sites for selective chemical attachment of nanoparticles and nanomaterials. Attachment of nanoparticles is directed by the chemical selectivity of organosilanes or organothiols by either surface passivation or reactivity towards metals or molecules of nanoparticle shells by selecting functional group chemistries. Self assembled monolayers of organosilanes on oxide surfaces were first reported in 1980 by Sagiv.[174] Since then, a wide range of strategies have been developed to generate patterns of organosilanes, particularly for application as photoresists to microfabricate circuits and computer chips. Organosilane and organothiol monolayers have been applied for attaching nanoparticles to surfaces through different chemical linkages.[2, 36, 37, 104, 175-179] A new method combining particle lithography with chemical vapor deposition of organosilanes was recently introduced by Li et al.,[4] which can likewise be applied for patterning

nanoparticles with a few additional chemical steps.[11] The sequential steps for producing nanopatterns of organosilanes are shown in Figure 3.20. First, an evaporative mask of monodisperse latex or colloid is prepared by drying a drop of latex or colloidal silica mesospheres suspended in water on a clean flat surface (Figure 3.20A).

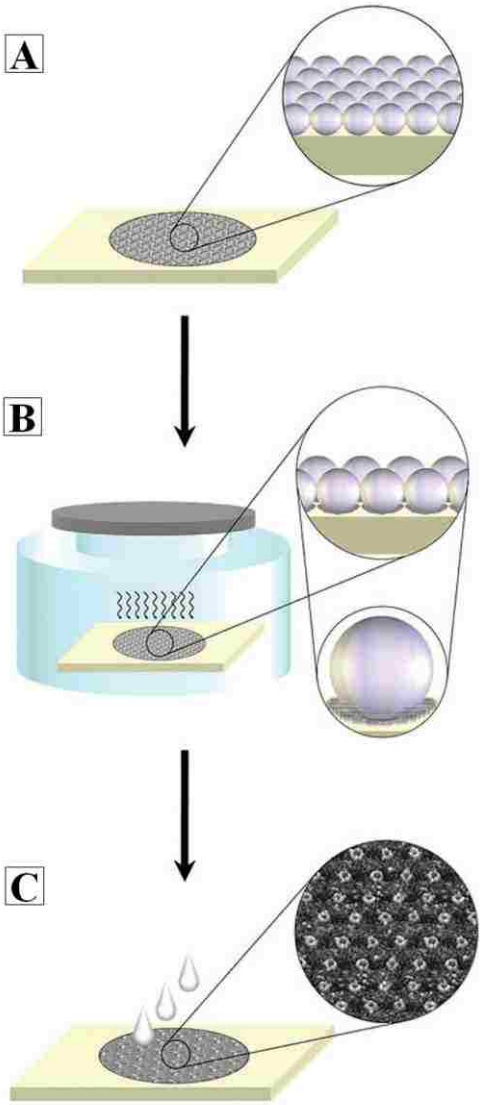

Figure 3.20. Steps for accomplishing particle lithography with organosilanes. (A) A mask of monodisperse latex spheres is prepared on a flat surface. (B) A vapor of organosilanes is produced inside a sealed container by heating. (C) The latex masks are removed by rinsing. Reproduced with permission from reference. [4]

The dried film of mesospheres are placed in a container with a few drops of the chosen organosilane and heated in an oven at 80 °C for several hours (Figure 3.20B). The heated temperatures generate a vapor of organosilanes which adsorbs onto uncovered interstitial areas of the surface between the spheres of the mask. Finally, the mesospheres are removed by rinsing in ethanol or water (Figure 3.20C). Organosilanes adhere strongly to the substrate via covalent bonding and are not washed from the surface during the rinsing step. The sample can then be used for further patterning steps to spatially define the adsorption of nanoparticles.

The successive steps of a nanopatterning experiment are presented in Figure 3.21, accomplishing precise placement of gold nanoparticles on well-defined nanopatterns of organosilanes produced by particle lithography. A molecular model for each step is shown on the left, with contact mode topography and lateral force AFM images of the surface changes shown at the center and right sides of the figure, respectively. In the first step, (Figures 3.21A-3.21C) porous patterns of octadecyltrichlorosilane (OTS) were prepared using the reaction scheme of Figure 3.20. Next, the uncovered pore areas of the surface were backfilled with a thiol-terminated organosilane by simple immersion in a solution of toluene containing mercaptopropyltrimethoxysilane (MPTMS), as shown in Figures 3.21D-3.21F. The sample was finally immersed in a solution of bare gold nanoparticles which attached selectively to areas with MPTMS (Figures 3.21G-3.21I). The contact mode AFM topographs (center frames) reveal changes in the thickness and height of nanostructures at each step of the experiment, while simultaneously acquired lateral force images (right panels) clearly distinguish differences in surface chemistry for the areas containing different molecules. In the final step, the topography and lateral force images reveal that clusters of approximately 2-5 nanoparticles have formed

selectively on the areas patterned with MPTMS, while the areas with OTS resisted the nonspecific attachment of gold nanoparticles (Figures 3.21H and 3.21I).

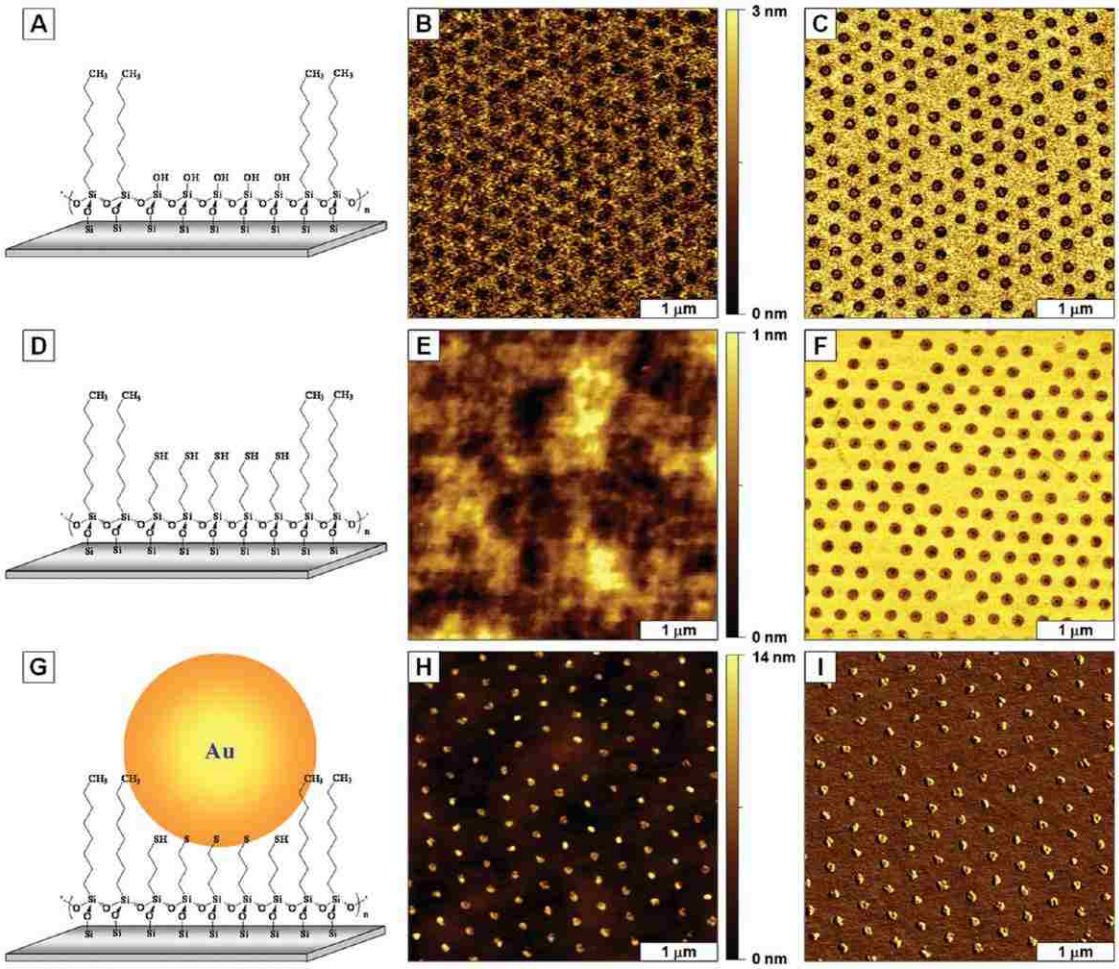

Figure 3.21. Selective attachment of gold nanoparticles on organosilane nanopatterns produced by particle lithography. (A) Model for OTS patterns formed on silicon. (B) Nanostructures of OTS viewed with a contact mode topograph, generated using particle lithography. The dark areas are uncovered silicon. (C) Corresponding lateral force image for **B**. (D) Change in surface structure after depositing MPTMS in the pore areas. (E) Patterns are indistinguishable in topography frame after the pores were filled MPTMS. (F) The lateral force image clearly reveals the size and locations of nanopatterns that were produced. (G) Model of the selective attachment of gold nanoparticles to MPTMS. (H) Patterns of gold nanoparticles can be resolved with contact mode AFM. (I) Lateral force image for **H**. Reproduced with permission from reference. [11]

3.6 Magnetic Characterizations of Metal Nanoparticles with SPM

Magnetic nanoparticles, such as iron-nickel alloy nanoparticles, are promising materials that have gained considerable technological and theoretical interest because the properties can be exploited in devices. Properties such as magnetic recording density, recording speed, noise suppression, and the lifetime of nanomaterials are significantly enhanced as the dimensions of the magnetic particle decreases.[115, 116] Nanoparticles of iron or iron alloys are the most widely used magnetic nanomaterials and have been applied in energy conversion and electronic devices,[116] in high-density data storage devices,[15, 67] ferrofluids,[180-182] and magnetic refrigeration systems.[183] Magnetic nanoparticles are also critical for biomedical applications such as magnetic resonance imaging,[63, 184, 185] hyperthermic treatment for malignant cells,[186, 187] magnetic separations,[63, 188] site-specific drug delivery[63] and the manipulation of cell membranes.[189] Nanoparticles have been conjugated with DNA, peptides and antibodies to generate magnetic nanoparticle bioconjugates with hybrid functionalities for applications in bioassays and bioimaging.[15, 63, 185, 188, 190-192] Superparamagnetic iron oxide nanoparticles were the first contrast agents used for MRI imaging that targeted liver cells.[193] A wide range of magnetic particles have been produced with different sizes (varying from 10 to 500 nm)[194] and have been prepared with a diverse range of coating materials, such as dextran, starch, albumin, silicones, and poly(ethyleneglycol).[195] Essentially, for nanoparticles with paramagnetic and superparamagnetic properties, the magnetic character vanishes in the absence of a magnetic field, which minimizes potential self-aggregation of the nanoparticles *in vivo.*

Physical and chemical properties greatly depend on size at some length scale since the properties of single atoms are very different than bulk materials.[172] An active area of research

interest is the investigation of size-scaling effects of magnetic properties for nanoparticles. Changes in magnetic properties with nanoscale dimensions are not well understood even for simple particles composed of pure materials, such as iron, cobalt or nickel.[196] Knowledge of magnetic nanoparticles cannot necessarily be inferred from known information of bulk materials since more of the atoms of the nanoparticle are surface atoms as particle dimensions are decreased, so that surface and interface effects predominate.[197] Nanoparticles have been shown to exhibit unique magnetic phenomena which are not observed when in bulk, such as giant magnetoresistance (GMR) and superparamagnetism.[198, 199] Understanding the size-scaling effects of magnetic nanomaterials will prove to be valuable for development of new nanomaterials with engineered properties. Scanning probe methods provide new approaches for investigating the magnetic properties of nanomaterials with nanoscale sensitivity at the level of individual nanoparticles.

3.6.1 Magnetic Force Microscopy Measurements of Nanoparticles

Magnetic force microscopy (MFM) was introduced in 1987, shortly after the discovery of the AFM.[200] MFM has become a valuable scanning probe technique that is currently employed in both industry and research for studying the magnetic properties of magnetic nanoparticles,[2, 201] magnetic thin films,[202] and high density magnetic storage media and recording heads.[203] For MFM, the AFM tip is coated with a magnetic thin film for imaging in non-contact mode. The most commonly used MFM cantilevers are silicon or silicon nitride microfabricated probes, which are coated with a thin ferromagnetic film several nanometers thick. Examples of magnetic materials used for coating tips include alloys of cobalt, chromium, nickel, platinum, or iron. Tips with a high aspect ratio have been reported to achieve lateral resolutions up to 10 nm using

MFM, [204] although the resolution is more commonly 200-500 nm for standard commercial probes. Essentially, for MFM imaging, a magnetic probe is used as a sensor to detect the strength and polarity of the sample. As the tip is scanned over a magnetic domain, the relatively weak magnetic fields will either attract or repel the magnetic tip, depending on the strength and polarity of the surface feature. Areas that are nonmagnetic or weakly magnetic are not detected, and the tip experiences no deflection. The relative strength of the magnetic fields can be mapped at different distances from the surface by changing the distance the probe is lifted from the surface. At further distances, the field strength is weaker.

A complexity of MFM imaging is that the surface topography affects the field strength experienced by an AFM tip scanned above the surface because of changes in tip-sample distance. The most common method of MFM operation involves a two-pass technique, or "lift mode" (Digital Instruments), which minimizes the contribution of topography MFM images.[205, 206] In lift mode, the magnetic tip is scanned twice along each linesweep for sequentially mapping the topography and magnetic domains. During the first scan, the topography is recorded and memorized using contact mode. For the second scan, the tip is first raised to a preset distance according to the topography profile recorded from the first scan, and then scanned along the same line to maintain a constant tip-sample separation distance. The tip-sample separation distance must be carefully chosen to overcome and eliminate Van der Waal attractive forces so that the cantilever deflection is affected only by long-range magnetic forces. As the tip is scanned above the sample during the second pass, the contrast is dependent on the interaction of magnetic dipoles between the magnetic tip and the surface.[91]

Results obtained from MFM provide a visual map of the magnetic domains of surfaces patterned with magnetic nanoparticles. Micropatterned arrays of magnetic nanoparticles of iron, nickel and cobalt were imaged using MFM by Zhong et al.[175] The hydrophilic, hydroxyl-terminated surface of a silicon wafer was patterned with a hydrophobic monolayer of OTS using microcontact printing with an elastomeric stamp, which defined surface sites for depositing a solution of metal salts. After the salt solutions had dried, the samples were heated in air at 600 °C and then converted into a magnetic metal through reduction by hydrogen gas at 400 °C. The magnetic properties of the 2D arrays of magnetic nanoparticles of cobalt, nickel and iron were studied using MFM.

The local magnetic properties of clusters of cobalt nanoparticles coated with oleic acid were studied with MFM by Leo et al.[207] Cobalt nanoparticles of 11 nm diameter were deposited on silicon substrates using either spin-coating or casting. Using a tip-sample separation of 50 nm the MFM image revealed features corresponding to clusters of cobalt nanoparticles that were approximately 0.3 μm in dimension. A magnetic field applied during the sample preparation step of nanoparticle deposition was shown to orient the magnetic moments of the cobalt nanoparticle clusters perpendicularly to the surface.

The ferromagnetic properties of different assemblies of monodisperse cobalt nanoparticles were investigated using by MFM and magnetometry by Puntes et al.[2] The magnetic interactions of cobalt nanoparticles are strong enough for MFM characterizations. However, multilayers and aggregation can occur when deposited on surfaces. Thus, to obtain a monolayer the nanoparticles were attached chemically to an amine-functionalized silicon substrate silanized with 3-[2-(2-aminoethylamino)ethylamino]propyl-trimethoxysilane. The topography (Figure

3.22A) and MFM images (Figure 3.22B) show the arrangement of a partial layer film of nanoparticles. In the MFM phase image the light colored areas correspond to repulsion of the tip, whereas darker areas correspond to attraction. In this example, the sample topography is also apparent in the MFM image because the magnetic dipole is at the center of the magnetic particles. The variation of the amplitude of the magnetic signal is a function of the density of particles. Areas with different nanoparticle density display different average magnetic contrast.

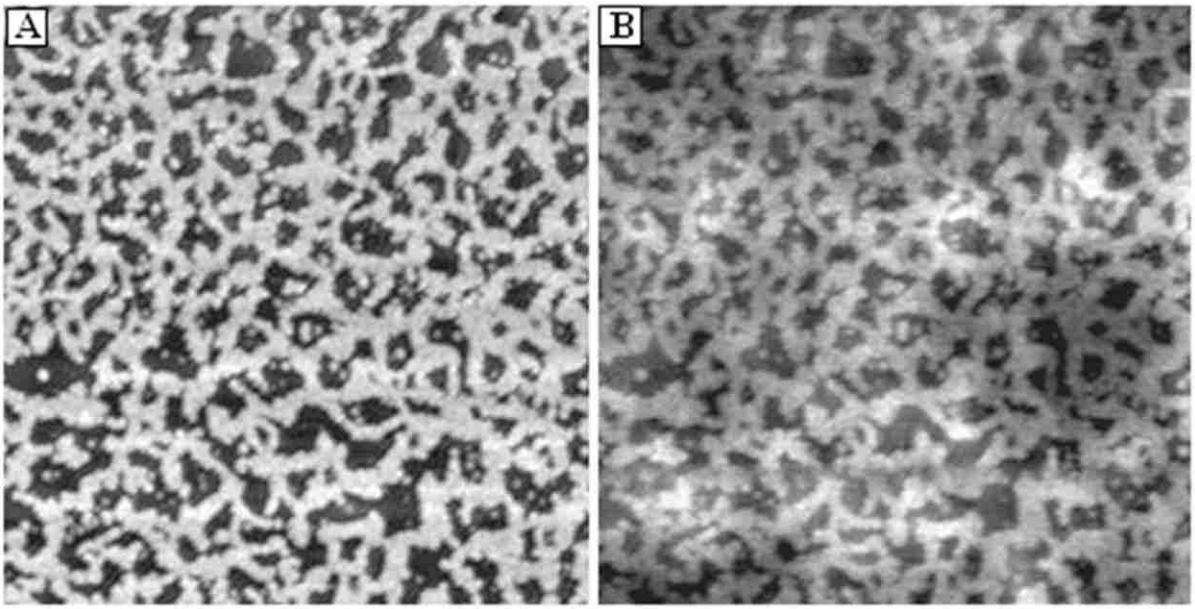

Figure 3.22. Magnetic characterization of monodisperse cobalt nanoparticles. (A) Tapping mode AFM topograph for a 2×2 μm^2 scan area, vertical scale is 10 nm. (B) MFM image for the same area acquired using lift mode. The sample displays a partial layer of 12-nm cobalt nanoparticles attached to a silicon surface by organosilane chemistry. Reproduced with permission from reference. [2]

The measurement limitations of MFM detection intrinsically depends on the size and spring constant of the magnetic probe. The topography resolution is generally poor with MFM, since the magnetic coatings on the underside of MFM tips results in probes that are blunt and bulky. For MFM, the strength of the magnetic field of the sample must be strong enough to

deflect or attract a micrometer-sized cantilever to enable mapping of the magnetic domains. The MFM approach provides a means to map the strength of the magnetic field at various distances, (e.g. 50, 100, 150 nm) from the surface. Thus, MFM provides a means to measure the relative strength and polarity of magnetic regions.

3.6.2 Magnetic Sample Modulation AFM Characterizations of Metal Nanoparticles

Obtaining magnetic characterizations of isolated nanoparticles has proven to be a challenge. A significant problem for AFM characterizations of magnetic nanoparticles is that nanoparticles can detach from the surface and attach to the tip due to magnetic attraction. Even if the magnetic nanoparticles adhere strongly to the surface, there is a problem with sample aggregation, since magnetic nanoparticles tend to be attracted to each other and aggregate on surfaces. Often, the magnetic fields produced by individual nanoparticles operating over short distances is pretty weak and are not sufficiently strong to attract or repel a magnetic probe affixed to a cantilever with dimensions of hundreds of microns. A specific problem for probes coated with a magnetic thin film is that the film can be worn away and detach from the tip, and the magnetic field diminishes over time which will require remagnetization. Also, it is difficult to precisely quantify the field strength of the magnetic MFM probes.

Magnetic sample modulation (MSM) is a promising alternative imaging mode for selectively mapping the magnetic response of individual nanoparticles.[208, 209] The MSM configuration uses contact mode operation combined with selective modulation of magnetic domains. In MSM, a soft, nonmagnetic cantilever is used as a force and motion sensor for

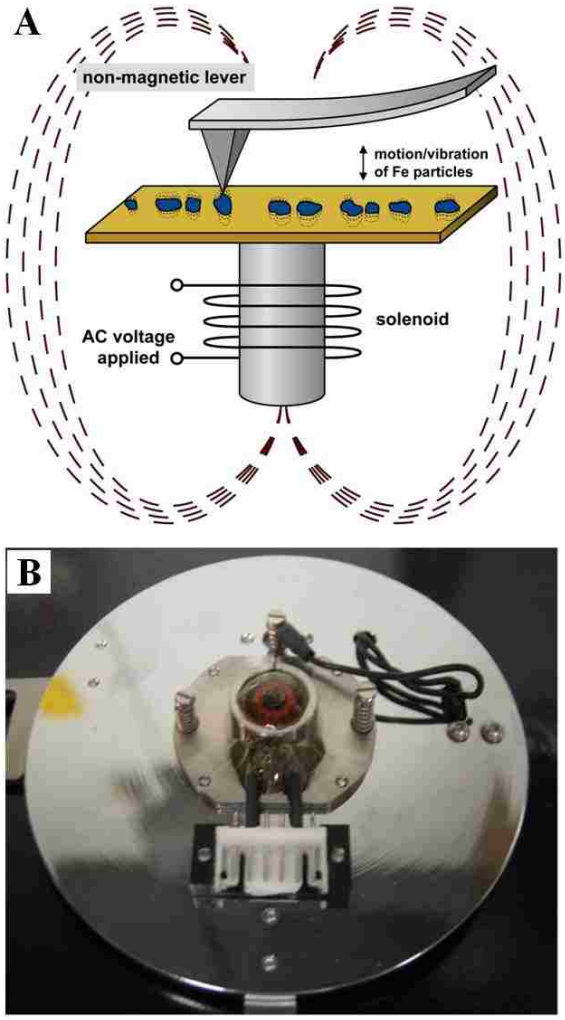

Figure 3.23. Operating principle for magnetic sample modulation AFM. A) Instrument setup. B) Photograph of a wire coil solenoid located beneath the sample plate used to generate an AC electromagnetic field. Reproduced with permission from reference. [5]

mapping the vibrational response of magnetic nanoparticles. An externally applied AC electromagnetic field (0.2 – 2 Tesla) induces magnetic nanomaterials to vibrate in rhythm with the flux of the oscillating magnetic field (Figure 3.23A). The physical motion of vibrating magnetic nanoparticles is sensed by a nonmagnetic tip operated in contact mode. The changes in the mechanical motion of the nanoparticles cause the tip to deflect, which is then detected with

the photodiode detector. Variations in the phase angle and amplitude of the tip as it interacts with vibrating magnetic nanostructures are sensitively mapped as a function of the tip position to generate MSM phase and amplitude images to differentiate between magnetic and nonmagnetic domains. In the instrument setup for MSM, a magnetic AC mode, or "MAC-mode" (Agilent Technologies) sample plate is used to generate an oscillating electromagnetic field (Figure 3.23B). The frequency and strength of the magnetic field are tuned by selecting the parameters for the AC current applied to the solenoid. The AFM tip and nosecone of the scanner used for MSM are composed of nonmagnetic materials so that vibration is not introduced indirectly by the scanner assembly in response to the electromagnetic field. Using the driving AC waveform as a reference, a lock-in amplifier is used to acquire the amplitude and phase components of the tip deflection signals to generate MSM phase and amplitude images. A lock-in amplifier provides extreme sensitivity for detecting small changes in tip movement. The positional feedback loop used in MSM is the same as in contact mode, thus enabling simultaneous acquisition of topography information.

The magnetic domains of electrolessly deposited iron oxide nanoparticles on organosilane patterns were characterized with MSM by Li et al., as shown in Figure 3.24.[208] Arrays of iron oxide nanoparticles were prepared by using steps of particle lithography with chemical vapor deposition of organosilanes followed by electroless deposition of iron oxide (Fe_3O_4). The topography, amplitude and phase images shown in Figures 3.24A-3.24C respectively, demonstrate changes in the response of nanoparticles as the field was turned on or off. Initially, the sample surface was scanned in contact mode starting at the bottom of the frame without applying a magnetic field. Without interrupting data acquisition, an AC electromagnetic

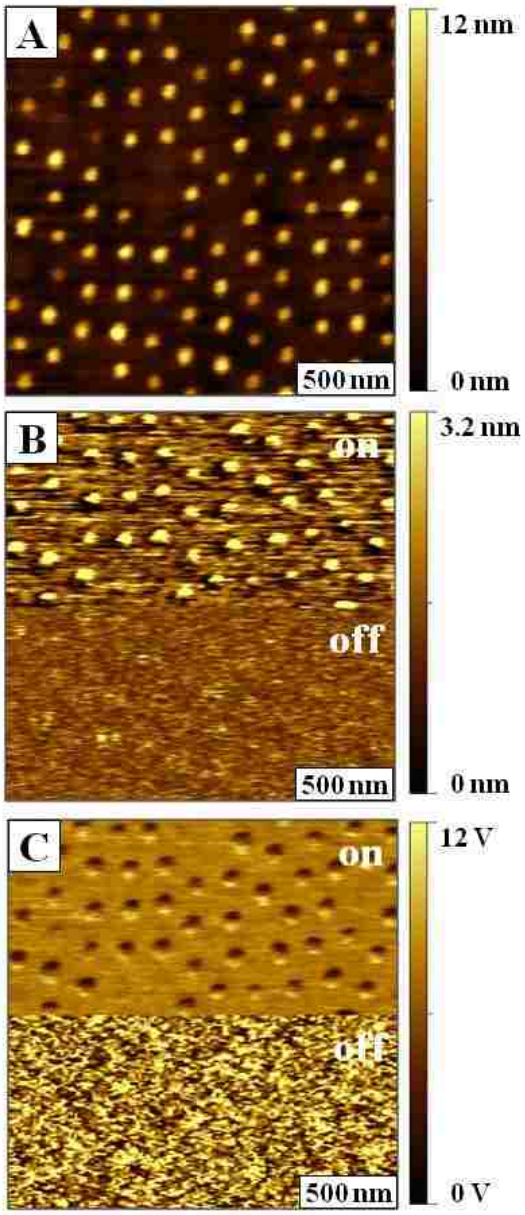

Figure 3.24. The magnetic response of iron oxide nanoparticles to an external AC electromagnetic field captured with MSM. (A) Topographic view of arrays of iron oxide deposits acquired simultaneously with (B) amplitude and (C) phase images. Midway through the scan the field was activated. Reproduced with permission from reference.[5]

field was turned on midway through the scan. In the topography image (Figure 3.24A), there is no noticeable difference in either contrast or surface features whether the field is turned on or off. However, for amplitude and phase images (Figures 3.24B and 3.24C), it is clear that the

magnetic field influences data acquisition. In the absence of an external field, no contrast is observed in the amplitude and phase images since the magnetic nanoparticles are not induced to vibrate. Once the external field is applied, the magnetic and nonmagnetic domains on the surface immediately become visible in MSM phase and amplitude channels. Unlike SPM imaging modes which use specifically designed tips to interrogate samples, for MSM imaging the changes in sample dynamics form the basis for measurements of material properties. The sample is driven to vibrate in response to an externally applied electromagnetic field and the tip is used as a force and motion sensor for mapping the vibrational response. For MSM, the samples are induced to vibrate in concert with the flux of an externally applied electromagnetic field and the sample vibration is transferred to drive the motion of soft, nonmagnetic probe. Lock-in-detection is used for sensitively tracking changes in the amplitude, phase and frequencies of motion compared to the driving AC electromagnetic field. The MSM technique provides exceptional sensitivity and is selective for distinguishing samples which have a magnetic moment in the presence of an applied AC electromagnetic field. The detection capabilities of the new MSM imaging mode pushes beyond the typical 200 nm detection limit of MFM to characterize magnetic particles as small as 1 nm.

Several other magnetic SPM imaging modes have been developed such as magnetic resonance force microscopy (MRFM),[210-213] magnetic AC or MAC-mode,[101, 214-216] and magnetic force modulation.[217] However, all of these methods require the use of tips with a magnetic coating for detecting magnetic forces. A clearly different imaging strategy is applied for development of MSM, which requires nonmagnetic tips. For MSM, the tip is used to detect the

motion and vibrational response of individual nanoparticles rather than directly measuring magnetism of bulk samples.

3.7 Conclusions and Future Prospectus

The exquisite resolution and precision of SPM and nanolithography have brought an evolution of new methods and experimental configurations which have already proven to be valuable for characterizations of nanoparticles. Perhaps the greatest asset of SPM-based characterizations is the capability to characterize different properties of nanoparticles and nanocrystals with sensitivity at the level of individual nanoparticles. Beyond the commercial goals of nanotechnology, SPM-based methods have become indispensable for fundamental investigations of the interrelations between chemical structure and properties of nanoparticles and nanocrystals. One can easily predict that further innovations for characterizations as well as further new strategies for nanolithography with nanoparticles will continue to be advanced in the future, contributing to discoveries in biotechnology, molecular electronics, engineered materials, and chemical/biochemical sensors.

CHAPTER 4. INVESTIGATION OF THE MAGNETIC PROPERTIES OF $FENI_3$ NANOPARTICLES USING CONTACT-MODE AFM COMBINED WITH MAGNETIC SAMPLE MODULATION

4.1 Introduction

The need for nanomaterials in microelectronics and data storage applications has inspired the development of ever smaller devices for improved performance and at low cost.[218] Materials with size-dependent properties have potential for optical,[219-221] magnetic,[222, 223] catalytic[224-226] and thermodynamic applications.[227, 228] Alloys of transition metal nanoparticles have also received interest for electronic and energy conversions areas.[229] Iron-nickel alloys in particular have been investigated for magnetic properties.[230]

The micromolding in capillaries (MICMIC) approach for patterning (also referred as soft lithography) can be used to fabricate microstructures. Materials that have been patterned using MIMIC include prepolymers,[231, 232] sol-gel materials,[232] inorganic salts,[232] polymer beads,[232] colloidal particles[232] and biomolecules.[233] Advantages of using MIMIC to pattern materials are simple steps of fabrication, few defects and applicability in ambient conditions.

In these investigations, microstructures of intermetallic $FeNi_3$ nanoparticles were prepared on a glass surface and characterized using magnetic sample modulation atomic force microscopy (MSM-AFM). The microstructures of nanoparticles were used as test platforms for systematic development of MSM-AFM measurement protocols. In previous work, MSM-AFM was applied to detect the vibration of iron oxide nanoclusters anchored on patterns of self-assembled monolayers (SAMs).[234] Unprecedented sensitivity was achieved with MSM-AFM for mapping ferritin proteins.[18] Often, magnetic nanomaterials aggregate on the surfaces due to

magnetic coupling. Particle lithography[4, 235-244] approaches provide a means for precise arrangement and positioning of electrolessly deposited iron clusters and ferritin at the nanoscale.

4.2.1 Synthesis of Intermetallic $FeNi_3$ Nanoparticles

Composite nanoparticles of $FeNi_3$ were prepared by modifying the procedure reported by Liao, et al.[245] Briefly, 0.1010 g of $Fe(NO_3)_2 \cdot 9\,H_2O$ and 0.3004 g of ($Ni(NO_3)_2 \cdot 6\,H_2O$, 98%) were added to 100 mL of deionized water. The pH of the solution was adjusted to 11 using NaOH. Hydrazine hydrate (reducing agent) and sodium dodecyl sulfate were added to the solution and stirred vigorously. The solutions were placed in a microwave vessel and heated for 1 h with pressures kept above 300 psi.

4.2.2 Principle of Magnetic Sample Modulation AFM

A hybrid approach for magnetic measurements (Figure 4.1) is achieved using atomic force microscopy (AFM) combined with magnetic sample modulation (MSM).

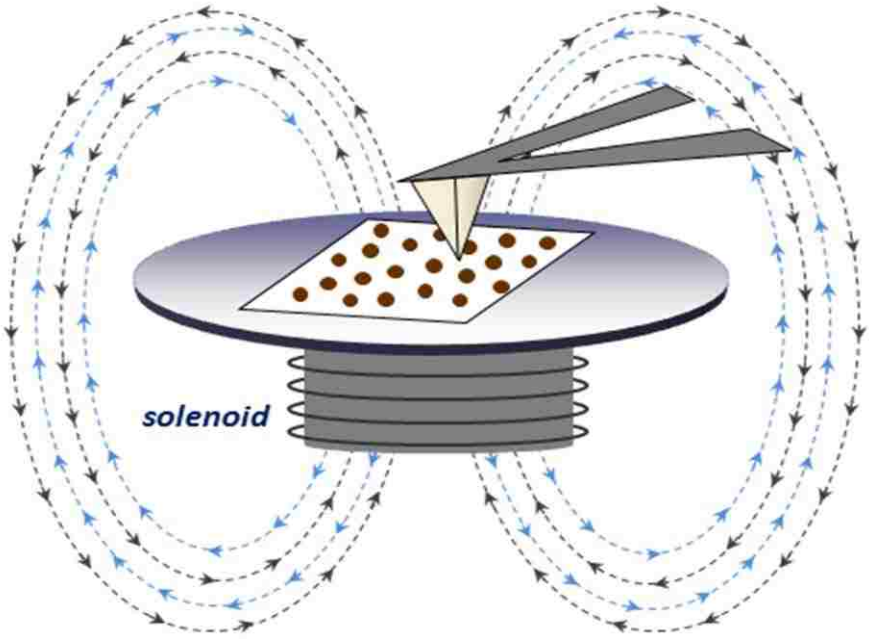

Figure 4.1. Set-up for magnetic sample modulation-AFM.

Magnetic nanoparticles vibrate in response to the flux of the oscillating magnetic field. The dynamics of actuated nanoparticles can be investigated by changing the modulation frequency and strength of the electromagnetic field. An oscillating magnetic field is produced by applying an AC voltage to a wire coil solenoid, placed underneath the sample stage. A soft, non-magnetic tip is operated as a motion sensor to detect the vibrational response of magnetic nanoparticles.

4.2.3 Capillary Filling of $FeNi_3$ Nanoparticles

To prepare microstripe patterns of $FeNi_3$ nanoparticles, a clean PDMS mold with relief patterns oriented downwards was placed in contact with a clean glass substrate (Figure 4.2A). An aqueous drop of $FeNi_3$ nanoparticles (10-25 µL) was then deposited close to the open ends of

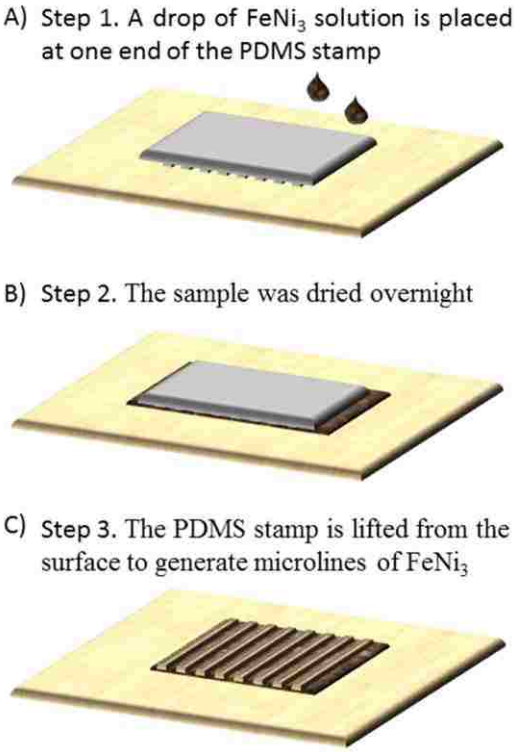

Figure 4.2. Steps for capillary filling to generate micropatterns of $FeNi_3$ nanoparticles.

the microchannels of the PDMS stamp. The sample was left overnight to dry in ambient conditions (Figure 4.2B). During the drying step, the channels fill spontaneously via capillary action to produce stripe patterns. High resolution AFM views reveal well-defined microarrays formed upon removing the stamp from glass (Figure 4.2C).

4.2.4 Preparation of Substrates.

Unpolished 12 mm round glass cover slides were obtained from Ted Pella Inc. (Redding, CA). The glass substrates used were thoroughly cleaned in piranha solution (mixture of H_2O_2 and H_2SO_4 at 1:3 ratios) before depositing the solution of nanoparticles.

4.3 Results and Discussion

Proof-of-concept results for MSM-AFM imaging of the $FeNi_3$ nanoparticles are shown in Figure 4.3. The top row of images are conventional contact-mode AFM images acquired without an electromagnetic field (Figures 4.3A,B), thus there are no features detected in the amplitude and phase channels (Figures 4.3C,D). Three stripes were produced within the 10 x 10 μm^2 area of the surface, measuring 2 μm in width. A spacing between stripe patterns measured 4 μm. A cursor profile across three patterns revealed a height of 10 ± 2 nm, corresponding to a multilayer of nanoparticles. At this magnification, the shapes and morphology of $FeNi_3$ nanoparticles within the stripes cannot be clearly resolved. The nanoparticles are densely packed within the micropatterns and form a continuous, regular line structure. When a magnetic field was applied to the sample, the topography and lateral force images (Figures 4.3E,F) are indistinguishable from the conventional contact mode images in the top row. Additional frames of MSM-amplitude (Figure 4.3G) and MSM-phase (Figure 4.3H) were obtained when the field was applied. The MSM-phase and MSM-amplitude frames exhibit distinct color contrast for the

nanoparticle stripes. Both the MSM-amplitude and MSM-phase channels display dark contrast for areas covered with the nanoparticles while the bare regions of mica(0001) showed lighter color. The shapes and morphology of individual nanoparticles cannot be resolved in the MSM-AFM frames. During the acquisition of MSM-AFM the probe was driven at a frequency of 8.57 kHz and the magnetic field strength was set at 0.48 T.

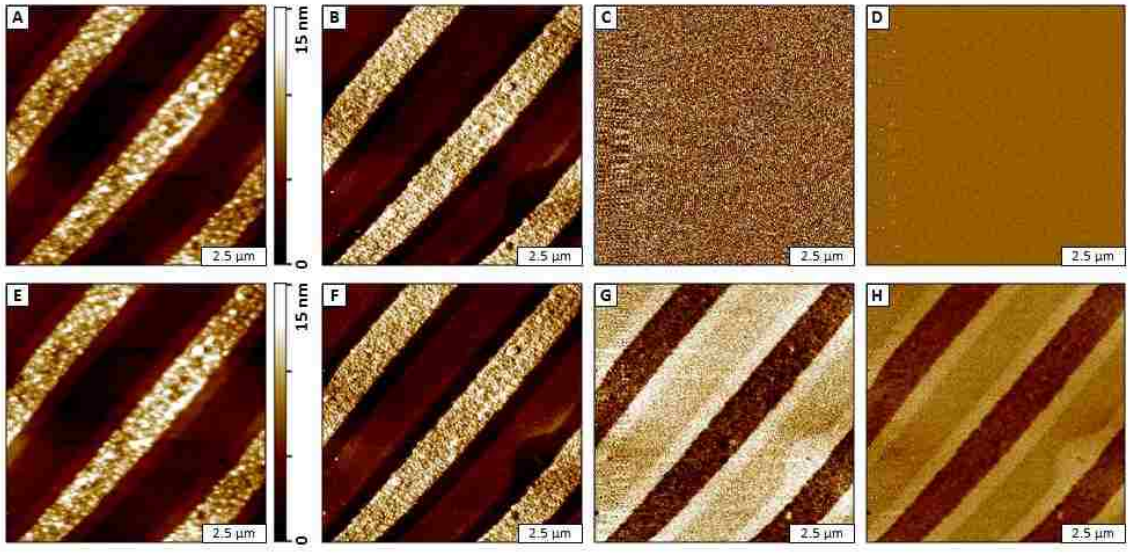

Figure 4.3. Stripe micropatterns of $FeNi_3$ nanoparticles characterized with AFM. Contact-mode AFM views without an applied magnetic field: (A) topograph; (B) lateral force (C) amplitude; (D) phase images. Frames acquired using MSM-AFM at 0.48 T and 5.95 kHz: (E) topography; (F) lateral force; (G) amplitude; (H) phase images.

The MSM-AFM approach offers unique capabilities to obtain information about the dynamics of the actuated particles by changing the modulation frequency. An example of a dynamic experiment for testing the changes in MSM images while ramping the driving frequency is provided in Figure 4.4. For this experiment, the frequency of oscillation was changed at different time points throughout the scan, to compare changes in contrast within a single frame. Several prominent resonance peaks were detected when an AFM tip is placed in contact with an area of the sample that was vibrating, as displayed in Figure 4.4E. The

frequencies for driving the sample vibration were selected at the different resonances, designated with red arrows. For the dynamic MSM experiment, at this magnification the topography and lateral force frames do not show distinguishable changes for the frequencies selected (Figures 4.4A,B). The transition points cannot be distinguished within the topography and lateral force frames. However, for the amplitude and phase frames there are sharp transitions when the frequency was changed, and the changes can be readily tracked. For the MSM-amplitude image, the contrast increases intensity for the frequencies with a higher amplitude response. For example, the most prominent, broad peaks were detected at 5.95 kHz (1) and 8.57 (2) kHz. The sharpest contrast and resolution were achieved for these settings within Figure 4.4C. The changes of the MSM-phase image (Figure 4.4D) do not correlate with the amplitude-response spectra of Figure 4.4E. The optimized contrast for the phase channel was achieved at 13.57 kHz, which has a relatively small amplitude peak. The data in Figure 4.4 was acquired using field strength of 0.48 T. Further experiments are planned to evaluate frequencies up to 300 kHz.

The development of the MSM-AFM imaging mode has been a challenge, because of the complexity of sample responses. When choosing a driving frequency, the tip must be placed on a vibrating area of the surface, no frequency profiles can be acquired for the background areas of the sample that do not contain magnetic nanomaterials. Different frequency profiles are observed for different sizes and material composition of nanoparticles. The resonance peaks for driving the vibration of samples for magnetic modulation do not coincide with the natural resonance frequencies of the AFM cantilevers (15-25 KHz).

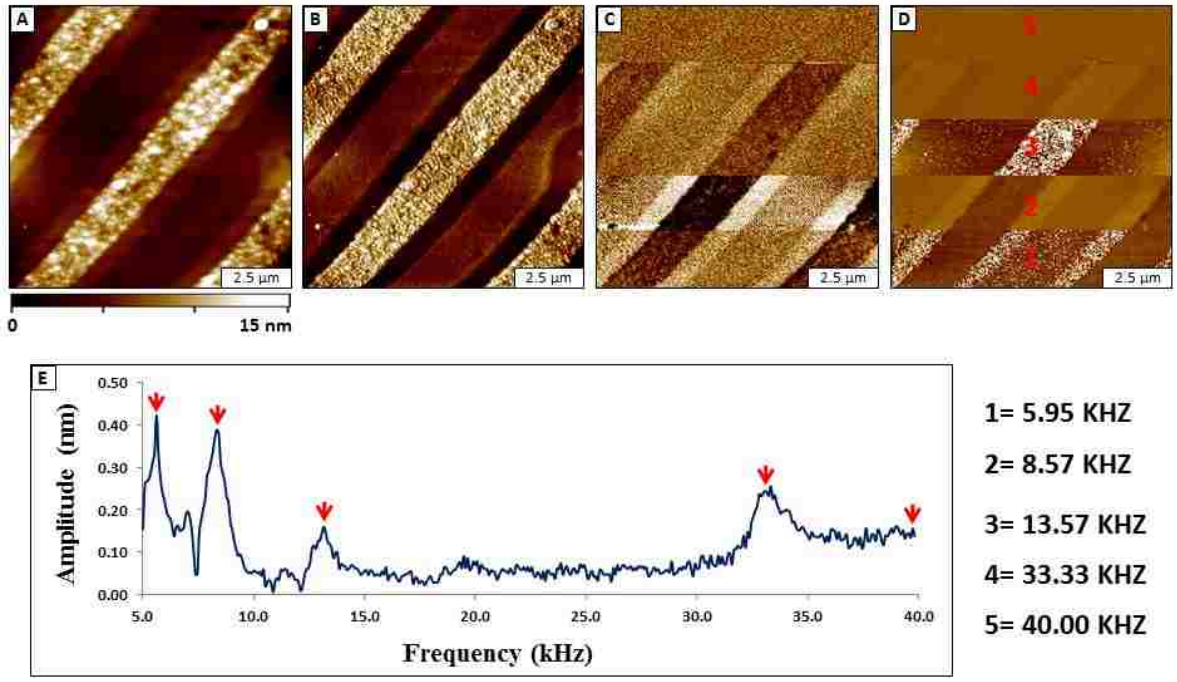

Figure 4.4. MSM-AFM images acquired with incremental changes of selected resonance frequencies of magnetic actuation.

A dynamic protocol for MSM-AFM was developed for systematically changing the parameters of the average electromagnetic field strength during experiments. The response of $FeNi_3$ nanoparticles to changes in the magnitude of the applied AC electromagnetic field is shown in Figure 4.5, for four different settings. At this magnification, there is no distinguishable changes detected for the topography and lateral force images (Figures 4.5A,B) at the different transition points. However, successive changes in contrast are readily detected in both amplitude (Figure 4.5C) and phase MSM (Figure 4.5D) channels. When the strength of the applied field was set 0.01 T, there is not sufficient sample vibration for resolving surface features in the MSM-amplitude and MSM-phase images. However, nanoparticles could be resolved in the MSM-AFM channels when the sample was actuated at 0.1, 0.2 and 0.3 T. Interestingly, at higher field of 0.3 T there is a contrast flip, the nanoparticle stripes become dark and the substrate is

bright, which suggests that there is a shift or broadening of the vibrational resonance with greater magnetization. Experiments are in progress to test the reproducibility of this effect and to track changes in the frequency profiles as the magnetic field is ramped. A future objective for this protocol will be to acquire frequency profiles of individual nanoparticles with changes in field strength.

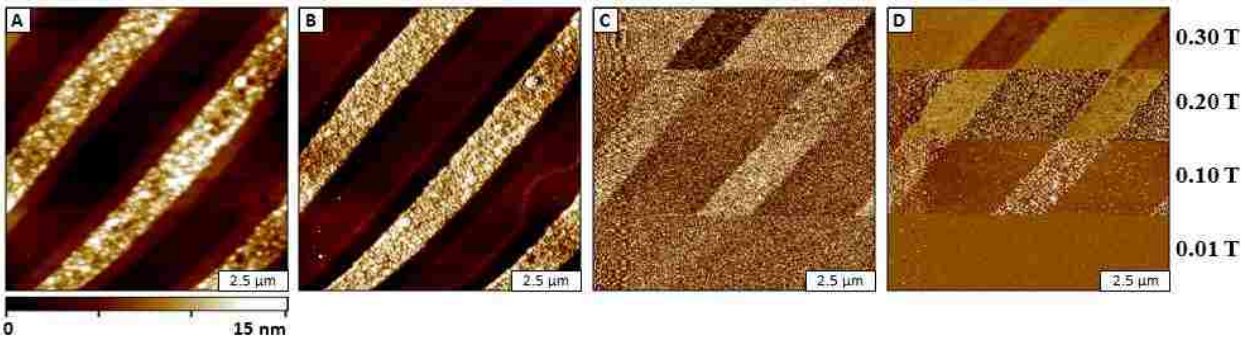

Figure 4.5. Changes within MSM-AFM images as the field strength was incrementally increased.

Hysteresis measurements from SQUID magnetometry previously published for the $FeNi_3$ nanoparticles indicate that the alloy nanoparticles exhibit ferromagnetic properties. Future experiments will be developed to determine if superparamagnetic properties become evident for nanoparticles with smaller dimensions, and if differences in vibrational response can be detected with MSM-AFM imaging for polydisperse samples of $FeNi_3$ nanoparticles. The shapes of the nanoparticles within the stripes are visible within the topography images, however to advance to the level of viewing MSM changes for individual nanoparticles more sophisticated methods of particle lithography will be applied for future investigations. To advance towards quantitative measurements for magnetic materials at the nanoscale requires a clearer understanding of contributions of elasticity, surface adhesion and mass to correlate the magnetization of nanomaterials. Parameters to be considered are the size and chemical composition of the

nanostructures as well as coupling between adjacent nanoparticles. Further experiments are planned to compare the mechanical and magnetic response spectra for magnetic materials at various field strengths using systematically designed nanoscale test platforms. For development of experimental protocols with MSM-AFM, the tip can be placed in contact with specific locations of the surface to obtain frequency spectra of the vibration of individual nanoparticles. Protocols will be developed to survey the effects of different sizes and composition of nanoparticles using a combination of MSM mapping and frequency profiles.

4.4 Conclusion

A rapid approach for lithography to produce stripe patterns of nanoparticles can be accomplished by capillary filling of PDMS molds. For mapping magnetic domains the frequencies are determined experimentally for each sample, which have not been found to occur at the natural resonance frequencies of the AFM probes. With the ramping of the electromagnetic field, the magnitude of vibration is increased when acquiring MSM-AFM images; a phenomenon revealed by changes in contrast in the MSM-amplitude and MSM-phase images.

CHAPTER 5. CHARACTERIZATION OF DNA-TEMPLATED NANOPARTICLES USING MAGNETIC SAMPLE MODULATION AFM

5.1 Introduction

Other SPM imaging modes that use magnetic fields have previously been engineered. Examples of such imaging modes include magnetic AC,[101] magnetic resonance force microscopy (MRFM)[246] and magnetic force modulation (MFM).[247] The use of magnetically coated AFM probes is a common requirement for these previously developed modes. In contrast for MSM, a non-magnetic cantilever is used as a motion sensor to sensitively detect vibration of magnetic nanoparticles. Thus far, MSM has been applied to map the vibration of individual ferritin (metalloproteins) with sizes ~ 12 nm[18] as well as iron oxides immobilized on silane structures via electroless deposition.[234] Cobalt nanoparticles synthesized using DNA-templating steps and patterned on the surface via particle lithography was applied as test platforms for MSM characterization.

There are synthetic methods for fabricating metal nanomaterials. Some of the strategies include using reducing agents to reduce metal salts,[248] laser ablation,[249,250] pyrolysis,[251,252,253] and photoreduction.[254,255] Investigation of metal nanoparticles may have unexpected properties that can be exploited for applications in magnetic recording technology.[256,257] Nickel and cobalt nanoparticles in particular have a wide range of potential applications such as in cooling of microelectronic devices.[258] The synthesis of nickel and cobalt nanoparticles have been reported previously using organometallic precursors requiring the reaction to undergo decomposition at elevated temperatures,[259] microemulsions[260] and soft templates.[261] Viruses have also been used as biological templates to grow nanoparticles in two or three dimensions.[262] However, we have

fabricated monodisperse nickel and cobalt nanoparticles in high yield using plasmid DNA nanocavities as template for the deposition of nanomaterials.[263]

Particle lithography can be used to produce arrays of nanoparticles on surfaces with control of the arrangement, size and interparticle spacing.[264] The patterns generated can be tuned precisely to produce uniform dimensions reproducibly.[265] Also known as nanosphere lithography (NSL), particle lithography exploits a self-assembly process using structural mesospheres to form a two-dimensional colloidal crystal on substrates.[264,266,267] Self-assembly provides a convenient way to organize materials on surfaces at both the nanoscale and microscale. Particle lithography is an approach which can be used to generate nanopatterned surfaces. Latex or silica mesospheres are applied as structural templates to guide the deposition of nanomaterials. Materials that have been patterned previously using particle lithography include proteins,[235] metals,[238] inorganic materials,[239] alkanethiol self-assembled monolayers,[240] metal oxides[268] and polymers.[241,242,243] Particle lithography may be useful in the future as a tool for generating periodic arrays of nanoparticles for data storage. Properties of materials at the nanoscale[269,270] have been shown to be significantly different from those of the bulk.[271] The potential applications of patterned arrays of magnetic nanomaterials include magnetic data storage,[272] optical gratings,[273] nanostructured catalysis,[274] electrical transport,[275] electrochemistry[276] and in fabrication of biosensing surfaces.[277]

5.2 Experimental Approach

5.2.1 Synthesis of Metal Nanoparticles Using Plasmid DNA Templates.

A solution of plasmid DNA protein Von Hippel-Lindau (5.6 kbp, concentration 0.5 µg/µL) in TE (Tris/EDTA) buffer (50 mM tris-HCl, pH 8.0, 1 mM EDTA) was added to 5 µM

$CoCl_2$ and $NiCl_2$ in deionized water for synthesis of cobalt and nickel nanoparticles, respectively. The mixture was left at room temperature for 60 minutes before being exposed to UV radiation (λ = 254 nm) for 60 minutes. The solution was finally filtered through a 200 nm nanoporous membrane.[263]

5.2.2 Materials and Reagents.

Latex and silica mesospheres (500 nm in diameter) were acquired from Duke Scientific (Palo Alto, CA). Ruby muscovite mica was obtained from S&J Trading, Inc. (Glen Oaks, NY).

5.2.3 Atomic Force Microscopy.

A model 5500 scanning probe microscope (SPM) equipped with PicoScan v5.3.3 software was used for AFM experiments (Agilent Technologies AFM, Inc. Chandler, AZ). Cantilevers (NSL-20) from Nanoworld Holdings AG (Schaffhausen, Switzerland) were used for imaging cobalt structures with tapping mode of operation. These probes have relatively high force constants (k_{avg} = 48 N/m) and a resonance frequency of 190 kHz. AFM probes (NSC 14/15**)** from MikroMasch (Wilsonville, Oregon) which have average force constants of 5 N/m were used for characterization of nickel structures and driven to oscillate at 193 kHz resonance frequency. Images were acquired using tapping mode AFM in air for cobalt and nickel structures.

A MAC-mode sample stage was used to produce an AC electromagnetic field for MSM studies. Characterization of the vibrational response of cobalt nanoparticles was done using soft silicon nitride (Si_3N_4) probes with force constants ranging from 0.1 to 0.5 N m^{-1} with contact mode AFM. Silicon nitride cantilevers were acquired from Veeco Probes, Santa Barbara, CA. For MSM characterizations, the tips were installed on an empty plastic nose cone assembly that

did not contain metal components. Digital processing of AFM images was done using Gwyddion (version 2.9) software, supported by the Czech Metrology Institute.[278] Estimates of surface areas covered by cobalt and nickel patterns on mica(0001) were acquired using UTHSCA Image Tool software.[279]

5.2.4 "Two-Particle" Lithography

The basic steps to fabricate arrays of nanoparticle patterns using "two-particle" lithography are outlined in Figure 5.1, as previously reported.[8]

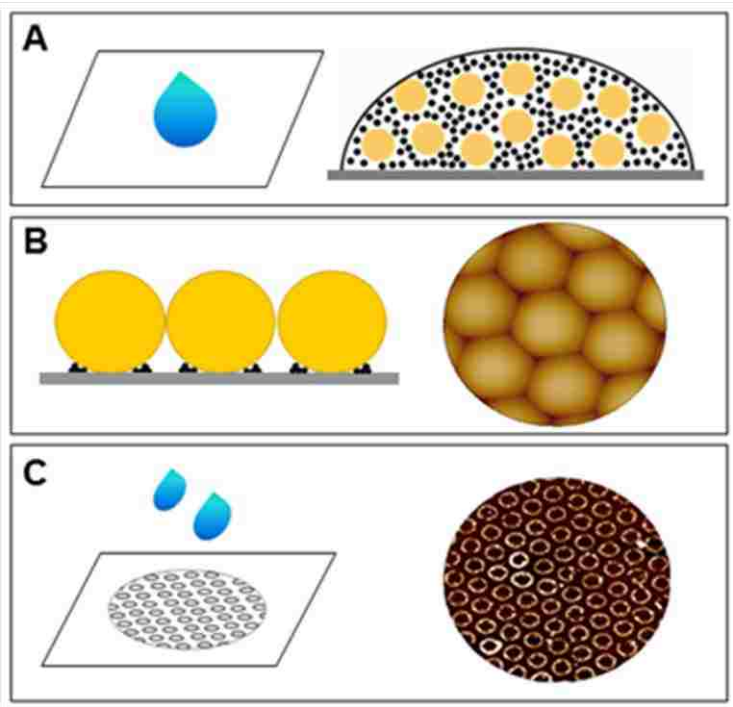

Figure 5.1. Steps for "two-particle" lithography. A) A solution containing metal nanoparticles and latex was deposited on flat surface of mica(0001). B) The samples were dried at ambient temperature. C) The latex templates were removed by rinsing.

The latex or silica mesospheres were washed by steps of centrifugation and rinsing with deionized water to remove trace amounts of stabilizers and surfactants. This was accomplished by centrifuging a solution of the mesospheres for 10 min at 14,000 rpm until a pellet formed. The

supernatant was removed and the pellet was resuspended in deionized water. A solution of nanoparticles was added to the washed pellet and mixed using a vortex mixer. Using a micropipette, a drop of the mixture (15-20 μL) was deposited (Figure 5.1A) at the center of a freshly cut piece of mica (1 x 1 cm^2) and dried in air for 3 hours. During the drying step, the larger mesospheres organized into a close-packed arrangement, surrounded by smaller nanoparticles (Figure 5.1B). The template spheres were removed in the final step by rinsing several times using deionized water. The nanoparticles remained bound to the mica, despite rinsing, to produce nanostructures of metal nanoparticles (Figure 5.1C).

5.3 Results and Discussion

5.3.1. Surface Templates of Latex and Silica Mesospheres

Topographic views of the samples before rinsing away the mesosphere templates are shown in Figure 5.2. The crystalline arrangement of a mixture of mesospheres and nanoparticles prepared on mica substrates are shown for latex and colloidal silica mesospheres in Figures 5.2A and 5.2B, respectively. Metal nanoparticles are not visible on the surfaces of the mesospheres, only the larger mesospheres can be detected for this step. The metal nanoparticles are located near the substrate, beneath the layer of mesospheres. The periodicity measured 593 ± 10 nm for the latex mesospheres, as shown with a representative cursor profile. The measured diameter is larger than that of structural templates (500 nm) due to smaller nanoparticles (cobalt and nickel) surrounding the base of the mesospheres. An interesting structural feature is evident for the latex spheres, with a seam line across each sphere. This surface defect is occasional viewed for latex spheres that are 500 nm or larger, and results from the synthesis and drying conditions of the sample. Silica mesospheres mixed with nickel nanoparticles exhibit a similar crystalline

arrangement when dried on mica(0001), as shown in Figure 5.2B, however the spheres are nearly perfectly symmetric without surface defects. The interparticle spacing for the silica mesospheres measured 518 ± 2 nm.

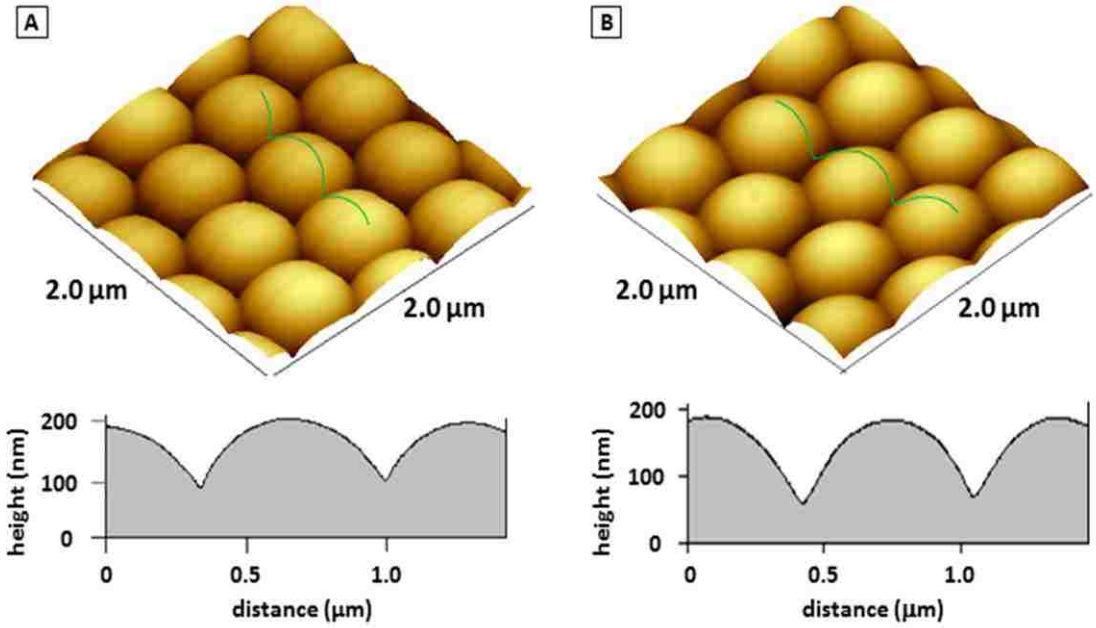

Figure 5.2. Structural templates of mesospheres mixed with nanoparticles, prepared on mica(0001). A) Latex spheres with cobalt nanoparticles and the corresponding cursor profile. B) Silica mesospheres with nickel nanoparticles and line plot.

5.3.2. Periodic Arrays of Rings of Nickel Nanoparticles

Rings of nickel nanoparticles produced using the "two particle" lithography are displayed in the AFM images of Figure 5.3. The wide area (10 x 10 μm^2) viewed in Figure 5.3A reveals the periodic arrangement of rings of nickel nanoparticles that are present after rinsing away the template mesospheres. There are 270 rings in the image which translates to 1.69 billion nanostructures in an area covering 1 cm x 1 cm. The surface coverage of the ring patterns is

estimated to be 24% of the total area. In the successive close-up views of Figures 5.3B and 5.3C, the fine details of the arrangement of ring nanostructures are revealed.

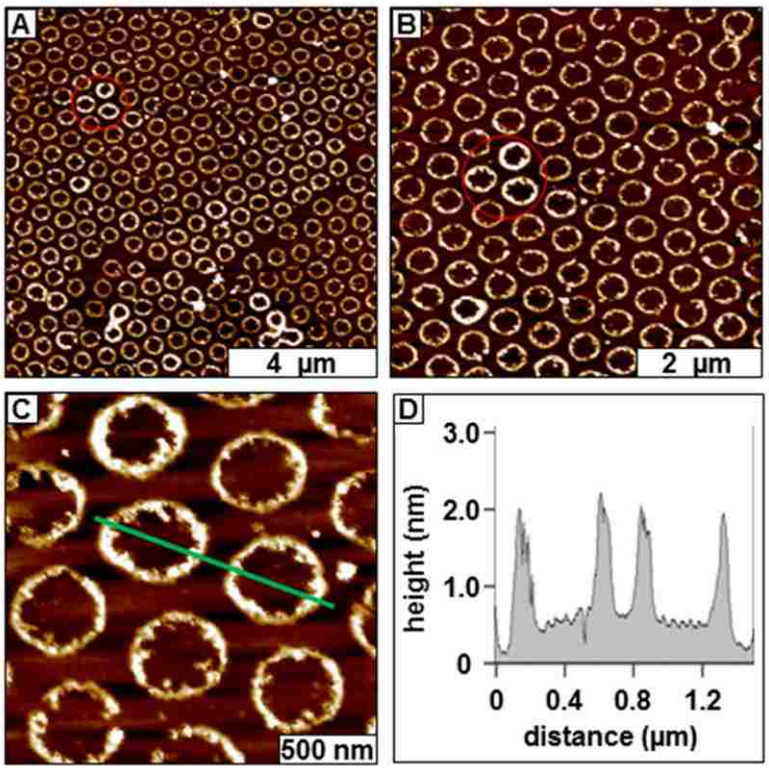

Figure 5.3. Successive zoom-in topography images of rings of nickel nanoparticles prepared on mica(0001). A) Wide area frame. B) Zoom-in of A. C) close up view of B. D) Line profile across two rings.

When patterning nickel nanoparticles using "two particle" lithography, ring structures that reflect the order and periodicity of the template mesospheres are produced. A hexagonal arrangement is evident in Figure 5.3C where each (central) ring is surrounded by six neighbors. The nickel rings are 2.0 nm tall with the periodicity (center-to-center) measuring 539 ± 3.0 nm (Figure 5.3D), which closely matches the diameter of silica mesospheres (500 nm) that were used as a template. The mechanism of how the nanoparticles collect at the base of the mesospheres is not yet fully understood. When mixtures of the nanoparticles and mesospheres

are dried on flat surfaces, water carries the nanoparticles to the base of the mesospheres to form rings. Electrostatic interactions between the surfaces of the spheres as well as the substrate serve to distribute the nanoparticles homogeneously throughout the surface.

5.3.3. Patterning of Cobalt Nanoparticles on Mica(0001)

Using the same approach, cobalt nanoparticles were patterned on mica using 500 nm latex mesospheres (Figure 5.4). Rings of cobalt nanoparticles are displayed in the AFM topograph (Figure 5.4A). A few individual nanoparticles are located between the rings, which appear to have smaller diameters. The approximate surface coverage for patterned cobalt ring-

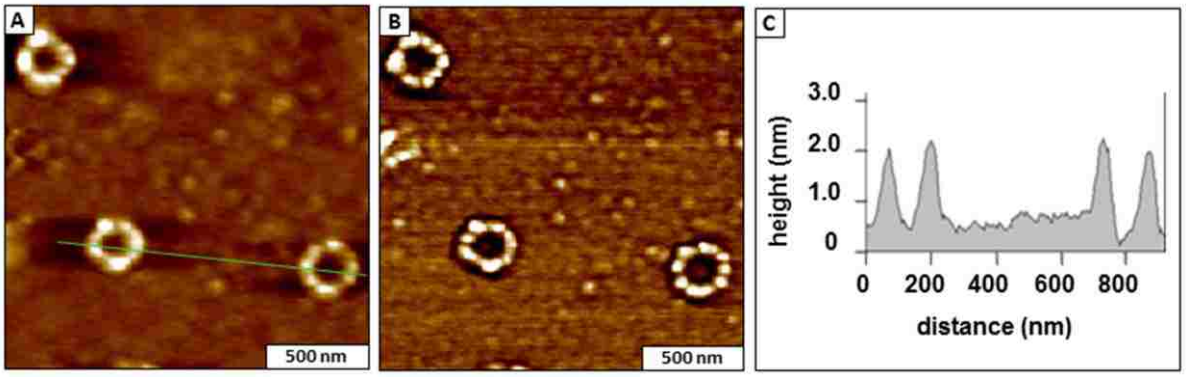

Figure 5.4. Rings of cobalt nanoparticles produced using two-particle lithography A) Topography view. B) Simultaneously acquired phase image. C) Corresponding cursor profile.

structures is about 8% of the total area. A processing artifact which is caused by parabolic flattening of the image is shown in the topograph, with a dark band at the edges of with each ring in Figure 5.4A. The phase image (Figure 5.4B) reveals distinct bright contrast for the metal nanoparticles of the rings, a few white dots pinpoint the individual nanoparticles in the surrounding areas outside the rings. Phase images clearly define the shapes of the individual nanoparticle, for example, nine cobalt nanoparticles are visible for the pattern at the right bottom corner of Figure 5.4B). Each ring has an outer diameter of 230 ± 15 nm, shown by the cursor

plot (Figure 5.4C). The height of cobalt nanoparticles in the chain forming the rings is 2.0 ± 0.3 nm, which closely matches the size of the nickel nanoparticles formed with plasmid DNA templates.

5.3.4 Nanostructured Films of Nickel Nanoparticles

Changing the ratio of mesospheres to nanoparticles produced a different surface morphology with "two particle" lithography (Figure 5.5). When using a higher ratio of mesospheres to nanoparticles, metal nanoparticles fill the interstitial spaces between the

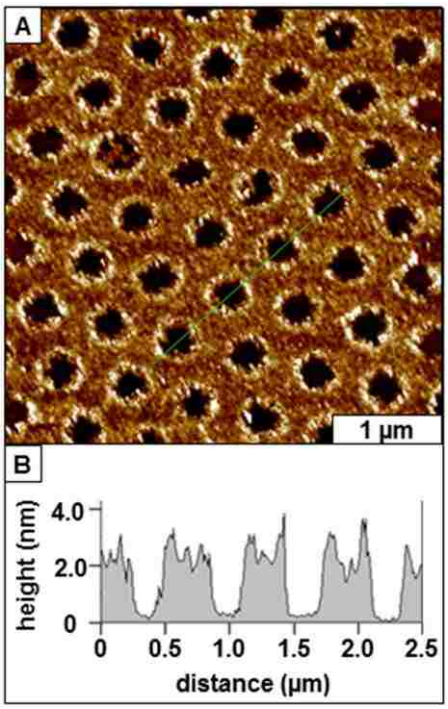

Figure 5.5. Patterned film of DNA-templated nickel nanoparticles produced at higher concentration. A) Topography image; B) Line profile for A.

mesospheres. At higher concentration of nanoparticles, the areas between rings fill in to form a continuous layer, and dark circular areas of uncovered substrate are revealed after removing the mesosphere templates. There are 52 circular areas of uncovered substrate within the 4 × 4 μm^2

frame of Figure 5.5A, which would scale to an overall pattern density of 325 million nanostructures per cm^2.

The pores have slightly brighter perimeter than the surrounding areas. In the cursor profile a uniform depth of 2.2 ± 0.2 nm is measured, which matches the thickness of a single layer of nanoparticles. The center-to-center distance between neighboring patterns measured 446 ± 24 nm (Figure 5.5B). The deformation and shrinkage of latex spheres upon drying has previously been reported.[280,281] Approximately 84% of the mica surface is covered with nickel nanoparticles.

5.4 Magnetic Sample Modulation AFM

Magnetic sample modulation imaging uses an AC-generated electromagnetic field to induce physical movement of magnetic or paramagnetic nanomaterials. Certain types of magnetic or paramagnetic nanoparticles vibrate in response to an alternating electromagnetic field, and thus can be detected by AFM imaging with a soft, nonmagnetic cantilever. The flux of an AC electromagnetic field is used to induce physical movement of magnetic nanomaterials, thus we refer to the new AFM-based imaging mode as "magnetic sample modulation" or MSM-AFM (Figure 5.6). The magnetic flux is generated by applying an AC current to the solenoid located beneath the sample plate. The positional feedback is the same as operation in contact-mode, to maintain a constant deflection of the tip. A lock-in amplifier enables sensitive detections of slight changes in the phase and amplitude of tip oscillation caused by the vibration of nanoparticles. Magnetic sample modulation imaging has mapping capabilities to sensitively distinguish the vibration of magnetic nanomaterials. Acquisition of topography as well as

concurrent amplitude and phase channels can be accomplished with nanoscale resolution (≤ 1 nm).

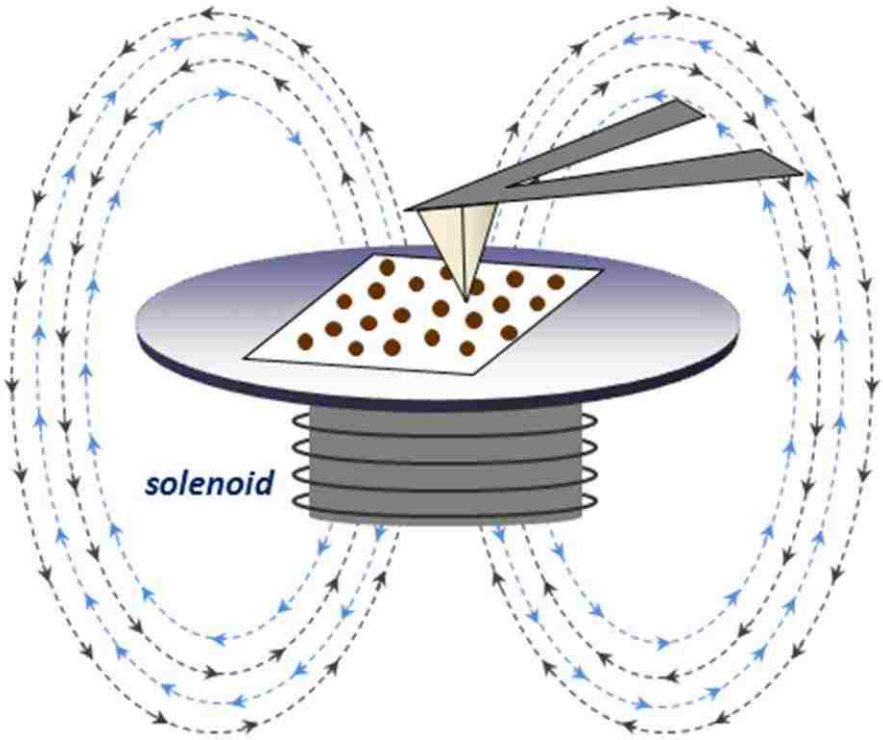

Figure 5.6. Instrument set-up for MSM studies.

5.4.1. Imaging Cobalt Nanoparticles Using MSM-AFM.

Proof-of-concept experiment for MSM characterizations of rings of cobalt nanoparticles is presented in Figure 5.7. First, a contact mode AFM image was acquired without applying an electromagnetic field for the top half of the frame (Figures 5.7A-5.7C). With the oscillating magnetic field turned off, the phase and amplitude channels do not exhibit any features. Half-way through the image frame, the field was turned on, to display the shapes of nanoparticle ring structures in the amplitude and phase channels. Magnetic nanomaterials vibrate in response to the flux of the applied magnetic field, and this periodic vibration is sensed by the scanning AFM

probe. The field strength applied to generate MSM images for was 0.05 T and 0.15 T for Figures 5.7A-5.7C and 5.7D-5.7F respectively. Noticeably, using a stronger magnetic field produced sharper contrast in both the amplitude and phase images of Figures 5.7E-5.7F. The mapping capabilities of the MSM imaging mode for distinguishing areas of magnetic samples is demonstrated with this experiment. Essentially the change in amplitude and phase of the vibrating nanoparticles is compared to the signal of the driving AC current to provide selective mapping of magnetic materials.

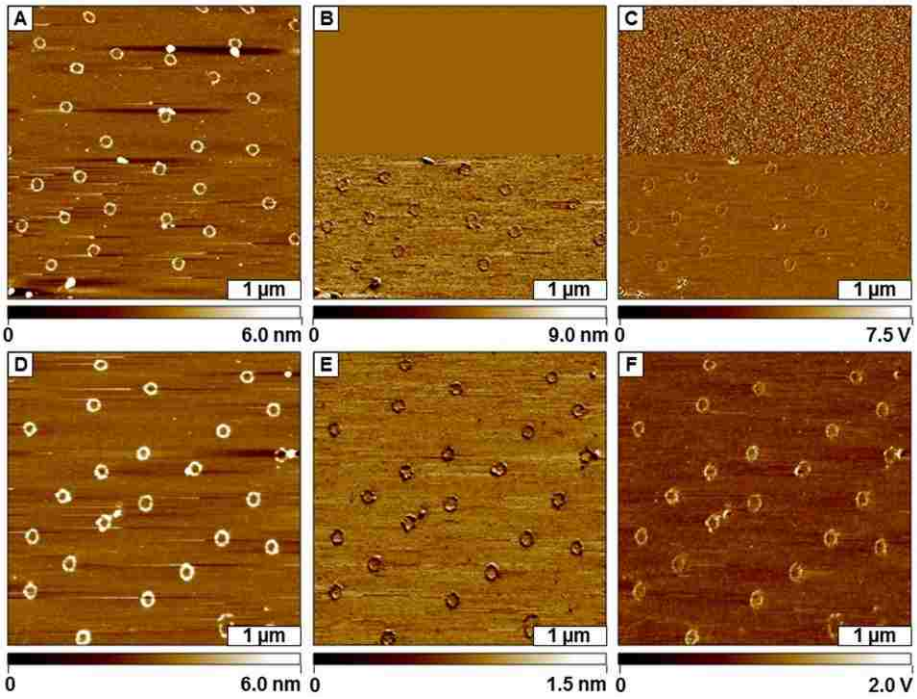

Figure 5.7. MSM images of cobalt nanoparticles. The magnetic field was turned off for the top half of the frame for A, B, C. and then switched on to generate bottom half of the image. For D, E, F the images were acquired with the magnetic field switched on.

Dynamic information can be obtained from MSM frequency spectra by changing either the amplitude or the driving oscillation of the cantilever. For these spectra, the tip must be placed in contact with a vibrating sample. Spectra of the resonance responses for the nanoparticle

vibrations are acquired by changing the parameters of the AC drive current over a range of different field strengths and frequencies. First a spectrum (red line) was acquired when the AFM tip is disengaged from the surface. No significant peaks are apparent when the cantilever is lifted up from the surface when the magnetic field is turned on. Next, a spectrum is generated with AFM tip placed in contact with the surface (blue line). A tall, sharp peak with broad shoulders is displayed with a resonance frequency at 116 kHz (Figure 5.8). The MSM images in Figures 5.7D-Fwere acquired at 116 kHz.

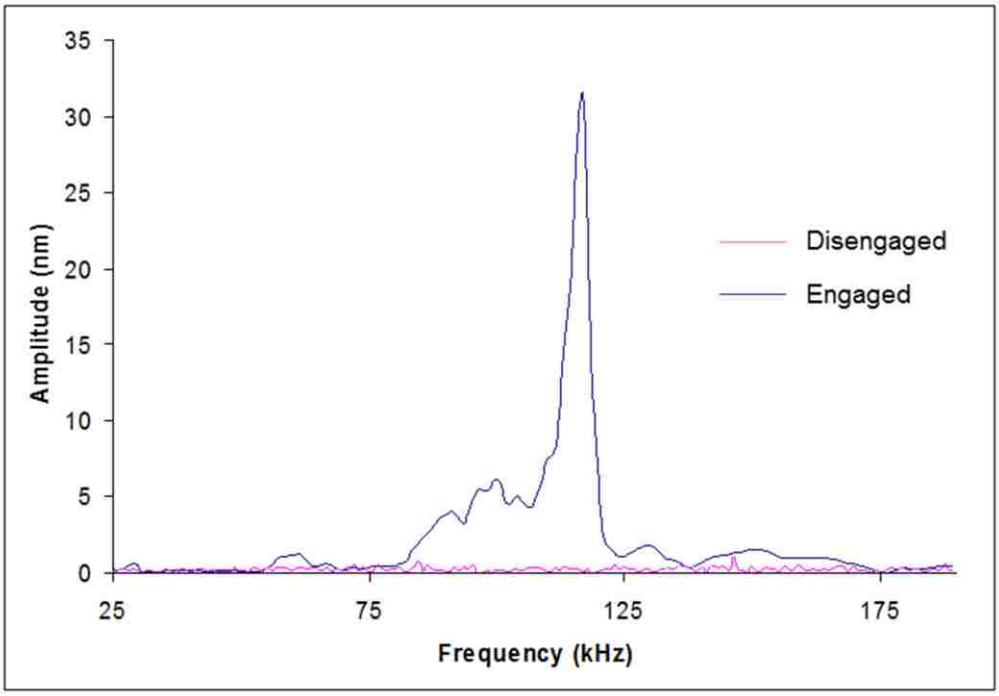

Figure 5.8. Frequency spectra acquired using MSM.

5.5 Conclusion

New experimental protocols for *dynamic* measurements with MSM-AFM were designed and tested using ring nanostructures of cobalt nanoparticles. A method has been developed to

arrange nanoparticles on surfaces, providing a means to control the surface coverage of metal nanoparticles. Ring nanostructures were formed at lower concentration of nanoparticles, and nanostructured films were produced at a higher ratio of the nanoparticles to the mesospheres. Nanostructures with well-defined geometries furnish excellent test platforms for AFM and MSM characterizations. Well-defined nanopatterns of cobalt nanoparticles prepared by “two particle” lithography were used as test platforms for MSM-AFM studies. The MSM mode was successful for detecting the vibration of magnetic nanoparticles as small as 2 nm.

CHAPTER 6. DYNAMIC MEASUREMENTS USING CONTACT MODE AFM COMBINED WITH MAGNETIC SAMPLE ACTUATION FOR TEST STRUCTURES OF COBALTACARBORANE PORPHYRINS

6.1 Introduction

Nanotechnology has made it possible to synthesize and specifically tailor the magnetic properties of nanoparticles for various applications.[106] Magnetic nanomaterials have diverse applications including magnetic fluids,[282, 283] catalysis,[284, 285] magnetic separations,[286] magnetic resonance imaging,[287] data storage,[288, 289] and biosensing.[63] As material composition changes, the magnetic moment of nanomaterials are observed to change; however size-dependent magnetic properties often are not well-defined due to the difficulties of making measurements for individual nanoparticles or nanomaterials. Most commonly, measurements of magnetic properties are based on average measurements from bulk samples of hundreds to thousands of nanoparticles, rather than based on local measurements of individual, distinct entities. The magnetic properties of aggregate samples are not the same as individual nanoparticles, largely due to cooperative effects of magnetism. The size and composition of nanoparticles affects the resulting magnetic properties.

Characterization of magnetic properties in microstructures of DNA molecules templated with Fe_3O_4 nanoparticles was accomplished using magnetic force microscopy.[290] The strategy of the conventional SPM imaging mode for magnetic detection known as magnetic force microscopy (MFM)[2, 291-295] is quite different from our newly invented magnetic sample modulation (MSM) mode. For MFM, one *must* use an AFM tip that is coated with a magnetic material to sense the relatively weak long-range forces of magnetic areas of surfaces operating over distances of 50-200 nm from the surface. For MFM, the strength of the magnetic field must

be strong enough to deflect or attract a micrometer-sized cantilever to enable mapping of the magnetic domains. The MFM approach provides a means to map the strength of the magnetic field at various distances, (e.g. 50, 100, 150 nm) from the surface. When the tip is attracted towards the surface, dark contrast is generated in images; as the tip is repelled by the surface, brighter contrast results. Thus, MFM indicates the relative strength and polarity of magnetic regions. The limitation of MFM detection intrinsically depends on the size and spring constant of the magnetic lever. The topography resolution is generally poor with MFM, since the magnetic coatings on the underside of MFM tips results in probes that are blunt and bulky. The conventional approach of MFM requires that the samples have a permanent magnetic field that can be sensed by a relatively bulky magnetic probe. A common problem for MFM imaging of nanoparticles is that the samples detach from the surface and become attached to the magnetic tip. Another limitation of MFM is that the susceptibility of superparamagnetic nanomaterials cannot be characterized, unless exposed to an external magnetic field.

Superparamagnetism is one example of the interesting size-dependent phenomena of certain metal nanoparticles. Nanoparticles with superparamagnetic behavior are similar to paramagnetic substances which lose their magnetization when the magnetic field is removed, however superparamagnetic particles exhibit a much higher magnetic moment.[296, 297] Iron oxide magnetic nanoparticles tend to be either paramagnetic or superparamagnetic depending on size. Superparamagnetic particles of Fe_2O_3 and Fe_3O_4 do not retain any magnetism after removal of the magnetic field, which is a critical requirement for MRI contrast agents.[189] Size scaling relationships can be used to tailor magnetic properties of materials from the bulk ferromagnetic level to the superparamagnetic regime. Ferromagnetic materials exhibit an intense magnetic field

when an external magnetic field is applied, but in a bulk sample the material will usually be nonmagnetized because of the random orientation of spin domains. A small externally imposed magnetic field can cause the magnetic domains to line up with each other to magnetize ferromagnetic materials.

In nearly all of the established modes of dynamic SPM imaging, the nature of the tip is used as a mechanism for detection of forces. For example, a biased tip is used for scanning polarization force microscopy,[298-300] a magnetized tip is used for magnetic force microscopy,[291, 301-303] a chemically functionalized tip is used for chemical force microscopy,[304, 305] a metal tip is used for current imaging,[306-309] an actuated tip is used for tapping mode and phase imaging[310-315] and so on. Unlike previous SPM imaging modes which use specifically designed tips to interrogate samples, for MSM imaging the changes in *sample* dynamics form the basis for measurements of material properties. The sample is driven to vibrate in response to an externally applied electromagnetic field and the tip is used as a motion sensor for mapping the vibrational response. For magnetic sample modulation or MSM, the samples are induced to vibrate in concert with the flux of an externally applied electromagnetic field. A soft, *non-magnetic* AFM tip is operated in contact mode to detect the force and motion of nanomaterials which vibrate in response to the externally applied oscillating magnetic field. A clearly different imaging strategy is applied for development of MSM, which *requires* nonmagnetic tips. For MSM, the tip is used to detect motion and vibrational response rather than directly measuring magnetism. Lock-in-detection is used for sensitively tracking changes in the amplitude, phase and frequencies of motion compared to the driving AC electromagnetic field. The MSM technique provides

exceptional sensitivity and is selective for distinguishing samples which have a magnetic moment in the presence of an applied AC electromagnetic field.

Other scanning probe microscopy (SPM) imaging modes that use magnetic fields to detect magnetic materials have previously been developed and applied. Examples of such SPM imaging modes include magnetic AC,[101] magnetic resonance force microscopy (MRFM)[246] and magnetic force microscopy (MFM).[247] These imaging modes require the use of magnetically coated probes for characterization. In contrast, a nonmagnetic cantilever is used to detect and map the vibration of nanoparticles for MSM-AFM imaging. Thus far, MSM-AFM has been applied to characterize the vibrational response of individual ferritin (metalloproteins) with sizes ~ 12 nm,[18] as well as iron oxide nanoclusters immobilized on silane nanopatterns prepared by electroless deposition.[234]

In this report, experiments were developed using a new MSM-AFM imaging mode to probe the magnetic response of metalloporphyrin nanocrystals. Custom test platforms were prepared using particle lithography with organosilane templates to enable characterization at the level of individual cobaltacarborane porphyrin nanocrystals. Measurement protocols were developed with MSM to systematically vary the conditions of applied imaging force, frequency changes and field strength. The capabilities of the MSM imaging mode for acquiring spectra of the vibrational resonances of vibrating magnetic nanomaterials were evaluated using test platforms of magnetic nanostructures produced by particle lithography. These investigations will enable evaluation of dynamic parameters of the magnetic response of materials at the nanoscale.

6.2 Experimental Approach

6.2.1 Atomic Force Microscopy.

A model 5500 scanning probe microscope equipped with PicoScan v5.3.3 software was used for AFM experiments (Agilent Technologies AFM, Inc. Chandler, AZ). Conventional contact-mode AFM images (Figure 6.3) were generated using silicon nitride (Si_3N_4) cantilevers (Veeco Probes, Santa Barbara, CA) and characterized in air. A MAC-mode sample stage was used to produce an electromagnetic AC field for MSM studies. Characterization of the vibrational response of porphyrins functionalized with cobaltacarborane moieties (Figure 6.2) was done using probes with force constants ranging from 0.1 to 0.5 Nm^{-1} operated in contact mode. Silicon nitride probes were loaded on an empty plastic nose cone assembly (no metallic parts). Digital processing of the images was done using Gwyddion (version 2.9) software supported by the Czech Metrology Institute; Gwyddion is freely available online.[278] The surface area covered by OTS on Si(111) in Figure 6.3 was estimated using UTHSCA Image Tool software.[316]

6.2.2 Operating Principle of Magnetic Sample Modulation AFM

Magnetic sample modulation AFM (Figure 6.1) is a hybrid approach combining contact-mode AFM with magnetic sample actuation.[18, 234] The MSM-AFM mode is used for sensitive and selective mapping of magnetic or paramagnetic nanoparticles, as well as for measuring the dynamic response of magnetic nanomaterials. This imaging mode is referred to as MSM-AFM because samples are induced to vibrate in response to the flux of an external AC electromagnetic field, using an average field strength ranging from 0.04 - 0.7 Tesla.

A wire-coil (solenoid) placed underneath the sample stage is used to generate an AC electromagnetic field to selectively drive the motion of magnetic or superparamagnetic samples.

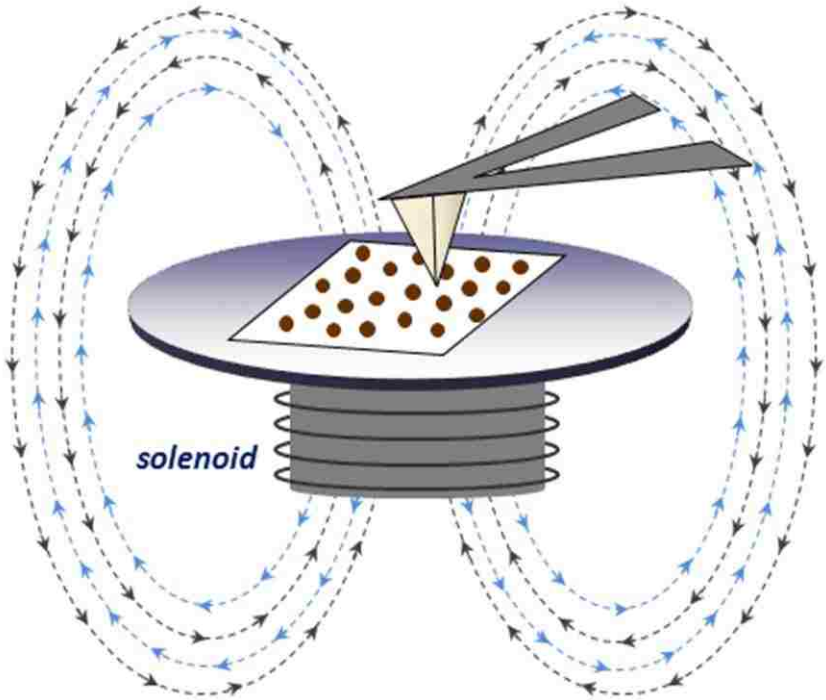

Figure 6.1. Imaging principle for MSM-AFM.

The samples need to be free to vibrate on the surface, such as by tethering the nanomaterials on a molecular linker. A soft, nonmagnetic tip is scanned in continuous contact with the surface while the samples are vibrating; therefore the probe is used to map and track the periodic motion of the modulated samples. The nonmagnetic probe is operated as a motion sensor, the rhythm and oscillation of the sample is sensitively detected with a lock-in amplifier. Phase and amplitude images are acquired by using the driving AC current as an input reference signal for lock-in detection. The hybrid MSM approach provides characterizations at the level of individual nanocrystals for detecting dynamic changes in vibrational resonance signatures. Examples of the dynamic measurements include changes in the driving frequency, varying the strength of the

electromagnetic field as well as the frequency sweep experiment while incrementally changing the applied the magnetic flux. Differences in amplitude versus size–and coupling effects of magnetic nanomaterials can also be obtained using MSM-AFM.

6.2.3 Materials and Reagents

Flame annealed gold-coated mica substrates with thickness ~150 nm were obtained from Agilent Technologies, Inc. (Chandler, AZ). Boron-doped Si(111) wafers acquired from Virginia Semiconductor Inc. (Fredericksburg, VA) were cut into 1 x 1 cm^2 pieces. The Si(111) substrates were then cleaned by soaking in piranha solution (3:1 v/v ratio of concentrated sulfuric acid and 30% hydrogen peroxide) for 2 h. Sulfuric acid as well as hydrogen peroxide were obtained from Sigma-Aldrich. Piranha can be corrosive and caution is needed when handling this reagent. Silicon substrates were removed from the piranha solution and rinsed with ethanol and as well as copious amounts of deionized water (Millipore, 18 mΩ·cm, Boston, MA) before drying in ambient conditions. Monodisperse silica mesospheres (1 wt% solution) with particle diameters of 250 nm were obtained from Duke Scientific (Palo Alto, CA) and used as template surface mask for particle lithography. Octadecyltrichlorosilane (OTS) was acquired from Gelest (Morrisville, PA) and used without further purification. Anhydrous ethanol used for rinsing samples was purchased from Pharmco (Aaper, TX).

6.2.4 Synthesis of Octa-substituted Cobaltacarborane Porphyrin Nanocrystals

Cobaltacarborane porphyrin with sixteen carborane clusters per macrocycle (Figure 6.2) was synthesized in excellent yield (90-97%) via a ring-opening zwitterionic reaction [3,3´-Co(8-$C_4H_8O_2$-1,2-$C_2B_9H_{10}$)(1´,2´-$C_2B_9C_{11}$)].[317] All of the synthetic reactions were monitored by means

of 0.25 mm silica gel plates with or without UV indicator (60F-254). Silica gel acquired from Sorbent Technologies (32-63 μm) was used for flash column chromatography.

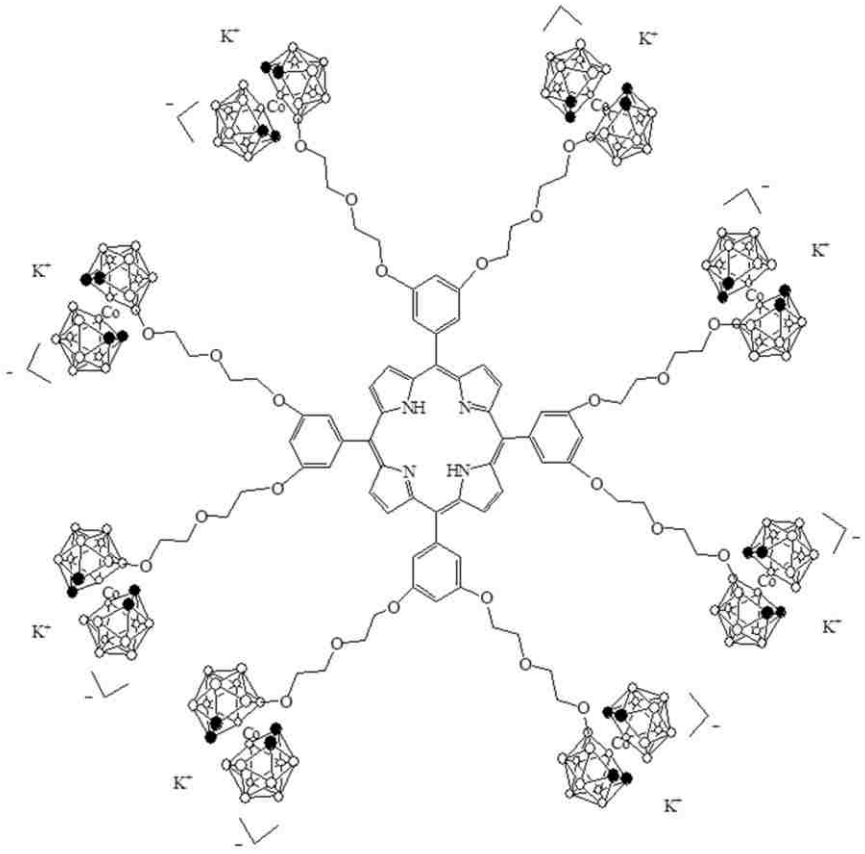

Figure 6.2. Chemical structure of octa-substituted cobaltacarborane porphyrin.

6.2.5 Porphyrin Preparation and Deposition:

Porphyrin samples were first dissolved in dimethyl sulfoxide (DMSO), and then added at 1% vol/vol to HEPES buffer (20 mM). Atomic force microscopy was used to characterize arrays of porphyrin nanocrystals.

6.2.6 Particle Lithography Using Solution Immersion

Monodisperse silica spheres (250 μL) were centrifuged three times in deionized water at 14,000 rpm to remove the surfactants and stabilizers. The pellet formed after centrifugation was

resuspended in 250 µL of ethanol. A volume (15 µL) of the cleaned (without surfactants) silica solution in ethanol was placed on a 1 x 1 cm^2 piece of Si(111) and left to dry in ambient environment for 10 minutes. The air dried sample was then placed in the oven at 140 °C for 12 h. As the solvent evaporates during the drying step, the silica particles are pulled together via a convective flow of the evaporating liquid to form hexagonally packed nanostructures on the surface. The substrate with the mask of silica mesospheres was immersed into a vessel containing OTS (10 µL) molecules dissolved in anhydrous toluene (10 mL) to make a make 0.1% (v/v). Octadecyltrichlorosilane molecules form a self-assembled monolayer (SAM) on the unmasked areas of the Si(111) wafer. The regions of contact between the silica template and the Si(111) surface remain protected from adsorption of OTS. The silicon wafer with OTS and silica spheres was then immersed in deionized water to terminate the reaction of OTS.[318] Next, the samples were sonicated in both ethanol and water for 30 min to ensure efficient removal of the mask of mesospheres. The substrate with the OTS grown was then dried with a stream of nitrogen and characterized using AFM to reveal a nanostructured film of OTS with small holes of uncovered substrate (Figure 6.3).

6.3 Results and Discussion

6.3.1 Patterning of OTS via Particle Lithography

A nanostructured film of OTS produced by particle lithography with solution immersion is displayed in Figure 6.3. Nanoholes of uncovered substrate are periodically arranged within a monolayer film of OTS. The topography frames reveal the periodic arrangement of nanoholes within the OTS film (Figures 6.3A-B). Within the 2 × 2 μm^2 frame of Figure 6.3B there are 45 nanoholes, which cover ~15% of the surface. This would scale to approximately 1.13 billion

nanoholes per cm^2. The 3D view of the topography in Figure 6.3C displays the topograhic landscape of the OTS film providing a view of the nanopores. The average (n=100) depth of the OTS matrix measured 2.5 nm (Figure 6.3D) referencing the uncovered area of Si(111) as the baseline; this is in good agreement with the theoretical thickness of a single layer for a fully saturated OTS SAM. The diameters of the pores nanopatterns measured 60 nm.

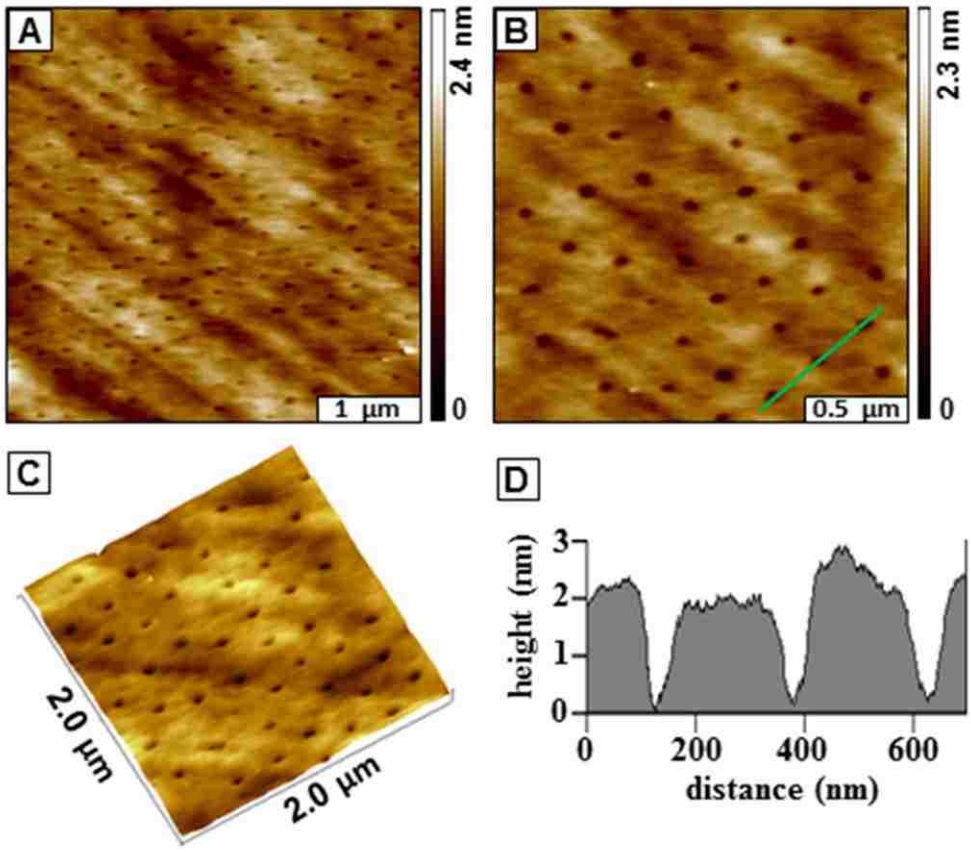

Figure 6.3. Nanostructured film of OTS prepared on Si(111) generated via particle lithography and solution immersion. A) Wide area topography, 4 x 4 μm^2. B) Higher magnification, 2 x 2 μm^2. C) 3D view of the image in **B**. D) Cursor profile along the line in **B**.

The OTS nanostructures with nanohole patterns provide a surface template to backfill the uncovered areas with other molecules, such as porphryins. The surface of OTS is terminated with methyl groups and serves as an excellent resist material. Most of the nanoholes on the OTS

matrix exhibit a close packed arrangement, there are a few defects that were observed in both Figure 6.3A and 6.3B. The defects in which holes did not form are attributable to imperfect assembly of colloidal particles on the relatively rough surface of polished silicon. The center-to-center spacing between the holes corresponds to the diameters of the silica mesospheres (250 nm) used as a surface mask.

6.3.2 MSM-AFM Imaging of Designed Test Platforms of Cobaltacarborane Porphyrins

Nanostructures of cobaltacarborane porphyrins were deposited within the nanoholes of the OTS matrix, as shown in Figure 6.4. The porphyrin solution used for backfilling was dissolved in DMSO and 1% vol/vol HEPES buffer to make 1 x 10-6 M. The immersion time to adsorb the porphyrin into the nanoholes was done for 5 h.

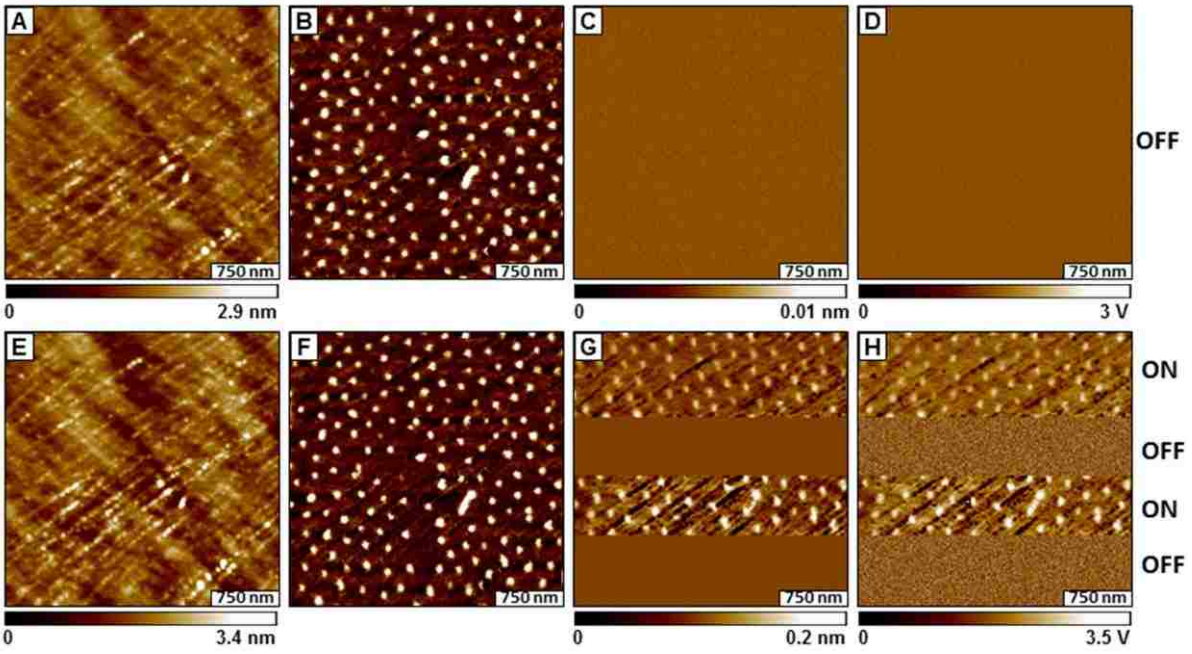

Figure 6.4. Characterization of cobaltacarborane porphyrin nanocrystals using MSM-AFM. (A, B, C, D) Conventional contact-mode AFM images with the magnetic field turned off. (E, F, G, H) Images acquired with the AC electromagnetic field turned on. In each row, from left-to-right the image frames are topography, lateral force, MSM-amplitude and MSM-phase channels.

Octadecyltrichlorosilane with methyl headgroups provided a resist layer that prevented nonspecific deposition of porphyrins, thus the porphyrin nanocrystals formed selectively within circular areas of uncovered substrate. The areas covered by the porphyrins are not clearly discernible in the topography view (Figure 6.4A), only a few circular protrusions are evident against the background. However, the lateral force image (Figure 6.4B) clearly reveals the areas of the porphyrin nanocrystals, displayed by as bright dots against the surrounding dark areas of the OTS matrix film. A close-packed arrangement of the porphyrins is observed throughout most areas of the sample with few defects areas. An area with perfect arrangement would have 174 nanostructures within the frame; there are actually 167 nanostructures detected in Figure 6.4B, which is an approximate defect density of 4%. With a molecular dimension of ~2.0 nm, porphyrin molecules deposited in the holes within the OTS matrix are difficult to be resolved in the topography frame. This is attributable to OTS having a height of ~ 2.5 nm which is similar to that of the porphyrins. Differences in tip-sample interactions between the AFM probe and porphyrin nanocrystals provide distinct contrast for the lateral force image.

Conventional contact mode AFM images (Figure 6.4A-D) were acquired without applying the electromagnetic field to the sample for the top row of images in Figures 6.4A-D. When the oscillating magnetic field was turned off, the images are acquired with conventional contact-mode and do not exhibit changes in amplitude or phase frames. The same area of the sample was scanned again with the AC electromagnetic field switched on and off (0.2 T, 64 kHz) to acquire the images in the bottom row. The field was alternated between on and off in Figures 6.4E-H.

With the electromagnetic field turned on, the vibration of magnetic nanomaterials is readily detected in the amplitude and phase channels. To the best of our knowledge, the magnetic responses of cobaltacarborane porphyrin nanocrystals have not been previously characterized. However, these materials cannot be characterized by electromagnetic fields of NMR spectrometers because of the magnetic/superparamagnetic properties.

6.3.3 Dynamic Protocols for MSM-AFM Imaging at Different Frequencies

Dynamic protocols were developed to evaluate the response of nanopatterned samples to different experimental parameters such as the driving frequency and field strength. The MSM imaging mode offers unique capabilities to obtain information about the dynamics of the actuated particles by changing the modulation frequency. An example experiment testing the changes in MSM images with frequency is shown in Figure 6.5.

Changes in amplitude and phase images were observed when different frequencies were chosen to drive the sample oscillation. The MSM amplitude and phase images exhibit distinct changes in resolution at 64, 110 and 194 kHz (Figures 6.5C-D). The field strength was kept constant at 0.2 T when acquiring the dynamic measurements in Figures 6.5A-D. Although porphyrin nanocrystals can be resolved in the MSM amplitude frame, (Figure 6.5C) the locations of nanocrystals are not clearly distinguishable at 110 kHz for the MSM phase image (Figure 6.5D). A representative spectrum of the frequency response profile is shown in Figure 6.5E, which indicates the amplitude response at a certain location of the surface. The magnitude of the response at each of the selected frequencies scales with the intensity of the amplitude image of Figure 6.5C. Interestingly, the lateral force image of Figure 6.5B also revealed changes in contrast according to the magnitude of the vibration of the sample. The greatest amplitude

response was at detected at 64 kHz, and shows less frictional interaction, and the lowest amplitude was at 194 kHz, showing larger frictional contrast. This suggests that greater sample vibration reduced the frictional effects of the tip-surface interaction.

Several prominent peaks (Figure 6.5E, red line) were generated when the frequency was swept when the tip was placed in contact with the vibrating sample. As a control, a reference spectrum was acquired with the tip lifted from the surface. A nearly flat line profile was obtained during the frequency sweep when the tip was disengaged (Figure 6.5E, black line). The flat line profile demonstrates that the AFM tip did not vibrate in response to the external magnetic field.

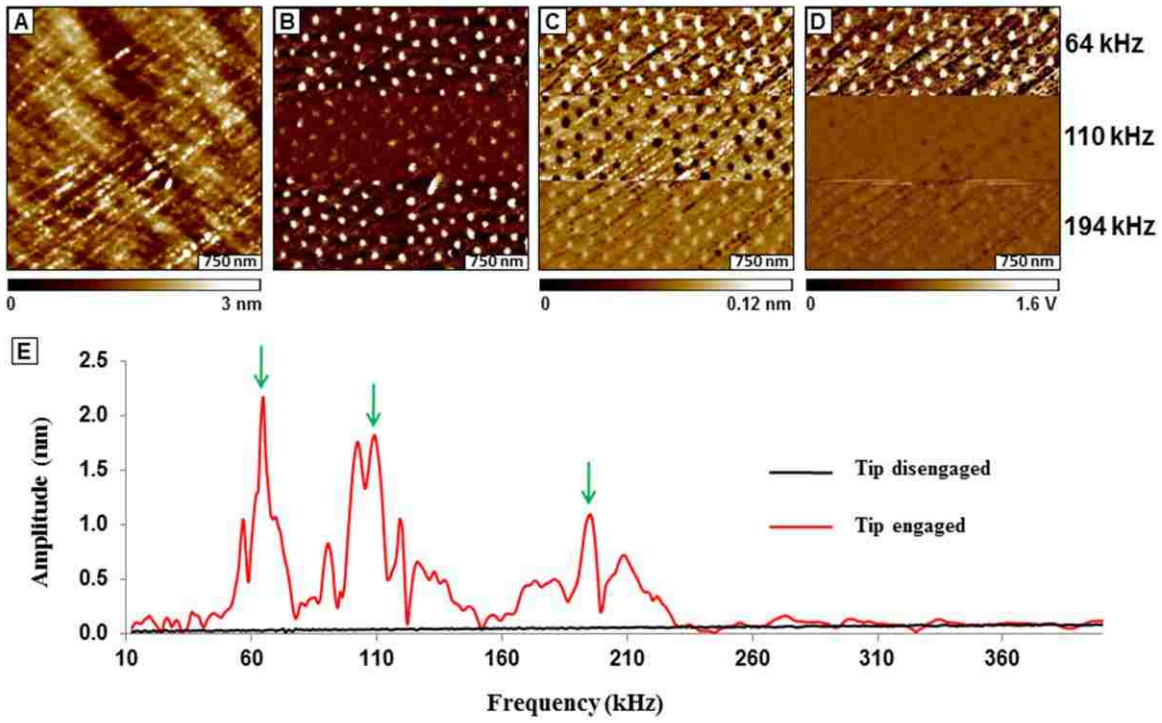

Figure 6.5. Images and frequency spectrum of porphyrin nanocrystals acquired with different driving frequencies within a single image. A) Topography image; B) lateral force frame; C) MSM-amplitude channel; D) MSM-phase frame. E) Spectrum indicating frequencies selected for image acquisition.

When the tip was parked on a magnetic porphyrin nanocrystal, the red line profile was obtained, shown in Figure 6.5. The most prominent MSM peaks were selected at 64, 110 and 194 kHz for the dynamic imaging experiment. The MSM-amplitude images scale proportionately with the magnitude of spectral peaks, however the phase images do not scale accordingly. Changes in the phase angle of vibrational response are complex, and are not readily interpretable for AFM sample modulation experiments. Interestingly, at field strength of 110 kHz there is a contrast flip for the amplitude frame, the nanocrystals become dark and the substrate is bright. This suggests that there is a shift or broadening of the vibrational resonance with greater magnetization.

6.3.4 Dynamic MSM-AFM Protocols for Imaging at Different Field Strengths

The effect of electromagnetic field strength was evaluated for MSM-AFM images by systematically ramping the field from 0.1, 0.2 and 0.3 T during image acquisition. The driving frequency was kept constant (64 kHz) during data acquisition for Figure 6.6. When the electromagnetic strength was increased from 0.1 to 0.3 T, the lateral force (Figure 6.6B), MSM-amplitude (Figure 6.6C) and MSM-phase (Figure 6.6D) channels displayed corresponding incremental changes in contrast for the porphyrin nanocrystals. However, changes in the resolution of the topography frame are not readily detectable (Figure 6.6A).

The MSM amplitude and phase channels clearly distinguish the locations of the nanopatterns of cobaltacarborane porphyrins at each field strength setting, (Figures 6.6C and 6.6D, respectively), which demonstrates the capabilities for sensitive mapping of vibrating nanostructures. For this example, both the MSM-phase and MSM-amplitude frames scale according to the strength of the applied magnetic field (Figures 6.6C,D). The lateral force images show the reverse trend for image contrast, at higher field strength (0.3 T) the sizes of the crystals

appear smaller, and greater frictional contrast is observed at low field (0.1 T). This can be rationalized by the changes in vibration of the samples at the nanoscale; a sample with greater vibration would experience less tip-surface interaction force. Lateral force images therefore show less frictional response as the field strength was increased, because the tip-sample interactions with the vibrating nanocrystals are reduced.

A graph of the applied magnetic field at 0.1, 0.2 and 0.3 T plotted against the average intensity of the lateral force signal in (V) is shown in Figure 6.6F. The intensity of the lateral force image changed incrementally when a magnetic field was ramped from 0.1 to 0.3 T. Differences of the tip-sample interaction forces are produced by changes in sample vibration, such that greater sample motion produced less frictional contrast.

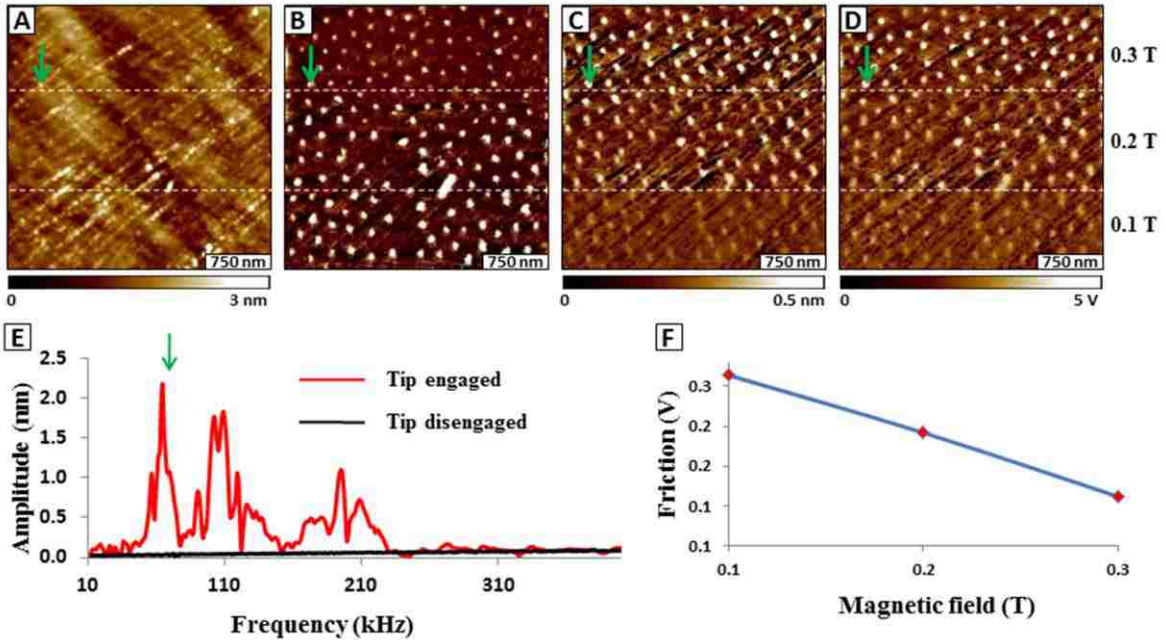

Figure 6.6. Successive changes in MSM-AFM images with electromagnetic field strength. A) Topography image; B) lateral force frame; C) MSM-amplitude; D) MSM-phase image. E) Frequency plot indicating the peak at 64 kHz used to generate the image. F) Graph of the relationship between friction (V) versus applied magnetic field.

6.3.5 MSM-AFM Measurements with Individual Porphyrin Nanocrystals

Using MSM-AFM, the tip can be placed in contact with specific locations of the surface to obtain frequency spectra for detecting the vibration of individual nanocrystals. The response of cobaltacarborane porphyrins to the magnitude of the applied AC field is shown in the plot of Figure 6.7. The green arrow shown in the inset AFM image indicates the position of the porphyrin nanocrystal where the tip was placed, while the frequency was swept.

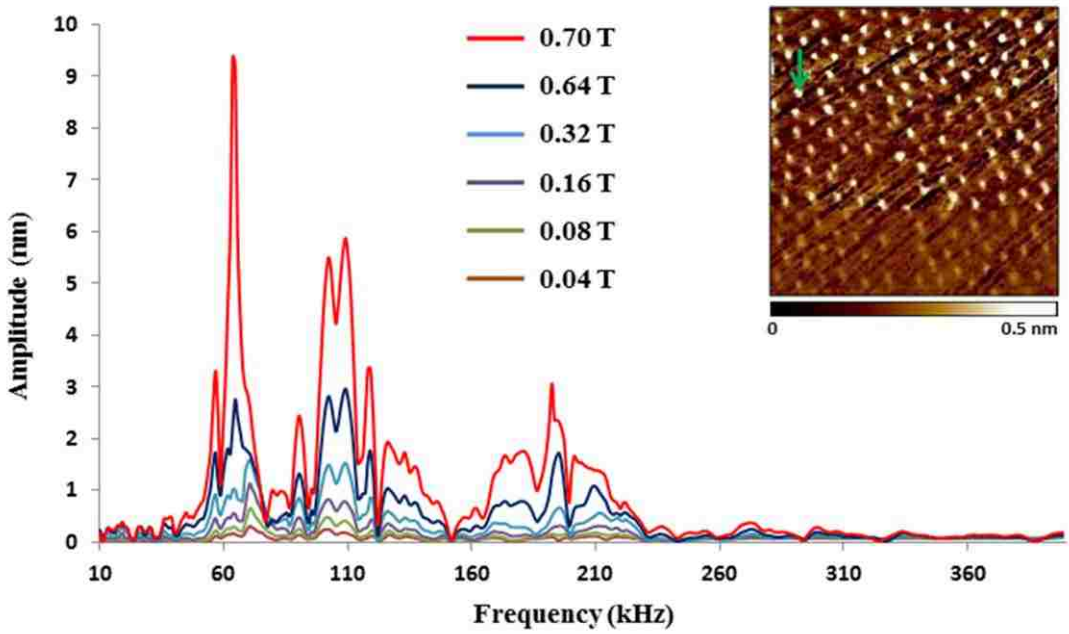

Figure 6.7. Amplitude response of a single porphyrin nanostructure acquired at different field strengths. The amplitude spectra were acquired by parking the probe on the nanocrystal indicated by a green arrow within the inset AFM image.

As the field strength was incrementally ramped, corresponding changes in the amplitude response was measured and plotted demonstrating highly symmetric peak profiles (Figure 6.7). The amplitude peaks increased proportionately as the field strength was ramped. An amplitude response of 0.2 nm was observed when the applied field was set at 0.04 T and a higher amplitude response of 9.6 nm was obtained when the magnetic strength was applied at 0.7 T. The

resonance signatures are not identical for different size nanostructures, further experiments are being designed to evaluate the size-dependent resonance profiles for nanostructures of different sizes and different composition.

Characterizations with MSM-AFM provide unique capabilities to obtain information about the dynamics of individual nanocrystals that are actuated with different parameters of field strength. By increasing the applied magnetic field, precise and reproducible mechanical signatures were obtained for a single nanocrystal of porphyrins. The magnitude of the changes in the amplitude response corresponds to physical displacement of the probe in the z-direction, within a certain range for tip distances of 0.2 - 9.6 nm as the applied magnetic field was increased from 0.04 to 0.7 T. The displacement of probes in the z-direction with AFM measurements can be sensitively measured at sub-nanometer distances, as shown with details of local MSM-AFM spectra acquired at 0.04 T and 0.08 T for this sample.

6.3.6 Size-Dependent Response of the Vibrational Amplitude with MSM

The mapping capabilities of the MSM-AFM imaging mode can be used to acquire quantitative information of magnetic response for selected local regions. Rich information about the actual physical response (z direction) of the nanocrystals to the applied magnetic field can be extracted from the amplitude images by making cursor measurements of the magnetic nanostructures. The porphyrin nanocrystals ranged from 75 to 140 nm in diameter, using individual cursor profiles of the topography images. The non-linear trend of the magnetic response versus the size of the nanostructures is plotted in Figure 6.8. In general, a greater vibrational amplitude is measured for larger porphyrin crystals, within the size range of 70 - 140

nm. It has been reported that with an increase in size and volume of ferromagnetic materials, mass magnetization also becomes enhanced.[191, 319]

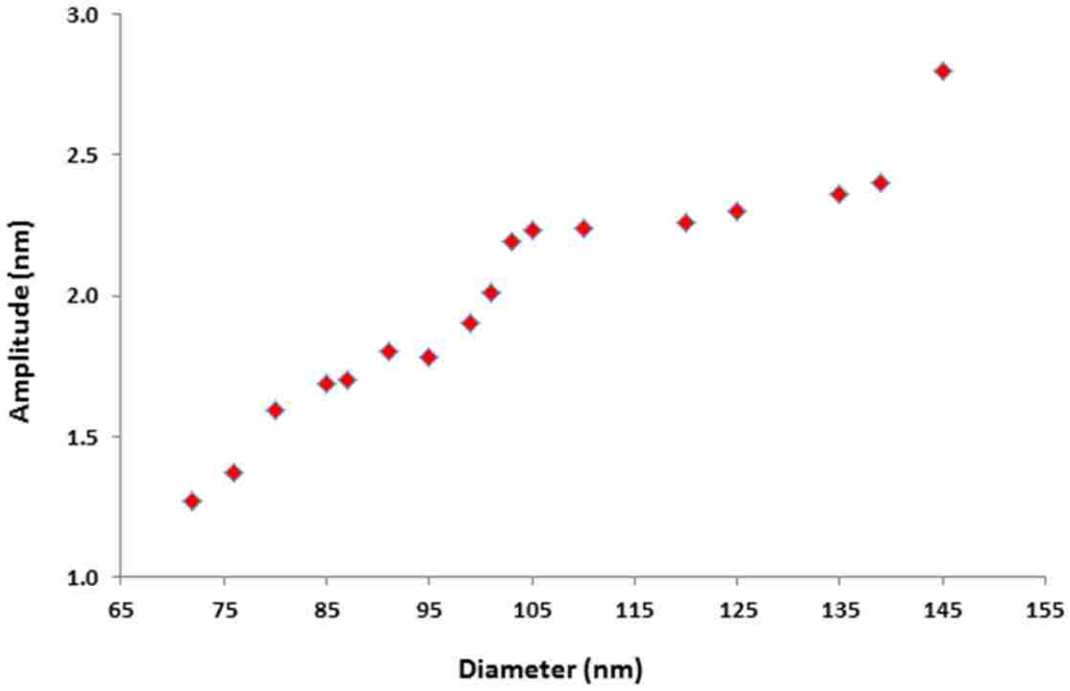

Figure 6.8. Amplitude response plotted versus the sizes of porphyrin nanocrystals.

6.3.7 Summary

The MSM-AFM imaging mode holds promise for providing greater sensitivity than existing scanning probe methods for magnetic measurements, enabling characterizations at the level of individual nanoparticles. Nanolithography provides approaches to prepare designed test platforms of cobaltacarborane nanocrystals, to provide discrete sizes and arrangements of nanoclusters. Designed test platforms prepared on organosilane templates enable measurements

of isolated, individual nanostructures to prevent the effects of aggregation or magnetic coupling between neighboring particles.

To advance towards quantitative nanomagnetic measurements requires a clearer understanding of contributions of elasticity, surface adhesion and mass to correlate with the magnetization of nanomaterials. Parameters to be considered are the size and chemical composition of the nanostructures, the elasticity and adhesion strength of the SAM linker molecules. Further experiments are planned to compare the mechanical and magnetic response spectra for magnetic materials at various field strengths using systematically designed test platforms with scalable differences in size, arrangement and composition. For development of experimental protocols with MSM, the tip can be placed in contact with specific locations of the surface to obtain frequency spectra of the vibration of individual nanoparticles. Preliminary investigations indicate that the profiles of frequency spectra change according to the size of the nanoparticles. Protocols will be developed to survey the effects of different sizes and composition of nanoparticles using a combination of MSM mapping and frequency profiles.

The development of the MSM imaging mode has been a challenge, because of the complexity of sample responses. When choosing a driving frequency, the tip must be placed selectively on a vibrating area of the surface. Different frequency profiles are observed for different sizes and material composition of nanoparticles, as one would predict. Protocols will be developed to tune in the optimized driving frequency and AC field strength for MSM characterizations. These preliminary investigations demonstrate that the resonance peaks for driving the vibration of samples for magnetic modulation do not coincide with the natural resonance frequencies of the AFM cantilevers. For mapping magnetic domains, the magnetic

field at selected frequencies was determined experimentally for each sample, which have not been found to occur at the natural resonance frequencies of the AFM probes. We have also begun to develop experimental protocols for systematically changing the parameters of the field strength of magnetic oscillation. As the field was incrementally ramped, increases in the vibrational response of the nanoparticles produced corresponding changes for both the amplitude and phase channels.

CHAPTER 7. CHARACTERIZATION OF MAGNETIC NANOGUMBOS USING CONTACT-MODE AFM IMAGING WITH MAGNETIC SAMPLE MODULATION

7.1 Introduction

A hybrid AFM imaging mode referred as magnetic sample modulation (MSM-AFM) has been developed for characterizing magnetic or paramagnetic nanomaterials.[18, 234] Thus far, MSM-AFM has been applied to characterize the physical motion of ferritin metalloproteins with ~12 nm diameters,[18] as well as electrolessly deposited iron oxide nanostructures measuring 10 ± 3 nm that were patterned on organosilane templates.[234] The MSM-AFM imaging mode has capabilities to resolve and map magnetic response at the level of individual nanoparticles or proteins. Magnetic or superparamagnetic nanomaterials are induced to selectively vibrate when an oscillating electromagnetic field is applied to the sample. Using a non-magnetic AFM tip as a motion sensor, the subtle changes in motion of the vibrating samples can be sensitively mapped. In this report, the applicability of MSM-AFM imaging is tested for samples of ionic liquid nanoparticles prepared with iron salts.

The term ionic liquids is used to described a group of molten salts with melting points at or below 100 °C.[320] The broad class of ionic liquids comprise semi-organic salts or mixtures of salts with low melting points.[320, 321] Room temperature ionic liquids consist of nitrogen or phosphorus organic cations with alkyl chains, examples include tetraalkylphosphonium, tetraalkylammonium, N-alkylpyridinium or N,N′-dialkylimidazolium cations.[322-324] The synthesis of an ionic liquid which shows a strong response to magnetic field was first discovered by Hayashi and Hamaguchi in 2004.[325] The magnetic ionic liquid, [bmim]$FeCl_4$, was prepared by mixing 1-butyl-3-methylimidazolium chloride ([bmim]Cl) and $FeCl_3$. Ionic liquids with paramagnetic properties have also been prepared.[326-331] Examples are methylbutylpyrrolidinium

tetrachloroferrate(III), methyltributylammonium tetrachloroferrate(III), butylmethylimidazolium tetrachloroferrate(III) and tetrabutylammonium bromotrichloroferrate(III).

The synthesis of the micro- and nanoparticles developed from the frozen ionic liquid 1-butyl-2,3-dimethylimidazolium hexafluorophosphate ([bm2Im][PF6]) via a melt emulsion quench approach has been previously reported.[28] A novel class of ionic liquids described as, *g*roup of *u*niform *m*aterials *b*ased on *o*rganic *s*alts (GUMBOS) have also been reported by Tesfai et al.[3] Nanoparticles of GUMBOS include organic salts with melting points above 100°C. The nanoGUMBOS ionic liquids were synthesized to contain either BF_4 or $FeCl_4$ to compare nonmagnetic and magnetic properties, respectively.[3] The capability of nanoGUMBOS to host functional magnetic properties has potential for biomedical, electronics, analytical and separations applications.

This report will focus on MSM-AFM characterizations of magnetic nanoGUMBOs with sizes below 100 nm. For MSM-AFM characterizations, samples are induced to vibrate in response to an electromagnetic field with alternating polarity. The samples adhere weakly to substrates, and can be induced to vibrate by the flux of an AC electromagnetic field. A fairly wide range of materials have magnetic or paramagnetic properties, and the magnitude of vibration of the samples depends on the size and material composition.

7.2 Experimental Methods

7.2.1 Principle of Magnetic Sample Modulation-AFM

The MSM mode is a hybrid of contact mode AFM combined with selective actuation of magnetic samples (Figure 7.1). Three images are acquired concurrently with MSM, topography, MSM-amplitude and MSM-phase frames, which provide information about the locations and

vibration of samples. Frequency spectra can be acquired by placing the tip in contact with a vibrating sample and sweeping the frequency at selected field strength. For MSM, conventional contact mode images can be acquired by turning off the magnetic field.

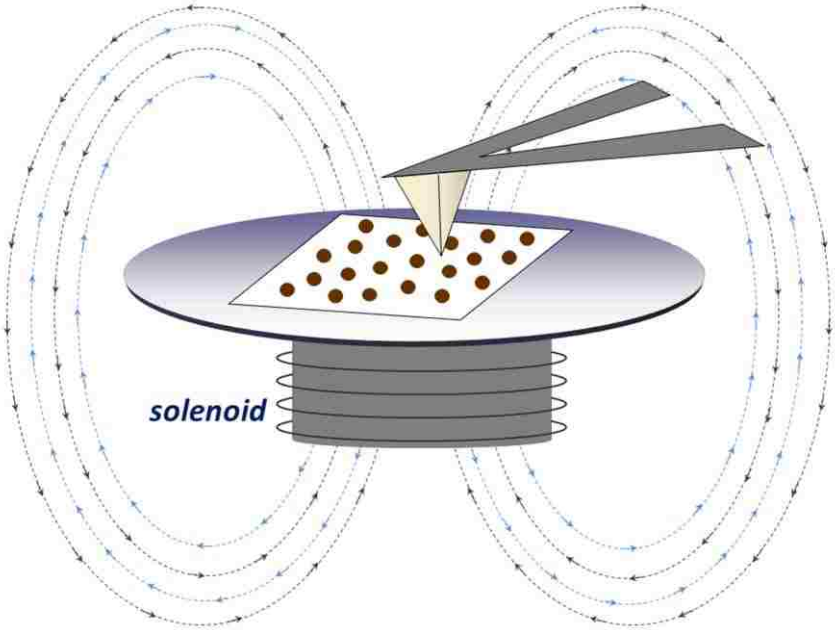

Figure 7.1. Operation principle of magnetic sample modulation AFM.

When the electromagnetic field is off, the topography image should reveal the shapes and morphologies of the nanomaterials irrespective of whether the sample has magnetic or non-magnetic characteristics. When an electromagnetic field is applied to the solenoid and the same area of the sample is scanned again, changes in both the amplitude and phase channels reveal regions which respond to the magnetic flux. Changes in the amplitude and phase of the sample vibration are mapped using the driving AC current as a reference signal. The AFM tip is used as a motion sensor to selectively detect the oscillation of vibrating magnetic domains. Investigations with MSM-AFM use a lock-in amplifier to compare signals, which enables the tip to detect very small changes in sample motion.

7.2.2 Methods and Materials

1-Butyl-2,3-dimethylimidazolium chloride [Bm_2Im][Cl] (97%), sodium tetrafluoroborate [Na][BF_4] (99%), iron(III) chloride hexahydrate (Fluka, 98%), sodium bis(2-ethylhexyl)sulfosuccinate (AOT), and *n*-heptane (Sigma, 99%) were acquired from Sigma Aldrich (St. Louis, MO) and used as received without further purification. Elga model PURELAB ultra water filtration system was used to obtain ultrapure water (18.2 MΩ·cm).

7.2.3 Synthesis of Magnetic Ionic particles (nanoGUMBOS)

The preparation of the magnetic nanoGUMBOS (Figure 7.2) was done using a modified reverse-micellar method; a procedure previously reported by Tesfai et al.[3] Using the modified reverse-micellar approach produced nanoGUMBOS with controllable sizes.

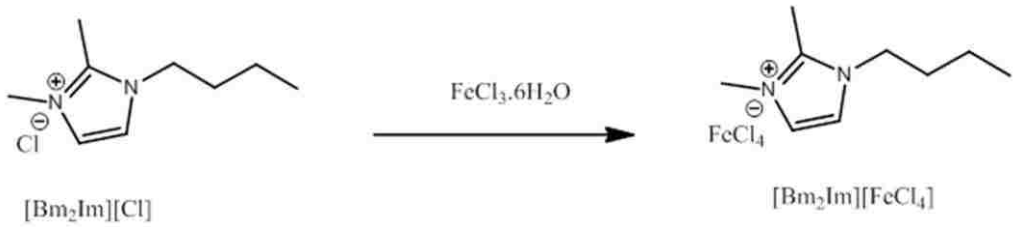

Figure 7.2. Synthesis steps and chemical structure for [Bm2Im][FeCl4].

7.2.4 Preparation of Substrates

Ruby muscovite mica (S&J Trading Co., NY) was used as a substrate for AFM characterizations. Pieces of mica (1 × 1 cm^2) were cut and cleaved immediately before depositing a drop of nanoGUMBOS solution measuring 15-20 µL. Samples were dried in ambient conditions for at least 12 h before imaging.

7.2.5 Atomic Force Microscopy

An Agilent 5500 SPM system equipped with a multipurpose AFM scanner was used for surface characterizations (Agilent Technologies, Chandler, AZ). Picoscan v5.3.3 software was used for data acquisition. For MSM-AFM studies, a MAC-mode sample plate was used to generate an alternating electromagnetic field to induce vibration of samples. The AFM nosecone used for MSM investigations contained no metal components. Nonmagnetic silicon nitride cantilevers with force constants ranging from 0.1 to 0.5 N m^{-1} (Veeco Probes, Santa Barbara, CA) were used for MSM-AFM imaging. Digital images were processed with Gwyddion open source software, supported by the Czech Metrology Institute, which is freely available on the Internet (http://gwyddion.net/).[332] The surface area covered by the nanoGUMBOS was estimated using UTHSCA Image Tool for Windows version 3.00 (San Antonio, TX).[316]

7.2.6 Sample Preparation

A sample of $[Bm_2Im][FeCl_4]$ nanoGUMBOS was prepared by depositing a drop of the liquid sample (~15 μL) on freshly cleaved mica, and then drying the sample for in air 12 h.

7.3 Results and Discussion

An area of the nanoGUMBOS sample (5 × 5 μm^2) was first scanned with conventional contact-mode AFM with the electromagnetic field turned off (Figures 7.3A,B,C). The topography frame (Figure 7.3A) reveals the shapes and morphologies of the nanoGUMBOS. Without the influence of an electromagnetic field, there are no features apparent in the amplitude and phase channels (Figures 7.3B and 7.3C, respectively). The center row of images was acquired with the electromagnetic field turned on, with the probe scanned in continuous contact with the surface. A prominent circular structure in the upper left corner of each frame provides a

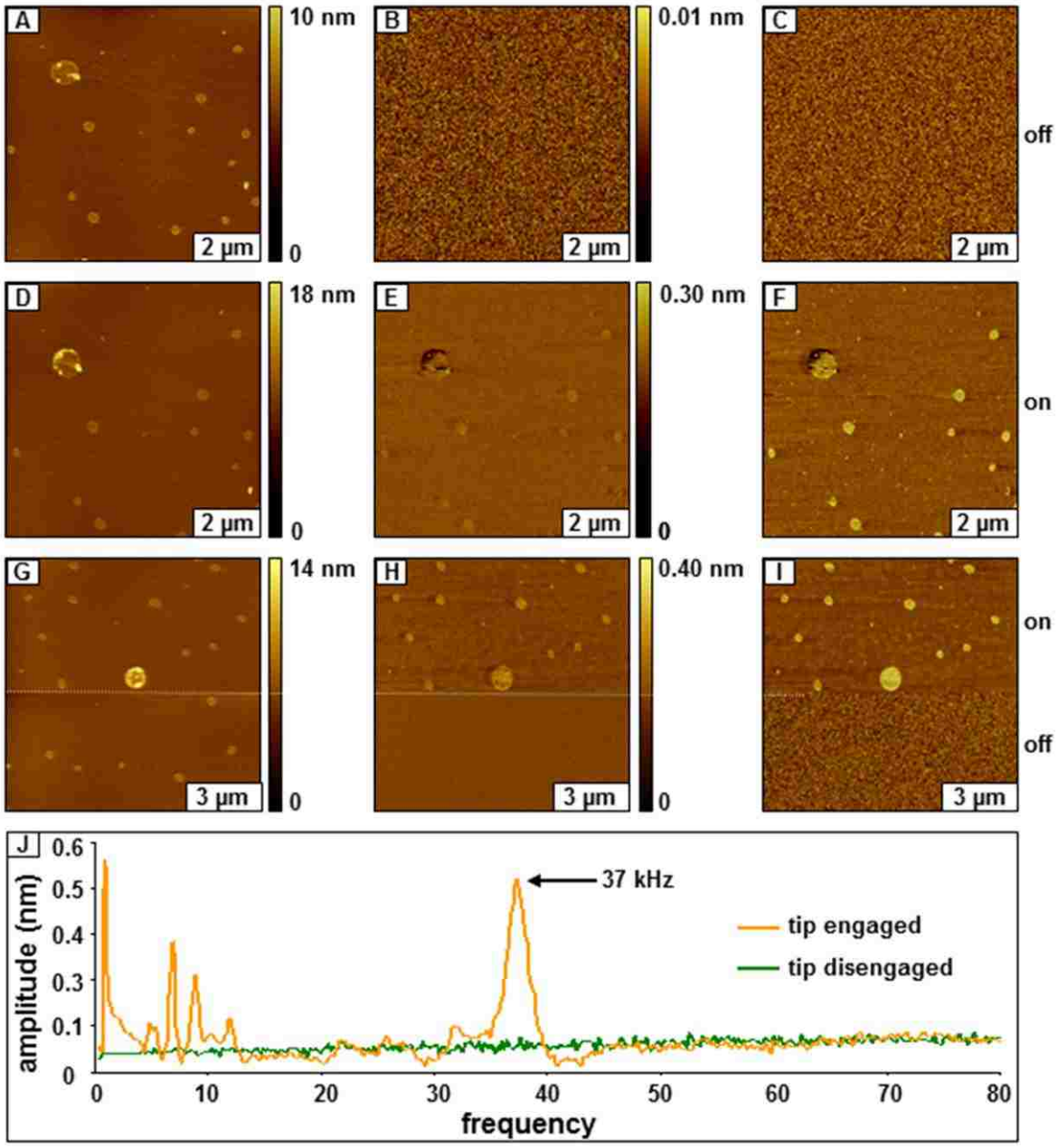

Figure 7.3. Magnetic nanoGUMBOS characterized using contact mode and MSM-AFM. Contact mode images acquired with the magnetic field switched off: (A) topography, (B) amplitude, (C) phase frames. Data acquired with MSM-AFM with 0.2 T at 37 kHz: (D) MSM-topograph, (E) MSM-amplitude, (F) MSM-phase images. Changes with field switched on then off: (G) topograph, (H) amplitude, (I) phase channel. (J) Example frequency spectra.

landmark for comparing the frames, which appears to be an aggregate composed of several smaller nanoparticles. Under the influence of the AC electromagnetic field, small nanoparticles at the edges of the circle have shifted position and show brighter contrast. The locations of the nanoGUMBOS are visible in the topography frame as well as in the MSM amplitude and phase channels (Figures 7.3D,E,F). Interestingly, very small nanoparticles that were not clearly resolved in the topograph of Figure 7.3A became apparent when the sample was actuated in Figure 7.3D. The phase frame of Figure 7.3F clearly shows the locations of exquisitely tiny nanoparticles which are buried in the background noise of the topography frames. In the topography views, only nanoGUMBOS with larger sizes are resolved.

A different area of the sample was characterized for Figures 7.3G,H,I to obtain a direct comparison of MSM and contact mode operation within a single frame. The field was switched on to acquire the top half of the frames to map the locations of nanoGUMBOS in amplitude and phase channels. The field was switched off midway through the scan, and the amplitude and phase channels changed correspondingly to reveal only background noise. The magnitude of the electromagnetic field was 0.2 T (measured with a portable magnetometer). For this example, the greatest sensitivity was detected in the phase frame of Figure 7.3I, where ultra-small nanoparticles were resolved that were not visible in the topograph.

Frequency profiles can be acquired by placing the AFM probe in contact with a vibrating area of the sample, an example is shown in Figure 7.3J. The frequency spectra shows the changes in z-deflection of the AFM probe as the AC frequency was ramped. When the AFM tip was disengaged from the surface, a relatively flat baseline was detected (green line) with the electromagnetic field turned on. However, when the AFM tip was placed in contact with

magnetic nanoGUMBOS, several prominent peaks became apparent (orange line) for frequencies ranging from 0 to 80 kHz. The tallest, broad resonance peak at 37 kHz was selected for acquiring MSM images. However, any of the resonance peaks shown on the spectrum can be used to drive the vibration of magnetic nanomaterials sample for MSM characterizations.

The effect of the magnetic field strength for MSM imaging was evaluated by acquiring a single frame and successively changing the settings at different time points. The electromagnetic field was ramped at different increments from 0.01 to 0.5 T, as shown in Figure 7.4.

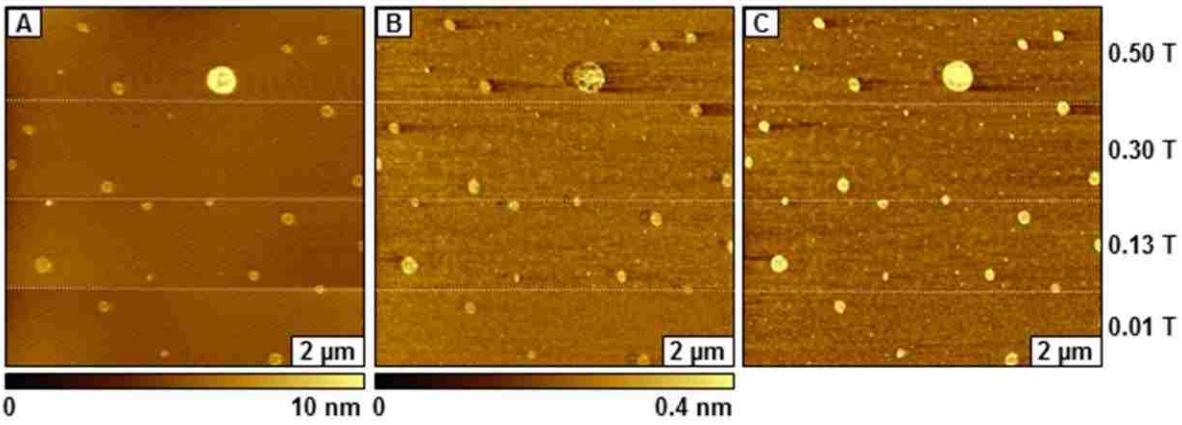

Figure 7.4. MSM-AFM images of nanoGUMBOS acquired with successive changes in the electromagnetic field applied during data acquisition. (A) Topography frame; (B) MSM-amplitude; (C) MSM-phase image.

The dashed white lines drawn on the images are used as a guide to distinguish where the settings were changed during the scan. Both the MSM-amplitude and MSM-phase frames show a gradual change in contrast as the field strength was increased, the brightest colors and clearest resolution was achieved at 0.5 T. Essentially, lighter contrast in the MSM channels results from weaker vibration of the sample. The MSM-phase channel reveals the locations of the smaller nanoparticles most sensitively; more of the bright yellow dots are detected in the phase frame. In some cases, the adhesion of samples to the substrate can be overcome when using higher

magnetic fields, leading to sample displacement. Both the scanning motion of the AFM probe and the effects of the magnetic field can cause samples to be displaced from the surface. The *in situ* protocol used in Figure 7.4 for testing the effects of different field strengths is helpful for deriving the optimum parameters for MSM imaging.

To understand the influence of selected oscillation frequencies, a dynamic experiment was conducted by maintaining a constant field strength with different driving frequencies (Figure 7.5). For MSM-AFM studies, it is important to select a frequency that will ensure sensitivity and

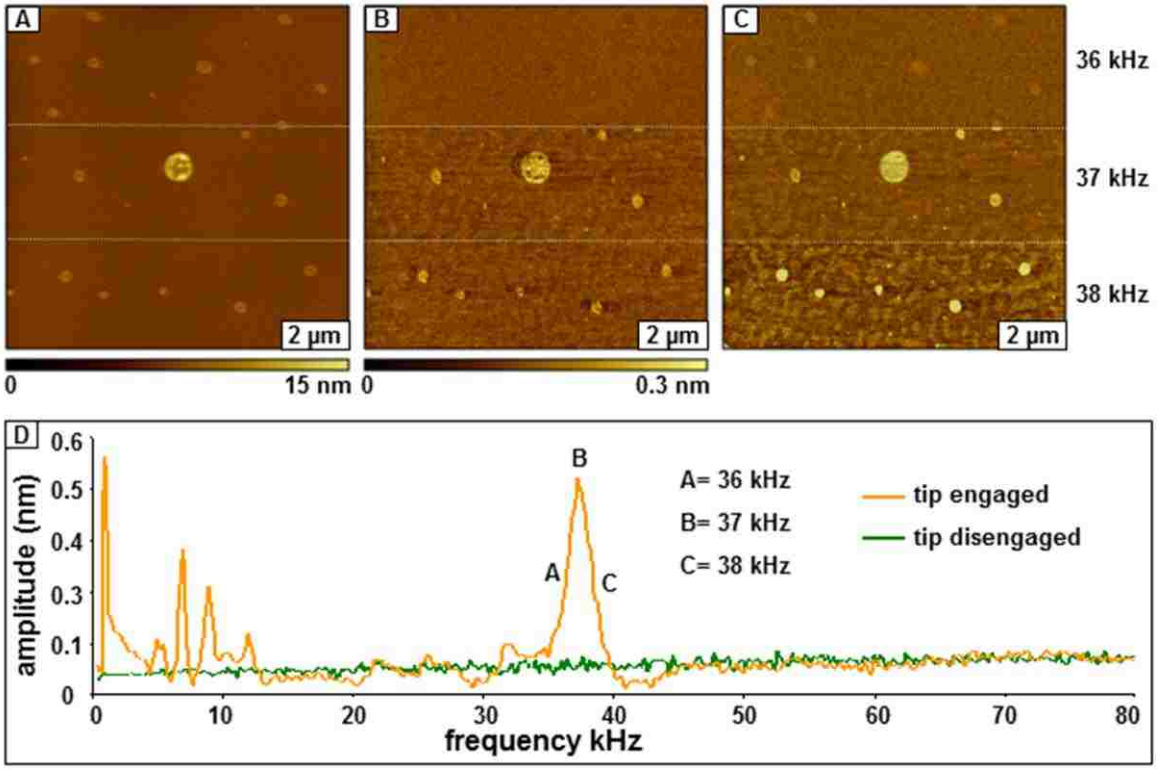

Figure 7.5. MSM-AFM images acquired at different frequencies. (A) Topography; (B) MSM-amplitude; C) MSM- phase images. D) Frequency spectrum designating the frequencies selected for sample actuation.

provide high resolution. As shown in Figure 7.5J, an intense and relatively broad resonance peak was detected at 37 kHz. For the images of Figure 7.5, data was acquired near resonance as well

as at the 37 kHz resonance frequency. Faint color contrast is detected at 36 kHz for both amplitude and phase channels. The brightness of the image contrast for MSM-amplitude channels scales according to the amplitude intensity of the spectra, with the brightest contrast observed at the peak maximum of 37 kHz. However, the MSM-phase channel reveals sharp contrast even at an off-resonance frequency of 38 kHz. Thus, the sample dynamics for registering changes in the phase angle of vibrational motion are more complex than the amplitude response.

7.4 Conclusion

New protocols for MSM-AFM measurements were developed and used successfully for characterization of samples of magnetic nanoGUMBOS. Better resolution of ultra-small nanoparticles was achieved using MSM-AFM in comparison to conventional contact mode images, enabling detection of nanoparticles as small as 1 nm in diameter. Exquisite sensitivity was achieved for phase images using MSM-AFM, and the optimized parameters did not scale according to resonance frequencies. Parameters of the magnetic field strength or the driving frequency can be tuned to optimize resolution of MSM-AFM. The hybrid imaging mode of MSM-AFM offers exceptional sensitivity and selectivity for detecting the vibration of nanomaterials in response to an external electromagnetic field.

CHAPTER 8. STUDIES OF THE GROWTH, EVOLUTION AND SELF-AGGREGATION OF B-AMYLOID FIBRILS USING TAPPING-MODE ATOMIC FORCE MICROSCOPY

8.1 Introduction

Progression of several diseases are characterized by protein misfolding and conformational changes leading to plaque deposits in either the body or organs. Amyloid deposits localized in regions of the brain, including the central nervous system, have been linked to a number of neurogenerative diseases that include Alzheimer's (AD), Huntington's, Parkinson's and Prion diseases. [333-336] Alzheimer's disease is globally the most prevalent neurodegenerative disorder of humans, mainly affecting the elderly. Plaques found in AD patients are composed primarily of fibers of the amyloid 3-protein fragment, $A\beta_{1-40}$. The principal component of senile plaques is the β–amyloid peptide (Aβ), which is derived from proteolytic cleavage of the transmembrane amyloid precursor protein by β- and γ-secretases. Amyloid deposits in the brain, which consist of senile plaques and neurofibrillar tangles, are characteristic of the development of AD. [337] A body of evidence associates the density of senile plaques with the severity of AD dementia. [337, 338] Two isoforms of Aβ are most often produced depending on the γ-secretase cleavage site; $A\beta_{1-40}$ and $A\beta_{1-42}$.

The peptide Aβ is a normal, soluble component of human plasma and cerebrospinal fluid. [339, 340] It is toxic only after it undergoes aggregation and/or conformational changes to produce oligomers or fibrils. [341-344] The most common isoforms are Aβ40 and Aβ42, which differ only by the length of the C terminus. The most prevalent form of AD is correlated with an increased level of 40-residue Aβ protein, however, the pathology and molecular mechanisms of action are not completely understood. [345]

Reproduced with permission from Encyclopedia of Analytical Chemistry

Synthetic Aβ has been shown to aggregate *in vitro* via various intermediate species including soluble oligomers, protofibrils, and insoluble fibrils. [346] The species generated by the *in vitro* process are dependent upon certain conditions, such as acidic pH, metal ions, osmolytes, and interaction with lipid membranes. [347-351] There are numerous and complex factors influencing the nucleation of fibrils and the rate of fibril growth *in vivo*, such as parameters of pH, ionic strength, peptide concentration, temperature and mixing protocol. [352] The mechanism of Aβ aggregation into toxic species has been shown to proceed via two distinct pathways. In the presence of pre-formed fibrils or plaques, Aβ aggregates by consecutive association onto the ends of existing fibrils. [353, 354] However, in the absence of seeding, Aβ monomers aggregate into fibrils by a two step-polymerization process; nucleation and elongation, in which nucleation is the rate determining step. [341, 355-357] An energy barrier must be overcome for Aβ monomers to fold into nuclei during the nucleation phase. [358] Once the nuclei have been generated, rapid elongation of fibrils occurs during the linear phase.

A nucleation dependent model has been established for the assembly process of amyloid proteins into fibrils, which as also been characterized as a hierarchical assembly model (HAM). [359, 360] The model predicts that monomeric amyloid protein self-aggregates via a nucleated polymerization mechanism into seed particles and then form protofilaments, which elongate by addition of monomers at the ends of protofilaments. Two or three protofilaments can associate to form protofibrils that intertwine to form fibrils. Protofibrils are soluble aggregrates of Aβ with heights of approximately 3 nm and lengths of 10-200 nm. [361] In general, the HAM model predicts that fibrils and protofibrils will exhibit clumping, periodicity, variations in height, and branching. An overview of the characteristic nanostructures and dimensions reported from AFM

studies is presented in Table 8.1. Characterizations of the growth of $A\beta_{1-40}$ into oligomeric or fibrillic assemblies provides insight into the mechanism of fibrillogenesis and progression of AD. Detailed knowledge of the early stages of fibrillization can aid in developing strategies to mitigate fibril formation for therapeutic treatment. [362, 363]

Table 8.1. Dimensions reported for nanostructures formed during amyloid fibrillization using AFM studies.

Time	Isomer	Description	Reported Dimensions	Media	AFM Experiment	Reference
<1 hr	1-42	oligomers	Diameter: 1-1.5 nm	Air	Tapping Mode	[346]
1 week	1-40	Protofibrils	Diameter: 3.1±0.58 nm Length: 20-70 nm	Air	Tapping Mode	[361]
1 week	1-40	Protofibrils	Diameter: 2-3 nm	Air	Contact Mode	[352]
1 week	1-42	Protofibrils	Diameter: 4.2±0.31nm	Air	Tapping Mode	[361]
4 weeks	1-40	Type 1 Fibrils	Diameter: 7.8±0.45 nm Length: > 1 μm	Air	Tapping Mode	[361]
4 weeks	1-42	Type 1 Fibrils	Diameter: 7.3±0.53 nm	Air	Tapping Mode	[361]
5 weeks	1-40	Type 2 Fibrils	Diameter: 4.5±0.43 nm	Air	Tapping Mode	[361]
5 weeks	1-42	Type 2 Fibrils	Diameter: 3.8±0.43 nm	Air	Tapping Mode	[361]
10 weeks	1-40	Fibrils	Diameter: 4-6 nm	Air	Tapping Mode	[352]

There are several distinct advantages and a few disadvantages for choosing AFM characterizations rather than electron microscopies for imaging amyloid structures. The 3D morphology of fibrils can be observed directly in ambient environments using AFM, whereas sample pretreatment with metal stains and UHV chambers are required for 2D experiments with electron microscopy. With AFM, the lateral dimensions of samples can be slightly distorted by convolution of the tip geometry, however the vertical dimensions are quite accurate and can be comparable to EM measurements. Detailed discussion and models of AFM tip-sample

convolution for Aβ fibrils have been reported previously. [352, 361, 364] Electron microscopy studies of amyloid-β have been reviewed previously [365], therefore this report will selectively highlight recent work with AFM characterizations of Aβ.

A number of studies have been accomplished with AFM for imaging Aβ. Images of fresh and 24 hour samples were acquired for $A\beta_{1-40}$ reconstituted in phospholipid vesicles, using contact-mode AFM in phosphate buffered saline (PBS) media. [345] Studies of the growth and kinetics of Aβ oligomers [366] and protofibrils [361, 364, 367] have been accomplished by several researchers using AFM. The kinetics of Aβ42 interactions with planar lipid bilayers was studied *in situ* using tapping-mode AFM combined with fluorescence microscopy. [368] The role of metal ions in forming β-amyloid fibrils and deposits was conducted using *ex situ* AFM and other characterization tools. [369] Amyloid fibrils formed after 24 h incubation under different growth conditions in either buffer or two-phase polar/non-polar interfacial systems were investigated using AFM, electron microscopy and circular dichroism characterizations. [367] A surface plasmon resonance (SPR) analytical system was developed for monitoring Aβ42 fibrillization under various conditions using side-by-side AFM images to characterize the species that formed. [370] A number of investigations have targeted approaches to prevent or mitigate fibrillogenesis, and have applied AFM for characterizing the changes in sample morphologies under various conditions. [371]

In this report, nanostructures prepared *in vitro* that formed during the growth of $A\beta_{1-40}$ fibrils were characterized using AFM at selected time points and compared with observations from previous reports. [357], [352] With a sharp probe, AFM can resolve structures with nanometer dimensions. Unlike electron microscopies, scanning probe characterizations provide 3D

structural information without requiring metal staining protocols or vacuum environments. Tapping-mode AFM was applied to investigate the time course for growth of Aβ into oligomers, protofibrils and mature fibrils over longer time in which bundles and tangled arrangements of fibrils became apparent.

8.2 Materials and Methods

8.2.1 Peptide ($A\beta_{1-40}$) Monomerization

A 40-mer peptide ($A\beta_{1-40}$) was obtained commercially (Invitrogen Corp., Carlsbad, CA, USA). The lyophilized $A\beta_{1-40}$ was pretreated to form monomeric solutions by first dissolving it in neat trifluoroacetic acid (TFA) (1 mg/mL) and sonicating for 20 min. Upon removal of TFA using a centrivac, a slight yellowish residue was produced. The peptide ($A\beta_{1-40}$) sample was then dissolved in one mL hexafluoroisopropanol (HFIP) and incubated for 1 h at 37 ^{o}C. A white powder formed after evaporation of HFIP, which was lyophilized overnight then dissolved 1:1 in 2 mM NaOH and in PBS (100 mM, 300 mM NaCl, pH 7.4). The sample was then centrifuged for 20 min at 13,000 rpm.

8.2.2 Thioflavin T Fluorescence (ThT)

Assembly of $A\beta_{1-40}$ into fibrils was monitored by a ThT binding assay. [372] To characterize various intermediate structures in the aggregation pathway, fibril samples from monomeric $A\beta_{1-40}$ (40 μM) were aged at 37 °C under periodic agitation. The fibrillization process was tracked using a discontinous assay in which samples were removed at various time intervals and analyzed using ThT fluoresence. In this assay, the fluorescence intensity is proportional to the amount of amyloid or amyloid-like aggregates that form. [373] At various time intervals, a 10 μL sample of $A\beta_{1-40}$ was mixed with 10 μL of ThT (100 μM in water) and diluted

20-fold in PBS (180 µL). Fluorescence spectra were acquired in a low-binding, 96-well plate with a transparent bottom (Corning, Inc.) using a BMG LabTech plate reader with excitation wavelength at 440 nm and emission at 480 nm. The fluorescence intensity of the blank PBS solution was acquired for subtraction of background fluorescence of measurements.

8.2.3 AFM Sample Preparation

A 10 µL sample of monomeric $A\beta_{1-40}$ in PBS buffer (50 mM, 150 mM, NaCl, pH 7.4) was diluted two-fold and deposited onto the surface of freshly cleaved mica(0001) for 10 min. The excess sample left on the mica surface was carefully removed by wicking onto a tissue. The samples were washed three times with 40 µL deionized water to remove buffer salts and unbound peptides and then dried for 10 min.

8.2.4 Atomic Force Microscopy

An Agilent 5500 AFM equipped with PicoScan v5.3.3 software was used for surface characterization of Aβ samples (Agilent Technologies AFM, Inc. Chandler, AZ). The scanner has a maximum scan range of 10×10 µm. Tapping-mode AFM probes (NSL-20) were obtained from Nanoworld Holdings AG (Schaffhausen, Switzerland). The probes had an average force constant of 48 N/m and were driven to oscillate at 185 ± 10 kHz for AFM imaging.

8.3 Results

Thioflavin T is a reagent that becomes strongly fluorescent upon binding to amyloid fibrils and is generally considered to be a standard test which is diagnostic of the growth of Aβ fibrils. [373] The changes in ThT fluorescence for samples of $A\beta_{1-40}$ that were extracted at various time points during a 90 day incubation period are plotted in Figure 8.1. The growth curve is consistent with previous studies of $A\beta_{1-40}$ and other peptides. [374] The increase in ThT

fluorescence signifies that amyloid fibrils have formed, however the size, morphology and organization of intermediate structures that are present at various times cannot be fully determined from the ThT assay. Thus, simultaneous sample aliquots were deposited onto mica(0001) substrates for *ex situ* characterizations with AFM.

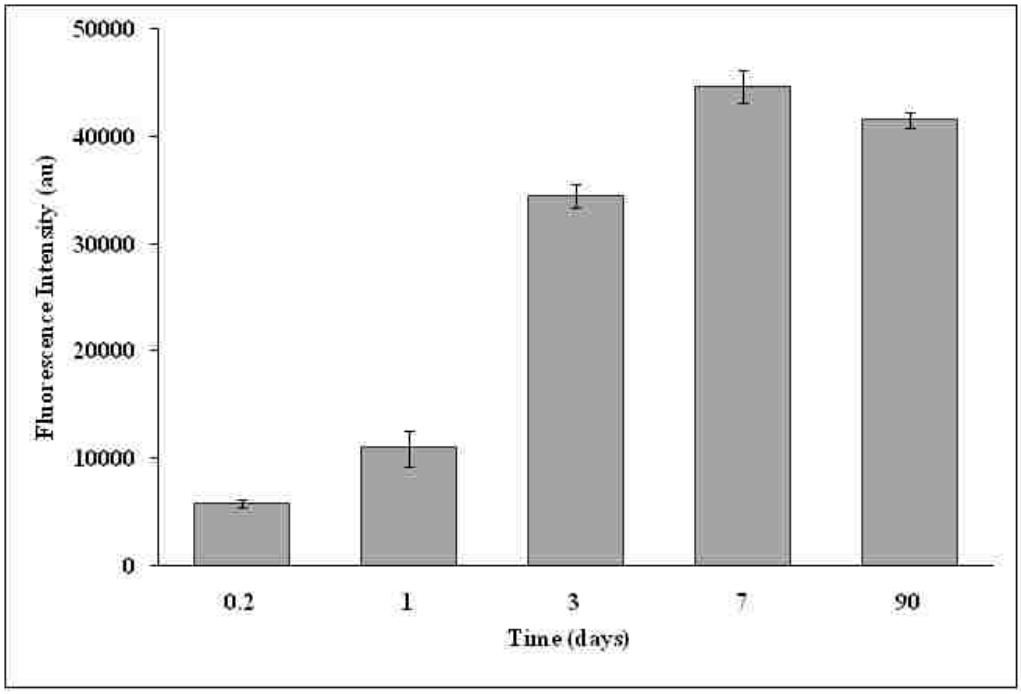

Figure 8.1. Fluorescence intensity (ThT) for $A\beta_{1-40}$ peptide obtained at different intervals of sample incubation.

A side-by-side overview of the successive growth stages of $A\beta_{1-40}$ is shown with representative tapping-mode topographs in Figures 8.2 and 8.3. At any particular time point viewed within AFM frames, multiple stages of fibrillogenesis are evident, since samples were not dialyzed or size-sorted to select certain events or morphologies. Spherical particles, described previously as oligomers are the main structures formed at the early stage (~ 5 h) of $A\beta_{1-40}$ assembly, and are considered to be the nucleus or seed for growth of protofibrils (Figures 8.2A

and 8.2A'). The mean heights of the spherical particles are 3.6±1.4 nm, measured from multiple cursor profiles (*n*=100) across individual nanostructures. The smallest beads measured 1.5 nm while the largest particles measured 4.2 nm in height. The heights and shapes of the spherical particles are consistent with nanostructures previously observed during the early hours of $A\beta_{1-40}$ fibrillogenesis, the smallest particles are monomers, dimers and trimers which form nucleation sites for the growth of protofibrils. [375] Within the zoom-in view of Figure 8.2A' there are a few areas with greater size and heights, indicated by the bright spots. Cursor line profiles are shown across a row of the smaller nanoparticles with a red line (top) indicating sizes ranging from 1 to 6 nm within this frame. The taller nanoparticles have heights ranging from 10 to 12 nm for the line profile at the bottom (black line), however heights as tall as 16 nm for the protofibrils are apparent within the topography frame. It has previously been shown that for the initial steps of forming protofibrils, growth of protofibrils can be detected in vertical direction from the sample plane. [367] After one full day of aging, the small oligomers were observed to grow in height and length (Figures 8.2B and 8.2B'), and spherical nanoparticles are still present. Within Figure 8.2B, the length of the protofibrils measured from 50 to 600 nm at this time point, and these values are representative of the dimensions measured for other frames from the same sample. A representative cursor measurement for one of the longer protofibrils reveals a length of 600 nm, (red line trace in Figure 8.2B') with three branch junctions of 2 nm height spaced at approximate intervals of 200 nm. A second cursor line (black line trace in Figure 8.2B') across the length of the type II fibril shows a height of 5.5 nm. The average values of the dimensions of the short protofibrillar structures for this time interval exhibit an average of 4.7±1.9 nm for heights, and length of 603±120, which is consistent with previous reports for type I fibrils. [357, 376]

After 3 days, immature fibrils of longer length and greater thickness were observed (Figures 8.2C and 8.2C') and a few sparse, spherical seed particles are still present. Two types of fibrils are apparent in the AFM images, thinner rods without branch points and junctions are

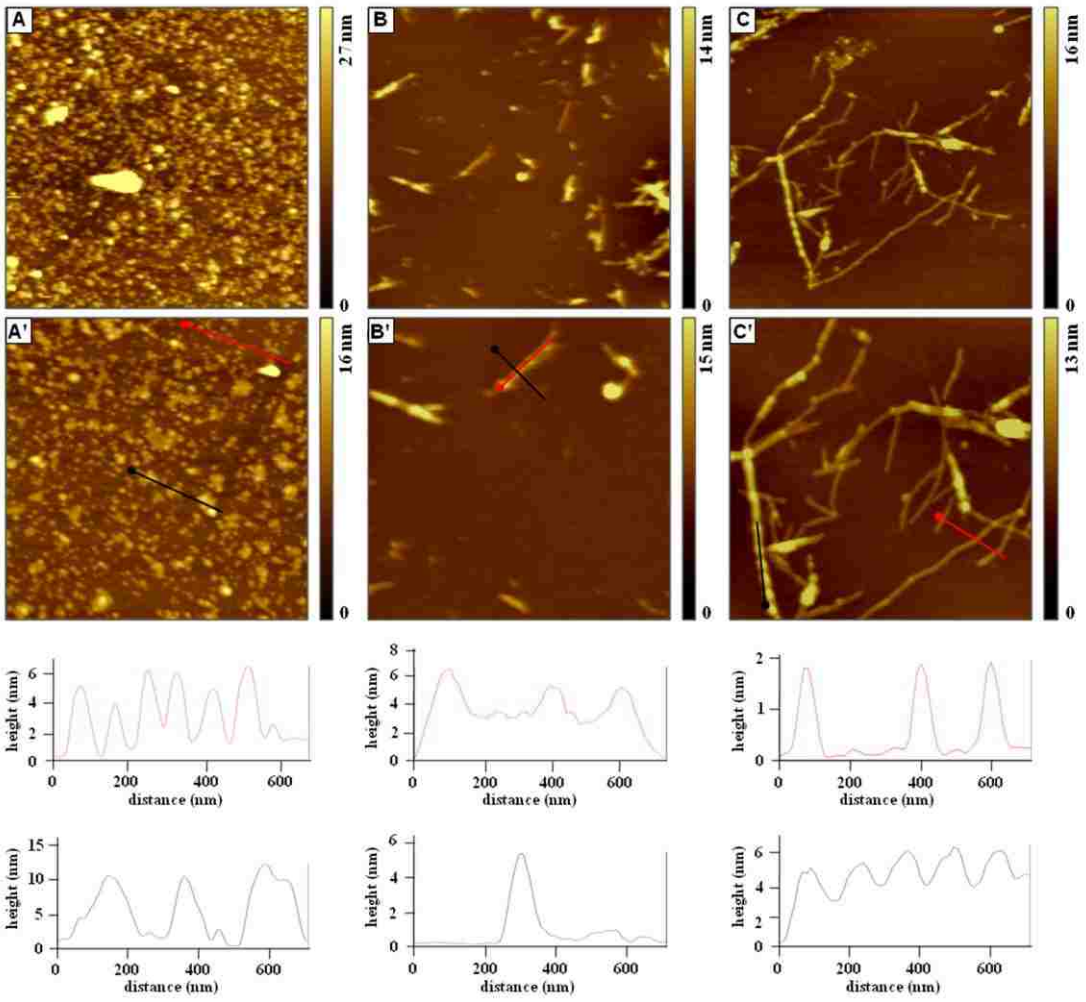

Figure 8.2. Time-lapse AFM images of the successive changes in morphology during the early phases of the growth of $A\beta_{1\text{-}40}$ fibrils obtained *ex situ*. Tapping-mode topographs obtained at **A, A':** 0.2 days; **B,B':** 1 days; **C,C':** 3 days. Upper frames show a representative 5 x 5 μm^2 area, the lower panels are high magnification views (2 x 2 μm^2) with corresponding cursor line profiles, respectively.

referred to as type I fibrils or protofibrils, and are identified by diameters of 6-13 nm. [377] Over time, the fibrils self-associate and become intertwined to form thicker braided structures, with

multiple branch points and junctions. The mature, braided fibril assemblies (with diameters of 8.5 nm) are refered to as type II fibrils. [359] Within the wide area topograph, an assortment of type I and type II fibrils are present, with varied lengths and surface arrangements. The fibrils exhibit multiple branch points and junctions, and some of the type II fibrils have type I branches stemming from type II fibrils, which is consistent with observations from previous studies. [359] A zoom-in view is presented in Figure 8.2C', which more clearly displays the differences in fibril morphologies. A red line trace shown on the right of the figure spans across three type I fibrils, which have a regular diameter of only 2 nm. At the left of Figure 8.2C' is a type II fibril with a larger diameter, and the periodic 2 nm corrugation of the fibril surface is shown with a cursor trace along the length of the fibril (black line). The branches stemming from branch points at the ends of type II fibrils are often smaller in diameter, measuring 5.5±1.5 nm which is indicative of type I fibrils becoming braided into larger type II fibrils. Cursor measurements were selected for fibrils which are laying flat on the mica substrate, however some of the fibrils are piled together so that they do not touch the surface. Measurements of the protofibrils from several AFM topographs (*data not shown*) revealed an average length of 840±45 nm, which is in agreement with results reported from TEM measurements. [376]

A series of AFM images acquired at later stages of elongation and aggregation of $A\beta_{1\text{-}40}$ fibrils 7 days, 14 days and 150 days) are shown in Figure 8.3. After one week of incubation, (Figures 8.3A and 8.3A'), the fibrils have increased in surface density and span several microns in length (5.1±0.5 μm). The predominant structures are type I and II fibrils, however a few protofibrils and seed structures are also apparent. The average height of the fibrils overall measure 7.1±2.2 nm, corresponding to the diameter of type II fibrils. The fibrils are randomly

oriented (Figure 8.3A) and have begun coiling to form arcs and circular shapes. The zoom-in view of Figure 8.3A' shows a selected area in the upper right where lateral association of fibrils is observed for the intertwining of type I fibrils into braided bundles, and several Y junctions are also evident within the selected frame. Cursor profiles were selected along the surface of the Aβ fibrils, to show the morphology differences of type I and II strands.

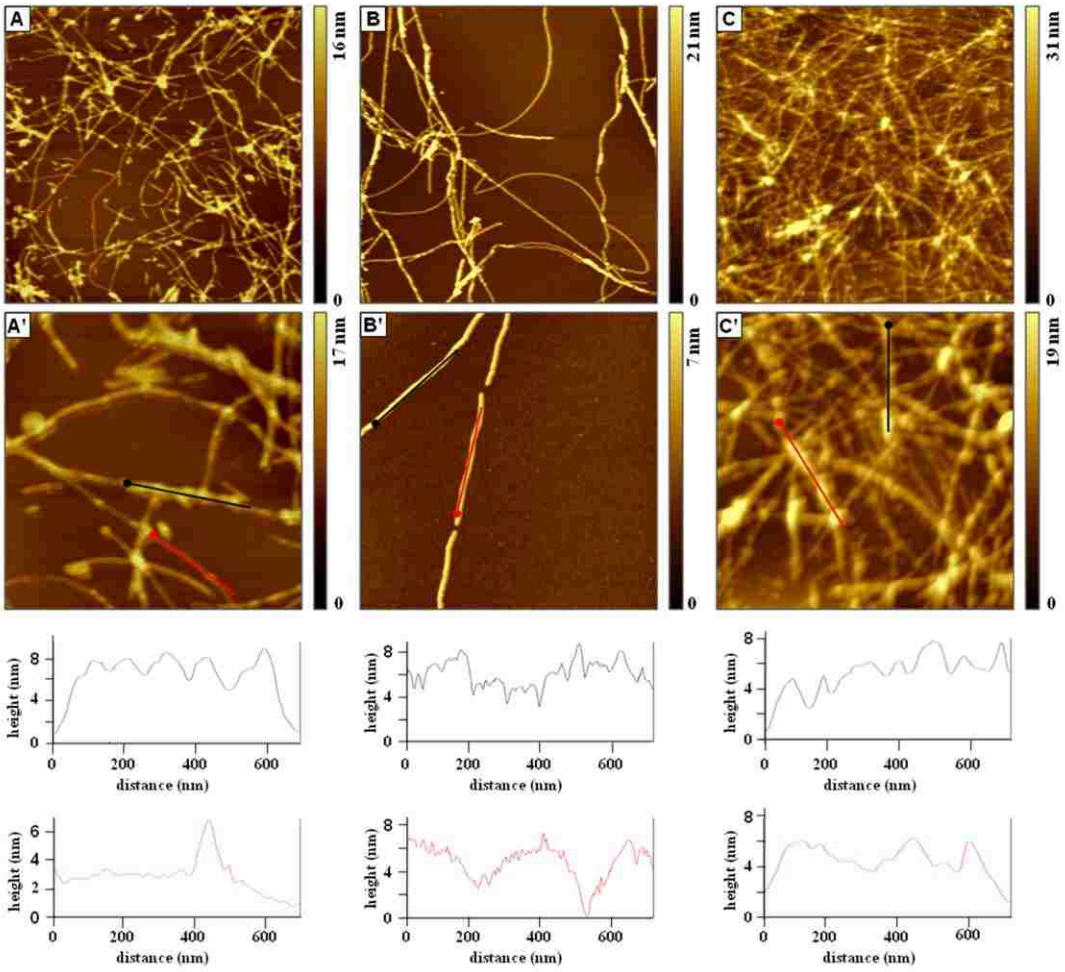

Figure 8.3. Changes in sample morphologies during the later stages of elongation and aggregation of $A\beta_{1\text{-}40}$ fibrils. Tapping-mode topographs and corresponding height profiles obtained after **A, A':** 7 days; **B,B':** 14 days; and **C,C':** 150 days. Upper frames show a representative 5 x 5 μm^2 area, the lower panels are high magnification views (2 x 2 μm^2) and cursor measurements, respectively.

The upper cursor line (black line) reveals a corrugation of ~ 2 nm, for the knot-like structures which are considered to be the sites of branches for type II fibrils. The second cursor line was acquired along the surface of a type I fibril, and exhibits a zig-zag profile with a much smaller periodicity, on the order of 1.0 nm. This corresponds to the helicity of the type I fibrils, as previously described. [364]

After 2 weeks of aging, the fibrils of $A\beta_{1-40}$ (Figures 8.3B and 8.3B') are elongated and continue to form branches spanning several microns in length. Both type I and type II fibrils are evident, however there are far fewer spherical particles and protofibrils than at previous time points. The high magnification AFM image (2 x 2 μm^2) in Figure 8.3B' shows segments of type I fibrils that are closely aligned in an end-to-end association. Cursor line measurements were acquired along the backbone of the type I fibrils to more clearly view the morphology attributable to the helicity, showing a peak to valley dimension of approximately 1.5±0.5 nm. The average variation along the fibril axis has previously been reported as 1.6±0.3 nm. [364]

After extended incubation for 5 months, the samples were examined to investigate changes in size, morphology or surface arrangement of fibrils, which has not been previously reported. An intricate arrangement of a mesh of fibril bundles and tangles was observed, shown in Figures 8.3C and 8.3C'. Most of the fibrils are type II, with an average diameter of 12±5.2 nm. The absolute lengths of the fibrils could not be accurately assessed, due to the limited range of the AFM scanner (10×10 μm), and also because shear forces from sample agitation could have shortened the fibrils. The zoom-in view of Figure 8.3C' reveals that the fibrils vary in thickness, and the arrangement of branch points and bundles appears to be random. The fibrils connect at multiple points to form a mesh, however AFM views cannot resolve whether the connections

between touching fibrils are chemically bonded or are a physical (non-bonded) association. Cursor measurements along the length of two thicker fibrils reveal an irregular periodicity of 1-2 nm, consistent with the braiding of type I fibrils to form type II strands, previously reported with a corregation of 1.6±0.3 nm. [364]

Additional zoom-in views were obtained to evaluate the size and morphologies of $A\beta_{1-40}$ structures at various stages of fibrillogenesis. A high magnification view (0.5 x 0.5 μm^2) for an $A\beta_{1-40}$ sample prepared after 5 hours shows spherical assemblies and aggregates (Figure 8.4) which correspond to nucleus or seed nanoparticles. In the topography frame, the heights of globular structures vary from 0.6 to 2.2 nm (Figure 8.4A). The simultaneously acquired phase image (Figure 8.4B) reveals the edges and shapes of the Aβ nanoparticles more clearly. Often phase images can more sensitively reveal fine ultrastructural details of surface morphology more clearly because the effects of size attenuation do not complicate phase images. The uniform color contrast observed for Aβ structures in the phase image indicates a consistent chemical composition, without contaminants. Phase images map the changes in the probe oscillation as it is scanned across the sample surface. Differences in softness and adhesion will exhibit changes in color contrast in the phase images. Therefore, the structures in Figure 8.4B are likely comprised of the same chemical material. Mapping the positions of particles between the topography and phase images, the larger bright nanoparticles consist of clusters of 2-3 smaller nanoparticles, the shapes of the clusters are clearly outlined in the phase channel. For the larger bright areas of Figure 8.4A, what may appear to be a single spot or nanostructures in the topography frame is more clearly elucidated as a cluster of several smaller seeds in the phase frame. A few circled areas are mapped as examples of the detailed fine structures. A

representative cursor line profile shown in Figure 8.4C displays the range of heights for the seed nanoparticles. The histogram of Figure 8.4D was acquired with individual cursor measurements of each nanoparticle in Figure 8.4A, showing that most of the seeds have a diameter of 1 ± 0.4 nm. The presence of spherical beads is an indication that initial stages of $A\beta_{1\text{-}40}$ assembly form with a nucleation step, consistent with a nucleation-dependent polymerization mechanism. [355, 357]

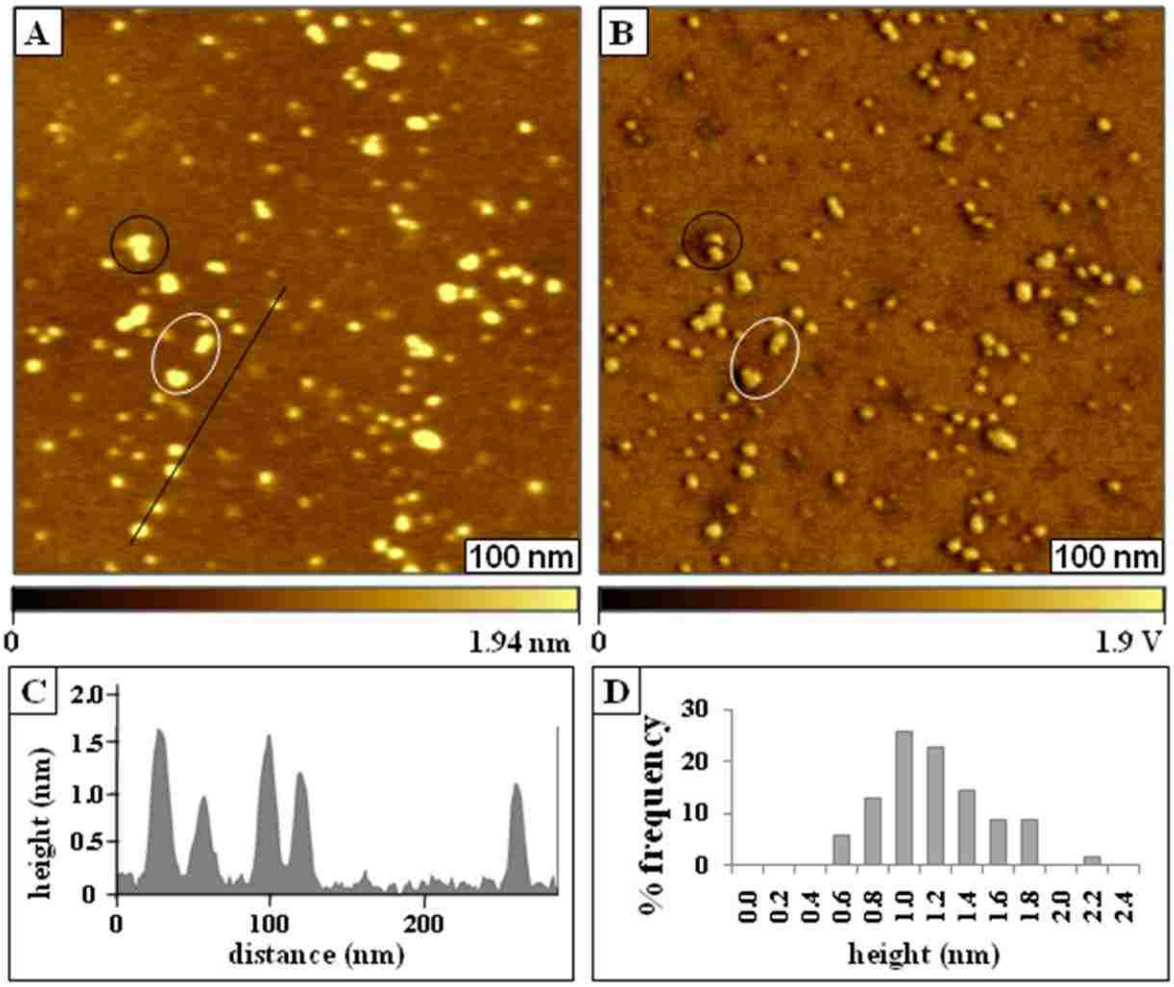

Figure 8.4. High magnification views of Aβ1-40 nuclei or seed nanostructures (500 x 500 nm2) after t = 5 h. A: Topography frame; B: simultaneously acquired phase image; C: representative cursor profile for the line in A; D: height histogram for A.

Zoom-in topographs for $A\beta_{1\text{-}40}$ fibrils after 1 and 2 weeks are displayed in Figure 8.5A and 5B, respectively. The topography frame in Figure 8.5A shows both types of fibrils are present after one week, however with shorter lengths and diameters. A few seed particles can also be detected and the background also shows faint outlines of short protofibril structures. The fibrils are relatively short and straight, with several branchpoints of type I fibrils extending from type II junctions, where the intertwining of fibrils is apparent. A striking feature captured after 2 weeks aging, reveals the end-to-end orientation of type I fibrils which provides insight to the process of fibril elongation through addition of linear fragments to ends of the fibrils (Figure 8.5B). The diameter of fibril measures 3.2 nm, shown with a cursor line profile in Figure 8.3C, consistent with the expected dimensions for a type I fibril.

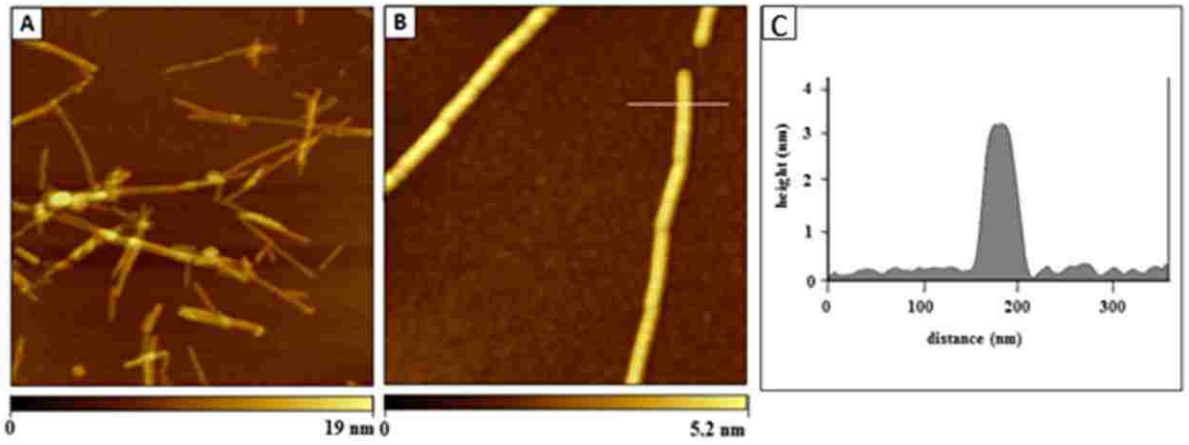

Figure 8.5. High magnification views of Aβ1-40 nanostructures (1 x 1 μm2). A: t = 7 days; B: t = 14 days; C: cursor plot for the line in B.

Additional zoom-in views for $A\beta_{1\text{-}40}$ fibrils formed after 5 months aging are displayed in Figure 8.6, characterized using *ex-situ* AFM. A few areas with protofibrils and seeds are visible on the mica surface, however for the most part the topography frames are dominated by thicker,

type II fibrils with multiple branches. As more time has elapsed, the $A\beta_{1-40}$ fibrils are arranged closely in dense bundles and assemblies. A zoom-in view of Figure 8.6A is presented in Figure 8.6B, which shows three bright fibril segments in the central area of the frames that serve as prominent landmarks for the magnified view. On the right side of the frames a bundle of 5-6 individual fibrils aligned in a side-by-side parallel arrangement is revealed. The side-by-side association of fibrils is likely an initial step to the intertwining and braiding/weaving of fibrils. A different area was selected in Figure 8.6C, cursor measurements would not be insightful for the dimensions of the densely-packed piles of fibrils, since many of the segments of the mesh-like arrangement are not touching the surface. The branching has become more complex and intricate with points of 3 or more branches extending from fibril junctions. A periodic corrugation is exhibited along the length of the thicker type II fibrils, with many local areas of knot-like interconnections woven together.

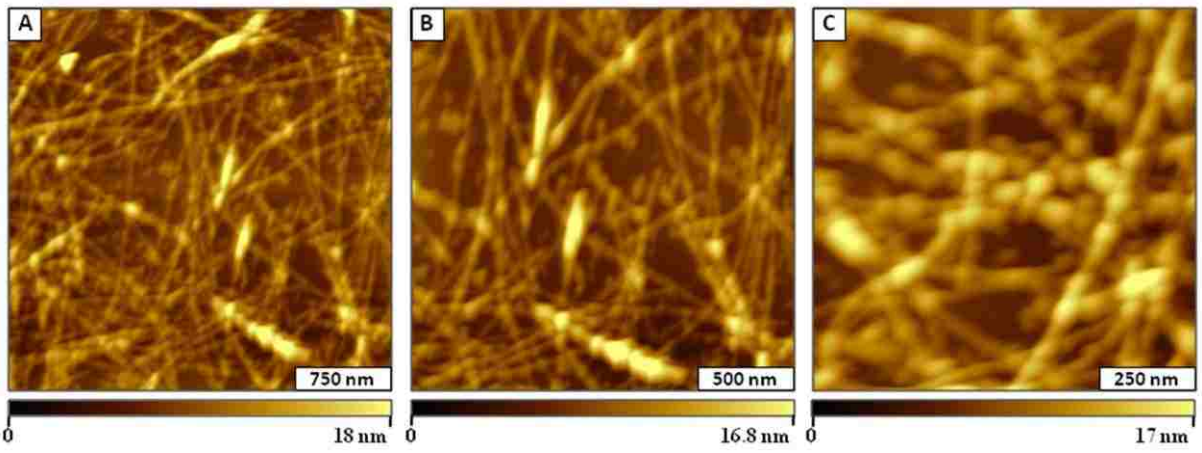

Figure 8.6. Bundles of $A\beta_{1-40}$ fibrils observed after 150 days. Successive zoom-in AFM topographic views for **A:** 3 x 3 μm^2 **B:** 2 x 2 μm^2 **C:** 1 x 1 μm^2 scan areas.

Phases of the progressive growth and evolution of *in vitro* fibrillogenesis of $A\beta_{1-40}$ can be distinctly characterized with successive increases in the diameter and length of nano- and

microstructures. Average measurements obtained from AFM topographs are summarized in Table 8.2, with the qualification that at each time point the dominant surface structures were not isolated. Seed nanoparticles, protofibrils and fibrils of varied diameters were observed at each selected time point. For the most part, the length and heights of surface structures progressively increased throughout the time course of $A\beta_{1\text{-}40}$ incubation.

Table 8.2. Average lengths and heights of amyloid beta after different incubation intervals, obtained with AFM cursor measurements.

time (days)	**Fibril length (± SD, nm)**	**Fibril height (± SD, nm)**	**Predominant surface structures**
$t \sim 0.2$ (5 h)	30 ± 5	3.6 ± 1.4	seeds (nuclei)
$t = 1$	600 ± 120	4.7 ± 1.9	protofibrils
$t = 3$	840 ± 45	5.5 ± 1.5	immature (type I) fibrils
$t = 7$	5100 ± 500	7.1 ± 2.2	mature (type II) fibrils
$t = 14$	6200 ± 700	7.2 ± 2.2	mature (type II) fibrils
$t = 150$	4200 ± 330	12 ± 5.2	bundles of (type II) fibrils

8.4 Discussion

The processes of peptide self-aggregation and fibrillogenesis of $A\beta_{1\text{-}40}$ follows a nucleation-dependent polymerization pathway, forming nuclei and seed nanoparticles as the initial step. Additions of $A\beta_{1\text{-}40}$ monomers lead to the evolution of protofibrils and fibrillar nanostructures. At various time points, seed nuclei, protofibrils and fibrils are apparent, and growth of fibrils arises from different types of addition steps. Self-association, annealing of protofibril ends, lateral association of protofibrils and addition of dimers or protofibrils contribute to the elongation, branching and intertwining of fibrils. [376] Aggregation of Aβ peptides to form mature fibrils has been attributed to interactions of their hydrophobic regions, and

hydrogen bonding between two accessible "faces" of Aβ sheets also enables fibrillization. The results summarized in Table 2 provide further insight and details of the growth of $A\beta_{1-40}$ fibrils, as well as the secondary organization of fibrils after an extended period of 5 months.

Two growth models have been reported for Aβ fibrillogenesis, a process of elongation and direct fibril-protofibril association. [367] Elongation occurs by deposition of monomers onto protofibils, and is reported to occur at both ends of fibrils. *In vitro* growth conditions for Aβ, such as ionic strength, pH, temperature, and agitation have been shown to significantly influence the morphology and kinetics of fibrillogenesis. [378, 379] For example, in the absence of NaCl, growth was observed to occur at a very slow rate or not at all. [380] In the absence of agitation, as well as when different Aβ peptide concentrations or buffer conditions are used during incubation, significant differences in the time course of fibrillogenesis are observed. For example the growth of Aβ fibrils was accelerated by shaking or agitating the solutions during incubation. [381] The capability of AFM for continuously monitoring the growth and changes in morphology for individual fibrils provides distinct analytical advantages over electron microscopy methods which entail extensive sample pretreatment with metal stains and require maintaining vacuum environments for imaging.

8.5 Conclusions

Characterizations using AFM are becoming indispensible for elucidating and tracking the evolution of biological nanostructures such as insoluble protein aggregates and amyloid beta fibrils during time-dependent studies. For this report, sequences of structural changes were viewed with time-lapse images for $A\beta_{1-40}$ seed nanostructures, protofibrils and fibrils, accomplished *ex situ* using tapping-mode AFM. The different stages of the incubation time were

monitored for growth periods up to 5 months and provide a useful frame of reference for future studies with other peptides and modifications. The assembly stages of fibrils formation follows a pathway starting with seed nanoparticles, protofibrils and the development of mature fibrils. The mature fibrils displayed structures spanning into microns in length and eventually densely branched network assemblies. Typically, amyloid aggregates have been shown to exhibit structural polymorphisms. After 5 months incubation, secondary organization and interweaving of mature fibrils produced bundles and a mesh of interconnected $A\beta_{1\text{-}40}$ fibrils.

CHAPTER 9. CONCLUSIONS AND FUTURE PROSPECTUS

9.1 Conclusions

Perhaps the greatest accomplishment of SPM-based characterizations is the capability to visualize nanomaterials and characterize properties with sensitivity at the level of individual nanoparticles or molecules. Beyond the commercial goals of nanotechnology, SPM-based methods have become indispensible for fundamental investigations of the interrelations between chemical structure and properties of nanomaterials. Further innovations for SPM characterizations as well as new methods for nanolithography will continue to be advanced in the future, contributing to discoveries for biotechnology, molecular electronics, engineered materials, and chemical/biochemical sensors.

Sample characterizations using MSM-AFM were demonstrated for molecular systems of cobalt-functionalized porphyrins, arrays of ring nanopatterns of nanoparticles, and ionic liquid nanoGUMBOS. With MSM-AFM, nanomaterials with magnetic or superparamagnetic properties respond to the flux of an applied electromagnetic field. Parameters of the frequency and field strength of the AC field can be selected, and changes in sample motion are sensitively detected using a lock in amplifier. Small changes in amplitude and phase components of the periodic oscillation of samples are tracked and used to construct MSM amplitude and phase images. New protocols were developed for *in situ* measurements, in which dynamic parameters of the driving frequencies and electromagnetic field were captured in images. Changes in the MSM-AFM channels reveal variation in the magnitude of vibration of the samples. With AFM, a cantilever can be precisely placed on a single nanoparticle or nanocrystal while incrementally changing the field strength. Reproducible mechanical signatures were observed in the amplitude signal for a

single nanocrystal of metalloporphyrin. The magnitude of the changes in the amplitude response corresponds to physical displacement of the cantilever. The new MSM imaging mode provides greater sensitivity than current scanning probe methods for magnetic measurements at the level of individual nanoparticles or nanocrystals.

9.2 Future Prospectus

The MSM-AFM imaging approach provides a new magnetic spectroscopy for evaluating and viewing samples with superparamagnetic character, with exceptional sensitivity and selectivity. By precisely placing the cantilever on a single nanoparticle or nanocrystal vibrational response information can be correlated to the size and composition of nanomaterials.

Characterizations of nanomaterials using MSM-AFM will provide nanoscale information of magnetic phenomena. To advance towards quantitative measurements for magnetic materials using MSM-AFM will require an understanding in the contributions of elasticity, surface adhesion and mass of nanomaterials. Further experiments are planned to compare the physical displacement of the nanomaterials and spectra obtained for magnetic materials at various field strengths using systematically designed test platforms with scalable differences in size and composition. Frequency studies of individual nanostructures actuated with MSM-AFM will be investigated to evaluate shifts or broadening of spectral peaks.

The choice of focusing research efforts on model systems of porphyrins and phthalocyanines is highly practical, because of the associated electrical, optical and chemical properties of these functional classes of molecules. Porphyrin,[382-387] phthalocyanines,[388-390] metallocyanine and metalloporphyrin systems are excellent materials for molecular electronics, due to their diverse structural motifs and associated electrical, optical and chemical properties,

and thermal stability. At a basic level, electronic properties are controlled by the degree of π delocalization.[391] Porphyrins and phthalocyanines can be organized into supramolecular arrays, aggregates and crystals with diverse functions. The rigid planar structures and π-conjugated backbones of porphyrins convey robust electrical characteristics. The architecture of porphyrins has been proposed as viable for electronic components for molecular-based information-storage devices,[392-395] gas sensors,[396, 397] photovoltaic cells,[398, 399] organic light-emitting diodes,[400-403] and molecular wires.[404-406]

9.2.1 Preliminary Studies Using Conductive Probe AFM with Cobaltacarborane Porphyrins

Scanning probe characterizations are becoming prevalent for molecular electronics investigations. For comparing molecular conductance, a particular problem is presented for reproducibility at the nanoscale. The discrepancies when comparing the various measurements is most likely attributable to variations in the orientation of molecules on surfaces. The surface orientation of molecules is known to affect the conductive properties of pi-conjugated systems, and has been corroborated by molecular mechanics calculations. Geometric considerations such as molecular coupling to the substrate, the angle of molecular orbitals relative to the surface, distance/proximity effects due to the tilt of the molecular backbone, as well as lateral intermolecular interactions have been implicated to have a causal role for conductance measurements at the molecular level.[407-414]

Films of porphyrins have been characterized previously with UHV-STM studies using surfaces such as silver,[412, 415, 416] copper,[417, 418] gold[419-424] and graphite.[425-429] Our initial investigations have focused on I-V measurements with porphyrins containing different substituents. Different solvents, surfaces, and concentration parameters were systematically

evaluated to determine how these parameters affect the surface assembly of porphyrins. Our investigations reveal that for preparing samples of porphyrins the drying step largely determines the resulting surface structures. During the drying process, the strong convective forces during solvent evaporation pull porphyrins together to produce “stacks” or columnar structures of porphyrins.

Investigations with conductive probe AFM (CP-AFM) were used to characterize the surface morphology and map the conductive domains of cobaltacarborane porphyrins prepared on Au(111) conductive films. A comparison of the surface morphologies for cobaltacarborane porphyrins deposited on mica (0001), Au(111) was accomplished with nanoscale resolution. Examples of characterizations using CP-AFM for samples of cobaltacarborane porphyrins are presented in Figure 9.1. Characteristic shapes of Au(111) terrace domains can be resolved in the topography frame (Figure 9.1A). However these features cannot be resolved in the simultaneously acquired lateral force and current frames. The stacks of cobaltacarborane porphyrin with almost uniform round domains exhibit lateral dimensions ranging from 120 to 260 nm (Figure 9.1A).

Current images which are typically acquired simultaneously with topography are generated by applying a bias voltage to a conductive or semiconductive surface. A conductive AFM probe is then brought into contact with the cobaltacarborane stacks and the current produced is used to construct the current image. The current map in Figure 9.1C was acquired by applying -1.0 V bias to the sample and using a pre-amp within the scanner nosecone to sensitively detect the current flowing through the sample. Within the current image, cobaltacarborane porphyrins display bright contrast indicating that the surface structures are

more conductive than the bare Au(111) substrate. The stacks of porphyrins have heights corresponding to multiple layers of porphyrin molecules, arranged in a coplanar configuration. The stacks are mainly located at the edges of Au(111) steps.

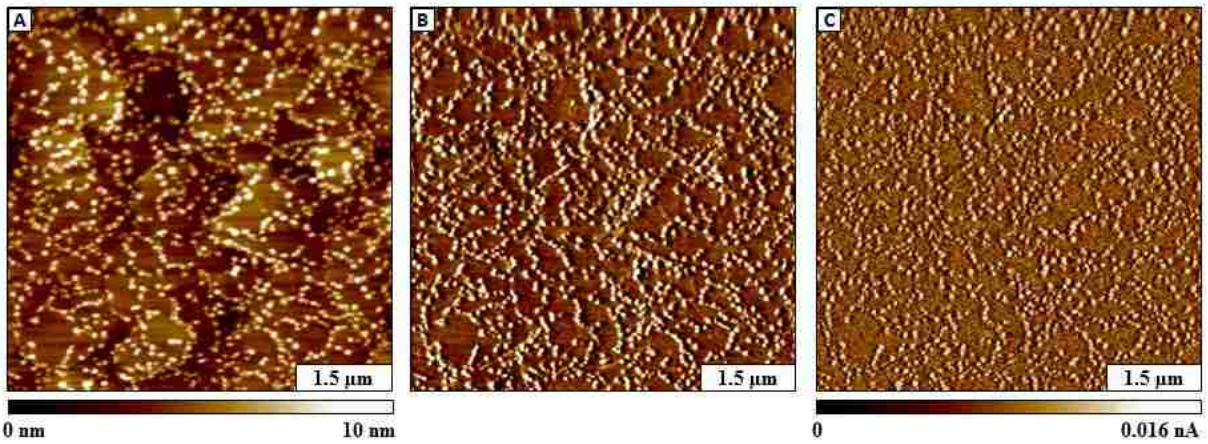

Figure 9.1. Characterization of octa-substituted cobaltacarborane porphyrins using CP-AFM acquired with a sample bias of -1 V. (A) Topography image of a wide area; B) corresponding lateral force view; C) simultaneously acquired current image.

Previously, it has been reported that charge densities are higher at the step edges of Au(111). Porphyrins deposit preferentially at the step edges for samples that were dried in ambient conditions. Round stacks with multilayers of porphyrins results from noncovalent π-π stacking interactions between the porphyrin macrocycles. Most of the porphyrin stacks (~90%) on Au(111) formed heights measuring 3–5 nm, which corresponds to a double layer, the remaining ~10 % have a thickness corresponding to either a single or triple layer.

Current-voltage (I-V) plots for cobaltacarborane porphyrins were acquired at specific sites within the images, and a representative profile is displayed in Figure 9.2. The porphyrin stacks displayed conductivity throughout the range of -0.4 to +0.8 V. The onset of current conduction was observed to occur at +0.2 V in the positive sweep, and at ~-0.05V for the negative bias direction. There is an asymmetric response for the cobaltacarborane sample; an

overlay of the forward and reverse sweeps shows considerable hysteresis, with a nearly linear I-V trend in the positive sweep, and an exponential profile for the negative bias direction.

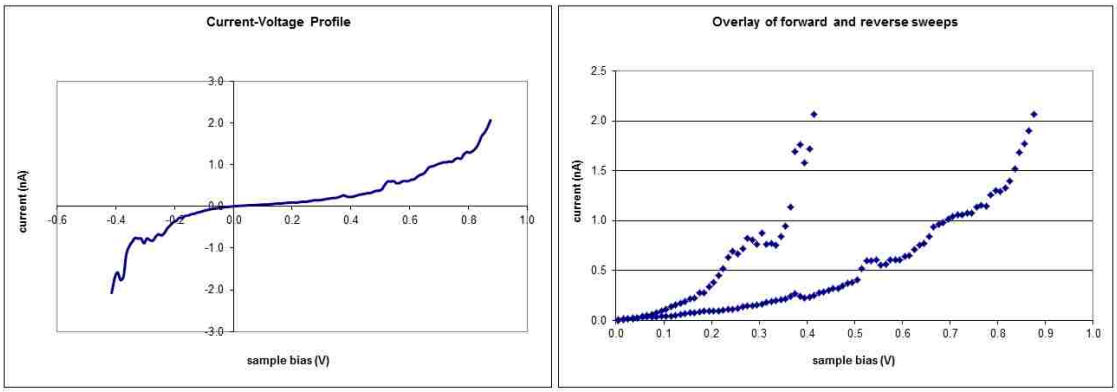

Figure 9.2. Current-Voltage profile and an overlay of forward and reverse sweeps for octa-substituted cobaltacarborane porphyrin prepared on Au(111).

A considerable challenge is posed for developing effective, reproducible methods for measurements in nanosized systems, for scaling molecular electronic devices to nanometer length scales, and for systematically evaluating the effects of molecular structure on electrical properties. The function and efficiency of porphyrins in devices is largely attributable to how the molecules are organized on surfaces. Understanding how the self-organization and surface assembly influence electrical properties is critical for optimizing the function of these molecules in device applications. Accurate and precise electronic property measurements will shed insight on the fundamental mechanisms that give rise to properties such as resistance and rectification with changes in chemical structure. Although systematic studies of the electronic properties of a range of porphyrin architectures have been conducted for a variety of coordinated metals and surfaces, there have been no reports which add the dynamic parameter of an externally applied electromagnetic field, which will be particularly relevant for systems with coordinated magnetic atoms.

9.2.2 Preliminary Studies with Cobaltacarborane Porphyrins Using IMM-AFM

Beyond electrical measurements, characterizations with AFM and STM also furnish high-resolution views of the local morphology of molecular films and nanostructures, to enable assessment of sample quality. Crystalline nanostructures of cobaltacarborane porphyrins formed after several months of incubation in solution, as shown in Figure 9.3. Nanocrystals (needles) deposited on mica were characterized using indirect magnetic modulation (IMM-AFM). For IMM-AFM studies, the tip is operated in contact mode, and is actuated indirectly by a magnetic nosecone which responds to the magnetic field of the sample stage. Some of the porphyrin needles exhibit spiral geometries as shown in the topography (Figure 9.3A and Figure 9.3D) and lateral force frames. The lengths of the needle structures range from 0.2 to 2 μm (average cursor measurement of 100 crystals), with regular diameters measuring 1.0 nm.

A key strategy for future studies will be to apply nanoscale lithographies to generate molecular test platforms of well-defined composition, orientation and dimension for molecular assemblies of porphyrins. Well-defined nanopatterns will provide reproducibility for the molecular orientation, packing density and nanostructure dimensions for multiple successive measurements of conductive and magnetic properties. Our research group has considerable expertise with AFM characterizations and lithography for various nanomaterials,[41, 430-435] with developing unique capabilities for preparing designed test platforms with tailorable dimensions and arrangements of molecules. Planned experiments will uncover rich structural information and mechanisms of surface assembly, applying the tools of high-resolution scanning probe

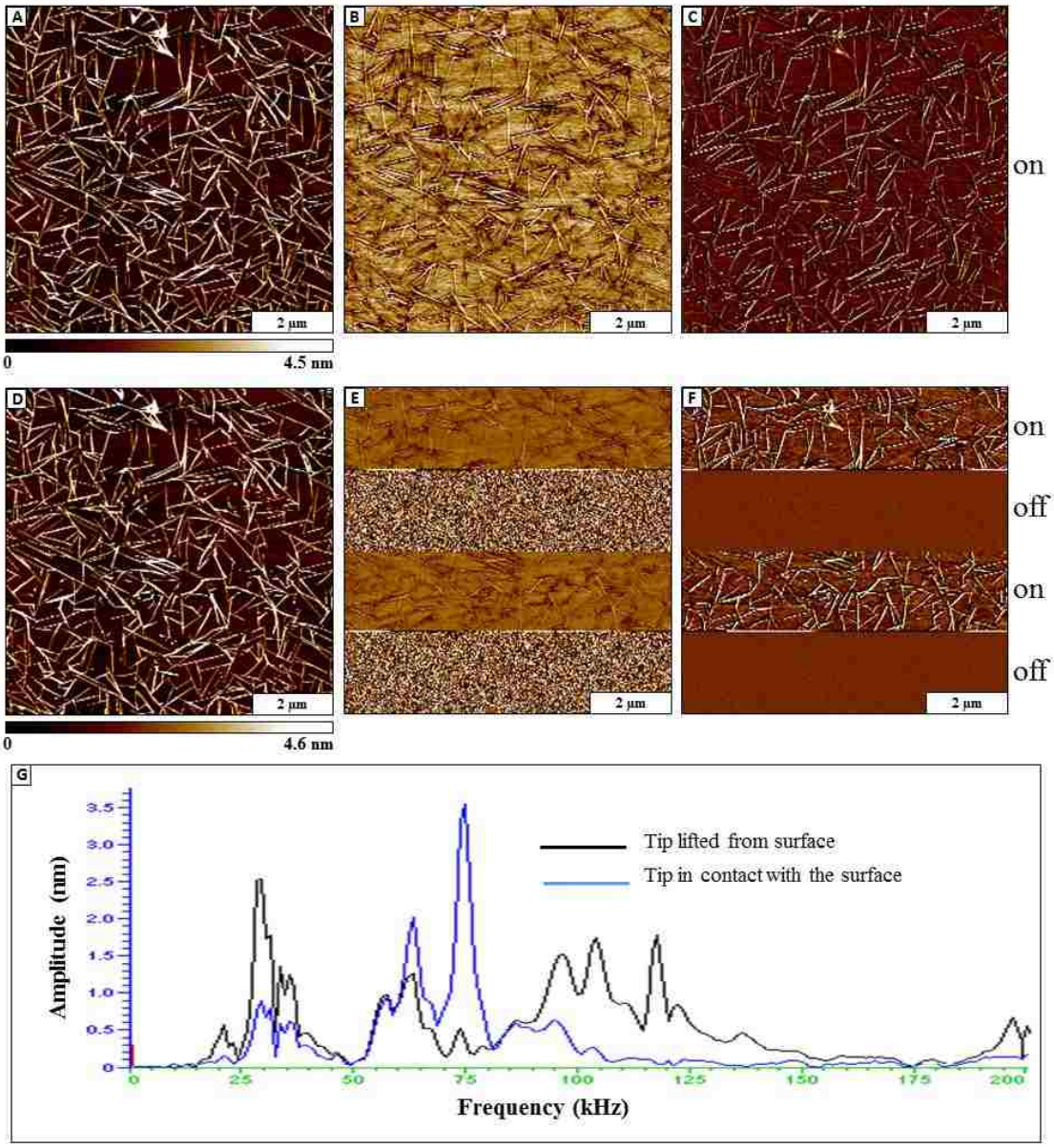

Figure 9.3. Characterization of porphyrin nanocrystals using IMM-AFM. The top row (A, B, C) images were acquired with the magnetic field switched on. Magnetic field was turned on for C, D, F (first and third quarter frame) and switched off to generate second and furth quarter frame. G) Frequency spectra for IMM acquired with the tip engaged or removed from the surface.

microscopy, photoemission spectroscopy and other spectroscopies (FTIR, EXAFS). Using nanofabrication, the orientation of porphyrin molecules can be altered by changing the self-

assembly pathway with spatial confinement.[436, 437] Porphyrins and phthalocyanines provide excellent model systems for conductance measurements as well as for studies of surface assembly pathways with *in situ* AFM. Future directions for this research will be to continue to develop lithography methods with porphyrins and phthalocyanines to generate nanoscale test structures for ultrasensitive and reproducible measurements of conductive and magnetic properties. The objective is to discover new information at the nanoscale about the molecules to be investigated, targeting related architectures of porphyrins and phthalocyanines which manifest photonic and/or photovoltaic properties. Reliable measurements of conductive properties when these molecules are coordinated to different metals will provide information for predictive modeling of current transport.

For IMM-AFM studies, a resonance frequency of 75 kHz and field strength of measuring ~0.18 T was applied to the tip-sample contact (Figure 9.3G). Porphyrin nanostructures are well resolved in both amplitude and phase IMM channels with the field turned on during the entire scan (Figures 9.3A,B,C). The IMM-AFM images of the bottom row (Figure 9.3D,E,F) were obtained in contact mode AFM image by alternating the magnetic field between on and off. With the field on (first and third frame) the entire nosecone assembly and tip are actuated, revealing structural details of the needle structures in both IMM-AFM amplitude and phase channels (Figures 9.3E,F). However, when the oscillating magnetic field was turned off, the phase and amplitude views did not display contrast (second and fourth quarter). When the electromagnetic field was on, amplitude and phase channels sensitively displayed contrast differences between the nanocrystals of porphyrins and the bare areas of the mica surface. The amplitude and phase channels clearly reveal the locations and morphology of porphyrin needles, which demonstrates

the mapping capabilities of the IMM-AFM imaging mode. Essentially the phase lag of the vibrating nosecone assembly is compared to the driving AC signal using a lock-in amplifier and the difference between the two is used to provide selective mapping of nanostructures on the surface.

The frequency spectra for IMM-AFM acquired with tip placed in contact with the sample and when lifted from the surface show interesting changes in peak profiles. Certain peaks increase intensity, while other peaks are diminished and/or shift position. The cobaltacarborane sample material should also exhibit a vibrational response to the AC electromagnetic field, leading to complexity for interpreting the spectral changes. The most prominent peak at 75kHz when the tip was in contact with the surface was selected for IMM imaging (blue line).

9.3 Future Directions

Fundamental questions to be investigated with the future SPM experiments are the roles of molecular architecture, surface orientation, nanopattern geometries and intermolecular interactions for measurements of charge transport. Spatial confinement clearly affects molecular orientation, which influences electronic properties. Nanopatterning experiments provide capabilities for controlling the overall dimensions of nanostructures, as well as the surface density. The importance of coupling between adjacent molecules in molecular electronics has not been previously investigated, due to the difficulties of defining molecular assembly and geometric constraints. Conductive probe studies will be accomplished with different molecular designs and surface arrangements. It is likely that as the dimensions of nanopatterns become successively smaller, quantum effects may be detectable in I-V spectra. Fundamentally, the goals

are to elucidate the role of molecular structure, packing and orientation for electron tunneling, which are largely unknown.

BIBLIOGRAPHY

1. Liu, Y.; Male, K. B.; Bouvrette, P.; Luong, J. H. T., Control of the Size and Distribution of Gold Nanoparticles by Unmodified Cyclodextrins. *Chemistry of Materials* **2003,** 15, 4172-4180.

2. Puntes, V. F.; Gorostiza, P.; Aruguete, D. M.; Bastus, N. G.; Alivisatos, A. P., Collective Behaviour in Two-Dimensional Cobalt Nanoparticle Assemblies Observed by Magnetic Force Microscopy. *Nature Materials* **2004,** 3, 263-268.

3. Tesfai, A.; El-Zahab, B.; Kelley, A. T.; Li, M.; Garno, J. C.; Baker, G. A.; Warner, I. M., Magnetic and Nonmagnetic Nanoparticles from a Group of Uniform Materials Based on Organic Salts. *Acs Nano* **2009,** 3, (10), 3244-3250.

4. Li, J. R.; Garno, J. C., Elucidating the role of surface hydrolysis in preparing organosilane nanostructures via particle lithography. *Nano Letters* **2008,** 8, (7), 1916-1922.

5. Chen, J. X.; Liao, W. S.; Chen, X.; Yang, T. L.; Wark, S. E.; Son, D. H.; Batteas, J. D.; Cremer, P. S., Evaporation-Induced Assembly of Quantum Dots into Nanorings. *Acs Nano* **2009,** 3, (1), 173-180.

6. Yang, G. H.; Tan, L.; Yang, Y. Y.; Chen, S. W.; Liu, G. Y., Single electron tunneling and manipulation of nanoparticles on surfaces at room temperature. *Surface Science* **2005,** 589, (1-3), 129-138.

7. Grobelny, J.; Tsai, D. H.; Kim, D. I.; Pradeep, N.; Cook, R. F.; Zachariah, M. R., Mechanism of nanoparticle manipulation by scanning tunnelling microscopy. *Nanotechnology* **2006,** 17, (21), 5519-5524.

8. Lewandowski, B. R.; Kelley, A. T.; Singleton, R.; Li, J. R.; Lowry, M.; Warner, I. M.; Garno, J. C., Nanostructures of Cysteine-Coated CdS Nanoparticles Produced with "Two-Particle" Lithography. *Journal of Physical Chemistry C* **2009,** 113, (15), 5933-5940.

9. Terrill, R. H.; Postlethwaite, T. A.; Chen, C. H.; Poon, C. D.; Terzis, A.; Chen, A. D.; Hutchison, J. E.; Clark, M. R.; Wignall, G.; Londono, J. D.; Superfine, R.; Falvo, M.; Johnson, C. S.; Samulski, E. T.; Murray, R. W., Monolayers in three dimensions: NMR, SAXS, thermal, and electron hopping studies of alkanethiol stabilized gold clusters. *Journal of the American Chemical Society* **1995,** 117, (50), 12537-12548.

10. Garno, J. C.; Yang, Y. Y.; Amro, N. A.; Cruchon-Dupeyrat, S.; Chen, S. W.; Liu, G. Y., Precise positioning of nanoparticles on surfaces using scanning probe lithography. *Nano Letters.* **2003,** 3, (3), 389-395.

11. Li, J. R.; Lusker, K. L.; Yu, J. J.; Garno, J. C., Engineering the Spatial Selectivity of Surfaces at the Nanoscale Using Particle Lithography Combined with Vapor Deposition of Organosilanes. *Acs Nano* **2009,** 3, (7), 2023-2035.

12. Yang, D. Q.; Sacher, E., Platinum nanoparticle interaction with chemically modified highly oriented pyrolytic graphite surfaces. *Chemistry of Materials* **2006,** 18, (7), 1811-1816.

13. Todorovic, M.; Schultz, S.; Wong, J.; Scherer, A., Writing and reading of single magnetic domain per bit perpendicular patterned media. *Applied Physics Letters.* **1999,** 74, (17), 2516-2518.

14. Guyodo, Y.; Banerjee, S. K.; Penn, R. L.; Burleson, D.; Berauo, T. S.; Seda, T.; Solheid, P., Magnetic properties of synthetic six-line ferrihydrite nanoparticles. *Physics of the Earth and Planetary Interiors* **2006,** 154, (3-4), 222-233.

15. Darling, S. B.; Bader, S. D., A materials chemistry perspective on nanomagnetism. *Journal of Materials Chemistry* **2005,** 15, (39), 4189-4195.

16. Douglass, D. C.; Bucher, J. P.; Bloomfield, L. A., Magic Numbers in the Magnetic-Properties of Gadolinium Clusters. *Physical Review Letters* **1992,** 68, (11), 1774-1777.

17. Li, J.; Wang, Y. J.; Zou, B. S.; Wu, X. C.; Lin, J. G.; Guo, L.; Li, Q. S., Magnetic properties of nanostructured Mn oxide particles. *Applied Physcs Letters* **1997,** 70, (22), 3047-3049.

18. Daniels, S. L.; Ngunjiri, J. N.; Garno, J. C., Investigation of the magnetic properties of ferritin by AFM imaging with magnetic sample modulation. *Analytical and Bioanalytical Chemistry* **2009,** 394, (1), 215-223.

19. Paulo, A. S.; Garcia, R., Unifying theory of tapping-mode atomic-force microscopy. *Physical Review B* **2002,** 66, (4).

20. Bustamante, C.; Keller, D., Scanning force microscopy in biology *Physics Today* **1995,** 48, (12), 32-38.

21. Dunlap, D. D.; Maggi, A.; Soria, M. R.; Monaco, L., Nanoscopic structure of DNA condensed for gene delivery. *Nucleic Acids Research* **1997,** 25, (15), 3095-3101.

22. Lyubchenko, Y. L.; Shlyakhtenko, L. S., Visualization of supercoiled DNA with atomic force microscopy in situ. *Proceedings of the National Academy of Sciences of the United States of America* **1997,** 94, (2), 496-501.

23. Stark, M.; Moller, C.; Muller, D. J.; Guckenberger, R., From images to interactions: High-resolution phase imaging in tapping-mode atomic force microscopy. *Biophysical Journal* **2001,** 80, (6), 3009-3018.

24. Garcia, R.; Magerle, R.; Perez, R., Nanoscale compositional mapping with gentle forces. *Nature Materials* **2007,** 6, (6), 405-411.

25. Vie, V.; Giocondi, M. C.; Lesniewska, E.; Finot, E.; Goudonnet, J. P.; Le Grimellec, C., Tapping-mode atomic force microscopy on intact cells: optimal adjustment of tapping conditions by using the deflection signal. *Ultramicroscopy* **2000,** 82, (1-4), 279-288.

26. Junno, T.; Deppert, K.; Montelius, L.; Samuelson, L., Controlled manipulation of nanoparticles with an atomic-force microscope. *Applied Physics Letters* **1995,** 66, (26), 3627-3629.

27. Serem W, K.; Lusker K, L.; Garno J, C., Using Scanning Probe Microscopy to Characterize Nanoparticles and Nanocrystals. *Encyclopedia of Analytical Chemistry* **2010,** DOI: 10.1002/9780470027318.a9155.

28. Tesfai, A.; El-Zahab, B.; Bwambok, D. K.; Baker, G. A.; Fakayode, S. O.; Lowry, M.; Warner, I. M., Controllable formation of ionic liquid micro- and nanoparticles via a melt-emulsion-quench approach. *Nano Letters* **2008,** 8, (3), 897-901.

29. Serem, W. K.; Bett, C. K.; Ngunjiri, J. N.; Garno, J. C., Studies of the Growth, Evolution, and Self-Aggregation of beta-Amyloid Fibrils Using Tapping-Mode Atomic Force Microscopy. *Microscopy Research and Technique* **2011,** 74, (7), 699-708.

30. Binnig, G.; Rohrer, H.; Gerber, C.; Weibel, E., Tunneling through a controllable vacuum gap. *Applied Physics Letters* **1982,** 40, (2), 178-180.

31. Binnig, G.; Quate, C. F.; Gerber, C., Atomic force microscope. *Physical Review Letters* **1986,** 56, (9), 930-933.

32. Lauritsen, J. V.; Reichling, M., Atomic resolution non-contact atomic force microscopy of clean metal oxide surfaces. *Journal of Physics-Condensed Matter* **2010,** 22, (26).

33. Wang, G. L.; Zhang, J.; Murray, R. W., DNA Binding of an Ethidium Intercalator Attached to a Monolayer-Protected Gold Cluster. *Analytical Chemistry* **2002,** 74, 4320-4327.

34. Bullen, H. A.; Garrett, S. J., TiO2 nanoparticle arrays prepared using a nanosphere lithography technique. *Nano Letters* **2002,** 2, (7), 739-745.

35. Eppler, A. S.; Rupprechter, G.; Anderson, E. A.; Somorjai, G. A., Thermal and Chemical Stability and Adhesion Strength of Pt Nanoparticle Arrays Supported on Silica Studied by Transmission Electron Microscopy and Atomic Force Microscopy. *Journal of Physical Chemistry B* **2000,** 104, 7286-7292.

36. Li, Q.; Zheng, J.; Liu, Z., Site-Selective Assemblies of Gold Nanoparticles on an AFM Tip-Defined Silicon Template. *Langmuir* **2003,** 19, 166-171.

37. Zhu, T.; Zhang, X.; Wang, J.; Fu, X.; Liu, Z., Assembling colloidal Au nanoparticles with functionalized self-assembled monolayers. *Thin Solid Films* **1998,** 327-329, 595-598.

38. Talley, C. E.; Jackson, J. B.; Oubre, C., Surface-enhanced Raman scattering from individual Au nanoparticles and nanoparticle dimer substrates. *Nano Letters* **2005,** 5, 1569-1574.

39. De Hollander, R. B. G.; Van Hulst, N. F.; Kooyman, R. P. H., Near field plasmon and force microscopy. *Ultramicroscopy* **1995,** 57, 263-269.

40. Ramanaviciene, A.; Schuhmann, W.; Ramanavicius, A., AFM study of conducting polymer polypyrrole nanoparticles formed by redox enzyme – glucose oxidase – initiated polymerisation. *Colloids and Surfaces B* **2006,** 48, 159-166.

41. Drain, C. M.; Smeureanu, G.; Patel, S.; Gong, X.; Garno, J.; Arijeloye, J., Porphyrin Nanoparticles as Supramolecular Systems. *New Journal of Chemistry* **2006,** 30, 1834–1843.

42. Sangpour, P.; Akhavan, O.; Moshfegh, A. Z., The Effect of Au/Ag Ratios on Surface Composition and Optical Properties of Co-Sputtered Alloy Nanoparticles in Au–Ag:SiO2 Thin Films. *Journal of Alloys and Compounds* **2009,** 486, 22-28.

43. Liu, X.; Fu, L.; Hong, S.; Dravid, V. P.; Mirkin, C. A., Arrays of Magnetic Nanoparticles Patterned via Dip-Pen Nanolithography. *Advanced Materials* **2002,** 14, 231-234.

44. Zamborini, F. P.; Smart, L. E.; Leopold, M. C.; Murray, R. W., Distance-dependent electron hopping conductivity and nanoscale lithography of chemically-linked gold monolayer protected cluster films. *Analytica Chimica Acta* **2003,** 496, 3-16.

45. Carlsson, N.; Junno, T.; Montelius, L.; Pistol, M. E.; Samuelson, L.; Seifert, W., Growth of self-assembled InAs and InAsxP1-x dots on InP by metalorganic vapour phase epitaxy. *Journal of Crystal Growth* **1998,** 191, 347-356.

46. Bosacchi, A.; Frigeri, P.; Franchi, S.; Allegri, P.; Avanzini, V., InAs/GaAs Self-Assembled Quantum Dots Grown by ALMBE and MBE. *Journal of Crystal Growth* **1997,** 175/176, 771-776.

47. Paranthoen, C.; Platz, C.; Moreau, G.; Bertru, N.; Dehaese, O.; Le Corre, A.; Miska, P.; Even, J.; Folliot, H.; Labbe, C.; Patriarche, G.; Simon, J. C.; Loualiche, S., Growth and Optical Characterizations of InAs Quantum Dots on InP Substrate: Towards a 1.55 mm Quantum Dot Laser. *Journal of Crystal Growth* **2003,** 251, 230–235.

48. Aoki, T.; Hiroshima, M.; Kitamura, K.; Tokunaga, M.; Yanagida, T., Non-contact scanning probe microscopy with sub-piconewton force sensitivity. *Ultramicroscopy* **1997,** 70, (1-2), 45-55.

49. Weisenhorn, A. L.; Maivald, P.; Butt, H. J.; Hansma, P. K., Measuring adhesion, attraction, and repulsion between surfaces in liquids with atomic force microscope *Physical Review B* **1992,** 45, (19), 11226-11232.

50. Cappella, B.; Dietler, G., Force-distance curves by atomic force microscopy. *Surface Science Reports* **1999,** 34, (1-3), 1-+.

51. Putman, C. A. J.; Vanderwerf, K. O.; Degrooth, B. G.; Vanhulst, N. F.; Greve, J., Tapping mode atomic-force microscopy in liquid. *Applied Physics Letters* **1994,** 64, (18), 2454-2456.

52. Hierlemann, A.; Campbell, J. K.; Baker, L. A.; Crooks, R. M.; Ricco, A. J., Structural distortion of dendrimers on gold surfaces: A tapping-mode AFM investigation. *Journal of the American Chemical Society* **1998,** 120, (21), 5323-5324.

53. Raghavan, D.; Gu, X.; Nguyen, T.; VanLandingham, M.; Karim, A., Mapping polymer heterogeneity using atomic force microscopy phase imaging and nanoscale indentation. *Macromolecules* **2000,** 33, (7), 2573-2583.

54. Li, J. R.; Garno, J. C., Indirect Modulation of Nonmagnetic Probes for Force Modulation Atomic Force Microscopy. *Analytical Chemistry* **2009,** 81, (4), 1699-1706.

55. Kroto, H. W.; Heath, J. R.; O'Brien, S. C.; Curl, R. F.; Smalley, R. E., C60: Buckminsterfullerene. *Nature* **1985,** 318, 162-163.

56. Iijima, S., Helical Microtubules of Graphitic Carbon. *Nature* **1991,** 354, 56-58.

57. Brus, L. E., Electron Electron and Electron-Hole Interactions in Small Semiconductor Crystallites - the Size Dependence of the Lowest Excited Electronic State. *Journal of Chemical Physics* **1984,** 80, 4403-4409

58. Peng, X.; Manna, L.; Yang, W.; Wickham, J.; Scher, E.; Kadavanich, A.; Alivisatos, A. P., Shape Control of CdSe Nanocrystals. *Nature* **2000,** 404, 59-61.

59. El-Sayed, M. A., Some Interesting Properties of Metals Confined in Time and Nanometer Space of Different Shapes. *Accounts of Chemical Research* **2001,** 34, 257-264.

60. Lu, A. H.; Schmidt, W.; Matoussevitch, N.; Bonnemann, H.; Spliethoff, B.; Tesche, B.; Bill, E.; Kiefer, W.; Schuth, F., Nanoengineering of a Magnetically Separable Hydrogenation Catalyst. *Angewandte Chemie International Edition* **2004,** 43, 4303–4306.

61. Guillou, N.; Gao, Q.; Forster, P. M.; Chang, J. S.; Nogues, M.; Park, S. E.; Ferey, G.; Cheetham, A. K., Nickel(ii) Phosphate VSB-5: A Magnetic Nanoporous Hydrogenation Catalyst with 24-Ring Tunnels. *Angewandte Chemie International Edition* **2001,** 40, 2831–2834.

62. Tartaj, P.; Morales, M. D.; Veintemillas-Verdaguer, S.; Gonzalez-Carreno, T.; Serna, C. J., The Preparation of Magnetic Nanoparticles for Applications in Biomedicine. *Journal of Physics D: Applied Physics* **2003,** 36, R182–R197.

63. Pankhurst, Q. A.; Connolly, J.; Jones, S. K.; Dobson, J., Applications of Magnetic Nanoparticles in Biomedicine. *Journal of Physics D: Applied Physics* **2003,** 36, R167–R181.

64. Gupta, A. K.; Gupta, M., Synthesis and Surface Engineering of Iron Oxide Nanoparticles for Biomedical Applications. *Biomaterials* **2005,** 26, 3995-4021.

65. Ross, C., Patterned Magnetic Recording Media. *Annual Review of Materials Research* **2001,** 31, 203–235.

66. Moser, A.; Takano, K.; Margulies, D. T.; Albrecht, M.; Sonobe, Y.; Ikeda, Y.; Sun, S. H.; Fullerton, E. E., Magnetic Recording: Advancing into the Future. *Journal of Physics D: Applied Physics* **2002,** 35, R157–R167.

67. Terris, B. D.; Thomson, T., Nanofabricated and self-assembled magnetic structures as data storage media *Journal of Physics D: Applied Physics* **2005,** 38, R199-R222.

68. Alivisatos, A. P., Semiconductor clusters, nanocrystals, and quantum dots *Science* **1996,** 271, 933-937.

69. Bruchez, M.; Moronne, M.; Gin, P.; Weiss, S.; Alivisatos, A. P., Semiconductor Nanocrystals as Fluorescent Biological Labels. *Science* **1998,** 281, 2013-2016.

70. Villarrubia, J. S., Algorithms for scanned probe microscope image simulation, surface reconstruction, and tip estimation. *Journal of Research of the National Institute of Standards and Technology* **1997,** 102, (4), 425-454.

71. Markiewicz, P.; Goh, M. C., Atomic-force microscopy probe tip visualization and improvement of images using a simple deconvolution procedure. *Langmuir* **1994,** 10, (1), 5-7.

72. Williams, P. M.; Shakesheff, K. M.; Davies, M. C.; Jackson, D. E.; Roberts, C. J.; Tendler, S. J. B., Blind reconstruction of scanning probe image data. *Journal of Vacuum Science & Technology B* **1996,** 14, (2), 1557-1562.

73. Wilson, D. L.; Kump, K. S.; Eppell, S. J.; Marchant, R. E., Morphological Restoration of Atomic-Force Microscopy Images *Langmuir* **1995,** 11, (1), 265-272.

74. Neumeister, J. M.; Ducker, W. A., Lateral, normal, and longitudinal spring constants of atomic-force microscopy cantilevers. *Review of Scientific Instruments* **1994,** 65, (8), 2527-2531.

75. Hutter, J. L.; Bechhoefer, J., Calibration of atomic-force microscope tips. *Review of Scientific Instruments* **1993,** 64, (7), 1868-1873.

76. Sader, J. E.; Larson, I.; Mulvaney, P.; White, L. R., Method for the calibration of atomic-force microscope cantilevers. *Review of Scientific Instruments* **1995,** 66, (7), 3789-3798.

77. Stamm, K. L.; Garno, J. C.; Liu, G. Y.; Brock, S. L., A general methodology for the synthesis of transition metal pnictide nanoparticles from pnictate precursors and its application to iron-phosphorus phases. *Journal of the American Chemical Society* **2003,** 125, (14), 4038-4039.

78. Perera, S. C.; Fodor, P. S.; Tsoi, G. M.; Wenger, L. E.; Brock, S. L., Application of de-silylation strategies to the preparation of transition metal pnictide nanocrystals: The case of FeP *Chemistry of Materials* **2003,** 15, 4034-4038.

79. Zou, J.; Baldwin, R. K.; Pettigrew, K. A.; Kauzlarich, S. M., Solution Synthesis of Ultrastable Luminescent Siloxane-Coated Silicon Nanoparticles. *Nano Letters* **2004,** 4, 1181-1186.

80. Baldwin, R. K.; Pettigrew, K. A.; Garno, J. C.; Power, P. P.; Liu, G. Y.; Kauzlarich, S. M., Room temperature solution synthesis of alkyl-capped tetrahedral shaped silicon nanocrystals. *Journal of the American Chemistry Society* **2002,** 124, (7), 1150-1151.

81. Gong, X. C.; Milic, T.; Xu, C.; Batteas, J. D.; Drain, C. M., Preparation and characterization of porphyrin nanoparticles. *Journal of the American Chemical Society* **2002,** 124, (48), 14290-14291.

82. Drain, C. M.; Smeureanu, G.; Patel, S.; Gong, X. C.; Garno, J.; Arijeloye, J., Porphyrin nanoparticles as supramolecular systems. *New Journal of Chemistry* **2006,** 30, (12), 1834-1843.

83. Ogoshi, T.; Fujiwara, T.; Bertolucci, M.; Galli, G.; Chiellini, E.; Chujo, Y.; Wynne, K. J., Tapping Mode AFM Evidence for an Amorphous Reticular Phase in a Condensation-Cured Hybrid Elastomer: r,ö-Dihydroxypoly(dimethylsiloxane)/Poly(diethoxysiloxane)/Fumed Silica Nanoparticles. *Journal of the American Chemical Society* **2004,** 126, 12284-12285.

84. Dong, R.; Yu, L. Y. E., Investigation of surface changes of nanoparticles using TM-AFM phase imaging *Environmental Science and Technology* **2003,** 37, 2813-2819.

85. Aytun, T.; Mutaf, O. F.; el-Atwani, O. J.; Ow-Yang, C. W., Nanoscale Composition Mapping of Segregation in Micelles with Tapping-Mode Atomic Force Microscopy. *Langmuir* **2008,** 24, 14183-14187.

86. Schmitz, I.; Schreiner, M.; Friedbacher, G.; Grasserbauer, M., Phase imaging as an extension to tapping mode AFM for the identification of material properties on humidity-sensitive surfaces. *Applied Surface Science* **1997,** 115, 190-198.

87. Rasa, M.; Kuipers, B. W. M.; Philipse, A. P., Atomic Force Microscopy and Magnetic Force Microscopy Study of Model Colloids. *Journal of Colloid and Interface Science* **2002,** 250, 303-315.

88. Shi, Z.; Han, M.; Song, F.; Zhou, J.; Wan, J.; Wang, G., Hierarchical Self-assembly of Silver Nanocluster Arrays on Triblock Copolymer Templates. *Journal of Physical Chemistry B* **2006,** 110, 18154-18157.

89. Grabar, K. C.; Brown, K. R.; Keating, C. D.; Stranick, S. J.; Tang, S. L.; Natan, M. J., Nanoscale Characterization of Gold Colloid Monolayers: A Comparison of Four Techniques. *Analytical Chemistry* **1997,** 69, 471-477.

90. Huo, S. J.; Xue, X. K.; Li, Q. X.; Xu, S. F.; Cai, W. B., Seeded-growth approach to fabrication of silver nanoparticle films on silicon for electrochemical ATR surface-enhanced IR absorption spectroscopy. *Journal of Physical Chemistry B* **2006,** 110, (51), 25721-25728.

91. Guo, Q. J.; Teng, X. W.; Yang, H., Overpressure Contact Printing. *Nano Letters* **2004,** 4, 1657-1662.

92. Nazir, R.; Mazhar, M.; Akhtar, M. J.; Shah, M. R.; Khan, N. A.; Nadeem, M.; Siddique, M.; Mehmood, M.; Butt, N. M., Superparamagnetic bimetallic iron-palladium nanoalloy: synthesis and characterization. *Nanotechnology* **2008,** 19, (18), 6.

93. Sode, A.; Musgrove, A.; Bizzotto, D., Stability of PtZn Nanoparticles Supported on Carbon in Acidic Electrochemical Environments. *Jornal of Physical Chemistry C* **2010,** 114, (1), 546-553.

94. Beek, W. J. E.; Wienk, M. M.; Janssen, R. A. J., Hybrid Solar Cells from Regioregular Polythiophene and ZnO Nanoparticles. *Advanced Functuntional Materials* **2006,** 16, 1112-1116.

95. Xu, L. P.; Pradhan, S.; Chen, S. W., Adhesion force studies of janus nanoparticles. *Langmuir* **2007,** 23, (16), 8544-8548.

96. Sun, L.; Crooks, R. M., Dendrimer-Mediated Immobilization of Catalytic Nanoparticles on Flat, Solid Supports. *Langmuir* **2002,** 20, 9335-9339.

97. Mu, L.; Feng, S. S., Vitamin E TPGS used as emulsifier in the solvent evaporation/extraction technique for fabrication of polymeric nanospheres for controlled release of paclitaxel (Taxol (R)). *Journal of Controlled Release* **2002,** 80, (1-3), 129-144.

98. Kumar, M.; Bakowsky, U.; Lehr, C. M., Preparation and characterization of cationic PLGA nanospheres as DNA carriers. *Biomaterials* **2004,** 25, (10), 1771-1777.

99. Dong, Y. C.; Feng, S. S., Methoxy poly(ethylene glycol)-poly(lactide) (MPEG-PLA) nanoparticles for controlled delivery of anticancer drugs. *Biomaterials* **2004,** 25, (14), 2843-2849.

100. Hansma, P. K.; Cleveland, J. P.; Radmacher, M.; Walters, D. A.; Hillner, P. E.; Bezanilla, M.; Fritz, M.; Vie, D.; Hansma, H. G.; Prater, C. B.; Massie, J.; Fukunaga, L.; Gurley, J.; Elings, V., Tapping mode atomic-force microscopy in liquids. *Applied Physics Letters* **1994,** 64, (13), 1738-1740.

101. Han, W. H.; Lindsay, S. M.; Jing, T. W., A magnetically driven oscillating probe microscope for operation in liquids. *Applied Physics Letters* **1996,** 69, (26), 4111-4113.

102. Garcia, R.; San Paulo, A., Attractive and repulsive tip-sample interaction regimes in tapping-mode atomic force microscopy. *Physical Review B* **1999,** 60, (7), 4961-4967.

103. Marth, M.; Maier, D.; Honerkamp, J.; Brandsch, R.; Bar, G., A unifying view on some experimental effects in tapping-mode atomic force microscopy. *Journal of Applied Physics* **1999,** 85, (10), 7030-7036.

104. Daniel, M. C.; Astruc, D., Gold nanoparticles: Assembly, supramolecular chemistry, quantum-size-related properties, and applications toward biology, catalysis, and nanotechnology. *Chemical Reviews* **2004,** 104, (1), 293-346.

105. Shan, J.; Tenhu, H., Recent advances in polymer protected gold nanoparticles: synthesis, properties and applications. *Chemical Communication* **2007**, (44), 4580-4598.

106. Hyeon, T., Chemical synthesis of magnetic nanoparticles. *Chemical Communication* **2003**, 927-934.

107. Gunnarsson, L.; Bjerneld, E. J.; Xu, H.; Petronis, S.; Kasemo, B.; Kall, M., Interparticle coupling effects in nanofabricated substrates for surface-enhanced Raman scattering. *Applied Physics Letters* **2001,** 78, 802-804.

108. He, L.; Musick, M. D.; Nicewarner, S. R.; Salinas, F. G.; Benkovic, S. J.; Natan, M. J.; Keating, C. D., Colloidal Au-Enhanced Surface Plasmon Resonance for Ultrasensitive

Detection of DNA Hybridization. *Journal of the American Chemical Society* **2000,** 122, 9071-9077.

109. Hutter, E.; Fendler, J. H.; Roy, D., Surface Plasmon Resonance Studies of Gold and Silver Nanoparticles Linked to Gold and Silver Substrates by 2-Aminoethanethiol and 1,6-Hexanedithiol. *Journal of Physical Chemistry B* **2001,** 105, 11159-11168.

110. Jain, P. K.; Huang, X.; El-Sayed, I. H.; El-Sayed, M. A., Review of Some Interesting Surface Plasmon Resonance-enhanced Properties of Noble Metal Nanoparticles and Their Applications to Biosystems. *Plasmonics* **2007,** 2, 107-118.

111. Turkevich, J.; Stevenson, P. C.; Hillier, J., A study of the nucleation and growth processes in the synthesis of colloidal gold. *Discussions of the Faraday Society* **1951**, (11), 55-&.

112. Frens, G., Controlled Nucleation for Regulation of Particle-Size in Monodisperse Gold Suspensions. *Nature Physical Science* **1973,** 241, 20-22.

113. Brown, K. R.; Walter, D. G.; Natan, M. J., Seeding of Colloidal Au Nanoparticle Solutions. 2. Improved Control of Particle Size and Shape. *Chemistry of Materials* **2000,** 12, 306-313.

114. Ferrando, R.; Jellinek, J.; Johnston, R. L., Nanoalloys: From Theory to Applications of Alloy Clusters and Nanoparticles. *Chemical Reviews* **2008,** 108, 845-910.

115. Li, X. G.; Chiba, A.; Takahashi, S., Preparation and Magnetic Properties of Ultrafine Particles of Fe-Ni Alloys. *Journal of Magnetism and Magnetic Materials* **1997,** 170, 339-345.

116. Liao, Q.; Tannenbaum, R.; Wang, Z. L., Synthesis of FeNi3 Alloyed Nanoparticles by Hydrothermal Reduction. *Journal of Physical Chemistry B* **2006,** 110, 14262-14265.

117. Kelley, A. T.; Daniels, S. L.; Serem, W. K.; Flurry, N.; Chan, J. Y.; Garno, J. C., Vibrational response of FeNi3 nanoparticles to the flux of a modulated electromagnetic field detected by contact-mode atomic force microscopy *Chemistry of Materials* **2010,** *in submission*.

118. Baker, G. A.; Baker, S. N.; Pandey, S.; Bright, F. V., An Analytical View of Ionic Liquids. *Analyst* **2005,** 130, 800-808.

119. Rogers, R. D.; Seddon, K. R., Ionic Liquids - Solvents of the Future. *Science* **2003,** 302, 792-793.

120. Del Popolo, M. G.; Voth, G. A., On the Structure and Dynamics of Ionic Liquids. *Journal of Physical Chemistry B* **2004,** 108, 1744-1752.

121. Pinkert, A.; Marsh, K. N.; Pang, S.; Staiger, M. P., Ionic Liquids and Their Interaction with Cellulose. *Chemical Reviews* **2009,** 109, 6712-6728.

122. Schwarz, U. D.; Haefke, H.; Reimann, P.; Guentherodt, H. J., Tip Artifacts in Scanning Force Microscopy. *Journal of Microscopy* **1994,** 173, 183-197.

123. Ramirez-Aguilar, K. A.; Rowlen, K. L., Tip Characterization from AFM Images of Nanometric Spherical Particles. *Langmuir* **1998,** 14, 2562-2566.

124. Brust, M.; Walker, M.; Bethell, D.; Schiffrin, D. J.; Whyman, R., Synthesis of thiol-derivatized gold nanoparticles in a 2-phase liquid-liquid system. *Journal of Chemical Society, Chemical Communications* **1994**, (7), 801-802.

125. Templeton, A. C.; Wuelfing, M. P.; Murray, R. W., Monolayer protected cluster molecules. *Accounts of Chemical Research* **2000,** 33, (1), 27-36.

126. Chen, S. W.; Ingram, R. S.; Hostetler, M. J.; Pietron, J. J.; Murray, R. W.; Schaaff, T. G.; Khoury, J. T.; Alvarez, M. M.; Whetten, R. L., Gold nanoelectrodes of varied size: Transition to molecule-like charging. *Science* **1998,** 280, (5372), 2098-2101.

127. Hostetler, M. J.; Wingate, J. E.; Zhong, C. J.; Harris, J. E.; Vachet, R. W.; Clark, M. R.; Londono, J. D.; Green, S. J.; Stokes, J. J.; Wignall, G. D.; Glish, G. L.; Porter, M. D.; Evans, N. D.; Murray, R. W., Alkanethiolate gold cluster molecules with core diameters from 1.5 to 5.2 nm: Core and monolayer properties as a function of core size. *Langmuir* **1998,** 14, (1), 17-30.

128. Brust, M.; Kiely, C. J., Some Recent Advances in Nanostructure Preparation from Gold and Silver: A Short Topical Review. *Colloids and Surfaces A: Physicochemical Engineering Aspects* **2002,** 202, 175-186.

129. Jackson, A. M.; Hu, Y.; Silva, P. J.; Stellacci, F., From Homoligand- to Mixed-Ligand-Monolayer-Protected Metal Nanoparticles: A Scanning Tunneling Microscopy Investigation. *Journal of the American Chemical Society* **2006,** 128, 11135-11149

130. Wuelfing, W. P.; Zamborini, F. P.; Templeton, A. C.; Wen, X.; Yoon, H.; Murray, R. W., Monolayer-Protected Clusters: Molecular Precursors to Metal Films. *Chemistry of Materials* **2001,** 13, 87-95.

131. Mayya, K. S.; Schoeler, B.; Caruso, F., Preparation and Organization of Nanoscale Polyelectrolyte-Coated Gold Nanoparticles. *Advanced Functional Materials* **2003,** 13, 183-188.

132. Hu, L.; Zhang, Z.; Zhang, M.; Efremov, M. Y.; Olson, E. A.; de la Rama, L. P.; Kummamuru, R. K.; Allen, L. H., Self-Assembly and Ripening of Polymeric Silver-Alkanethiolate Crystals on Inert Surfaces. *Langmuir* **2009,** 25, 9585-9595.

133. Ibanez, F. J.; Gowrishetty, U.; Crain, M. M.; Walsh, K. M.; Zamborini, F. P., Chemiresistive Vapor Sensing with Microscale Films of Gold Monolayer Protected Clusters. *Analytical Chemistry* **2006,** 78, 753-761.

134. Laaksonen, T.; Ruiz, V.; Liljeroth, P.; Quinn, B. M., Quantised charging of monolayer-protected nanoparticles. *Chemical Society Reviews* **2008,** 37, (9), 1836-1846.

135. Pietron, J. J.; Murray, R. W., Mediated electrocatalysis with polyanthraquinone-functionalized monolayer-protected clusters. *Journal of Physical Chemistry B* **1999,** 103, (21), 4440-4446.

136. Wuelfing, W. P.; Zamborini, F. P.; Templeton, A. C.; Wen, X. G.; Yoon, H.; Murray, R. W., Monolayer-protected clusters: Molecular precursors to metal films. *Chemistry of Materials* **2001,** 13, (1), 87-95.

137. Kim, Y. J.; Johnson, R. C.; Hupp, J. T., Gold nanoparticle-based sensing of "spectroscopically silent" heavy metal ions. *Nano Letters* **2001,** 1, (4), 165-167.

138. Boal, A. K.; Rotello, V. M., Fabrication and self-optimization of multivalent receptors on nanoparticle scaffolds. *Journal of the American Chemical Society* **2000,** 122, (4), 734-735.

139. Bigioni, T. P.; Harrell, L. E.; Cullen, W. G.; Guthrie, D. K.; Whetten, R. L.; First, P. N., Imaging and tunneling spectroscopy of gold nanocrystals and nanocrystal arrays. *The European Physical Journal D* **1999,** 6, 355-364.

140. Andres, R. P.; Bein, T.; Dorogi, M.; Feng, S.; Henderson, J. I.; Kubiak, C. P.; Mahoney, W.; Osifchin, R. G.; Reifenberger, R., "Coulomb Staircase" at Room Temperature in a Self-Assembled Molecular Nanostructure. *Science* **1996,** 272, 1323-1325.

141. Hou, J. G.; Wang, B.; Yang, J.; Wang, X. R.; Wang, H. Q.; Zhu, Q.; Xiao, X., Nonclassical Behavior in the Capacitance of a Nanojunction. *Physical Review Letters* **2001,** 86, 5321-5324.

142. Graf, H.; Vancea, J.; Hoffmann, H., Single-electron tunneling at room temperature in cobalt nanoparticles. *Applied Physics Letters* **2002,** 80, 1264-1266.

143. Khan, N. A.; Uhl, A.; Shaikhutdinov, S.; Freund, H.-J., Alumina supported model Pd–Ag catalysts: A combined STM, XPS, TPD and IRAS study. *Surface Science* **2006,** 600, 1849-1853.

144. Jiang, P.; Liu, Z. F.; Cai, S. M., In situ CdS nanocluster formation on scanning tunneling microscopy tips for reliable single-electron tunneling at room temperature. *Applied Physics Letters* **1999,** 75, 3023-3025.

145. Wu, W.; Tucker, J. R.; Solomon, G. S.; Harris, J. S., Atom-resolved scanning tunneling microscopy of vertically ordered InAs quantum dots. *Applied Physics Letters* **1997,** 71, 1083-1085.

146. Harrell, L. E.; Bigioni, T. P.; Cullen, W. G.; Whetten, R. L.; First, P. N., Scanning tunneling microscopy of passivated Au nanocrystals immobilized on Au(111) surfaces. *Journal of Vacuum Science and Technology B* **1999,** 17, 2411-2416.

147. Dubois, J. G. A.; Gerritsen, J. W.; Shafranjuk, S. E.; Boon, E. J. G.; Schmid, G.; Kempen, H. v., Coulomb staircases and quantum size effects in tunnelling spectroscopy on ligand-stabilized metal clusters. *Europhysics Letters* **1996,** 33, 279-284.

148. Andres, R. P.; Bein, T.; Dorogi, M.; Feng, S.; Henderson, J. I.; Kubiak, C. P.; Mahoney, W.; Osifchin, R. G.; Reifenberger, R., "Coulomb staircase" at room temperature in a self-assembled molecular nanostructure. *Science* **1996,** 272, (5266), 1323-1325.

149. Fujisawa, T.; Hayashi, T.; Hirayama, Y.; Cheong, H. D.; Jeong, Y. H., Electron counting of single-electron tunneling current. *Applied Physics Letters* **2004,** 84, (13), 2343-2345.

150. Chaki, N. K.; Aslam, M.; Gopakumar, T. G.; Sharma, J.; Pasricha, R.; Mulla, I. S.; Vijayamohanan, K., Effect of chain length and the nature of the monolayer on the electrical behavior of hydrophobically organized gold clusters. *Journal of Physical Chemistry B* **2003,** 107, (49), 13567-13574.

151. Harrell, L. E.; Bigioni, T. P.; Cullen, W. G.; Whetten, R. L.; First, P. N., Scanning tunneling microscopy of passivated Au nanocrystals immobilized on Au(111) surface. *Journal of Vacuum Science & Technology B* **1999,** 17, (6), 2411-2416.

152. Chi, L. F.; Hartig, M.; Drechsler, T.; Schwaack, T.; Seidel, C.; Fuchs, H.; Schmid, G., Single-electron tunneling in Au-55 cluster monolayers. *Applied Physics a-Materials Science & Processing* **1998,** 66, S187-S190.

153. Chen, S. W., Self-assembling of monolayer-protected gold nanoparticles. *Journal of Physical Chemistry B* **2000,** 104, (4), 663-667.

154. Li, J.-R.; Garno, J. C., Elucidating the Role of Surface Hydrolysis in Preparing Organosilane Nanostructures via Particle Lithography. *Nano Letters* **2008,** 8, 1916-1922.

155. Hanarp, P.; Sutherland, D. S.; Gold, J.; Kasemo, B., Control of nanoparticle film structure for colloidal lithography. *Colloids and Surfaces A: Physicochemical and Engineering Aspects* **2003,** 214, 23-36.

156. Gundiah, G.; John, N. S.; Thomas, P. J.; Kulkarni, G. U.; Rao, C. N. R.; Heun, S., Dip-pen nanolithography with magnetic Fe2O3 nanocrystals. *Applied Physics Letters* **2004,** 84, (26), 5341-5343.

157. Ben Ali, M.; Ondarcuhu, T.; Brust, M.; Joachim, C., Atomic force microscope tip nanoprinting of gold nanoclusters. *Langmuir* **2002,** 18, (3), 872-876.

158. Thomas, P. J.; Kulkarni, G. U.; Rao, C. N. R., Dip-pen lithography using aqueous metal nanocrystal dispersions. *Journal of Materials Chemistry* **2004,** 14, (4), 625-628.

159. Wang, Y.; Zhang, Y.; Li, B.; Lu, J. H.; Hu, J., Capturing and depositing one nanoobject at a time: Single particle dip-pen nanolithography. *Applied Physics Letters* **2007,** 90, (13).

160. Wang, W. C. M.; Stoltenberg, R. M.; Liu, S. H.; Bao, Z. N., Direct Patterning of Gold Nanoparticles Using Dip-Pen Nanolithography. *Acs Nano* **2008,** 2, (10), 2135-2142.

161. Amro, N. A.; Xu, S.; Liu, G. Y., Patterning surfaces using tip-directed displacement and self-assembly. *Langmuir* **2000,** 16, (7), 3006-3009.

162. Garno, J. C.; Yang, Y. Y.; Amro, N. A.; Cruchon-Dupeyrat, S.; Chen, S. W.; Liu, G. Y., Precise positioning of nanoparticles on surfaces using scanning probe lithography. *Nano Letters* **2003,** 3, (3), 389-395.

163. Xu, S.; Liu, G. Y., Nanometer-scale fabrication by simultaneous nanoshaving and molecular self-assembly. *Langmuir* **1997,** 13, (2), 127-129.

164. Liu, G. Y.; Xu, S.; Qian, Y. L., Nanofabrication of self-assembled monolayers using scanning probe lithography. *Accounts of Chemical Research* **2000,** 33, (7), 457-466.

165. Piner, R. D.; Zhu, J.; Xu, F.; Hong, S. H.; Mirkin, C. A., "Dip-pen" nanolithography. *Science* **1999,** 283, (5402), 661-663.

166. Ginger, D. S.; Zhang, H.; Mirkin, C. A., The Evolution of Dip-Pen Nanolithography. *Angewandte Chemie International Edition* **2004,** 43, 30-45.

167. Salaita, K.; Wang, Y.; Mirkin, C. A., Applications of dip-pen nanolithography. *Nature Nanotechnology* **2007,** 2, 145-155.

168. Hoeppener, S.; Maoz, R.; Cohen, S. R.; Chi, L. F.; Fuchs, H.; Sagiv, J., Metal Nanoparticles, Nanowires, and Contact Electrodes Self-Assembled on Patterned Monolayer Templates - A Bottom-up Chemical Approach. *Advanced Materials* **2002,** 14, 1036-1041.

169. Wang, X. F.; Bullen, D. A.; Zou, J.; Liu, C.; Mirkin, C. A., Thermally Actuated Probe Array for Parallel Dip-Pen Nanolithography. *Journal of Vacuum Science and Technology B* **2004,** 22, 2563-2567

170. Huo, F.; Zheng, Z.; Zheng, G.; Giam, L. R.; Zhang, H.; Mirkin, C. A., Polymer Pen Lithography. *Science* **2008,** 321, 1658-1660

171. Vettiger, P.; Cross, G.; Despont, M.; Drechsler, U.; Durig, U.; Gotsmann, B.; Haberle, W.; Lantz, M. A.; Rothuizen, H. E.; Stutz, R.; Binnig, G. K., The "millipede" - Nanotechnology entering data storage. *IEEE Transactions and Nanotechnology* **2002,** 1, 39-55.

172. Haynes, C. L.; Van Duyne, R. P., Nanosphere Lithography: A Versatile Nanofabrication Tool for Studies of Size-Dependent Nanoparticle Optics. *Journal of Physical Chemistry B* **2001,** 105, 5599-5611.

173. Tan, B. J. Y.; Sow, C. H.; Koh, T. S.; Chin, K. C.; Wee, A. T. S.; Ong, C. K., Fabrication of size-tunable gold nanoparticles array with nanosphere lithography, reactive ion etching, and thermal annealing. *Journal of Physical Chemistry B* **2005,** 109, (22), 11100-11109.

174. Sagiv, J., Organized monolayers by adsorption.1. formation and structure of oleophobic mixed monolayers on solid-surfaces. *Journal of the American Chemical Society* **1980,** 102, (1), 92-98.

175. Zhong, Z.; Gates, B.; Xia, Y., Soft Lithographic Approach to the Fabrication of Highly Ordered 2D Arrays of Magnetic Nanoparticles on the Surfaces of Silicon Substrates. *Langmuir* **2000,** 16, 10369-10375.

176. Shipway, A. N.; Katz, E.; Willner, I., Nanoparticle Arrays on Surfaces for Electronic, Optical, and Sensor Applications. *ChemPhysChem* **2000,** 1, 18-52.

177. Grabar, K. C.; Allison, K. J.; Baker, B. E.; Bright, R. M.; Brown, K. R.; Freeman, R. G.; Fox, A. P.; Keating, C. D.; Musick, M. D.; Natan, M. J., Two-dimensional arrays of

colloidal gold particles: A flexible approach to macroscopic metal surfaces. *Langmuir* **1996,** 12, 2353-2361.

178. Chen, C. F.; Tzeng, S. D.; Lin, M. H.; Gwo, S., Electrostatic Assembly of Gold Colloidal Nanoparticles on Organosilane Monolayers Patterned by Microcontact Electrochemical Conversion. *Langmuir* **2006,** 22, 7819-7824.

179. He, H. X.; Zhang, H.; Li, Q. G.; Zhu, T.; Li, S. F. Y.; Liu, Z. F., Fabrication of Designed Architectures of Au Nanoparticles on Solid Substrate with Printed Self-Assembled Monolayers as Templates. *Langmuir* **2000,** 16, 3846-3851.

180. Sousa, M. H.; Tonrinho, F. A.; Depeyrot, J.; daSilva, G. J.; Lara, M. C. F. L., New electric double-layered magnetic fluids based on copper, nickel, and zinc ferrite nanostructures *Journal of Physical Chemistry B* **2001,** 105, 1168-1175.

181. Shen, L. F.; Laibinis, P. E.; Hatton, T. A., Bilayer surfactant stabilized magnetic fluids: Synthesis and interactions at interfaces *Langmuir* **1999,** 15, 447-453.

182. Roger, J.; Pons, J. N.; Massart, R.; Halbreich, A.; Bacri, J. C., Some biomedical applications of ferrofluids. *The European Physical Journal- Applied Physics* **1999,** 5, 321-325.

183. Morup, S., Superferromagnetic nanostructures. *Hyperfine Interactions* **1994,** 90, 171-185.

184. Wang, Y.-X. J.; Hussain, S. M.; Kresting, G. P., Superparamagnetic iron oxide contrast agents: physicochemical characteristics and applications in MR imaging. *European Journal of Radiology* **2001,** 11, 2319-2331.

185. Mornet, S.; Vasseur, S.; Grasset, F.; Duguet, E., Magnetic nanoparticle design for medical diagnosis and therapy. *Journal of Materials Chemistry* **2004,** 14, 2161-2175.

186. Chang, E.; Chalikonda, S.; Friedl, J.; Xu, H.; Phan, G. Q.; Marincola, F. M.; Alexander, H. R.; Bartlett, D. L., Targeting vaccinia to solid tumors with local hyperthermia *Human Gene Therapy* **2005,** 16, 435-444.

187. Ito, A.; Shinkai, M.; Honda, H.; Yoshikawa, K.; Saga, S.; Wakabayashi, T.; Yoshida, J.; Kobayashi, T., Heat shock protein 70 expression induces antitumor immunity during intracellular hyperthermia using magnetite nanoparticles. *Cancer Immunology Immunotherapy* **2003,** 52, 80-88.

188. Latham, A. H.; Williams, M. E., Controlling Transport and Chemical Functionality of Magnetic Nanoparticles. *Accounts Chemical Research* **2008,** 41, 411-420.

189. Berry, C. C.; Curtis, A. S. G., Functionalisation of magnetic nanoparticles for applications in biomedicine. *Journal of Physics D-Applied Physics* **2003,** 36, R198-R206.

190. Herdt, A. R.; Kim, B. S.; Taton, T. A., Encapsulated magnetic nanoparticles as supports for proteins and recyclable biocatalysts. *Bioconjugate Chemistry* **2007,** 18, 183-189.

191. Jun, Y.-W.; Seo, J.-W.; Cheon, J., Nanoscaling Laws of Magnetic Nanoparticles and Their Applicabilities in Biomedical Sciences. *Accounts Chemical Research* **2008,** 41, 179-189.

192. Chu, M. Q.; Song, X.; Cheng, D.; Liu, S. P.; Zhu, J., Preparation of quantum dot-coated magnetic polystyrene nanospheres for cancer cell labelling and separation *Nanotechnology* **2006,** 17, 3268-3273.

193. Halavaara, J.; Tervahartiala, R.; Isoniemi, H.; Hockerstedt, K., Efficacy of sequential use of superparamagnetic iron oxide and gadolinium in liver MR imaging. *Acta Radiologica* **2002,** 43, 180-185.

194. Vanbeers, B.; Pringot, J.; Gallez, B., Iron-Oxide Enhanced MR-Imaging of the Liver. *J. De Radiologie* **1995,** 76, 991-995.

195. Babes, L.; Denizot, B.; Tanguy, G.; LeJeune, J. J.; Jallet, P., Synthesis of iron oxide nanoparticles used as MRI contrast agents: A parametric study. *Journal of Colloid and Interface Science* **1999,** 212, 474-482.

196. Iglesias, O.; Batlle, X.; Labarta, A., Particle Size and Cooling Field Dependence of Exchange Bias in Core/Shell Magnetic Nanoparticles. *Journal of Physical D: Applied Physics* **2008,** 41, 1-5.

197. Lu, A. H.; Salabas, E. L.; Schuth, F., Magnetic Nanoparticles: Synthesis, Protection, Functionalization, and Application. *Angewandte Chemie-International Edition* **2007,** 46, 1222-1224.

198. Gibbs, M. R. J., Nanomagnetism—nascent or fully formed? *Current Opinion in Solid State and Material Science* **2003,** 7, 83-86.

199. Pedreschi, F.; Sturm, J. M.; O'Mahony, J. D.; Flipse, C. F. J., Magnetic Force Microscopy and Simulations of Colloidal Iron Nanoparticles. *Journal of Applied Physics* **2003,** 94, 3446-3450.

200. Martin, Y.; Wickramasinghe, H. K., Magnetic Imaging by Force Microscopy with 1000A Resolution. *Applied Physics Letters* **1987,** 50, (20), 1455-1457.

201. Schreiber, S.; Savla, M.; Pelekhov, D. V.; Iscru, D. F.; Selcu, C.; Hammel, P. C.; Agarwal, G., Magnetic Force Microscopy of Superparamagnetic Nanoparticles. *Small* **2008,** 4, 270-278.

202. Wolff, U.; Singh, A.; Schultz, L.; Neu, V., Switching Behaviour of Patterned SmCo5 Thin Films Investigated by Magnetic Force Microscopy. *Journal of Magnetism and Magnetic Materials* **2007,** 310, 2210-2212.

203. Liou, S. H.; Malhotra, S. S.; Moreland, J.; Hopkins, P. F., High Resolution Imaging of Thin-Film Recording Heads by Superparamagnetic Magnetic Force Microscopy Tips. *Applied Physics Letters* **1997,** 70, 135-137.

204. Koblischkaa, M. R.; Hartmann, U.; Sulzbachb, T., Improving the Lateral Resolution of the MFM Technique to the 10 nm Range. *Journal of Magnetism and Magnetic Materials* **2004,** 272-276, 2138-2140.

205. Yacoot, A.; Koenders, L., Aspects of Scanning Force Microscope Probes and their Effects on Dimensional Measurement. *Journal of Physics D: Applied Physics* **2008,** 41, (10), 1-46.

206. Winkler, A.; Mühl, T.; Menzel, S.; Kozhuharova-Koseva, R.; Hampel, S.; Leonhardt, A.; Büchner, B., Magnetic Force Microscopy Sensors using Iron-Filled Carbon Nanotubes. *Journal of Applied Physics* **2006,** 99, 104905

207. Leo, G.; Chushkin, Y.; Luby, S.; Majkova, E.; Kostic, I.; Ulmeanu, M.; Luches, A.; Giersig, M.; Hilgendorff, M., Ordering of Free-Standing Co Nanoparticles. *Materials Science and Engineering C* **2003,** 23, 949–952.

208. Li, J. R.; Lewandowski, B. R.; Xu, S.; Garno, J. C., Detecting the Magnetic Response of Iron Oxide Capped Organosilane Nanostructures Using Magnetic Sample Modulation and Atomic Force Microscopy. *Analytical Chemistry* **2009,** 81, 4792-4802.

209. Daniels, S. L.; Ngunjiri, J. N.; Garno, J. C., Investigation of the Magnetic Properties of Ferritin by AFM Imaging with Magnetic Sample Modulation. *Analytical and Bioanalytical Chemistry* **2009,** 394, 215-223.

210. Zhang, Z.; Hammel, P. C.; Wigen, P. E., Observation of ferromagnetic resonance in a microscopic sample using magnetic resonance force microscopy. *Applied Physics Letters* **1996,** 68, 2005-2007.

211. Sidles, J. A.; Garbini, J. L.; Bruland, K. J.; Rugar, D.; Zuger, O.; Hoen, S.; Yannoni, C. S., Magnetic-Resonance Force Microscopy. *Review Modern Physics* **1995,** 67, 249-265.

212. Rugar, D.; Yannoni, C. S.; Sidles, J. A., Mechanical Detection of Magnetic Resonance. *Nature* **1992,** 360, 563-566.

213. Bausch, A. R.; Ziemann, F.; Boulbitch, A. A.; Jacobson, K.; Sackmann, E., Magnetic-Resonance Force Microscopy. *Reviews of Modern Physics* **1995,** 67, 249-265.

214. Leuba, S. H.; Lindsay, S. M., Magnetically driven oscillating probe ("MAC mode") scanning force microscopy (SFM) of chromatin fibers in aqueous buffer. *Biophysical Journal* **1998,** 74, A71.

215. Kienberger, F.; Stroh, C.; Kada, G.; Moser, R.; Baumgartner, W.; Pastushenko, V.; Rankl, C.; Schmidt, U.; Muller, H.; Orlova, E.; LeGrimellec, C.; Drenckhahn, D.; Blaas, D.; Hinterdorfer, P., Dynamic force microscopy imaging of native membranes. *Ultramicroscopy* **2003,** 97, 229-237.

216. Ge, G.; Han, D.; Lin, D.; Chu, W.; Sun, Y.; Jiang, L.; Ma, W.; Wang, C., MAC mode atomic force microscopy studies of living samples, ranging from cells to fresh tissue. *Ultramicroscopy* **2007,** 107, 299-307.

217. Florin, E.-L.; Radmacher, M.; Fleck, B.; Gaub, H. E., Atomic force microscope with magnetic force modulation. *Review of Scientific Instruments* **1994,** 65, 639-643.

218. Peercy, P. S., The drive to miniaturization. *Nature* **2000,** 406, (6799), 1023-1026.

219. Mulvaney, P., Surface plasmon spectroscopy of nanosized metal particles. *Langmuir* **1996,** 12, (3), 788-800.

220. Grabar, K. C.; Smith, P. C.; Musick, M. D.; Davis, J. A.; Walter, D. G.; Jackson, M. A.; Guthrie, A. P.; Natan, M. J., Kinetic control of interparticle spacing in Au colloid-based surfaces: Rational nanometer-scale architecture. *Journal of the American Chemical Society* **1996,** 118, (5), 1148-1153.

221. Feldstein, M. J.; Keating, C. D.; Liau, Y. H.; Natan, M. J.; Scherer, N. F., Electronic relaxation dynamics in coupled metal nanoparticles. *Journal of the American Chemical Society* **1997,** 119, (28), 6638-6647.

222. Shi, J.; Gider, S.; Babcock, K.; Awschalom, D. D., Magnetic clusters in molecular beams, metals, and semiconductors. *Science* **1996,** 271, (5251), 937-941.

223. New, R. M. H.; Pease, R. F. W.; White, R. L., Physical and magnetic-properties of submicron lithographically patterned magnetic islands. *Journal of Vacuum Science & Technology B* **1995,** 13, (3), 1089-1094.

224. Street, S. C.; Xu, C.; Goodman, D. W., The physical and chemical properties of ultrathin oxide films. *Annual Review of Physical Chemistry* **1997,** 48, 43-68.

225. Heiz, U.; Vanolli, F.; Sanchez, A.; Schneider, W. D., Size-dependent molecular dissociation on mass-selected, supported metal clusters. *Journal of the American Chemical Society* **1998,** 120, (37), 9668-9671.

226. Yang, M. X.; Gracias, D. H.; Jacobs, P. W.; Somorjai, G. A., Lithographic fabrication of model systems in heterogeneous catalysis and surface science studies. *Langmuir* **1998,** 14, (6), 1458-1464.

227. Volokitin, Y.; Sinzig, J.; deJongh, L. J.; Schmid, G.; Vargaftik, M. N.; Moiseev, II, Quantum-size effects in the thermodynamic properties of metallic nanoparticles. *Nature* **1996,** 384, (6610), 621-623.

228. Wang, Z. L.; Petroski, J. M.; Green, T. C.; El-Sayed, M. A., Shape transformation and surface melting of cubic and tetrahedral platinum nanocrystals. *Journal of Physical Chemistry B* **1998,** 102, (32), 6145-6151.

229. Tremel, W.; Kleinke, H.; Derstroff, V.; Reisner, C., Transition-metal chalcogenides - new views on an old topic. *Journal of Alloys and Compounds* **1995,** 219, 73-82.

230. Datta, A.; Pal, M.; Chakravorty, D.; Das, D.; Chintalapudi, S. N., Disorder in nanocrystalline Ni3Fe. *Journal of Magnetism and Magnetic Materials* **1999,** 205, (2-3), 301-306.

231. Kim, E.; Xia, Y. N.; Whitesides, G. M., Polymer microstructures formed by molding in capillaries. *Nature* **1995,** 376, (6541), 581-584.

232. Zhao, X. M.; Stoddart, A.; Smith, S. P.; Kim, E.; Xia, Y.; Prentiss, M.; Whitesides, G. M., Fabrication of single-mode polymeric waveguides using micromolding in capillaries. *Advanced Materials* **1996,** 8, (5), 420-&.

233. Delamarche, E.; Bernard, A.; Schmid, H.; Michel, B.; Biebuyck, H., Patterned delivery of immunoglobulins to surfaces using microfluidic networks. *Science* **1997,** 276, (5313), 779-781.

234. Li, J. R.; Lewandowski, B. R.; Xu, S.; Garno, J. C., Detecting the Magnetic Response of Iron Oxide Capped Organosilane Nanostructures Using Magnetic Sample Modulation and Atomic Force Microscopy. *Analytical Chemistry* **2009,** 81, (12), 4792-4802.

235. Garno, J. C.; Amro, N. A.; Wadu-Mesthrige, K.; Liu, G. Y., Production of periodic arrays of protein nanostructures using particle lithography. *Langmuir* **2002,** 18, (21), 8186-8192.

236. Li, J. R.; Henry, G. C.; Garno, J. C., Fabrication of nanopatterned films of bovine serum albumin and staphylococcal protein A using latex particle lithography. *Analyst* **2006,** 131, (2), 244-250.

237. Ngunjiri, J. N.; Daniels, S. L.; Li, J. R.; Serem, W. K.; Garno, J. C., Controlling the surface coverage and arrangement of proteins using particle lithography. *Nanomedicine* **2008,** 3, (4), 529-541.

238. Tessier, P.; Velev, O. D.; Kalambur, A. T.; Lenhoff, A. M.; Rabolt, J. F.; Kaler, E. W., Structured metallic films for optical and spectroscopic applications via colloidal crystal templating. *Advanced Materials* **2001,** 13, (6), 396-400.

239. Jiang, P.; Bertone, J. F.; Colvin, V. L., A lost-wax approach to monodisperse colloids and their crystals. *Science* **2001,** 291, (5503), 453-457.

240. McLellan, J. M.; Geissler, M.; Xia, Y. N., Edge spreading lithography and its application to the fabrication of mesoscopic gold and silver rings. *Journal of the American Chemical Society* **2004,** 126, (35), 10830-10831.

241. Briseno, A. L.; Han, S. B.; Rauda, I. E.; Zhou, F. M.; Toh, C. S.; Nemanick, E. J.; Lewis, N. S., Electrochemical polymerization of aniline monomers infiltrated into well-ordered truncated eggshell structures of polyelectrolyte multilayers. *Langmuir* **2004,** 20, (1), 219-226.

242. Choi, D. G.; Jang, S. G.; Yu, H. K.; Yang, S. M., Two-dimensional polymer nanopattern by using particle-assisted soft lithography. *Chemistry of Materials* **2004,** 16, (18), 3410-3413.

243. Marquez, M.; Patel, K.; Carswell, A. D. W.; Schmidtke, D. W.; Grady, B. P., Synthesis of nanometer-scale polymeric structures on surfaces from template assisted admicellar polymerization: A comparative study with protein adsorption. *Langmuir* **2006,** 22, (19), 8010-8016.

244. Cai, Y. G.; Ocko, B. M., Large-scale fabrication of protein nanoarrays based on nanosphere lithography. *Langmuir* **2005,** 21, (20), 9274-9279.

245. Liao, Q. L.; Tannenbaum, R.; Wang, Z. L., Synthesis of FeNi3 alloyed nanoparticles by hydrothermal reduction. *Journal of Physical Chemistry B* **2006,** 110, (29), 14262-14265.

246. Rugar, D.; Budakian, R.; Mamin, H. J.; Chui, B. W., Single spin detection by magnetic resonance force microscopy. *Nature* **2004,** 430, (6997), 329-332.

247. Yamamoto, S.; Yamada, H., Interpretation of direct and indirect force modulation methods using polymer films. *Langmuir* **1997,** 13, (18), 4861-4864.

248. Guo, F.; Zheng, H. G.; Yang, Z. P.; Qian, Y. T., Synthesis of cobalt nanoparticles in ethanol hydrazine alkaline system (EHAS) at room temperature. *Materials Letters* **2002,** 56, (6), 906-909.

249. Takami, A.; Kurita, H.; Koda, S., Laser-induced size reduction of noble metal particles. *Journal of Physical Chemistry B* **1999,** 103, (8), 1226-1232.

250. Kazakevich, P. V.; Simakin, A. V.; Voronov, V. V.; Shafeev, G. A. In *Laser induced synthesis of nanoparticles in liquids*, 2006; 2006; pp 4373-4380.

251. Puntes, V. F.; Krishnan, K.; Alivisatos, A. P., Synthesis of colloidal cobalt nanoparticles with controlled size and shapes. *Topics in Catalysis* **2002,** 19, (2), 145-148.

252. Puntes, V. F.; Krishnan, K. M.; Alivisatos, P., Synthesis, self-assembly, and magnetic behavior of a two-dimensional superlattice of single-crystal epsilon-Co nanoparticles. *Applied Physics Letters* **2001,** 78, (15), 2187-2189.

253. Kim, S. W.; Park, J.; Jang, Y.; Chung, Y.; Hwang, S.; Hyeon, T.; Kim, Y. W., Synthesis of monodisperse palladium nanoparticles. *Nano Letters* **2003,** 3, (9), 1289-1291.

254. Vesperinas, A.; Eastoe, J.; Jackson, S.; Wyatt, P., Light-induced flocculation of gold nanoparticles. *Chemical Communications* **2007**, (38), 3912-3914.

255. Fang, Q.; He, G.; Cai, W. P.; Zhang, J. Y.; Boyd, I. W., Palladium nanoparticles on silicon by photo-reduction using 172 nm excimer UV lamps. *Applied Surface Science* **2004,** 226, (1-3), 7-11.

256. Hyeon, T.; Lee, S. S.; Park, J.; Chung, Y.; Bin Na, H., Synthesis of highly crystalline and monodisperse maghemite nanocrystallites without a size-selection process. *Journal of the American Chemical Society* **2001,** 123, (51), 12798-12801.

257. Shevchenko, E. V.; Talapin, D. V.; Schnablegger, H.; Kornowski, A.; Festin, O.; Svedlindh, P.; Haase, M.; Weller, H., Study of nucleation and growth in the organometallic synthesis of magnetic alloy nanocrystals: The role of nucleation rate in size control of CoPt3 nanocrystals. *Journal of the American Chemical Society* **2003,** 125, (30), 9090-9101.

258. Poddar, P.; Srinath, S.; Gass, J.; Prasad, B. L. V.; Srikanth, H., Magnetic transition and large magnetocaloric effect associated with surface spin disorder in Co and CocoreAgshell nanoparticles. *Journal of Physical Chemistry C* **2007,** 111, (38), 14060-14066.

259. Sun, S. H.; Murray, C. B., Synthesis of monodisperse cobalt nanocrystals and their assembly into magnetic superlattices (invited). *Journal of Applied Physics* **1999,** 85, (8), 4325-4330.

260. Petit, C.; Taleb, A.; Pileni, M. P., Cobalt nanosized particles organized in a 2D superlattice: Synthesis, characterization, and magnetic properties. *Journal of Physical Chemistry B* **1999,** 103, (11), 1805-1810.

261. Zhong, Z. Y.; Gates, B.; Xia, Y. N.; Qin, D., Soft lithographic approach to the fabrication of highly ordered 2D arrays of magnetic nanoparticles on the surfaces of silicon substrates. *Langmuir* **2000,** 16, (26), 10369-10375.

262. Maruszewski, K.; Jasiorski, M.; Hreniak, D.; Strek, W.; Hermanowicz, K.; Heiman, K., Raman spectra of molecules adsorbed on Ag centers in sol-gel matrices. *Journal of Sol-Gel Science and Technology* **2003,** 26, (1-3), 83-88.

263. Samson, J.; Varotto, A.; Nahirney, P. C.; Toschi, A.; Piscopo, I.; Drain, C. M., Fabrication of Metal Nanoparticles Using Toroidal Plasmid DNA as a Sacrificial Mold. *Acs Nano* **2009,** 3, (2), 339-344.

264. Hulteen, J. C.; Vanduyne, R. P., Nanosphere Lithography - A Materials General Fabrication Process for Periodic Particle Array Surfaces. *Journal of Vacuum Science & Technology a-Vacuum Surfaces and Films* **1995,** 13, (3), 1553-1558.

265. Haes, A. J.; Zhao, J.; Zou, S. L.; Own, C. S.; Marks, L. D.; Schatz, G. C.; Van Duyne, R. P., Solution-phase, triangular Ag nanotriangles fabricated by nanosphere lithography. *Journal of Physical Chemistry B* **2005,** 109, (22), 11158-11162.

266. Hulteen, J. C.; Treichel, D. A.; Smith, M. T.; Duval, M. L.; Jensen, T. R.; Van Duyne, R. P., Nanosphere lithography: Size-tunable silver nanoparticle and surface cluster arrays. *Journal of Physical Chemistry B* **1999,** 103, (19), 3854-3863.

267. Dimitrov, A. S.; Nagayama, K., Continuous Convective Assembling of Fine Particles into Two-Dimensional Arrays on Solid Surfaces. *Langmuir* **1996,** 12, (5), 1303-1311.

268. Holland, B. T.; Blanford, C. F.; Do, T.; Stein, A., Synthesis of highly ordered, three-dimensional, macroporous structures of amorphous or crystalline inorganic oxides, phosphates, and hybrid composites. *Chemistry of Materials* **1999,** 11, (3), 795-805.

269. Alivisatos, A. P., Semiconductor clusters, nanocrystals, and quantum dots. *Science* **1996,** 271, (5251), 933-937.

270. Sundaram, M.; Chalmers, S. A.; Hopkins, P. F.; Gossard, A. C., New Quantum Structures. *Science* **1991,** 254, (5036), 1326-1335.

271. Haynes, C. L.; Van Duyne, R. P., Nanosphere lithography: A versatile nanofabrication tool for studies of size-dependent nanoparticle optics. *Journal of Physical Chemistry B* **2001,** 105, (24), 5599-5611.

272. Weekes, S. M.; Ogrin, F. Y.; Murray, W. A., Fabrication of large-area ferromagnetic arrays using etched nanosphere lithography. *Langmuir* **2004,** 20, (25), 11208-11212.

273. Jiang, P., Surface-templated nanostructured films with two-dimensional ordered arrays of voids. *Angewandte Chemie-International Edition* **2004,** 43, (42), 5625-5628.

274. Wang, X. D.; Summers, C. J.; Wang, Z. L., Large-scale hexagonal-patterned growth of aligned ZnO nanorods for nano-optoelectronics and nanosensor arrays. *Nano Letters* **2004,** 4, (3), 423-426.

275. Bezryadin, A.; Dekker, C.; Schmid, G., Electrostatic trapping of single conducting nanoparticles between nanoelectrodes. *Applied Physics Letters* **1997,** 71, (9), 1273-1275.

276. Gorer, S.; Ganske, J. A.; Hemminger, J. C.; Penner, R. M., Size-selective and epitaxial electrochemical/chemical synthesis of sulfur-passivated cadmium sulfide nanocrystals on graphite. *Journal of the American Chemical Society* **1998,** 120, (37), 9584-9593.

277. Valsesia, A.; Colpo, P.; Silvan, M. M.; Meziani, T.; Ceccone, G.; Rossi, F., Fabrication of nanostructured polymeric surfaces for biosensing devices. *Nano Letters* **2004,** 4, (6), 1047-1050.

278. Klapetek, P. N., D.; Czech Metrology Institute: Czech Republic, 2007, http://gwyddion.net/.

279. Wilcox, D.; Dove, B.; McDavid, D.; Greer, D., *UTHSCSA Image Tool for Windows Version 3.00. The University of Texas Health Science Center: San Antonio, TX*

1995-2002.

280. Lin, F.; Meier, D. J., A study of latex film formation by atomic force microscopy. A comparison of wet and dry conditions *Langmuir* **1995,** 11, (7), 2726-2733.

281. Tzitzinou, A.; Keddie, J. L.; Geurts, J. M.; Peters, A.; Satguru, R., Film formation of latex blends with bimodal particle size distributions: Consideration of particle deformability and continuity of the dispersed phase. *Macromolecules* **2000,** 33, (7), 2695-2708.

282. Berkowitz, A. E.; Lahut, J. A.; Vanburen, C. E., Properties of magnetic fluid particles. *Ieee Transactions on Magnetics* **1980,** 16, (2), 184-190.

283. Taketomi, S.; Ukita, M.; Mizukami, M.; Miyajima, H.; Chikazumi, S., Magnetooptical effects of magnetic fluid. *Journal of the Physical Society of Japan* **1987,** 56, (9), 3362-3374.

284. Guillou, N.; Gao, Q.; Forster, P. M.; Chang, J. S.; Nogues, M.; Park, S. E.; Ferey, G.; Cheetham, A. K., Nickel(II) phosphate VSB-5: A magnetic nanoporous hydrogenation catalyst with 24-ring tunnels. *Angewandte Chemie-International Edition* **2001,** 40, (15), 2831-2834.

285. Lu, A. H.; Schmidt, W.; Matoussevitch, N.; Bonnemann, H.; Spliethoff, B.; Tesche, B.; Bill, E.; Kiefer, W.; Schuth, F., Nanoengineering of a magnetically separable hydrogenation catalyst. *Angewandte Chemie-International Edition* **2004,** 43, (33), 4303-4306.

286. Uehara, M.; Mori, S.; Chen, C. H.; Cheong, S. W., Percolative phase separation underlies colossal magnetoresistance in mixed-valent manganites. *Nature* **1999,** 399, (6736), 560-563.

287. Mornet, S.; Vasseur, S.; Grasset, F.; Duguet, E., Magnetic nanoparticle design for medical diagnosis and therapy. *Journal of Materials Chemistry* **2004,** 14, (14), 2161-2175.

288. Moser, A.; Takano, K.; Margulies, D. T.; Albrecht, M.; Sonobe, Y.; Ikeda, Y.; Sun, S. H.; Fullerton, E. E., Magnetic recording: advancing into the future. *Journal of Physics D-Applied Physics* **2002,** 35, (19), R157-R167.

289. Terris, B. D.; Thomson, T., Nanofabricated and self-assembled magnetic structures as data storage media. *Journal of Physics D-Applied Physics* **2005,** 38, (12), R199-R222.

290. Nyamjav, D.; Kinsella, J. M.; Ivanisevica, A., Magnetic wires with DNA cores: A magnetic force microscopy study. *Applied Physics Letters* **2005,** 86, (9).

291. Martin, Y.; Wickramasinghe, H. K., Magnetic Imaging by Force Microscopy with 1000-a Resolution. *Applied Physics Letters* **1987,** 50, (20), 1455-1457.

292. Porthun, S.; Abelmann, L.; Lodder, C., Magnetic force microscopy of thin film media for high density magnetic recording. *Journal of Magnetism and Magnetic Materials* **1998,** 182, (1-2), 238-273.

293. Hehn, M.; Padovani, S.; Ounadjela, K.; Bucher, J. P., Nanoscale magnetic domain structures in epitaxial cobalt films. *Physical Review B* **1996,** 54, (5), 3428-3433.

294. Belliard, L.; Miltat, J.; Thiaville, A.; Dubois, S.; Duvail, J. L.; Piraux, L., Observing magnetic nanowires by means of magnetic force microscopy. *Journal of Magnetism and Magnetic Materials* **1998,** 190, (1-2), 1-16.

295. Qin, D. H.; Lu, M.; Li, H. L., Magnetic force microscopy of magnetic domain structure in highly ordered Co nanowire arrays. *Chemical physical Letters* **2001,** 350, (1-2), 51-56.

296. Douglass, D. C.; Cox, A. J.; Bucher, J. P.; Bloomfield, L. A., Magnetic-Properties Of Free Cobalt And Gadolinium Clusters. *Physical Review letters B* **1993,** 47, 12874-12889.

297. Bonnemain, B., Superparamagnetic agents in magnetic resonance imaging: Physicochemical characteristics and clinical applications - A review *J. Drug Targeting* **1998,** 6, 167-174.

298. Hu, J.; Xiao, X. D.; Salmeron, M., Scanning Polarization Force Microscopy - A Technique for Imaging Liquids and Weakly Adsorbed Layers. *Applied Physcis Letters* **1995,** 67, 476-478.

299. Luna, M.; Rieutord, F.; Melman, N. A.; Dai, Q.; Salmeron, M., Adsorption of water on alkali halide surfaces studied by scanning polarization force microscopy. *Journal of physical Chemistry A* **1998,** 102, (34), 6793-6800.

300. Hu, J.; Carpick, R. W.; Salmeron, M.; Xiao, X. D., Imaging and manipulation of nanometer-size liquid droplets by scanning polarization force microscopy. *Journal of Vacuum Science & Technology a-Vacuum Surfaces and Films* **1996,** 14, 1341-1343.

301. Chou, S. Y.; Krauss, P. R.; Kong, L. S., Nanolithographically defined magnetic structures and quantum magnetic disk. *Journal of Applield Physics* **1996,** 79, 6101-6106.

302. Rugar, D.; Mamin, H. J.; Guethner, P.; Lambert, S. E.; Stern, J. E.; McFadyen, I.; Yogi, T., Magnetic Force Microscopy - General Principles and Application to Longitudinal Recording Media. *Journal of Applied Physics* **1990,** 68, 1169-1183.

303. Hehn, M.; Ounadjela, K.; Bucher, J. P.; Rousseaux, F.; Decanini, D.; Bartenlian, B.; Chappert, C., Nanoscale magnetic domains in mesoscopic magnets. *Science* **1996,** 272, 1782-1785.

304. Frisbie, C. D.; Rozsnyal, L. F.; Noy, A.; Wrighton, M. S.; Lieber, C. M., Functional Group Imaging by Chemical Force Microscopy. *Science* **1994,** 265, 2071-2074.

305. Noy, A.; Frisbie, C. D.; Rozsnyai, L. F.; Wrighton, M. S.; Lieber, C. M., Chemical Force Microscopy - Exploiting Chemically-Modified Tips to Quantify Adhesion, Friction, and Functional Group Distributions in Molecular Assemblies. *Journal of the American Chemical Society* **1995,** 117, 7943-7951.

306. Wold, D. J.; Frisbie, C. D., Fabrication and characterization of metal-molecule-metal junctions by conducting probe atomic force microscopy *Journal of the American Chemical Society* **2001,** 123, 5549-5556.

307. Wold, D. J.; Haag, R.; Rampi, M. A.; Frisbie, C. D., Distance dependence of electron tunneling through self-assembled monolayers measured by conducting probe atomic force microscopy: Unsaturated versus saturated molecular junctions. *Journal of Physical Chemistry B* **2002,** 106, 2813-2816.

308. Kelley, T. W.; Granstrom, E. L.; Frisbie, C. D., Conducting probe atomic force microscopy: A characterization tool for molecular electronics *Advanced Materials* **1999,** 11, 261.

309. Rawlett, A. M.; Hopson, T. J.; Nagahara, L. A.; Tsui, R. K.; Ramachandran, G. K.; Lindsay, S. M., Electrical measurements of a dithiolated electronic molecule via conducting atomic force microscopy. *Applied Physcis Letters* **2002,** 81, 3043-3045.

310. Garcia, R.; Perez, R., Dynamic atomic force microscopy methods *Surface Science Reports* **2002,** 47, 197-301.

311. Magonov, S. N.; Reneker, D. H., Characterization of polymer surfaces with atomic force microscopy *Annual Review of Materials Research* **1997,** 27, 175-222.

312. McLean, R. S.; Sauer, B. B., Tapping-mode AFM studies using phase detection for resolution of nanophases in segmented polyurethanes and other block copolymers. *Macromolecules* **1997,** 30, 8314-8317.

313. Putman, C. A. J.; Vanderwerf, K. O.; Degrooth, B. G.; Vanhulst, N. F.; Greve, J., Viscoelasticity of Living Cells Allows High-Resolution Imaging by Tapping Mode Atomic-Force Microscopy. *Biophysical Journal* **1994,** 67, 1749-1753.

314. Winkler, R. G.; Spatz, J. P.; Sheiko, S.; Moller, M.; Reineker, P.; Marti, O., Imaging material properties by resonant tapping-force microscopy: A model investigation *Physical Review B* **1996,** 54, 8908-8912.

315. Noy, A.; Sanders, C. H.; Vezenov, D. V.; Wong, S. S.; Lieber, C. M., Chemically-sensitive imaging in tapping mode by chemical force microscopy: Relationship between phase lag and adhesion. *Langmuir* **1998,** 14, 1508-1511.

316. Wilcox, D.; Dove, B.; McDavid, D.; Greer, D., *UTHSCSA Image Tool for Windows Version 3.00. The University of Texas Health Science Center: San Antonio, TX.* **1995-2002**.

317. Hao, E.; Sibrian-Vazquez, M.; Serem, W.; Garno, J. C.; Fronczek, F. R.; Vicente, M. G. H., Synthesis, aggregation and cellular investigations of porphyrin-cobaltacarborane conjugates. *Chemistry-a European Journal* **2007,** 13, (32), 9035-9042.

318. Bae, C.; Shin, H. J.; Moon, J.; Sung, M. M., Contact area lithography (CAL): A new approach to direct formation of nanometric chemical patterns. *Chemistry of Materials* **2006,** 18, (5), 1085-1088.

319. Jun, Y.; Huh, Y.-M.; Choi, J.-S.; Lee, J.-H.; Song, H.-T.; Kim, S. J.; Yoon, S.; Kim, K.-S.; Suh, J.-S.; Cheon, J., Nanoscale size effect of magnetic nanocrystals and their utilziation for cancer diagnosis via magnertic resonance imaging. *Journal of the American Chemical Society* **2005,** 127, 5732-5733.

320. Baker, G. A.; Baker, S. N.; Pandey, S.; Bright, F. V., An analytical view of ionic liquids. *Analyst* **2005,** 130, (6), 800-808.

321. Rogers, R. D.; Seddon, K. R., Ionic liquids - Solvents of the future? *Science* **2003,** 302, (5646), 792-793.

322. Olivier-Bourbigou, H.; Magna, L.; Morvan, D., Ionic liquids and catalysis: Recent progress from knowledge to applications. *Applied Catalysis a-General* **2010,** 373, (1-2), 1-56.

323. Plechkova, N. V.; Seddon, K. R., Applications of ionic liquids in the chemical industry. *Chemical Society Reviews* **2008,** 37, (1), 123-150.

324. Greaves, T. L.; Drummond, C. J., Protic ionic liquids: Properties and applications. *Chemical Reviews* **2008,** 108, (1), 206-237.

325. Hayashi, S.; Hamaguchi, H. O., Discovery of a magnetic ionic liquid [bmim]FeCl4. *Chemistry Letters* **2004,** 33, (12), 1590-1591.

326. Krieger, B. M.; Lee, H. Y.; Emge, T. J.; Wishart, J. F.; Castner, E. W., Ionic liquids and solids with paramagnetic anions. *Physical Chemistry Chemical Physics* 12, (31), 8919-8925.

327. Yoshida, Y.; Saito, G. Z., Influence of structural variations in 1-alkyl-3-methylimidazolium cation and tetrahalogenoferrate(III) anion on the physical properties of the paramagnetic ionic liquids. *Journal of Materials Chemistry* **2006,** 16, (13), 1254-1262.

328. Okuno, M.; Hamaguchi, H. O.; Hayashi, S., Magnetic manipulation of materials in a magnetic ionic liquid. *Applied Physics Letters* **2006,** 89, (13).

329. Abbott, A. P.; Capper, G.; Davies, D. L.; Rasheed, R., Ionic liquids based upon metal halide/substituted quaternary ammonium salt mixtures. *Inorganic Chemistry* **2004,** 43, (11), 3447-3452.

330. Tang, S.; Babai, A.; Mudring, A. V., Europium-based ionic liquids as luminescent soft materials. *Angewandte Chemie-International Edition* **2008,** 47, (40), 7631-7634.

331. Mallick, B.; Balke, B.; Felser, C.; Mudring, A. V., Dysprosium room-temperature ionic liquids with strong luminescence and response to magnetic fields. *Angewandte Chemie-International Edition* **2008,** 47, (40), 7635-7638.

332. Klapetek, P. N., D. Czech Metrology Institute: Czech Republic, 2007, http://gwyddion.net/. **2007**.

333. Maurer, K., Historical background of Alzheimer's research done 100 years ago. *Journal of Neural Transmission* **2006,** 113, (11), 1597-1601.

334. Jellinger, K. A., Alzheimer 100 - highlights in the history of Alzheimer research. *Journal of Neural Transmission* **2006,** 113, (11), 1603-1623.

335. Cohen, F. E.; Kelly, J. W., Therapeutic approaches to protein-misfolding diseases. *Nature* **2003,** 426, (6968), 905-909.

336. Agorogiannis, E. I.; Agorogiannis, G. I.; Papadimitriou, A.; Hadjigeorgiou, G. M., Protein misfolding in neurodegenerative diseases. *Neuropathology and Applied Neurobiology* **2004,** 30, (3), 215-224.

337. Selkoe, D. J., The molecular pathology of Alzheimer's disease. *Neuron* **1991,** 6, (4), 487-98.

338. Iversen, L. L.; Mortishire-Smith, R. J.; Pollack, S. J.; Shearman, M. S., The toxicity in vitro of b-amyloid protein. *Biochemical Journal* **1995,** 311, (1), 1-16.

339. Seubert, P.; Vigo-Pelfrey, C.; Esch, F.; Lee, M.; Dovey, H.; Davis, D.; Sinha, S.; Schlossmacher, M.; Whaley, J.; et al., Isolation and quantification of soluble Alzheimer's b-peptide from biological fluids. *Nature (London, United Kingdom)* **1992,** 359, (6393), 325-7.

340. Pitschke, M.; Prior, R.; Haupt, M.; Riesner, D., Detection of single amyloid beta-protein aggregates in the cerebrospinal fluid of Alzheimer's patients by fluorescence correlation spectroscopy. *Nature Medicine* **1998,** 4, (7), 832-834.

341. Ghanta, J.; Shen, C.-L.; Kiessling, L. L.; Murphy, R. M., A strategy for designing inhibitors of b-amyloid toxicity. *Journal Of Biological Chemistry* **1996,** 271, (47), 29525-29528.

342. Pike, C. J.; Burdick, D.; Walencewicz, A. J.; Glabe, C. G.; Cotman, C. W., Neurodegeneration induced by b-amyloid peptides in vitro: the role of peptide assembly state. *Journal Of Neuroscience* **1993,** 13, (4), 1676-87.

343. Pike, C. J.; Walencewicz, A. J.; Glabe, C. G.; Cotman, C. W., Invitro aging of beta-amyloid protein causes peptide aggregation and neurotoxicity. *Brain Research* **1991,** 563, (1-2), 311-314.

344. Simmons, L. K.; May, P. C.; Tomaselli, K. J.; Rydel, R. E.; Fuson, K. S.; Brigham, E. F.; Wright, S.; Lieberburg, I.; Becker, G. W.; Brems, D. N.; Li, W. Y., Secondary structure of amyloid beta-peptide correlates with neurotoxic activity in-vitro *Molecular Pharmacology* **1994,** 45, (3), 373-379.

345. Lin, H.; Zhu, Y. W. J.; Lal, R., Amyloid beta protein (1-40) forms calcium-permeable, Zn2+-sensitive channel in reconstituted lipid vesicles. *Biochemistry* **1999,** 38, (34), 11189-11196.

346. Mastrangelo Iris, A.; Ahmed, M.; Sato, T.; Liu, W.; Wang, C.; Hough, P.; Smith Steven, O., High-resolution atomic force microscopy of soluble Abeta42 oligomers. *Journal of Molecular Biology* **2006,** 358, (1), 106-19.

347. Barrow, C. J.; Zagorski, M. G., Solution structures of beta peptide and its constituent fragments: relation to amyloid deposition. *Science* **1991,** 253, (5016), 179-82.

348. Hilbich, C.; Kisters-Woike, B.; Reed, J.; Masters, C. L.; Beyreuther, K., Aggregation and secondary structure of synthetic amyloid beta A4 peptides of Alzheimer's disease. *Journal of Molecular Biology* **1991,** 218, (1), 149-63.

349. Yang, D. S.; Yip, C. M.; Huang, T. H.; Chakrabartty, A.; Fraser, P. E., Manipulating the amyloid-beta aggregation pathway with chemical chaperones. *Journal Of Biological Chemistry* **1999,** 274, (46), 32970-4.

350. Lee, S.; Fernandez, E. J.; Good, T. A., Role of aggregation conditions in structure, stability, and toxicity of intermediates in the A beta fibril formation pathway. *Protein Science* **2007,** 16, (4), 723-732.

351. Yip Christopher, M.; Darabie Audrey, A.; McLaurin, J., Abeta42-peptide assembly on lipid bilayers. *Journal of Molecular Biology* **2002,** 318, (1), 97-107.

352. Stine, W. B.; Snyder, S. W.; Ladror, U. S.; Wade, W. S.; Miller, M. F.; Perun, T. J.; Holzman, T. F.; Krafft, G. A., The nanometer-scale structure of amyloid-beta visualized by atomic force microscopy. *Journal of Protein Chemistry* **1996,** 15, (2), 193-203.

353. Esler, W. P.; Stimson, E. R.; Ghilardi, J. R.; Vinters, H. V.; Lee, J. P.; Mantyh, P. W.; Maggio, J. E., In vitro growth of Alzheimer's disease beta-amyloid plaques displays first-order kinetics. *Biochemistry* **1996,** 35, (3), 749-57.

354. Maggio, J. E.; Stimson, E. R.; Ghilardi, J. R.; Allen, C. J.; Dahl, C. E.; Whitcomb, D. C.; Vigna, S. R.; Vinters, H. V.; Labenski, M. E.; Mantyh, P. W., Reversible in vitro growth of Alzheimer disease beta-amyloid plaques by deposition of labeled amyloid peptide. *Proceedings of the National Academy of Sciences of the United States of America* **1992,** 89, (12), 5462-6.

355. Lomakin, A.; Chung, D. S.; Benedek, G. B.; Kirschner, D. A.; Teplow, D. B., On the nucleation and growth of amyloid beta-protein fibrils: Detection of nuclei and

quantitation of rate constants. *Proceedings of the National Academy of Sciences of the United States of America* **1996,** 93, (3), 1125-1129.

356. Jarrett, J. T.; Berger, E. P.; Lansbury, P. T., Jr., The carboxy terminus of the b amyloid protein is critical for the seeding of amyloid formation: Implications for the pathogenesis of Alzheimer's disease. *Biochemistry* **1993,** 32, (18), 4693-7.

357. Harper, J. D.; Lieber, C. M.; Lansbury, P. T., Jr., Atomic force microscopic imaging of seeded fibril formation and fibril branching by the Alzheimer's disease amyloid-beta protein. *Chemistry & Biology* **1997,** 4, (12), 951-959.

358. Kusumoto, Y.; Lomakin, A.; Teplow, D. B.; Benedek, G. B., Temperature dependence of amyloid beta-protein fibrillization. *Proceedings of the National Academy of Sciences of the United States of America* **1998,** 95, (21), 12277-12282.

359. Kad, N. M.; Myers, S. L.; Smith, D. P.; Smith, D. A.; Radford, S. E.; Thomson, N. H., Hierarchical assembly of beta(2)-microglobulin amyloid in vitro revealed by atomic force microscopy. *Journal of Molecular Biology* **2003,** 330, (4), 785-797.

360. Khurana, R.; Ionescu-Zanetti, C.; Pope, M.; Li, J.; Nielson, L.; Ramirez-Alvarado, M.; Regan, L.; Fink, A. L.; Carter, S. A., A general model for amyloid fibril assembly based on morphological studies using atomic force microscopy. *Biophysical Journal* **2003,** 85, (2), 1135-1144.

361. Harper, J. D.; Wong, S. S.; Lieber, C. M.; Lansbury, P. T., Observation of metastable Aβ amyloid protofibrils by atomic force microscopy. *Chemistry & Biology* **1997,** 4, 119-125.

362. Mason, J. M.; Kokkoni, N.; Stott, K.; doig, A. J., Design strategies for anti-amyloid agents. *Current Opinion in Chemical Biology* **2003,** 13, 526-532.

363. Stains, C. I.; Mondal, K.; Ghosh, I., Molecules that Target beta-Amyloid. *ChemMedChem* **2007,** 2, 1674-1692.

364. Ionescu-Zanetti, C.; Khurana, R.; Gillespie, J. R.; Petrick, J. S.; Trabachino, L. C.; Minert, L. J.; Carter, S. A.; Fink, A. L., Monitoring the assembly of Ig light-chain amyloid fibrils by atomic force microscopy. *Proceedings of the National Academy of Sciences of the United States of America* **1999,** 96, 13175-13179.

365. Stromer, T.; Serpell, L. C., Structure and morphology of the Alzheimer's amyloid fibril. *Microscopy Research and Technique* **2005,** 67, (3-4), 210-217.

366. Shekhawat, G. S.; Lambert, M. P.; Sharma, S.; Velasco, P. T.; Viola, K. L.; Klein, W. L.; Dravid, V. P., Soluble state high resolution atomic force microscopy study of Alzheimer's β-amyloid oligomers. *Applied Physics Letters* **2009,** 95, 183701.

367. Nichols, M. R.; Moss, M. A.; Reed, D. K.; Hoh, J. H.; Rosenberry, T. L., Amyloid-β aggregates formed at polar-nonpolar interfaces differ from amyloid-β protofibrils produced in aqueous buffers. *Microscopy Research and Technique* **2005,** 67, (3-4), 164-174.

368. Yip, C. M.; Darabie, A. A.; McLaurin, J., Aβ42-Peptide Assembly on Lipid Bilayers. *Journal of Molecular Biology* **2002,** 318, (1), 97-107.

369. Ha, C.; Ryu, J.; Park, C. B., Metal Ions Differentially Influence the Aggregation and Deposition of Alzheimer's β-Amyloid on a Solid Template. *Biochemistry* **2007,** 46, 6118-6125.

370. Ryu, J.; Joung, H.-A.; Kim, M.-G.; Park, C. B., Surface Plasmon Resonance Analysis of Alzheimer's β-Amyloid Aggregation on a Solid Surface: From Monomers to Fully-Grown Fibrils. *Analytical Chemistry* **2008,** 80, 2400-2407.

371. Liu, R.; Yuan, B.; Emadi, S.; Zameer, A.; Schulz, P.; McAllister, C.; Lyubchenko, Y.; Goud, G.; Sierks, M. R., Single Chain Variable Fragments against β-Amyloid (Aβ) Can Inhibit Aβ Aggregation and Prevent Aβ-Induced Neurotoxicity. *Biochemistry* **2004,** 43, 6959-6967.

372. LeVine, H., Thioflavine T interaction with B-amyloid -sheet structures. *Amyloid: lnternational Journal of Experiments and Clinical Investigation* **1995,** 2, 1-6.

373. LeVine, H., Thioflavine T interaction with synthetic Alzheimer's disease B-amyloid peptides: Detection of amyloid aggregation in solution. *Protein Science* **1993,** 2, 404-410.

374. Naiki, H.; Gejyo, F.; Nakakuki, K., Concentration-Dependent Inhibitory Effects of Apolipoprotein E on Alzheimer's Î²-Amyloid Fibril Formation in Vitroâ€ *Biochemistry* **1997,** 36, (20), 6243-6250.

375. Goldsbury, C. S.; Wirtz, S.; Müller, S. A.; Sunderji, S.; Wicki, P.; Aebi, U.; Frey, P., Studies on the in Vitro Assembly of A[beta] 1-40: Implications for the Search for A[beta] Fibril Formation Inhibitors. *Journal of Structural Biology* **2000,** 130, (2-3), 217-231.

376. Walsh, D. M.; Lomakin, A.; Benedek, G. B.; Condron, M. M.; Teplow, D. B., Amyloid β-Protein Fibrillogenesis. Detection of a protofibrillar intermediate. *Journal Of Biological Chemistry* **1997,** 272, 22364-22372.

377. Gosal, W. S.; Clark, A. H.; Ross-Murphy, S. B., Fibrillar beta-lactoglobulin gels: Part 1. Fibril formation and structure. *Biomacromolecules* **2004,** 5, (6), 2408-2419.

378. Nichols, M. R.; Moss, M. A.; Reed, D. K.; Cratic-McDaniei, S.; Hoh, J. H.; Rosenberry, T. L., Amyloid-beta protofibrils differ from Amyloid-beta aggregates induced in dilute hexafluoroisopropanol in stability and morphology. *Journal Of Biological Chemistry* **2005,** 280, (4), 2471-2480.

379. Paravastu, A. K.; Petkova, A. T.; Tycko, R., Polymorphic fibril formation by residues 10-40 of the Alzheimer's beta-amyloid peptide. *Biophysical Journal* **2006,** 90, (12), 4618-4629.

380. Nichols, M. R.; Moss, M. A.; Reed, D. K.; Lin, W.-L.; Mukhopadhyay, R.; Hoh, J. H.; Rosenberry, T. L., Growth of β-amyloid (1-40) protofibrils by monomer elongation and lateral association. Characterization of distinct products by light scattering and atomic force microscopy. *Biochemistry* **2002,** 41, 6115-6127.

381. Goldsbury, C. S.; Wirtz, S.; Muller, S. A.; Sunderji, S.; Wicki, P.; Aebi, U.; Frey, P., Studies on the in Vitro Assembly of Aβ 1–40: Implications for the Search for Aβ Fibril Formation Inhibitors. *Journal of Structural Biology* **2000,** 130, 217-231.

382. Fox, M. A., Fundamentals in the Design of Molecular Electronic Devices: Long-Range Charge Carrier Transport and Electronic Coupling *Accounts of Chemical Research* **1999,** 32, 201-207.

383. Liu, C.-Y.; Pan, H.-L.; Fox, M. A.; Bard, A. J., High-Density Nanosecond Charge Trapping in Thin-Films of the Photoconductor ZnODEP. *Science* **1993,** 261, 897-899.

384. Adams, D. M.; Kerimo, J.; Liu, C.-Y.; Bard, A. J.; Barbara, P. F., Electric field modulated near-field photo-luminescence of organic thin films *Journal of Physical Chemistry B* **2000,** 104, 6728-6736.

385. Kimura, M.; Saito, Y.; Ohta, K.; Hanabusa, K.; Shirai, H.; Kobayashi, N., Self-Organization of Supramolecular Complex Composed of Rigid Dendritic Porphyrin and Fullerene *Journal of the American Chemical Society* **2002,** 124, 5274-5275.

386. Burrows, H. D.; Gonsalves, A. M. R.; Leitao, M. L. P.; Miguel, M. D. G.; Pereira, M. M., Phase transitions and self-assembly in meso-tetrakis(undecyl)porphyrin *Supramolecular Science* **1997,** 4, 241-246.

387. Tsuda, A.; Osuka, A., Fully Conjugated Porphyrin Tapes with Electronic Absorption Bands That Reach into Infrared. *Science* **2001,** 293, 79-82.

388. Inabe, T.; Tajima, H., PhthalocyaninessVersatile Components of Molecular Conductors. *Chemical Reviews* 104, 5503-5533.

389. vanNostrum, C. F.; Picken, S. J.; Schouten, A.-J.; Nolte, R. J. M., Synthesis and Supramolecular Chemistry of Novel Liquid Crystalline Crown Ether-Substituted Phthalocyanines: Toward Molecular Wires and Molecular Ionoelectronics. *Journal of the American Chemical Society* **1995,** 117, 9957-9965.

390. Hietschold, M.; Lackinger, M.; Griessl, S.; Heckl, W. M.; Gopakumar, T. G.; Flynn, G. W., Molecular structures on crystalline metallic surfaces – From STM images to molecular electronics. *Microelectronic Engineering* **2005,** 82, 207-214.

391. Reimers, J. R.; Hall, L. E.; Crossley, M. J.; Hush, N. S., Rigid fused Oligoporphyrins as Potential Versatile Molecular Wires. 2. B3LYP and SCF Calculated Geometric and Electronic Properties of 98 Oligoporphyrin and Related Molecules. *Jornal of Physical Chemistry A* **1999,** 103, 4385-4397.

392. Jiao, J.; Anariba, F.; Tiznado, H.; Schmidt, I.; Lindsey, J. S.; Zaera, F.; Bocian, D. F., Stepwise Formation and Characterization of Covalently Linked Multiporphyrin-Imid Architectures on Si(100). *Journal of the American Chemical Society* **2006,** 128, 6965-6974.

393. Roth, K. M.; Liu, Z.; Gryko, D. T.; Clausen, C.; Lindsey, J. S.; Bocian, D. F.; Kuhr, W. G., Ch. 5, Charge-Retention Characteristics of Self-Assembled Monolayers of Molecular-

Wire-Linked Porphyrins on Gold. In *Molecules as Components of Electronic Devices*, Lieberman, M., Ed. Oxford University Press: Washington DC, 2003.

394. Liu, C.-Y.; Pan, H. L.; Fox, M. A.; Bard, A. J., Reversible charge trapping/detrapping in a photoconductive insulator of liquid crystal zinc porphyrin. *Chemistry of Materials* **1997,** 9, 1422-1429.

395. Roth, K. M.; Dontha, N.; Dabke, R. B.; Gryko, D. T.; Clausen, C.; Lindsey, J. S.; Bocian, D. F.; Kuhr, W. G., Molecular approach toward information storage based on the redox properties of porphyrins in self-assembled monolayers. *Journal of Vacuum Science & Technology a-Vacuum Surfaces and Films* **2000,** 18, 2359.

396. Malinski, T.; Taha, Z., Nitric-Oxide Release from a Single Cell Measured In Situ by a Porphyrinic-Based Microsensor. *Nature* **1992,** 358, 676-678.

397. Filippini, D.; Alimelli, A.; Natale, C. D.; Paolesse, R.; D'Amico, A.; Lundstrom, I., Chemical Sensing with Familiar Devices. *Angewandte Chemie International Edition* **1999,** 45, 3800-3803.

398. Maree, C. H. M.; Roosendaal, S. J.; Savenije, T. J.; Schropp, R. E. I.; Schaafsma, T. J.; Habraken, F. H. P. M., Photovoltaic effects in porphyrin polymer films and heterojunctions. *Journal of Applied Physics* **1996,** 80, 3381-3389.

399. Murata, K.; Ito, S.; Takahashi, K.; Hoffman, B. M., Photocurrent from photocorrosion of aluminum electrode in porphyrin/Al Schottky-barrier cells. *Applied Physcis Letters* **1997,** 71, 674-676.

400. Harima, Y.; Okazaki, H.; Kunugi, Y.; Yamashita, K.; Ishii, H.; Seki, K., Formation of Schottky barriers at interfaces between metals and molecular semiconductors of p- and n-type conductances *Applied Physcs Letters* **1996,** 69, 1059-1061.

401. Chowdhury, A.; Chowdhury, J.; Pal, P.; Pal, A. J., Light-emitting diodes from molecularly thin porphyrin derivative: Effect of molecular packing. *Solid State Communications* **1998,** 107, 725-729.

402. Baldo, M. A.; O'Brien, D. F.; You, Y.; Shoustikov, A.; Sibley, S.; Thompson, M. E.; Forrest, S. R., Highly efficient phosphorescent emission from organic electroluminescent devices. *Nature* **1998,** 395, 151-154.

403. Kwong, R. C.; Sibley, S.; Dubovoy, T.; Baldo, M.; Forrest, S. R.; Thompson, M. E., Efficient, saturated red organic light emitting devices based on phosphorescent platinum(II) porphyrins. *Chemistry of Materials* **1999,** 11, 3709-3713.

404. Sendt, K.; Johnston, L. A.; Hough, W. A.; Crossley, M. J.; Hush, N. S.; Reimers, J. R., Switchable Electronic Coupling in Model Oligoporphyrin Molecular Wires Examined through the Measurement and Assignment of Electronic Absorption Spectra. *Journal of the American Chemical Society* **2002,** 124, 9299-9309.

405. Reimers, J. R.; Lu, T. X.; Crossley, M. J.; Hush, N. S., Molecular electronic properties of fused rigid porphyrin-oligomer molecular wires *Chemical physical Letters* **1996,** 256, 353-359.

406. Robertson, N.; McGowan, C. A., A comparison of potential molecular wires as components for molecular electronics. *Chemical Society Reviews* **2003,** 32, 96-103.

407. Kang, B. K.; Aratani, N.; Lim, J. K.; Kim, D.; Osuka, A.; Yoo, K.-H., Electrical transport properties and their reproducibility for linear porphyrin arrays. *Materials Science and Engineering C* **2006,** 26, 1023-1027.

408. Kang, B. K.; Aratani, N.; Lim, J. K.; Kim, D.; Osuka, A.; Yoo, K.-H., Length and temperature dependence of electrical conduction through dithiolated porphyrin arrays. *Chemical physical Letters* **2005,** 412, 303-306.

409. Sedghi, G.; Sawada, K.; Esdaile, L. J.; Hoffmann, M.; Anderson, H. L.; Bethell, D.; Haiss, W.; Higgins, S. J.; Nichols, R. J., Single Molecule Conductance of Porphyrin Wires with Ultralow Attenuation. *Journal of the American Chemical Society* **2008,** web release.

410. Yanov, I.; Kholod, Y.; Leszczynski, J.; Palacios, J. J., Electron transport properties of the porphyrin molecule located between gold electrodes. *Chemical physical Letters* **2007,** 445, 238-242.

411. Choi, J.; Chipara, M.; Xu, B.; Yang, C. S.; Doudin, B.; Dowben, P. A., Comparison of the pi-conjugated ring orientations in polyaniline and polypyrrole *Chemical Physics Letters* **2004,** 343, 193.

412. Auwarter, W.; Weber-Bargioni, A.; Riemann, A.; Schiffrin, A.; Groning, O.; Fasel, R.; Barth, J. V., Self-assembly and conformation of tetrapyridyl-porphyrin molecules on Ag(111). *Journal of Chemical Physics* **2006,** 124, 194708.

413. Venkataraman, L.; Klare, J. E.; Nuckolls, C.; Hybertsen, M. S.; Steigerwald, M. L., Dependence of single-molecule junction conductance on molecular conformation. *Nature* **2006,** 442, 904-907.

414. Kornilovitch, P. E.; Bratkovsky, A. M., Orientational dependence of current through molecular films. *Physical Review B* **2001,** 64, 195413.

415. Ogaki, K.; Batina, N.; Kunitake, M.; Itaya, K., In Situ Scanning Tunneling Microscopy of Ordering Processes of Adsorbed Porphyrin on Iodine-Modified Ag(111). *Journal of Physical Chemistry* **1996,** 100, 7185-7190.

416. Vaughan, O. P. H.; Turner, M.; Williams, F. J.; Hille, A.; Sanders, J. K. M.; Lambert, R. M., Direct Observation of Surface-Mediated Thioacetyl Deprotection: Covalent Tethering of a Thiol-Terminated Porphyrin to the Ag(100) Surface. *Journal of the American Chemical Society* **2006,** ASAP article.

417. Jung, T. A.; Schlittler, R. R.; Gimzewski, J. K.; Tang, H.; Joachim, C., Controlled room-temperature positioning of individual molecules: Molecular flexure and motion *Science* **1996,** 271, 181-184.

418. Guo, X.-L.; Dong, Z.-C.; Trifonov, A. S.; Miki, K.; Kimura, K.; Mashiko, S., STM-induced light emission from the surface of H_2TBP porphyrin/PFP porphyrin/Cu(1 0 0). *Applied Surface Science* **2005,** 241, 28-32.

419. Scudiero, L.; Barlow, D. E.; Hipps, K. W., Physical Properties and Metal Ion Specific Scanning Tunneling Microscopy Images of Metal(II) Tetraphenylporphyrins Deposited from Vapor onto Gold (111) *Journal of Pysical Chemistry B* **2000,** 104, 11899-11905.

420. Yoshimoto, S.; Yokoo, N.; Fukuda, T.; Kobayashi, N.; Itaya, K., Formation of highly ordered porphyrin adlayers induced by electrochemical potential modulation. *Chemical Communication* **2006**, 500-502.

421. Wan, L.-J.; Shundo, S.; Inukai, J.; Itaya, K., Ordered Adlayers of Organic Molecules on Sulfur-Modified Au(111): In Situ Scanning Tunneling Microscopy Study. *Langmuir* **2000,** 16, 2164-2168.

422. Arima, V.; Fabiano, E.; Blyth, R. I. R.; Sala, F. D.; Matino, F.; Thompson, J.; Cingolani, R.; Rinaldi, R., Self-Assembled Monolayers of Cobalt(II)-(4- tert-Butylphenyl)-Porphyrins: The Influence of the Electronic Dipole on Scanning Tunneling Microscopy Images. *Journal of the American Chemical Society* **2004,** 126, 16951-16958.

423. Terui, T.; Yokoyama, S.; Suzuki, H.; Mashiko, S.; Sakurai, M.; Moriwaki, T., Structures of thin films of tertiary-phenyl-porphyrin derivatives on gold surface. *Thin Solid Films* **2006,** 499, 157-160.

424. He, Y.; Ye, T.; Borguet, E., Porphyrin Self-Assembly at Electrochemical Interfaces: Role of Potential Modulated Surface Mobility. *Journal of the American Chemical Society* **2002,** 124, 11964-11970.

425. Otsuki, J.; Kawaguchi, S.; Yamakawa, T.; Asakawa, M.; Miyake, K., Arrays of Double-Decker Porphyrins on Highly Oriented Pyrolytic Graphite. *Langmuir* **2006,** 22, 5708-5715.

426. Tao, N. J.; Cardenas, G.; Cunha, F.; Shi, Z., In Situ STM and AFM Study of Protoporphyrin and Iron(II1) and Zinc(I1) Protoporphyrins Adsorbed on Graphite in Aqueous Solutions. *Langmuir* **1995,** 11, 4445-4448.

427. Zhou, Y.; Wang, B.; Zhu, M.; Hou, J. G., Observation of co-existence of 'face-on' and 'edge-on' stacking styles in a porphyrin monolayer. *Chemical physical Letters* **2005,** 403, 140-145.

428. Ohshiro, T.; Ito, T.; Philippe Buhlmann; Umezawa, Y., Scanning Tunneling Microscopy with Chemically Modified Tips: Discrimination of Porphyrin Centers Based on Metal Coordination and Hydrogen Bond Interactions. *Analytical Chemistry* **2001,** 73, 878-883.

429. Lensen, M. C.; Dingenen, S. J. T. v.; Elemans, J. A. A. W.; Dijkstra, H. P.; Klink, G. P. M. v.; Koten, G. v.; Gerritsen, J. W.; Speller, S.; Noltea, R. J. M.; Rowan, A. E., Synthesis and self-assembly of giant porphyrin discs. *Chemical Communication* **2004**, 762-763.

430. Ngunjiri, J. N.; Kelley, A. T.; LeJeune, Z. M.; Li, J.-R.; Lewandowski, B.; Serem, W. K.; Daniels, S. L.; Lusker, K. L.; Garno, J. C., Achieving precision and reproducibility for writing patterns of n-alkanethiol SAMs with automated nanografting. *Scanning* **2008,** 30, 123-136.

431. Yu, J.-J. N., J. N.; Kelley, A. T.; Garno, J. C., Nanografting versus Solution Self-Assembly of α,ω-Alkanedithiols on Au(111). *Langmuir* **2008,** 24, 11661-11668.

432. Auer, F.; Scotti, M.; Jordan, R.; Sellergren, B.; Garno, J. C.; Liu, G.-Y.; Ulman, A., Nanocomposites by Electrostatic Interactions: 1. Impact of Sublayer Quality on the Organization of Functionalized Nanoparticles at Charged Self-Assembled Layers. *Langmuir* **2000,** 16, 7554-7557.

433. Garno, J. C.; Yang, Y.; Amro, N. A.; Cruchon-Dupeyrat, S.; Chen, S.; Liu, G.-Y., Precise Positioning of Nanoparticles on Surfaces Using Scanning Probe Lithography. *Nano Letters* **2003,** 3, 389-395.

434. Stamm, K.; Garno, J. C.; Liu, G.-Y.; Brock, S. A., General Methodology for the Synthesis of Transition Metal Pnictide Nanoparticles from Pnictate Precursors and its Application to the Iron-Phosphorus Phase Diagram (communication). *Journal of the American Chemical Society* **2003,** 125, 4038-4039.

435. Baldwin, R.; Pettigrew, K.; Garno, J. C.; Power, P.; Liu, G.-Y.; Kauzlarich, S. M., Solution Synthesis of Alkyl Capped Tetrahedral Prisms of Si Nanoparticles (*communication*). *Journal of the American Chemical Society* **2002,** 124, 1150-1151.

436. Xu, S.; Laibinis, P. E.; Liu, G.-Y., Accelerating the kinetics of thiol self-assembly on gold - a spatial confinement effect. *Journal of the American Chemical Society* **1998,** 120, (36), 9356-9361.

437. Ryu, S.; Schatz, G., Nanografting: modeling and simulation. *Journal of the American Chemical Society* **2006,** 128, (35), 11563-11573.

APPENDIX A: PROTOCOL FOR DYNAMIC CHARACTERIZATIONS OF NANOMATERIALS USING MSM-AFM

I. *Cable Connections*. The configuration for MSM-AFM is accomplished using contact mode. The MSM phase and amplitude image channels associated with MSM-AFM are obtained with two extra cable connections. The first cable is connected from the **AUX** input of the head electronic box to the **PHASE** input of the MAC/AC controller. The second cable is connected from **AMPLITUDE** output of MAC/AC controller to the **AUX IN** in the PicoSPM II controller (Figure A.1).

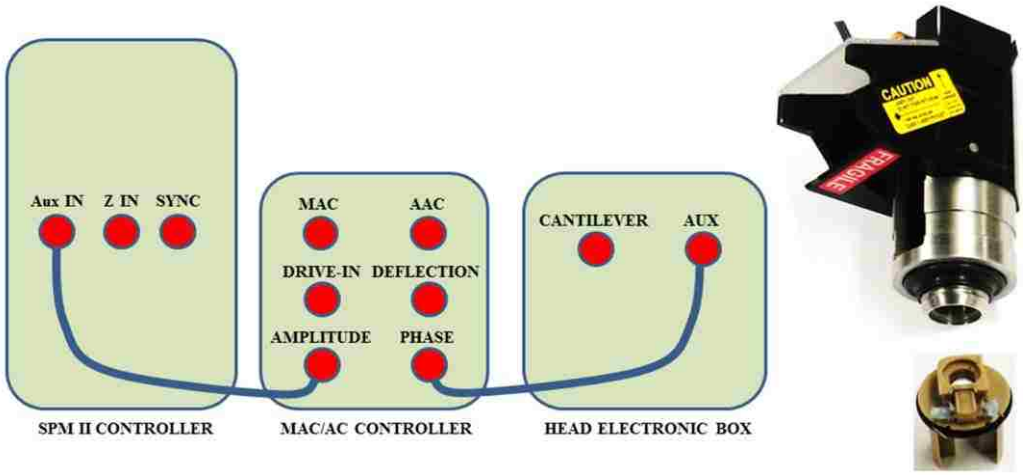

Figure A.1 Cable settings, connections, scanner and nosecone for magnetic sample modulation AFM.

II. *Hardware*. The magnetic AC (MAC) sample plate is used to generate the electromagnetic field for actuation of magnetic nanomaterials. A plastic nosecone without any magnetic parts is used for MSM-AFM measurements (Figure A.2).

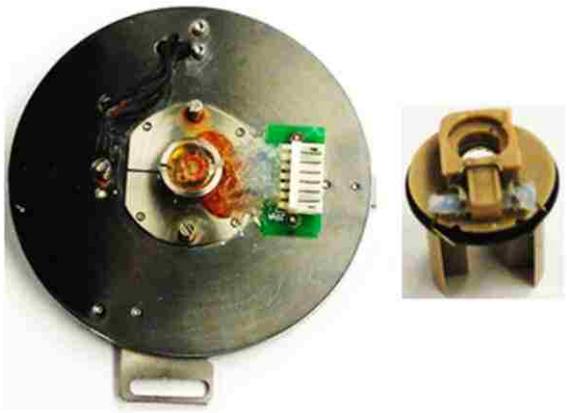

Figure A.2 Magnetic AC sample stage (left) and nosecone (right) used for MSM-AFM imaging.

III. *AFM Probes.* Triangular shaped silicon nitride cantilevers (MSCT-AUHW, Veeco Probes) with an average spring constant of 0.1 Nm^{-1} or less should be used. Do not use magnetic probes, or stiff probes with high spring constants.

IV. *Instrument Operation.* Focus the laser on the tip using the typical settings for contact mode AFM. Install the sample for imaging in air. Samples should have magnetic or paramagnetic character, and should respond to the flux of an AC electromagnetic field.

V. *Software Settings.* Open the PicoScan v5.3.3 software. Under **main menu**, select contact mode parameters for the Agilent 5500 AFM multipurpose scanner and MAC mode settings under AC parameters. Using the **Layout Editor,** choose eight channels capturing topography, friction, Aux IN BNC and Aux IN 5. Select both on top (raw) and bottom row (flattened).

VI. *Acquisition of Frequency Spectra.* Select the **AFM AC Mode Frequency** window. The frequency is swept both when the tip is disengaged (black line) and upon in contact with the sample surface (Figure A.3). Several sample resonance peaks are generated when the tip is

engaged (red line). Dynamic measurements can be investigated by selecting peaks on the spectrum while monitoring the contrast changes in amplitude and phase MSM views.

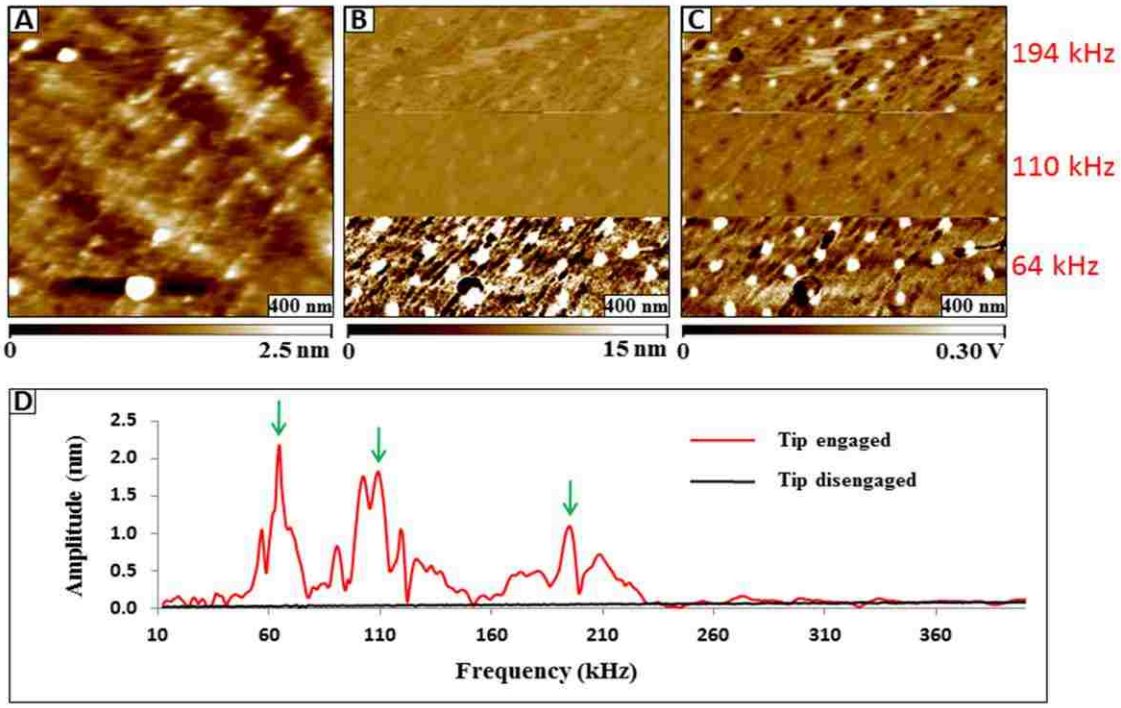

Figure A.3 Views of porphyrin nanocrystals acquired with different driving frequencies using dynamic MSM-AFM: A) Topography image. B) Amplitude view. C) Phase image. D) Spectrum showing selected frequencies peaks at 64, 110, 194 kHz, used to acquire image.

VII. *Acquisition of MSM Images with Dynamic Changes in Field Strength.* The AFM tip can be placed precisely on selected location. By incrementally changing the **Drive on %** (field strength), the magnitude of z-displacement of the tip can be determined in the amplitude signal. The contrast is much sharper in the amplitude MSM-AFM view when the field strength is at the highest (Figure A.4).

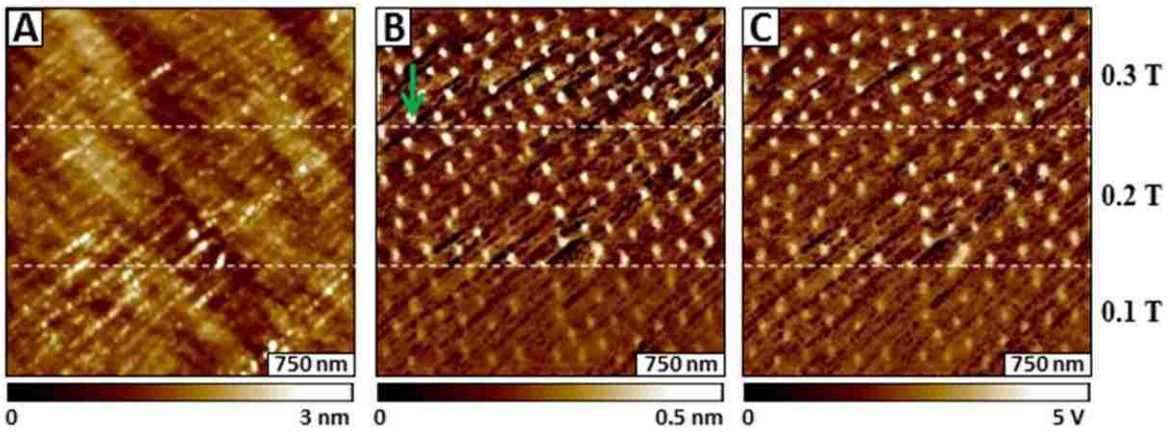

Figure A.4 Dynamic measurements for MSM-AFM images with changes in the electromagnetic field strength. A) Topography image. B) Amplitude view. C) Phase image.

VIII. *Acquisition of MSM Images with Dynamic Changes in Applied Magnetic Field.* The AFM tip can be placed precisely on selected location. By incrementally changing the field strength, the magnitude of z-displacement of the tip can be determined in the amplitude signal (Figure A.5).

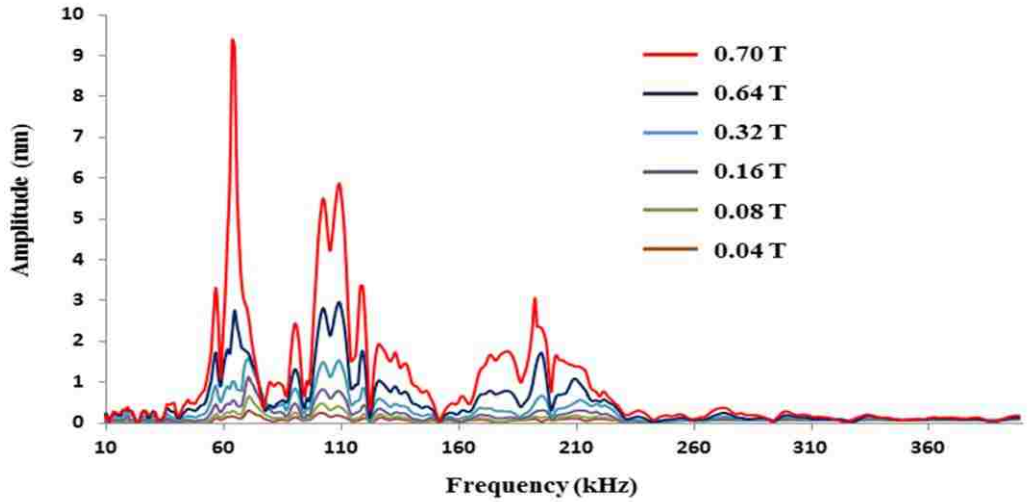

Figure A.5 Amplitude responses obtained by increasing the applied field strength. The amplitude spectra were acquired by parking the AFM probe on the nanocrystal of porphyrin indicated by a green arrow shown in Figure A.4.

APPENDIX B: PROTOCOL FOR CHARACTERIZATION OF CHARGE TRANSPORT USING CONDUCTIVE PROBE ATOMIC FORCE MICROSCOPY

1. Choose the contact-mode AFM settings for CS-AFM.
2. Place the sample on the AFM stage ensuring that there is a glass insulator.
3. Connect a conductive wire between the sample and the working electrode (Figure B1).
4. The continuity between the working electrode and the sample should be checked using a voltmeter to make sure that proper connection is accomplished.
5. Next, connect the sample stage connected to the microscope using the 3-pin cable.
6. Check the potential between the working electrode and ground using a voltmeter. The bias in the voltmeter should be the same as the voltage set point programmed in the software.

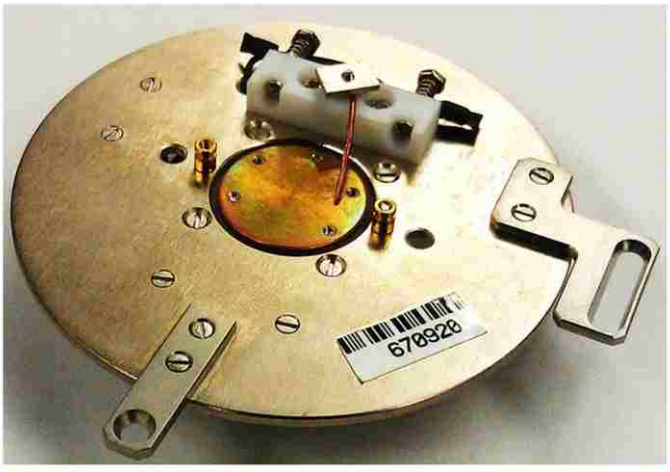

Figure B.1 Current sensing AFM sample plate.

Characterization using CS-AFM

1. Install the CS-AFM nose assembly into the scanner (Figure B.2).

Figure B.2 Scanner and CS-AFM nosecone for CS-AFM.

2. Load a conductive probe into nosecone assembly.
3. Align the laser on the cantilever, and then align the laser on the photodetector.
4. Use the software settings for contact mode AFM.
5. Using the software, select three buffers as follows; Topography, Deflection, and AuxIn BNC (CS-AFM Signal).
6. Use minimal force during imaging to reduce the wear of the conductive tip.
7. Execute an I-V spectroscopy sweep over the entire range (±10 V) and use this information to select a good voltage range to sweep, e.g. (±1 V
8. Start with 0.1 V and gradually ramp up the voltage to optimize the contrast in the CS-AFM image.

9. Acquire images with the reverse bias to determine if the image contrast flips, for example, change the bias setting from +0.1V to –0.1V.
10. Regularly check the connection between the working electrode and the sample using the voltmeter, to ensure a solid electrical connection.

APPENDIX C: LETTERS OF PERMISSION

Dear Serem

The Royal Society of Chemistry hereby grants permission for the use of the material specified below in the work described and in all subsequent editions of the work for distribution throughout the world, in all media including electronic and microfilm. You may use the material in conjunction with computer-based electronic and information retrieval systems, grant permissions for photocopying, reproductions and reprints, translate the material and to publish the translation, and authorize document delivery and abstracting and indexing services. The Royal Society of Chemistry is a signatory to the STM Guidelines on Permissions (available on request). Please note that if the material specified below or any part of it appears with credit or acknowledgement to a third party then you must also secure permission from that third party before reproducing that material. Please ensure that the published article carries a credit to The Royal Society of Chemistry in the following format: [Original citation] – Reproduced by permission of The Royal Society of Chemistry (RSC) for the Centre National de la Recherche Scientifique (CNRS) and the RSC and that any electronic version of the work includes a hyperlink to the article on the Royal Society of Chemistry website. The recommended form for the hyperlink is http://dx.doi.org/10.1039/DOI suffix, for example in the link http://dx.doi.org/10.1039/b110420a the DOI suffix is 'b110420a'. To find the relevant DOI suffix for the RSC paper in question, go to the Journals section of the website and locate your paper in the list of papers for the volume and issue of your specific journal. You will find the DOI suffix quoted there.

Regards

Gill Cockhead, Publishing Contracts & Copyright Executive
Royal Society of Chemistry,
Thomas Graham HouseScience Park,
Milton Road, Cambridge CB4 0WF,
UKTel +44 (0) 1223 432134,
Fax +44 (0) 1223 423623
http://www.rsc.org

Title: Studies of the growth, evolution, and self-aggregation of β-amyloid fibrils using tapping-mode atomi☐ force microscopy

Author: Wilson K. Serem,Cyrus K. Bett,Johnpeter N. Ngunjiri,Jayne C. Garno

Publication: Microscopy Research and Technique

Publisher: ☐ohn Wiley ☐nd Sons

Date: Jul 1, 2011

Order Completed

Thank you very much for your order.

This is a License Agreement between Wilson K Serem ("You") and John Wiley and Sons ("John Wiley and Sons"). The license consists of your order details, the terms and conditions provided by John Wiley and Sons, and the payment terms and conditions.

Get the printable license.

License Number	2772100926058
License date	Oct 18, 2011
Licensed content publisher	John Wiley and Sons
Licensed content publication	Microscopy Research and Technique
Licensed content title	Studies of the growth, evolution, and self-aggregation of β-amyloid fibrils using tapping-mode atomic force microscopy
Licensed content author	Wilson K. Serem,Cyrus K. Bett,Johnpeter N. Ngunjiri,Jayne C. Garno
Licensed content date	Jul 1, 2011
Start page	699
End page	708
Type of use	Dissertation/Thesis
Requestor type	Author of this Wiley article
Format	Print and electronic
Portion	Full article
Will you be translating?	No

Title: Single electron tunneling and manipulation of nanoparticles on surfaces at room temperature

Author: Guohua Yang,Li Tan,Yiyun Yang,Shaowei Chen,Gang-Yu Liu

Publication: Surface Science

Publisher: Elsevier

Date: 1 September 2005

Order Completed

Thank you very much for your order.

This is a License Agreement between Wilson K Serem ("You") and Elsevier ("Elsevier"). The license consists of your order details, the terms and conditions provided by Elsevier, and the payment terms and conditions.

Get the printable license.

License Number	2766790512309
License date	Oct 12, 2011
Licensed content publisher	Elsevier
Licensed content publication	Surface Science
Licensed content title	Single electron tunneling and manipulation of nanoparticles on surfaces at room temperature
Licensed content author	Guohua Yang,Li Tan,Yiyun Yang,Shaowei Chen,Gang-Yu Liu
Licensed content date	1 September 2005
Licensed content volume number	589
Licensed content issue number	1-3
Number of pages	10
Type of Use	reuse in a thesis/dissertation
Portion	figures/tables/illustrations
Number of figures/tables/illustrations	1
Format	both print and electronic
Are you the author of this Elsevier article?	No
Will you be translating?	No
Order reference number	3000448944
Title of your thesis/dissertation	DYNAMIC MEASUREMENTS WITH SCANNING PROBE MICROSCOPY: SURFACE STUDIES USING NANOSTRUCTURED TEST PLATFORMS OF METALLOPORPHYRINS, NANOPARTICLES AND AMYLOID FIBRILS
Expected completion date	Dec 2011

Estimated size (number of pages)	200
Elsevier VAT number	GB 494 6272 12
Permissions price	0.00 USD
VAT/Local Sales Tax	0.0 USD / 0.0 GBP
Total	0.00 USD

PERMISSION/LICENSE IS GRANTED FOR YOUR ORDER AT NO CHARGE

This type of permission/license, instead of the standard Terms & Conditions, is sent to you because no fee is being charged for your order. Please note the following:

- Permission is granted for your request in both print and electronic formats.
- If figures and/or tables were requested, they may be adapted or used in part.
- Please print this page for your records and send a copy of it to your publisher/graduate school.
- Appropriate credit for the requested material should be given as follows: "Reprinted (adapted) with permission from (COMPLETE REFERENCE CITATION). Copyright (YEAR) American Chemical Society." Insert appropriate information in place of the capitalized words.
- One-time permission is granted only for the use specified in your request. No additional uses are granted (such as derivative works or other editions). For any other uses, please submit a new request.

Order Completed

Thank you very much for your order.

This is a License Agreement between Wilson K Serem ("You") and Nature Publishing Group ("Nature Publishing Group"). The license consists of your order details, the terms and conditions provided by Nature Publishing Group, and the payment terms and conditions.

Get the printable license.

License Number	2775470906016
License date	Oct 24, 2011
Licensed content publisher	Nature Publishing Group
Licensed content publication	Nature Materials
Licensed content title	Collective behaviour in two-dimensional cobalt nanoparticle assemblies observed by magnetic force microscopy
Licensed content author	Victor F. Puntes , Pau Gorostiza , Deborah M. Aruguete , Neus G. Bastus and A. Paul Alivisatos
Licensed content date	Apr 1, 2004
Type of Use	reuse in a thesis/dissertation
Volume number	3
Issue number	4
Requestor type	academic/educational
Format	print and electronic
Portion	figures/tables/illustrations
Number of figures/tables/illustrations	1
High-res required	no
Figures	2
Author of this NPG article	no
Your reference number	3000448944
Title of your thesis / dissertation	DYNAMIC MEASUREMENTS WITH SCANNING PROBE MICROSCOPY: SURFACE STUDIES USING NANOSTRUCTURED TEST PLATFORMS OF METALLOPORPHYRINS, NANOPARTICLES AND AMYLOID FIBRILS
Expected completion date	Dec 2011

Estimated size (number of pages)	200
Total	0.00 USD

PERMISSION/LICENSE IS GRANTED FOR YOUR ORDER AT NO CHARGE

This type of permission/license, instead of the standard Terms & Conditions, is sent to you because no fee is being charged for your order. Please note the following:

- Permission is granted for your request in both print and electronic formats.
- If figures and/or tables were requested, they may be adapted or used in part.
- Please print this page for your records and send a copy of it to your publisher/graduate school.
- Appropriate credit for the requested material should be given as follows: "Reprinted (adapted) with permission from (COMPLETE REFERENCE CITATION). Copyright (YEAR) American Chemical Society." Insert appropriate information in place of the capitalized words.
- One-time permission is granted only for the use specified in your request. No additional uses are granted (such as derivative works or other editions). For any other uses, please submit a new request.

Dear Mr. Wilson Serem,

Thank you for placing your order through Copyright Clearance Center's RightsLink service. Nature Publishing Group has partnered with RightsLink to license its content. This notice is a confirmation that your order was successful.

Your order details and publisher terms and conditions are available by clicking the link below:
http://s100.copyright.com/CustomerAdmin/PLF.jsp?lID=2011101_1319479170016
Order Details
Licensee: Wilson K Serem
License Date: Oct 24, 2011
License Number: 2775470906016
Publication: Nature Materials
Title: Collective behaviour in two-dimensional cobalt nanoparticle assemblies observed by magnetic force microscopy
Type Of Use: reuse in a thesis/dissertation
Order Reference: 3000448944
Total: 0.00 USD
To access your account, please visit https://myaccount.copyright.com.
Please note: Online payments are charged immediately after order confirmation; invoices are issued daily and are payable immediately upon receipt.
To ensure we are continuously improving our services, please take a moment to complete our customer satisfaction survey.
B.1:v4.2

+1-877-622-5543 / Tel: +1-978-646-2777
customercare@copyright.com
http://www.copyright.com

CONTRACTS-COPYRIGHT (shared) Contracts-Copyright@rsc.org to wserem1

Dear Mr. Serem

The Royal Society of Chemistry hereby grants permission for the use of the material specified below in the work described and in all subsequent editions of the work for distribution throughout the world, in all media including electronic and microfilm. You may use the material in conjunction with computer-based electronic and information retrieval systems, grant permissions for photocopying, reproductions and reprints, translate the material and to publish the translation, and authorize document delivery and abstracting and indexing services. The Royal Society of Chemistry is a signatory to the STM Guidelines on Permissions (available on request). Please note that if the material specified below or any part of it appears with credit or acknowledgement to a third party then you must also secure permission from that third party before reproducing that material. Please ensure that the published article carries a credit to The Royal Society of Chemistry in the following format: [Original citation] – Reproduced by permission of The Royal Society of Chemistry (RSC) for the Centre National de la Recherche Scientifique (CNRS) and the RSC and that any electronic version of the work includes a hyperlink to the article on the Royal Society of Chemistry website. The recommended form for the hyperlink is http://dx.doi.org/10.1039/DOI suffix, for example in the link http://dx.doi.org/10.1039/b110420a the DOI suffix is 'b110420a'. To find the relevant DOI suffix for the RSC paper in question, go to the Journals section of the website and locate your paper in the list of papers for the volume and issue of your specific journal. You will find the DOI suffix quoted there.

Regards

Gill Cockhead Publishing Contracts & Copyright Executive
Gill Cockhead, Publishing Contracts & Copyright Executive
Royal Society of Chemistry, Thomas Graham HouseScience Park,
Milton Road, Cambridge CB4 0WF,
UK Tel +44 (0) 1223 432134,
Fax +44 (0) 1223 423623
http://www.rsc.org

VITA

Wilson Kiptugen Serem was born in Eldoret, Kenya, and attended Mother of Apostles Seminary for his high school education. He received a bachelor's of science degree in chemistry from the University of Nairobi in 1997. Thereafter he was awarded master's degree in chemistry from Moi University, Kenya, in 2002. Serem was hired as a lecturer at Masinde Muliro University of Science & Technology to teach general and introduction to organic chemistry between 2002 and 2005. He is currently on study leave for doctoral training at Louisiana State University. In 2005, Serem enrolled at LSU to pursue a chemistry doctorate degree with an emphasis in analytical chemistry, under the direction of Prof. Jayne Garno. During studies at LSU, Serem submitted two first author (*Journal of Microscopy Research & Technique* 2010 and *Encyclopedia of Analytical Chemistry* 2011) and seven co-authored journal articles *(Macromolecules* 2011, *ACS Chemical Neuroscience* 2010, *Langmuir* 2010, *ACS Chemical Neuroscience* 2010**,** *Nanomedicine*, 2008, *Scanning*, 2008, *Chemistry*, *A European Journal*, 2007) and six book chapters. Serem is completing work for three first author articles for publication. Serem presented his original research results in regional, national and international conferences totaling seventeen posters and two oral presentations (PACIFICHEM, Hawaii and NOBCChE, Philadelphia). Serem also co-authored five poster presentations. Serem received seven travel awards as follows: three LSU Graduate Travel stipends, Advancing Science Travel Award (NOBCChE, twice) and a Coates Graduate Award (twice). Serem won the best student poster award at an international conference, in the Colloids & Surfaces Symposium of the American Chemical Society 235st National meeting (Washington DC, 2008). He also won a best student poster award from the Society of Applied Spectroscopy (Orlando, FL 2009). At LSU,

Serem received the James G. Traynham Distinguished Graduate Student Award in 2009. In 2011, he received the prestigious Robinson Award for excellence in analytical chemistry research and teaching at LSU. Serem plans to continue postdoctoral studies at Texas A&M University, as a surface scientist under the direction of Prof. Daniel Shantz at the Materials Characterization Facility, beginning in November, 2011.